# NANOSTRUCTURED TUNGSTEN AND MOLYBDENUM OXIDES AS ADVANCED ELECTRODE MATERIALS FOR ENERGY STORAGE APPLICATIONS

A Thesis submitted in partial fulfillment for the Degree of

DOCTOR OF PHILOSOPHY

in the School of chemical sciences
Goa University

By

AKSHAY V. SALKAR
SCHOOL OF CHEMICAL SCIENCES
GOA UNIVERSITY
GOA

APRIL 2023

# DECLARATION

I, **Akshay Vinod Salkar** hereby declare that this thesis represents work which has been carried out by me and that it has not been submitted, either in part or full, to any other University or Institution for the award of any research degree.

Place: Taleigao
Date :

Akshay Vinod Salkar
Ph.D. Candidate
School of Chemical Sciences,
Goa University, Goa

# CERTIFICATE

I hereby certify that the above Declaration of the candidate, Mr. Akshay Vinod Salkar is true and the work was carried out under my supervision.

Dr. Pranay P. Morajkar
Research Guide,
School of Chemical sciences,
Goa University, Goa.

**To my parents, who have always believed in me and supported my dreams. This thesis is dedicated to you with love and gratitude.**

# ACKNOWLEDGEMENT

*In undertaking my Ph.D., I underwent a truly life-changing experience that I would not have been able to achieve without the support, guidance and unconditional help provided by many people around me. In this regard, I would like to express my deep gratitude to everyone who has helped make this thesis successful, whether directly or indirectly.*

*First and foremost, I would like to sincerely thank my thesis supervisor* ***Dr. Pranay P. Morajkar*** *for giving me an opportunity to conduct my research under his valuable guidance. My present research work is the result of his patience, enthusiasm, co-operation, and suggestions. Also, I am deeply grateful for the independence he provided me with to conduct the work and the patience he showed me when I failed. The role he has played in my life has been very important to me, and I will be forever grateful to him. I thank my co-guide* ***Prof. Sheshanath V. Bhosale*** *for being very supportive throughout my Ph.D. tenure. Special thanks to my subject experts* ***Prof. B. R. Srinivasan*** *and* ***Prof. Saroj S. Baral****. Your encouraging words and thoughtful, detailed feedback have been very important to me. The knowledge and ingenuity you possess will always be something I aspire to.*

*I express my sincere gratitude to our Honorable Vice-chancellor,* ***Prof. Harilal B. Menon****,* ***Registrar Prof. Vishnu S. Nadkarni****, and also to our former Vice-chancellor* ***Prof. Varun Sahni*** *and former Registrar,* ***Prof. Y. V. Reddy****, Goa University for allowing me to conduct my research work in this institute and frequent support during all the times of need. I am indeed thankful to* ***Prof. V. M. S. Verenkar*** *(Dean School of chemical sciences),* ***Prof. V. S. Nadkarni*** *(former Dean, School of chemical sciences),* ***Prof. B. R. Srinivasan*** *(former Head, Department of Chemistry, Goa University) for providing all the necessary facilities for my research work.*

*I take this opportunity to thank all my teachers and faculty members of School of Chemical Sciences, late* ***Dr. Pankaj Singh****,* ***Prof. R. N. Shirsat****,* ***Prof. Sunder Dhuri****,* ***Dr. Sandesh Bugde****,* ***Dr. Vivekanand Gobre****,* ***Dr. Anjani Nagvenkar****,* ***Dr. Shrikant Naik****,* ***Dr. Prajesh Volvoikar****,* ***Dr. Diptesh Naik****,* ***Dr. Prachi Torney****,* ***Dr. Rupesh Patre****,* ***Dr. Rohan Kunkalekar****,* ***Dr. Bidhan Shinkre****,* ***Dr. Digamber Porob****,* ***Dr. Delicia Barretto****,* ***Prof. Sheshanath Bhosale****,* ***Mr. Vishnu Chari****,* ***Dr. Kedar Naik****,* ***Dr. Kanchanmala Deshpande****,* ***Dr. Kiran Dhavaskar****,* ***Ms. Siddhali Girkar****,* ***Dr. Hari Kadam****,* ***Dr. Savita Kundaikar****,* ***Dr.***

*__Rohan Kunkalekar__, __Dr. Rupesh Kunkalkar__, __Dr. Vinod Mandrekar__, and __Dr. Amrita Kharangate__ for their encouragement and support. A special thanks goes out to __Dr. Purnakala Samant__, __Mrs. Mamta Prabhugaonkar__, __Dr. Vrushali Joshi__, __Prof. Ravi X. Fernandes__ and __Dr. Jyoti Sawant__ for their motivation and support.*

*I wish to thank __Prof. Chandrashekhar V. Rode__ (NCL, Pune), __Prof. Anand Khrishnasamy__ (IIT, Madras) and __Prof. Santosh Haram__ (Savitribai Phule Pune University), for allowing me to train with their research group. I also thank __Dr. Arkke Eskola__ (University of Helsinki, Finland) for hosting me at his institute for a research visit as part of the DST-INNO-INDIGO project visit. I also wish to thank __Prof. Siddhanath V. Bhosale__ and __Mr. Madan Biradar__ for their fruitful discussions and collaborative work on organic supercapacitors.*

*The most helpful and supportive person I've known during my Ph.D. has been my friend and a member of my research group, __Ms. Amarja P. Naik__ and I will always be grateful for her support. I also owe my gratitude towards my junior group member, __Ms. Sarvesha S. Shetgaonkar__ and __Ms. Samantha da Costa__ for creating a positive and friendly working environment. I am also thankful to my seniors from the department, __Dr. Johnross__, __Dr. Vishal__, __Dr. Sumit__, __Dr. Dattaprasad__, __Dr. Satu__, __Dr. Shambhu__, __Dr. Kedar__, __Dr. Chandan__, __Dr. Rahul__, __Dr. Sudesh__, __Dr. Pooja__, __Dr. Abhijeet__, __Dr. Prajyoti__, __Dr. Celia__, __Dr. Madhavi__, __Dr. Meera__, __Dr. Sagar__, __Dr. Daniel__, __Dr. Savita__, __Dr. Rita__ and __Dr. Sudarshana__ for their kind and supportive approach towards me.*

*I would also like to extend my thanks to my research colleagues and friends, __Ms. Lima__, __Ms. Luann__, __Mr. Shashank__, __Mr. Ketan__, __Dr. Vishal__, __Dr. Sarvesh__, __Dr. Rahul__, __Dr. Pratik__, __Ms. Neha__, __Ms. Sanjali,__ __Ms. Mangala__, __Ms. Seneca__, __Mr. Vipul__, __Ms. Sonam__, __Ms. Geeta__, __Mr. Pritesh__, __Ms. Sanjali__, __Mr. Ratan__, __Mr. Dinesh__, __Mr. Kerba__, __Ms. Gayatri__, __Mr. Vishal__, __Mr. Vilas__, __Mr. Harshad__, __Dr. Dileep__ and __Mr. Jostin__ for their support.*

*A special thanks to my friends __Dr. Amarja Naik__, __Ms. Lima Rodrigues__, __Ms. Luann D' Souza__, __Ms. Sarvesha Shetgaonkar__, and __Ms. Samantha da Costa__ for creating beautiful memories for life during this journey. I am also thankful to my cousins, __Mr. Rajit Raikar__, __Mr. Pramit Raikar__, and __Mr. Rushik Madkaikar__, for their constant support and encouragement during my Ph.D. journey.*

*I sincerely thank the non-teaching staff of the School of Chemical Sciences-Goa University, the librarian and other staff in the library of Goa University for being kind and helpful. Special gratitude goes out to the funding agency, DST-New Delhi, for the research assistantship through the DST-IMRCD/INNO-INDIGO project scheme that provided fellowship and funding for the work.*

*Last but not least, my heartfelt and due respect to my family, my father* ***Mr. Vinod P. Salkar****, my mother* ***Mrs. Vishakha V. Salkar****, my wife* ***Mrs. Srusti A. Salkar****, my father-in-law* ***Mr. Gopalkrishna Gazinkar****, my mother-in-law* ***Mrs. Savita Gazinkar****, and my brother-in-law* ***Mr. Vishwa Gazinkar****, for their strong support and encouragement in every step of this journey which has brought me to this present stage.*

*To conclude, I thank the almighty for all the blessings he has bestowed upon me and for giving me the strength and patience to complete my research.*

*……….Mr. Akshay V. Salkar*

# Contents

List of Abbreviations………………………………………………………………….. i

List of Tables………………………………………………………………………….. iii

List of Figures…………………………………………………………………………. V

## CHAPTER I: INTRODUCTION

**1.1** **Introduction**………………………………………………………………... **1**

**1.2** **History of supercapacitors**……………………………………………………... **2**

**1.3** **Types of supercapacitors and their mechanisms**………………………………. **4**

**1.3.1** Electric double-layer capacitors………………………………………. **4**

**1.3.2** Pseudocapacitors………………………………………………………… **6**

**1.4** **Electrochemical energy storage based on tungsten oxide and molybdenum oxides**………………………………………………………………………... **6**

**1.5** **Crystallographic characteristics of $WO_3$**………………………………...…….. **8**

**1.6** **Crystallographic characteristics of $MoO_3$**……………………………………… **11**

**1.7** **Role of ion intercalation and electrochemical charge storage**……………..…...…... **12**

**1.8** **Nanostructured $WO_3$ for supercapacitor applications**…………………..………… **13**

**1.9** **Nanostructured $MoO_3$ for supercapacitor applications**……………………...…..… **20**

**1.10** **Thesis objectives**…………………………………………………………...…….. **25**

**1.11** **References**……………………………………………………………………….. **25**

## CHAPTER II: EXPERIMENTATION

**2.1** **Chemicals used**………………………………………………………………. **42**

**2.2** **Experimental: Synthesis strategies & procedures**………………..…………………. **42**

2.2.1 Synthesis of $WO_3$ nanoparticles……………………….………………………. **42**

2.2.2 Synthesis of 1D $WO_{3-x}$ nanorods……………………….……………………… **42**

2.2.3 Synthesis of 2D $WO_{3-x}$ microsheets…………………………………………… **43**

2.2.4 Synthesis of 3D $WO_{3-x}$ microstructures……………………………………….. **43**

2.2.5 Effect of synthesis pH and calcination temperature on the growth of 1D $WO_{3-x}$ nanorods……………………………………………………………...……. **43**

2.2.6 Effect of urea to metal ratio on the $WO_{3-x}$ morphologies…….…………………... **43**

2.2.7 Effect of substituted ureas on the morphology of $WO_{3-x}$…….…………………… **43**

2.2.8 Synthesis of 3D $WO_{3-x}$/C microfibers using citric acid……………………….. **44**

2.2.9 pH dependent synthesis of 3D $WO_{3-x}$/C microfibers………………………….. **44**

2.2.10 Temperature dependent synthesis of 3D $WO_{3-x}$/C microfibers……………….. **45**

2.2.11 Effect of metal to SDA ratio on the growth of 3D $WO_{3-x}$/C microfibers……… **45**

2.2.12 Synthesis of $MoO_{3-x}$ nanoparticles…………………………………………….. **45**

2.2.13 Synthesis of 2D $MoO_{3-x}$ microplates……………….………………………… **46**

2.2.14 Synthesis of 2D $MoO_{3-x}$ microdisks…..……………..………………………… **46**

2.2.15 Influence of synthesis pH on $MoO_{3-x}$ morphologies………………………... **46**

2.2.16 Influence of calcination temperature on $MoO_{3-x}$ morphologies……………… **46**

2.2.17 Effect of metal to urea ratio on $MoO_{3-x}$ morphologies…………………….... **46**

2.2.18 Effect of using substituted ureas as structure directing agents on morphology of $MoO_{3-x}$…………………………..……………………………………………… **47**

2.2.19 Synthesis of 3D $MoO_{3-x}$ microflowers using citric acid………………………. **47**

2.2.20 pH dependent synthesis of 3D $MoO_{3-x}$ microflowers………………………. **47**

2.2.21 Temperature dependent synthesis of 3D $MoO_{3-x}$ microflowers……………… **48**

2.2.22 Effect of Mo to citric acid ratio on the morphology of 3D $MoO_{3-x}$ microflowers…………………………………………………………………………… **48**

**2.3 Instrumentation**……………………………………………………………….. **48**

2.3.1 Characterization techniques…………………………………………………… **48**

2.3.1.1 Thermogravimetric differential thermal analysis (TG-DTA)…………………. **49**

2.3.1.2 Infrared spectroscopy (IR)……………………………………………………….. **49**

2.3.1.3 Powder X-ray diffraction (XRD)……………………………………………… **50**

2.3.1.4 Scanning electron microscopy (SEM) & Energy Dispersive X-ray spectroscopy (EDS)……………………………………………………………………… **51**

2.3.1.5 High resolution transmission electron microscopy (HRTEM) and selected area electron diffraction (SAED) analysis…………………………………………………... **52**

2.3.1.6 X-ray photoelectron spectroscopy (XPS)……………………………………… **52**

2.3.1.7 BET surface area analysis……………………………………………………… **53**

2.3.1.8 Raman spectroscopy…………………………………………………………… **53**

2.3.1.9 Electron paramagnetic resonance spectroscopy……………………………….. **54**

2.3.2 Electrochemical charge storage measurements………………………………... **54**

2.3.2.1 Electrode preparation…………………………………………………………….. **55**

2.3.2.2 Optimizing the electrode mass loading percentages…………………………….. **56**

2.3.2.3 Cyclic Voltammetry (CV)………………………….……………………... 57

2.3.2.4 Galvanostatic charge-discharge analysis (GCD)……………………….……. 57

2.3.2.5 Electrochemical impedance spectroscopy (EIS)……………………….……. 58

2.4 **Formulas used for calculating electrochemical metrices**……………….……….... 58

2.4.1 Specific capacitance calculations…………….…………………………. 58

2.4.1.1 Three electrode CV measurements…………..…………..……………………. 58

2.4.1.2 Three electrode GCD measurements…………………..…………………….. 59

2.4.1.3 Two electrode CV measurements………………….…………….....………… 59

2.4.1.4 Two electrode GCD measurements………….………………………………. 59

2.4.2 Energy and power densities from two electrode GCD studies……………….… 59

2.4.3 Electroactive area………………………………………………………. 59

2.4.4 Diffusion coefficient…………….………………...……………………… 60

2.5 **References**……………………………………………………………………... 60

## CHAPTER III: $WO_{3-x}$ NANO AND MICROSTRUCTURES AS CHARGE STORAGE ELECTRODE MATERIALS

3.1 **Prologue**………………………………………………………………………... 63

3.2 **Results and discussions**……………………………………………………….. 64

3.2.1 TG-DTA studies……………………...………………………….…….…… 64

3.2.2 IR studies……………………...…………………….…………………….. 65

3.2.3 XRD studies………………………………………….………………….. 65

3.2.4 Morphological studies…………………………………………………….... 66

3.2.4.1 Effect of synthesis pH…………………………………………………… 66

3.2.4.2 Effect of W to urea ratio on the growth of 1D $WO_{3-x}$ nanorods…………...…. 68

3.2.4.3 Effect of calcination temperature on the growth of 1D $WO_{3-x}$ nanorods…….. 70

3.2.4.4 Effect of calcination time on the growth of 1D $WO_{3-x}$ nanorods……………... 70

3.2.5 HRTEM studies……………………………...…………………….…….. 71

3.2.6 XPS studies……………………...………………………………………. 72

3.2.7 Growth mechanism of $WO_{3-x}$ nanostructures…………………...…………… 74

3.3 **Evaluation of the charge storage properties of nanostructured $WO_{3-x}$ synthesized using urea**………………………...……………………………......................... 77

3.3.1 Three electrode charge storage studies……………………………………….. 77

3.3.2 Electrochemical performance of the $WO_{3-x}$//AC asymmetric supercapacitor

device……………………………………………………………………………..… **83**
**3.4 Effect of substituted ureas on growth characteristics of $WO_{3-x}$ nanorods**……….. **85**
3.4.1 SEM studies…..……....……………………………………………….... **87**
3.4.2 HRTEM studies……………………..…………………………….….....…... **88**
3.4.3 XRD studies……………….....……………………………...…..……… **89**
3.4.4 XPS studies……………………………………………………………… **91**
3.4.5 TG-DTA and IR studies……………..………………………………….... **94**
3.4.6 Influence of urea substitution on the growth characteristics of 1D $WO_{3-x}$ nanorods…………………..……………………………………………… **96**
**3.5 Evaluation of the charge storage properties of nanostructured $WO_{3-x}$ synthesized using substituted ureas**………………………………………………………….. **98**
3.5.1 Three electrode charge storage studies……………………………………… **98**
3.5.2 Electrochemical performance of the $WO_{3-x}$//AC asymmetric supercapacitor device……………………………………………….……...……………………… **103**
**3.6 Designing 3D $WO_{3-x}$/C microfibers using citric acid**………………………………... **105**
3.6.1 SEM studies………………………………………………….……….....……... **106**
3.6.2 HRTEM studies…………………………………………………………………. **108**
3.6.3 TG-DTA and elemental studies………………………………………………. **109**
3.6.4 IR and XRD studies…………………………………………………………... **110**
3.6.5 Raman and EPR studies…………………………………………...………. **111**
3.6.6 XPS studies…………………………………………………………....………… **113**
3.6.7 Growth mechanism of 3D $WO_{3-x}$/C microfibers……………………………... **116**
**3.7 Evaluation of the charge storage properties of microstructured 3D $WO_{3-x}$/C microfibers and hierarchical structures**……………………………………………... **118**
3.7.1 Three electrode charge storage studies………………………………………….. **118**
3.7.2 Electrochemical performance of the $WO_{3-x}$/C//AC asymmetric supercapacitor devices……………………………………………………………………………….. **122**
**3.8 The impact of nanostructuring in $WO_{3-x}$ on the charge storage performance**……. **124**
**3.9 Conclusions**…………………………………………………………………...….. **126**
**3.10 References**……………………………………………………………………… **127**

## CHAPTER IV: $MoO_{3-x}$ MICROSTRUCTURES AS CHARGE STORAGE ELECTRODE MATERIALS

**4.1 Prologue**……………………………………………………………………...... **138**

**4.2 Results and discussions**………………………………………………………….. **139**

4.2.1 Morphological studies……..…………………………………………………. **139**

4.2.2 TG-DTA studies……………………………………………………………… **142**

4.2.3 IR studies…………………………………………………………………….... **144**

4.2.4 XRD studies…………………………………………………………………... **144**

4.2.5 Raman studies………………………………………………………………… **145**

4.2.6 XPS and EPR studies…………………………………………………………. **146**

4.2.7 Plausible growth mechanism for 2D $MoO_{3-x}$ microplates and microdisks……... **148**

**4.3 Evaluation of the charge storage properties of microstructured 2D $MoO_{3-x}$ synthesized using urea**…………………………………………………………… **150**

4.3.1 Three electrode charge storage studies……………………………………….. **150**

4.3.2 Electrochemical performance of the $MoO_{3-x}$//AC asymmetric supercapacitor device……………………………………………………………………………..... **154**

**4.4 Effect of substituted ureas on growth characteristics of $MoO_{3-x}$ microstructures**…………………………………………………………………... **158**

4.4.1 SEM studies…………………………………………………………………... **158**

4.4.2 HRTEM studies………………………………………………………………. **159**

4.4.3 XRD studies…………………………………………………………………... **160**

4.4.4 XPS studies…………………………………………………………………… **161**

4.4.5 TG-DTA and IR studies……………………………………………………… **164**

**4.5 Evaluation of the charge storage properties of microstructured 2D $MoO_{3-x}$ synthesized using substituted ureas**…..………………………………………...… **165**

4.5.1 Three electrode charge storage studies……………………………………….. **165**

4.5.2 Electrochemical performance of the $MoO_{3-x}$//AC asymmetric supercapacitor device………………………………………………………………………………. **170**

**4.6 Designing 3D $MoO_{3-x}$ microflowers with exceptional charge storage performance**…………………………………………………………………...… **173**

4.6.1 SEM studies…………………………………………………………………... **174**

4.6.2 HRTEM studies………………………………………………………………. **176**

4.6.3 TG-DTA studies……………………………………………………………… **176**

4.6.4 IR and XRD studies………………………………………………………….. 177
4.6.5 Raman and XPS studies………………………………………………………. 179
4.6.6 Growth mechanism of 3D $MoO_{3-x}$ microflowers……………………………... 180
**4.7 Evaluation of the charge storage properties of 3D $MoO_{3-x}$ microflowers**………….. **182**
4.7.1 Three electrode charge storage studies……………………………………….. 182
4.7.2 Electrochemical performance of the MMF//AC asymmetric supercapacitor device……………………………………………………………………………… 185
**4.8 The impact of microstructuring in $MoO_{3-x}$ on the charge storage performance**….. **187**
**4.9 Conclusions**…………………………………………………………..……….. **188**
**4.10 References**……………………………………………………………………… **189**

## CHAPTER V: CONCLUSIONS OF THE THESIS

**5.1 Conclusions**…………………………………...…………………………….. **199**
**Appendix I**……………………………………………………………….………….... **204**
**Appendix II**…………………………………………………………..………………. **223**
**Appendix III**………………………………………………………….……………… **227**

# List of abbreviations

| | |
|---|---|
| SC | Supercapacitor |
| EDLC | Electric double layer capacitor |
| PC | Pseudocapacitor |
| TG-DTA | Thermogravimetric-Differential Thermal Analysis |
| IR | Infrared Spectroscopy |
| XRD | Powder X-ray Diffraction |
| SEM | Scanning Electron Microscopy |
| EDX | Energy-Dispersive X-ray Spectroscopy |
| HRTEM | High Resolution-Transmission Electron Microscopy |
| SAED | Selected area electron diffraction |
| BET | Brunauer-Emmett-Teller surface area analyzer |
| EPR | Electron Paramagnetic Resonance spectroscopy |
| XPS | X-ray Photoelectron Spectroscopy |
| CV | Cyclic Voltammetry |
| GCD | Galvanostatic charge-discharge |
| EIS | Electrochemical impedance spectroscopy |
| PD | Power density |
| ED | Energy density |
| $C_{sp}$ | Specific capacitance |
| EA | Electroactive area |
| CP | Toray carbon paper |
| AC | Actived carbon |
| PVDF | Poly (vinylidene fluoride) |
| PVA | Polyvinyl alcohol |
| WP | $WO_3$ nanoparticles |
| WN | $WO_{3-x}$ nanorods synthesized with urea |
| 3DW | 3D $WO_{3-x}$ hierarchical structures |
| 2DW | 2D $WO_{3-x}$ microsheets |
| WC | $WO_{3-x}$ nanorods synthesized using carbohydrazide |
| WM | $WO_{3-x}$ synthesized using N-methylurea |

| | |
|---|---|
| WSC | $WO_{3-x}$ synthesized using semicarbazide |
| WT | $WO_{3-x}$ synthesized using tetramethylurea |
| WF | $WO_{3-x}$/C microfibers synthesized using citric acid |
| WH | $WO_{3-x}$/C hierarchical structures synthesized using citric acid |
| MP | $MoO_{3-x}$ microplates synthesized using urea |
| MD | $MoO_{3-x}$ microdisks synthesized using urea |
| MA | $MoO_{3-x}$ agglomerated particles |
| MC | $MoO_{3-x}$ microplates synthesized using carbohydrazide |
| MSC | $MoO_{3-x}$ synthesized using semicarbazide |
| MM | $MoO_{3-x}$ synthesized using N-methylurea |
| MT | $MoO_{3-x}$ synthesized using tetramethylurea |
| MMF | $MoO_{3-x}$ microflowers synthesized using citric acid |

# List of tables

CHAPTER I: INTRODUCTION

**1.1** Analysis of the morphological modifications of nanostructured $WO_3$ and their supercapacitor performance based on the synthesis method. **17**

**1.2** Analysis of the morphological modifications of nanostructured $MoO_3$ and their supercapacitor performance based on the synthesis method. **23**

CHAPTER III: $WO_{3-x}$ NANO AND MICROSTRUCTURES AS CHARGE STORAGE ELECTRODE MATERIALS

**3.1** The percentage of species obtained from the XPS peak area integration of narrow scan spectra. **74**

**3.2** Summary of the electroactive and BET surface area for the different $WO_{3-x}$ nanostructures. **80**

**3.3** Summary of specific capacitance values calculated from CV curves obtained for the different $WO_{3-x}$ nanostructures. **81**

**3.4** Summary of specific capacitance values calculated from GCD curves obtained for the different $WO_{3-x}$ nanostructures. **82**

**3.5** The percentage of species obtained from the XPS peak area integration of narrow scan spectra of WC and WT. **92**

**3.6** Summary of the electroactive and BET surface area for the different $WO_{3-x}$ synthesized using substituted ureas. **100**

**3.7** Summary of specific capacitance values calculated from CV curves obtained for $WO_{3-x}$ synthesized using substituted ureas. **101**

**3.8** Summary of specific capacitance values calculated from GCD analysis obtained for $WO_{3-x}$ synthesized using substituted ureas. **102**

**3.9** The percentage of species obtained from the XPS peak area integration of narrow scan spectra of WF and WH. **115**

**3.10** Summary of specific capacitance values calculated from CV curves obtained for WF and WH. **120**

**3.11** Summary of specific capacitance values calculated from GCD analysis obtained for WF and WH. **121**

## CHAPTER IV: $MoO_{3-x}$ MICROSTRUCTURES AS CHARGE STORAGE ELECTRODE MATERIALS

**4.1** The percentage of species obtained from the XPS peak area integration of narrow scan spectra. **148**

**4.2** Summary of the electroactive and BET surface area for $MoO_{3-x}$ microstructures. **152**

**4.3** Summary of specific capacitance values calculated from CV curves obtained for the different $MoO_{3-x}$ microstructures. **153**

**4.4** Summary of specific capacitance values calculated from GCD curves obtained for the different $MoO_{3-x}$ microstructures. **154**

**4.5** The percentage of species obtained from the XPS peak area integration of narrow scan spectra of MC and MT. **163**

**4.6** Summary of the electroactive and BET surface area for the different $MoO_{3-x}$ synthesized using substituted ureas. **167**

**4.7** Summary of specific capacitance values calculated from CV curves obtained for $MoO_{3-x}$ synthesized using substituted ureas. **168**

**4.8** Summary of specific capacitance values calculated from GCD analysis obtained for $MoO_{3-x}$ synthesized using substituted ureas. **169**

**4.9** The percentage of species obtained from the XPS peak area integration of narrow scan spectra of MMF. **180**

**4.10** Summary of specific capacitance values calculated from CV curves obtained for MMF. **183**

**4.11** Summary of specific capacitance values calculated from GCD analysis of MMF. **184**

# List of figures

**CHAPTER I: INTRODUCTION**

**1.1** Ragone plot depicting the energy and power performance of various energy storage technologies. **2**
**1.2** Historical timeline of supercapacitor development. **3**
**1.3** EDLC and pseudocapacitive charge storage mechanisms. **5**
**1.4** Classification and significance of nanostructured materials. **8**
**1.5** Classification of $WO_3$ based on (A) Crystal phases [Reprinted with permission from ref.[79], Copyright (2010), AIP Publishing] and (B) Stoichiometry [Reprinted with permission from ref. [80], Copyright (2010), AIP Publishing]. **10**
**1.6** Classification of $MoO_3$ based on (A) Crystal phases and (B) Stoichiometry [Reprinted with permission from ref.[89], Copyright (2017), AIP Publishing]. **11**

**CHAPTER II: EXPERIMENTATION**

**2.1** General synthesis scheme for preparing nanostructured $WO_{3-x}$ **44**
**2.2** General synthesis scheme for preparing $WO_{3-x}$/C microfibers and hierarchical structures. **45**
**2.3** General synthesis scheme for preparing $MoO_{3-x}$ microstructures. **47**
**2.4** General synthesis scheme for preparing $MoO_{3-x}$ microflowers**.** **48**
**2.5** Schematic of a two-electrode supercapacitor device. **55**
**2.6** Electrode drop casting solution optimization. **56**

**CHAPTER III: $WO_{3-x}$ NANO AND MICROSTRUCTURES AS CHARGE STORAGE ELECTRODE MATERIALS**

**3.1** TG-DTA analysis of (A) Tungstic acid-urea hybrid gel and (B) Tungstic acid (without urea). **64**
**3.2** (A) IR spectra and (B) X-ray diffractograms of synthesized tungstic acid-urea hybrid gels dried/calcined at different temperatures. **66**
**3.3** Effect of variation in pH on the morphology of synthesized $WO_{3-x}$ at 550°C; SEM images of $WO_{3-x}$ in A,B,C, and D correspond to pH values of 1, 2.5, 5, and 10, respectively, synthesized without urea and A', B', C', and D' synthesized with urea. **67**
**3.4** Effect of W to urea ratio on the morphology of $WO_{3-x}$ (A) 1:1, (B) 1:3, (C) 1:6, and

(D) 1:9. **68**

**3.5** Temperature dependent morphological transformation of $WO_{3-x}$ at (A) 150 °C, (B) 250 °C, (C) 350 °C, (D) 450 °C, (E) 550 °C, and (F) 650 °C at pH = 2.5 and calcination time = 2h. **69**

**3.6** SEM images depicting self-assembly of $WO_{3-x}$ nanorod bundles into 3D nanoporous structure. A-C= represents the 3D growth of nanostructure, D = the side view of a stack of vertically aligned nanorod bundles, and E-F= top and complete view of the 3D porous structure. **71**

**3.7** (A) TEM image of synthesized $WO_{3-x}$ nanorod bundle, (B) HRTEM image of $WO_{3-x}$ nanorod, and (C) SAED pattern of $WO_{3-x}$ nanorod. **72**

**3.8** XPS spectra of (A-C)WP, (D-F) WN, (G-I) 3DW, and (J-L) 2DW. **75**

**3.9** Schematic illustration of the growth mechanism of $WO_{3-x}$ nanorods and subsequent transformation into sheets and microstructures. **75**

**3.10** (A) O-monoprotonated dimeric salt (B) O-monoprotonated monomeric salt obtained by reacting tetramethyl urea with tungsten hexachloride. **76**

**3.11** Supercapacitor performance investigated via (A) CV analysis at a scan rate of 10 mV $s^{-1}$; (B) GCD analysis at the current density of 2 A $g^{-1}$ ; (C) Nyquist plots in the frequency range of 1 mHz to 1 MHz; and (D) cycling stability performance evaluated at a constant current density of 8 A $g^{-1}$. **79**

**3.12** (A) CV curves of 3DW and AC recorded at a scan rate of 10 mV $s^{-1}$, (B) CV curves of 3DW//AC at variable voltage windows, (C) overlay of CV curves recorded at a scan rate of 5 mV $s^{-1}$, (D) overlay of GCD analysis recorded at the current density of 2 A $g^{-1}$, (E) overlays of Nyquist plots in the frequency range of 1 mHz to 1 MHz ,and (F) overlays of cycling stability performance measured in a two-electrode asymmetric setup evaluated at 8 A $g^{-1}$. **83**

**3.13** Ragone plot demonstrating the device performance of $WO_{3-x}$ nanostructures. **84**

**3.14** SEM images of $WO_{3-x}$ synthesized by calcining tungstic acid gels with (A, B) carbohydrazide, (C) urea, (D) semicarbazide (E) N-methylurea, and (F) tetramethylurea. **88**

**3.15** The TEM, HRTEM, and SAED analysis (A-C) for WC and (D-F) for WT, respectively. **89**

**3.16** XRD patterns of (A) WN, (B) WC, (C) WSC, (D) WM, and (WT). (I) overlay of XRD patterns, and (II) is a magnified subset of the rectangular area in (I). **90**

**3.17** XPS spectra of (A-C) WC and (D-F) WT. **93**

**3.18** TG-DTA curve of the as-synthesized mixture of (A) tungstic acid– carbohydrazide, (B) tungstic acid-semicarbazide (C) tungstic acid–N-methylurea and (D) tungstic acid–tetramethylurea hybrid gels. **94**

**3.19** Schematic illustration of the plausible $WO_{3-x}$ nanorod growth mechanism with in situ induction of partial surface oxygen vacancies during the calcination of tungstic acid- carbohydrazide precursor gels in air at 550 $^{o}$C. **96**

**3.20** Supercapacitor performance investigated via (A) CV analysis at a scan rate of 10 mV $s^{-1}$; (B) GCD analysis at the current density of 2 A $g^{-1}$ ; (C) Nyquist plots in thefrequency range of 1 mHz to 1 MHz; and (D) cycling stability performance evaluated at a constant current density of 8 A $g^{-1}$. **98**

**3.21** (A) Overlay of CV curves recorded at a scan rate of 5 mV $s^{-1}$ (B) Overlay of GCD analysis recorded at the current density of 2 A $g^{-1}$ (C) Overlays of Nyquist plots in the frequency range of 1 mHz to 1 MHz and (D) Overlays of cycling stability performance measured in a two-electrode asymmetric setup evaluated at 8 A $g^{-1}$. **103**

**3.22** Ragone plot demonstrating the device performance of $WO_{3-x}$ nanostructures. **105**

**3.23** (A-E) SEM micrograph of temperature-dependent morphological transformation of tungstic acid-citric acid hybrid gel (A) 250 °C, (B) 300 °C, (B1) Inset of B (C) 350 °C, (C1) Inset of C, (D) 450 °C and (E) 550°C. (F-H) Elemental mapping of D. **107**

**3.24** (A-D and F) represent the HRTEM and SAED analysis of WF, and (E and G) represent the HRTEM and SAED analysis of WH, respectively. **108**

**3.25** (A) TG-DTA of the as-synthesized tungstic acid-citric acid gel and (B) histogram of the C and H distribution. **109**

**3.26** (A) IR spectra and (B) XRD patterns depicting the transformation of tungstic acid-citric acid gel mixture at various temperatures from 150 to 650 °C. **111**

**3.27** (A-B) Raman spectra of WF and WH, respectively, and (C) Overlay EPR spectra of WF and WH, respectively. **112**

**3.28** XPS spectra of (A-D) WF and (E-H) WH. **114**

**3.29** Schematic illustration of the plausible growth mechanism of WF and WH. (A) depicts tungstic acid-citric acid hybrid gel, (B) capping effect induced by citric acid, (C) orientational growth of citric acid particles, (D) growth of carbon fiber encapsulated $WO_{3-x}$ single helices, (E) formation of $WO_{3-x}$/C double helical fibers, (F-G) self-assembled WF tripodal superstructures and (H) transformation of WF into WH. **117**

**3.30** Supercapacitor performance investigated via (A) CV analysis at a scan rate of 10 mV $s^{-1}$; (B) GCD analysis at the current density of 2 A $g^{-1}$ ; (C) Nyquist plots in the frequency range of 1 mHz to 1 MHz; and (D) cycling stability performance evaluated at a constant current density of 8 A $g^{-1}$. **119**

**3.31** (A) Overlay of CV curves recorded at a scan rate of 5 mV $s^{-1}$ (B) Overlay of GCD analysis recorded at the current density of 2 A $g^{-1}$ (C) Overlays of Nyquist plots in the frequency range of 1 mHz to 1 MHz and (D) Overlays of cycling stability performance measured in a two-electrode asymmetric setup evaluated at 8 A $g^{-1}$. **123**

**3.32** Ragone plot demonstrating the device performance of WF and WH microstructures **124**

**3.33** Comparative analysis of our synthesized $WO_{3-x}$ with some literature reports. **125**

**CHAPTER IV: $MoO_{3-x}$ MICROSTRUCTURES AS CHARGE STORAGE ELECTRODE MATERIALS**

**4.1** SEM micrographs (A, D & G); HRTEM micrographs (B, E & H); and SAED (D, F & I) analysis of pH 2.5, 5, and 8 respectively. **140**

**4.2** SEM images (A, B, and F, G) Mo: Urea ratio of 1:1 and 1:3 for MP and MD formation. (D-I and M-R) Intermediate calcination stages from 250-550 °C for MP and MD. C and L are the SEM images of MP and MD at optimized conditions. **141**

**4.3** TG-DTA analysis of (A) MP, (B) MD, and (C) MA **142**

**4.4** IR studies of (A) MP, (B) MD, and (C) MA wherein (I) represents post calcination and (II) represents pre-calcination. **143**

**4.5** XRD analysis of (A) MP, (B) MD, and (C) MA. **145**

**4.6** Raman analysis of (A) MP, (B) MD, and (C) MA. **146**

**4.7** (A) Overlay of EPR spectra, (B) Overlay of XPS full scan spectra, (C and D) Narrow scan spectra of Mo3d and O1s of MP, (E and F) Narrow scan spectra of Mo3d and O1s of MD. **147**

**4.8** Schematic illustration for the plausible growth mechanism of MP and MD. **149**

**4.9** Supercapacitor performance investigated via (A) CV analysis at a scan rate of 10 mV $s^{-1}$; (B) GCD analysis at the current density of 20 A $g^{-1}$; (C) Nyquist plots in the frequency range of 1 mHz to 1 MHz; and (D) cycling stability performance evaluated at a constant current density of 40 A $g^{-1}$. **151**

**4.10** (A) CV curves of MP and AC recorded at a scan rate of 10 mV $s^{-1}$; (B) CV curves of MP//AC at variable voltage windows; (C) Overlay of CV curves recorded at a scan rate of 10 mV $s^{-1}$; (D) Overlay of GCD analysis recorded at the current density of 2 A $g^{-1}$; (E) Overlays of Nyquist plots in the frequency range of 1 mHz to 1 MHz; and (F) Overlays of cycling stability performance measured in a two-electrode asymmetric setup evaluated at 6 A $g^{-1}$. **155**

**4.11** Ragone plot demonstrating the device performance of $MoO_{3-x}$ microstructures. **157**

**4.12** SEM images of $MoO_{3-x}$ synthesized by calcining ammonium molybdate with (A) urea, (B) carbohydrazide, (C) semicarbazide, (D) N-methylurea and, (E) tetramethylurea. **158**

**4.13** The TEM, HRTEM, and SAED analysis (A-C) for MC and (D-F) for MT, respectively. **159**

**4.14** XRD patterns of (A) MC, (B) MSC, (C) MM, and (D) MT. **161**

**4.15** XPS spectra of (A-C) MC and (D-F) MT. **162**

**4.16** TG-DTA curve of the as-synthesized mixture of (A) ammonium heptamolybdate–carbohydrazide, (B) ammonium heptamolybdate-semicarbazide (C) ammonium heptamolybdate–N-methylurea and (D) ammonium heptamolybdate–tetramethylurea mixtures. **164**

**4.17** Supercapacitor performance investigated via (A) CV analysis at a scan rate of 10 mV $s^{-1}$; (B) GCD analysis at the current density of 20 A $g^{-1}$ ; (C) Nyquist plots in the frequency range of 1 mHz to 1 MHz; and (D) cycling stability performance evaluated at a constant current density of 40 A $g^{-1}$. **166**

**4.18** (A) Overlay of CV curves recorded at a scan rate of 5 mV $s^{-1}$ (B) Overlay of GCD analysis recorded at the current density of 2 A $g^{-1}$ (C) Overlays of Nyquist plots in the frequency range of 1 mHz to 1 MHz and (D) Overlays of cycling stability performance measured in a two-electrode asymmetric setup evaluated at 6 A $g^{-1}$. **171**

**4.19** Ragone plot demonstrating the device performance of $MoO_{3-x}$ microstructures. **172**

**4.20** (A-E) SEM micrograph of temperature-dependent morphological transformation of ammonoium heptamolybdate-citric acid hybrid mixture (A) 150 °C, (B) 250 °C , (C) 350 °C, (D) 450 °C, and (E) 550 °C. **174**

**4.21** (A-C) SEM micrograph of $MoO_{3-x}$ microflowers at different Mo: Citric acid ratio (A) 1:1, (B) 1:3, and (C) 1:6. and (C-E) SEM micrograph of $MoO_{3-x}$ microflowers at at different pH values of (C) 2.5, (D) 5 and (E) 8. **175**

**4.22** (A) HRTEM and (B) SAED analysis of MFF respectively. **176**

**4.23** (A) TG-DTA of the ammonium heptamolybdate-citric acid mixture. **177**

**4.24** (A) IR spectra and (B) XRD patterns depicting transformation of ammonium heptamolybdate-citric acid mixture at various temperatures from 250 to 550 °C. **178**

**4.25** (A) Raman spectrum and (B-D) XPS spectra of MMF. **179**

**4.26** Schematic illustration for the plausible growth mechanism of MMF. **181**

**4.27** Supercapacitor performance investigated via (A) CV analysis at a scan rate of 10 mV $s^{-1}$; (B) GCD analysis at the current density of 2 A $g^{-1}$ ; (C) Nyquist plots in the frequency range of 1 mHz to 1 MHz; and (D) cycling stability performance evaluated at a constant current density of 40 A $g^{-1}$. **182**

**4.28** (A) Overlay of CV curves recorded at a scan rate of 5 mV $s^{-1}$ (B) Overlay of GCD analysis recorded at the current density of 2 A $g^{-1}$ (C) Overlays of Nyquist plots in the frequency range of 1 mHz to 1 MHz and (D) Overlays of cycling stability performance measured in a two-electrode asymmetric setup evaluated at 6 A $g^{-1}$. **185**

**4.29** Ragone plot demonstrating the device performance of MMF. **186**

**4.30** Comparative analysis of our synthesized $MoO_{3-x}$ with some literature reports. **187**

**CHAPTER V: CONCLUSIONS OF THE THESIS**

**5.1** Schematic illustration depicting the dimensionality-based charge storage performance of the various nano and microstructures of (A) $WO_{3-x}$ and (B) $MoO_{3-x}$. **201**

# CHAPTER I:

# INTRODUCTION

## 1.1 INTRODUCTION

For many decades, fossil fuels have been the dominant source of energy in the global economy. Fossil fuels, including coal, oil, and natural gas, are formed from the remains of dead plants and animals that have been buried and subjected to high heat and pressure over millions of years. Increasing population and unchecked industrial growth have also led to increased energy consumption by releasing unwanted agents that deteriorate the planet's ecological balance.[1] With fossil fuels potentially running out and greenhouse gas emissions affecting the environment, global demand for sustainable energy solutions has increased.[2,3] The most promising solutions for these problems are renewable energy resources, such as solar, hydro, and wind energy.[4,5] Due to large fluctuations in production, electricity from renewable energy sources must be stored efficiently to meet the world's energy needs.[6,7]

Among various energy-storage devices, batteries and supercapacitors are the two most prominent electrochemical energy storage technologies, as illustrated in the Ragone plot (refer figure 1.1) , which compares energy density in W h $kg^{-1}$ against power density in W $kg^{-1}$.[8,9] Consumer electronics widely use lithium-ion batteries because they have a high energy density (approximately 250 W h $kg^{-1}$).[10] However, batteries generate heat and form dendrites when operated at high power because of sluggish electron and ion transport, leading to serious safety issues.[11,12] Alternatively, supercapacitors (SCs), also known as electrochemical capacitors, can supplement or even replace batteries in some applications since they have high power, rapid charging, and long cycle lives (over 100,000 cycles).[13,14] Due to these advantages, SCs have increased interest, where high power density, fast charging, and high cycling stability are needed.[15] Supercapacitors can be found in various applications related to the transportation sector, including heavy-duty vehicles and regenerative braking systems.[14,16] Even though commercially available supercapacitors can deliver much higher energy densities (5 W h $kg^{-1}$) than traditional solid-state electrolytic capacitors, this performance is still well below batteries (up to 200 W h $kg^{-1}$) and fuel cells (up to 350 W h $kg^{-1}$).[17] Consequently, supercapacitors have not been widely adopted, and research has been ongoing to find ways to improve the energy-storage capability of supercapacitors without sacrificing their power density or cycling stability.[18]

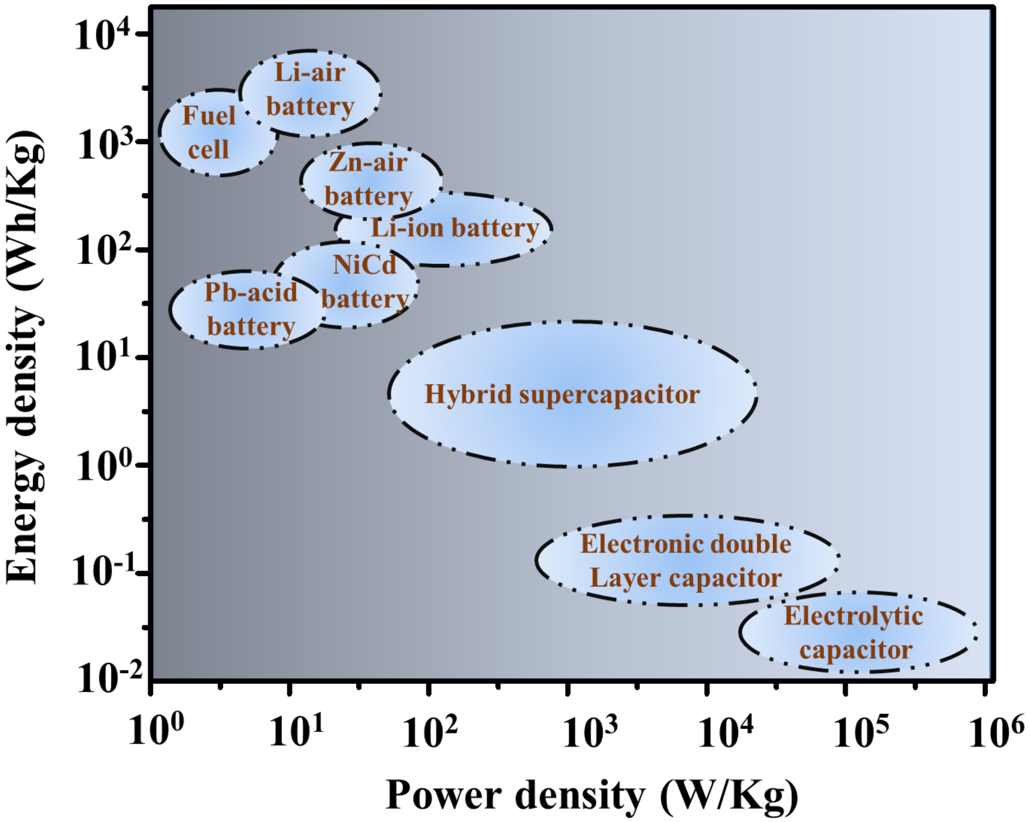

**Figure 1.1:** Ragone plot depicting the energy and power performance of various energy storage technologies.

## 1.2 HISTORY OF SUPERCAPACITORS

The discovery of the mechanism of charge storage sparked the development of supercapacitors. During the mid-18th century, a capacitor was demonstrated for the first time. The first capacitor was invented by German cleric Ewald Georg von Kleist in 1745 and a Dutch scientist Pieter van Musschenbroek in 1746 independently and was named a "Leyden Jar".[8] Electrostatics was fundamentally advanced by the discovery of the Leyden jar, which was used to conduct many early electrical experiments.[19,20] This device was the first to allow large amounts of electric charge to be accumulated and stored, which could be discharged at the experimenter's discretion, thus breaking through an early barrier to electrical conduction research.[21] In addition to this conceptual framework, a concept for storing static electricity at the interface between a solid electrode and a liquid electrolyte developed. This was over 100 years before the invention of the battery in 1880, which introduced the concept of an electric double layer.[8] (refer figure 1.2)

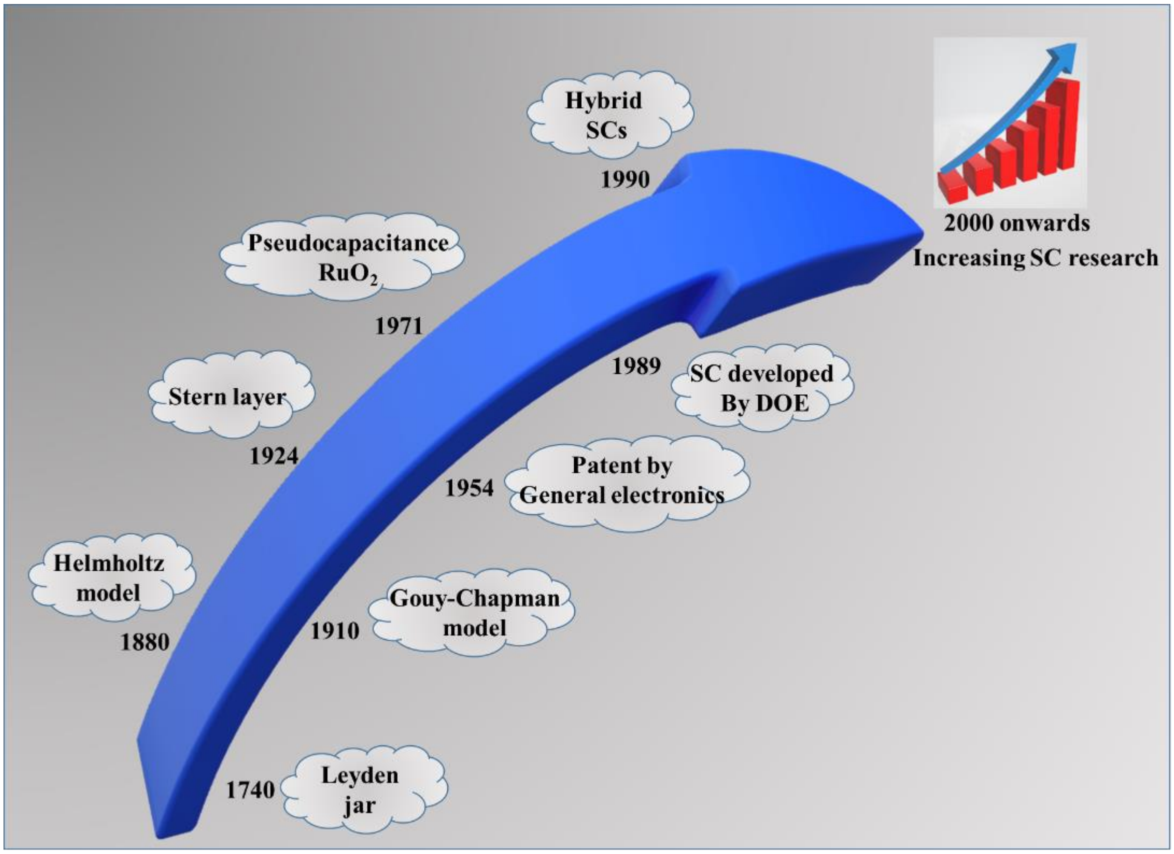

**Figure 1.2:** Historical timeline of supercapacitor development.

Until the 19th century, static electricity was a topic of little understanding. Helmholz was the first person to explore the capacitor's electrical charge-storage mechanism in 1853, and he designed the first electric model using colloidal suspensions.[22] Many pioneering interfacial electrochemists of the 19th and early 20th centuries developed the modern theory of electric double-layer capacitance between metal electrodes and liquid electrolytes, including Gouy, Chapman, Stern, and Grahame.[23] It was not until 1954 that H. I. Becker of General Electric filed for the first electrochemical capacitor patent.[24] A porous carbon electrode containing an aqueous electrolyte was described in this patent as the first energy storage device with an interfacial electric double layer for storing electricity. Although the patent was never commercialized, it was a pathbreaker for the production of supercapacitor devices.[8] Following a license agreement with SOHIO, Nippon Electric Corp. (NEC) introduced the world's first electrochemical capacitor in 1978, dubbed "SuperCapacitor", and is still being incorporated in clock ships and several memory devices.[25]

Based on $RuO_2$, a new electrochemical capacitor was developed in 1971, called a pseudocapacitor, that used Faradaic processes to store and deliver charge.[26] A new method of enhancing the charge-storage capacity of electrochemical capacitors was made possible by the discovery of pseudocapacitance. Based on the discovery of pseudocapacitance, a high-performance supercapacitor based on ruthenium oxide pseudocapacitance was developed in the 1980s by the Pinnacle Research Institute (PRI) called the PRI Ultracapacitor and was used in many military applications.[27] As part of the Electric and Hybrid Vehicle Program, the U.S. Department of Energy (DOE) began supporting a long-term supercapacitor study that aimed to develop high energy density supercapacitors for electric drivelines in 1989. Maxwell Technologies Inc., a world leader in supercapacitor manufacturing, subsequently contracted with the DOE to develop high-performance supercapacitors for numerous applications.[8] The amount of research on supercapacitors has steadily increased since 2000, owing to a growing demand for high-power, high-reliability, and safe energy-storage devices.

## 1.3 TYPES OF SUPERCAPACITORS AND THEIR MECHANISMS

In general, supercapacitors work similarly to conventional capacitors.[28] In supercapacitors, electrodes have a higher surface area than in conventional capacitors, and an electrolyte solution separates the electrodes using a separator.[29] A supercapacitor can be divided broadly into two classes based on its working mechanism as (a) electrochemical double-layer capacitors (EDLCs) and (b) Pseudocapacitors, a combination of the two is known as hybrid supercapacitors.[28]

### 1.3.1 Electric double-layer capacitors

EDLCs were developed by Standard Oil Company of Ohio in 1966 and are the simplest and most common supercapacitors.[30] They consist of symmetrical cell structures containing two high-surface-area carbon electrodes separated by a nonaqueous electrolyte. As suggested by its name a double-layer of electric charge forms at all electrode/electrolyte interfaces, as illustrated in figure 1.3. An EDLC’s specific capacitance can be maximized by using lightweight electrode materials with high surface areas, such as activated carbon, while the operating voltage can be maximized by using nonaqueous electrolytes with a wide stable potential window.[31] Manufacturers/suppliers of EDLCs offer a variety of formulations ranging from small single-cell 2.7 V capacitors with a few farads to integrated modules operating at voltages relevant to large-scale applications (e.g., 125 V).[32] Despite growing acceptance in the commercial marketplace, EDLC researchers continue to develop and adapt new electrode materials and electrolytes at both fundamental and applied levels. Many forms of nanostructured carbons are being explored as alternatives to activated carbon, including aerogels, nanotubes, carbide-derived carbons, and graphene, all aiming to improve specific energy while maintaining high specific power.[33–36] There is also an investigation into advanced electrolytes to extend the operating voltages of EDLCs and improve specific energy simultaneously.[37] Despite these advancements, EDLCs have fundamentally limited specific energies because they rely primarily on double-layer capacitance for charge storage, which limits their application.[38]

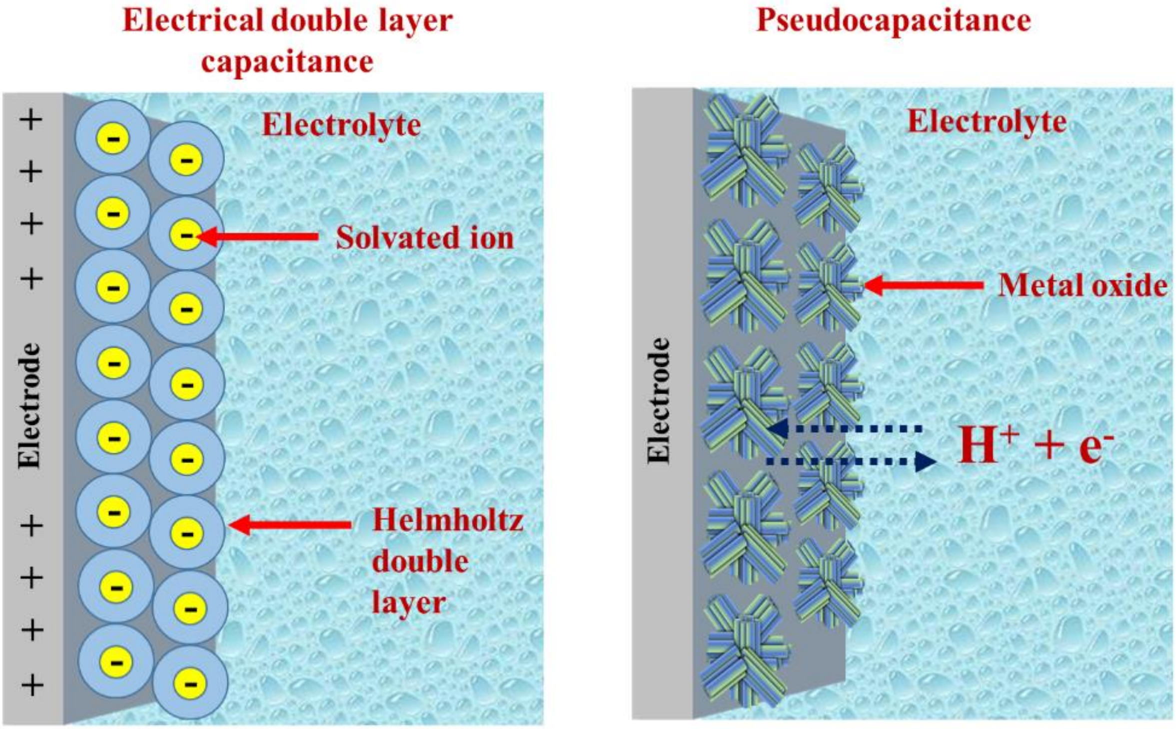

**Figure 1.3:** EDLC and pseudocapacitive charge storage mechanisms.

### 1.3.2 Pseudocapacitors

In pseudocapacitors, charges are stored electrostatically between electrodes and electrolytes.[39] The electrode material of a pseudocapacitor undergoes both reduction and oxidation when subjected to a voltage.[40] During this process, the charge passes across the electro-active material, resulting in a faradaic current passing through the material of the supercapacitor electrodes.[41] As illustrated in figure 1.3, it is possible to circumvent the limitations of double-layer capacitance by selecting active materials that undergo rapid and reversible electron-exchange reactions near the electrode surface. Compared to EDLCs, pseudocapacitors achieve higher specific capacitances and energy densities through the faradaic process.[42] Often, such materials exhibit broad and symmetric charge-discharge profiles reminiscent of those generated by double-layer capacitance, and for this reason, they are referred to as pseudocapacitors.[43] The most well-known pseudocapacitance material is ruthenium oxide, but many other transition metal oxides, metal nitrides, and conducting polymers demonstrate similar electrochemical performance.[44–46]

## 1.4 ELECTROCHEMICAL ENERGY STORAGE BASED ON TUNGSTEN OXIDE AND MOLYBDENUM OXIDES

Electrochemical energy storage devices have grown in popularity due to rapid advancements in portable electronics and electric vehicles.[47,48] In addition to offering a high energy density and fast charging/discharging rates, supercapacitors are regarded as promising high-efficiency energy storage systems with significant commercial potential. Electrical double-layer capacitors (EDLCs) and pseudocapacitors are the two mechanisms through which supercapacitors can store energy.[49] EDLCs, such as carbon-based EDLCs, produce low specific capacitance due to reversible adsorption of ions at the electrode-electrolyte interface.[38] Second, Faradaic charge storage can be achieved through reversible redox reactions, giving rise to pseudocapacitors.[50] Pseudocapacitance is known to occur in transition metal oxides. One of the most widely explored pseudocapacitive material is ruthenium oxide, which has a high theoretical (1400-2000 F $g^{-1}$) and practical capacitance (350-500 F $g^{-1}$).[51] However, due to its high cost and toxicity, it is not widely applicable in practical situations. The charge storage properties of various transition metal oxides and conducting polymers have been investigated, including manganese oxide, vanadium oxide, iron oxides, cobalt oxide, nickel oxide, tungsten oxides, molybdenum oxides, polypyrrole, polyaniline, etc.[52] In this list, Tungsten and molybdenum oxides rank relatively high due to their ability to switch between the oxidation states of +6 and +5 during electrochemical reactions, their low cost, and their environmentally friendly nature, which can also be further improved by nanostructuring as shown in figure 1.4.[53]

Carl Wilhelm Scheele, who discovered that tungstic acid could be made from scheelite in the late 1700s, is credited for discovering the chemistry of tungsten.[54] Later in 1783, Juan José Elhuyar and Fausto Elhuyar found an acid produced from wolframite that allowed them to isolate tungsten.[55] Research on tungsten and its compounds has increased since then. Additionally, $WO_3$ has been identified as a candidate for various other applications, including photocatalysis, gas sensing, electrochromic, dye-sensitized solar cells, electrocatalysis, etc.[56–59] The low electrical conductivity of $WO_3$ remains a significant shortcoming despite its popularity as a promising candidate for many applications. $WO_3$ must possess high conductivity and a high capacity to store and deliver a large amount of charge to be considered an ideal supercapacitor.[60] The electronic and structural properties of $WO_3$ and its defects can be tuned to enhance its specific characteristics. In defect engineering, oxygen vacancies are the most pervasive defect types in $WO_3$.[53] Experimental, and theoretical studies have shown that oxygen vacancies in $WO_{3-x}$ structures are highly conducive to electrode reactions while dramatically improving their conductivity.[61,62] There has been evidence that redox oxidation states ($W^{5+}/W^{6+}$) and oxygen deficiencies improve charge-storage performance by improving the electrochemical activity and introducing more active sites that enhance charge transfer dynamics between the electrolyte and the $WO_3$ matrix.[53,60] Thus, to improve the charge-storage performance of $WO_3$, it is most desirable to introduce defects such as oxygen vacancies in the material. (refer figure 1.3).

A very versatile oxide with similar characteristics to $WO_3$ is Molybdenum oxide ($MoO_3$). Molybdenum chemistry was also pioneered by Carl Wilhelm Scheele and has been used for various applications, such as catalysis, sensors, optoelectronics, electrochromics, and charge storage.[63–65] It is one of the most adaptable and functional transition metal oxide.[66] There are various stoichiometric forms of $MoO_3$, starting with the full stoichiometric $MoO_3$ to the more conducting $MoO_{3-x}$ ($2 < x < 3$).[67] As oxygen defects are induced, $Mo^{6+}$ ions can be reduced to $Mo^{+5}$ and finally $Mo^{4+}$ ($MoO_2$).[68] To date, several liquid- and vapor-phase approaches have been used to synthesize and deposit these oxides to satisfy the research and commercialization needs.[69] Molybdenum oxides have been fabricated into a variety of structures, including quantum dots, nanorods, nanobelts, two-dimensional sheets, and nanotubes, among others.[70–73] The crystal form of $MoO_3$ is found most commonly in its orthorhombic, monoclinic, and hexagonal phases, which form from the side and corner-sharing of $MoO_6$ octahedrons.[74] In the expanding world of flatland materials, orthorhombic $MoO_3$ has already been introduced as a stratified material, which can be exfoliated into two-dimensional planes with tremendous potential for energy storage technologies.[75]

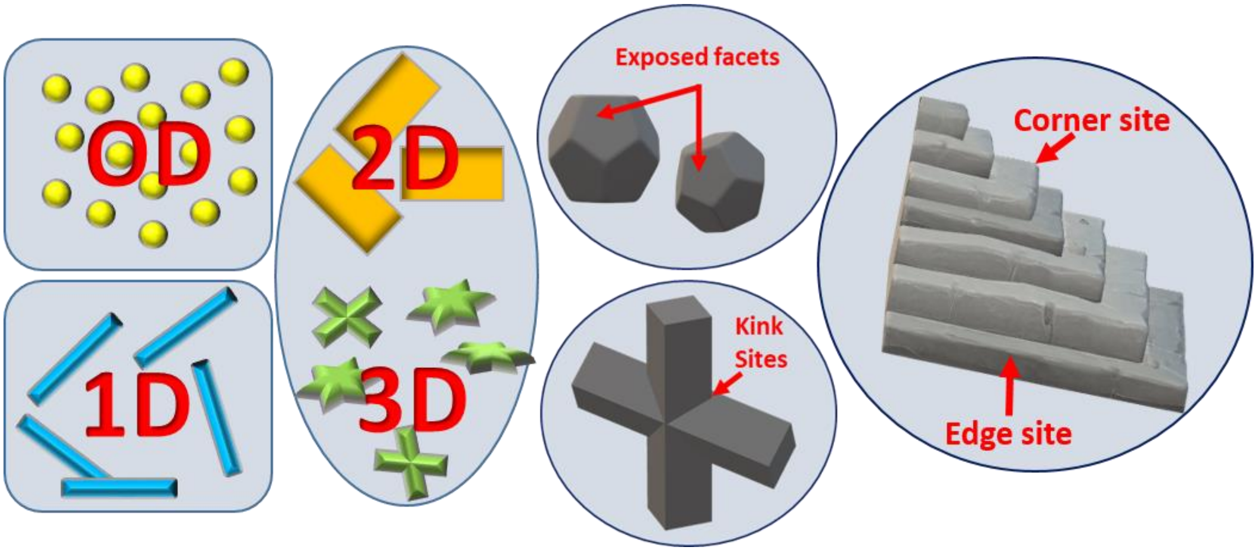

**Figure 1.4:** Classification and significance of nanostructured materials.

## 1.5 CRYSTALLOGRAPHIC CHARACTERISTICS OF $WO_3$

The structural diversity of $WO_3$ is particularly notable. In stoichiometric $WO_3$, phase transitions and structural polymorphism are known to occur. The ideal $WO_3$ crystal structure consists of a $ReO_3$-like structure. $WO_3$ polymorphs are a result of distortion from the cubic structure of $ReO_3$ (refer figure 1.5 A).[76] In this structure, oxygen atoms surround cations, resulting in an octahedral arrangement that appears as a 3D network of corner-sharing $WO_6$ octahedra, whose arrangement results in a simple cubic symmetry. The $WO_6$ octahedron consists of tungsten atoms at its center and oxygen atoms at the corners. $WO_2$ and oxygen planes are alternately disposed of in the main crystallographic direction to form the crystal network. Due to the tilting of $WO_6$ and the subsequent translation of the W atoms from the center of the octahedra, $WO_3$ has less symmetry than $ReO_3$.[51] Furthermore, the different crystal structures of $WO_3$ are temperature-dependent. The $WO_6$ octahedra undergo a displacement of the central W atoms by changing the temperature, which exhibits various polymorphic forms. Monoclinic I ($\gamma$-$WO_3$) is the most common phase of $WO_3$ that is stable at room temperature. Temperature range of 17-330°C is optimal for the stability of this phase. There are two other crystallographic phases of $WO_3$ below room temperature: monoclinic II ($\varepsilon$ -$WO_3$) at temperatures below -43°C and triclinic (**δ**-$WO_3$) at temperatures between - 43°C and 17°C. If $\gamma$-$WO_3$ is exposed to temperatures above 330°C, it transforms to orthorhombic ($\beta$-$WO_3$), which is stable at 740°C. Above 740°C, the orthorhombic phase is converted to tetragonal ($\alpha$-$WO_3$). At high temperatures, both the orthorhombic and tetragonal phases of $WO_3$ are stable, but upon cooling, they tend to revert to a monoclinic phase ($\gamma$-$WO_3$).[77] This phase transformation is caused by the tilting angle of the $WO_6$ octahedra, while the interatomic distances and angles remain nearly unchanged.[78] Figure 1.5 A shows some of these crystal structures.

As shown in figure 1.5 B, the oxygen vacancies induced in the crystal structure during crystallization lead to the non-stoichiometric $WO_{3-x}$ (i.e., $2 \leq x < 3$). Glemser and Sauer first identified the non-stoichiometric tungsten oxide.[81,82] They demonstrated that by introducing oxygen vacancies, the $WO_3$ phase structure could be changed to $WO_{2.9}$. $WO_x$ (x = 2.63-2.91), a non-stoichiometric tungsten compound with oxygen deficiency, can be divided into several well-defined sub-oxides with differing W to O ratios such as. $W_{32}O_{84}$ ($WO_{2.625}$), $W_3O_8$ ($WO_{2.667}$), $W_{18}O_{49}$ ($WO_{2.72}$), $W_{17}O_{47}$($WO_{2.765}$), $W_5O_{14}$($WO_{2.8}$), $W_{20}O_{58}$($WO_{2.9}$), $W_2O_5$, $WO_2$, and $W_{25}O_{73}$($WO_{2.92}$) and they are known as Magnéli phases (refer figure 1.5 B).[80] The crystal structure of $WO_{2.62}$ and $WO_{2.66}$ is orthorhombic; monoclinic for $WO_{2.72}$, $WO_{2.765}$, $WO_{2.9}$, and $WO_{2.92}$; and tetragonal for $WO_{2.8}$. Magnéli phases can also be formed through the reduction of monoclinic $WO_3$. This reduction process results in the change from corner-sharing of the $WO_6$ octahedra to edge-sharing as the oxygen vacancies increase.[83] Additionally, the edge-sharing $WO_6$ octahedra with channels form hexagonal tunnels and pentagonal columns in these sub-oxides. With partially reduced $W^{5+}$ species, the lattice structure of $WO_x$ can uphold considerable oxygen deficiency. Sub-oxides become highly metallic and conductive when they hold sufficient oxygen vacancies.[84] In addition, oxygen vacancies affect the number of free electrons and the Fermi level of $WO_x$ as well as the energy gaps. Several recent studies indicate that these properties increase with the increase in non-stoichiometry.[85,86]

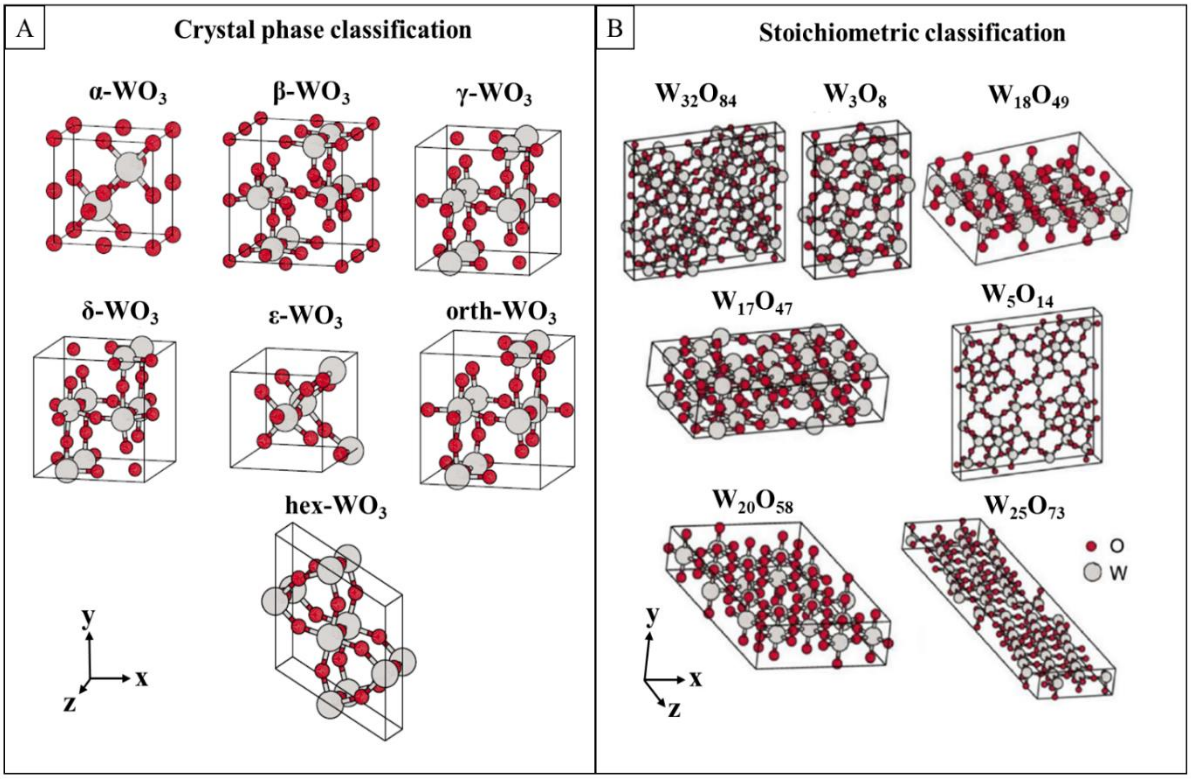

**Figure 1.5:** Classification of $WO_3$ based on (A) Crystal phases [Reprinted with permission from ref.[79], Copyright (2010), AIP Publishing] and (B) Stoichiometry [Reprinted with permission from ref. [80], Copyright (2010), AIP Publishing].

Nanostructuring also plays a crucial role in improving energy storage in tungsten oxide, along with defect engineering. The nonstructural design of $WO_3$ endows several key features, such as the generation of kink sites, exposing electrochemically active facets, heterostructure formation, and porosity generation.[87] (refer figure 1.4). Researchers have reported a wide variety of nanostructures of $WO_3$ with dimensions ranging from 0D to 3D, such as spherical nanoparticles, nanoclusters, nanorods, nanotubes, nanobowls, nanosheets, sponge-like, wedge-like, snowflake-like, etc.[87,88] During the formation of each of these synthesized structures, unique experimental conditions and methods are required. This has been discussed in more detail in section 1.8.

## 1.6 CRYSTALLOGRAPHIC CHARACTERISTICS OF MOO3

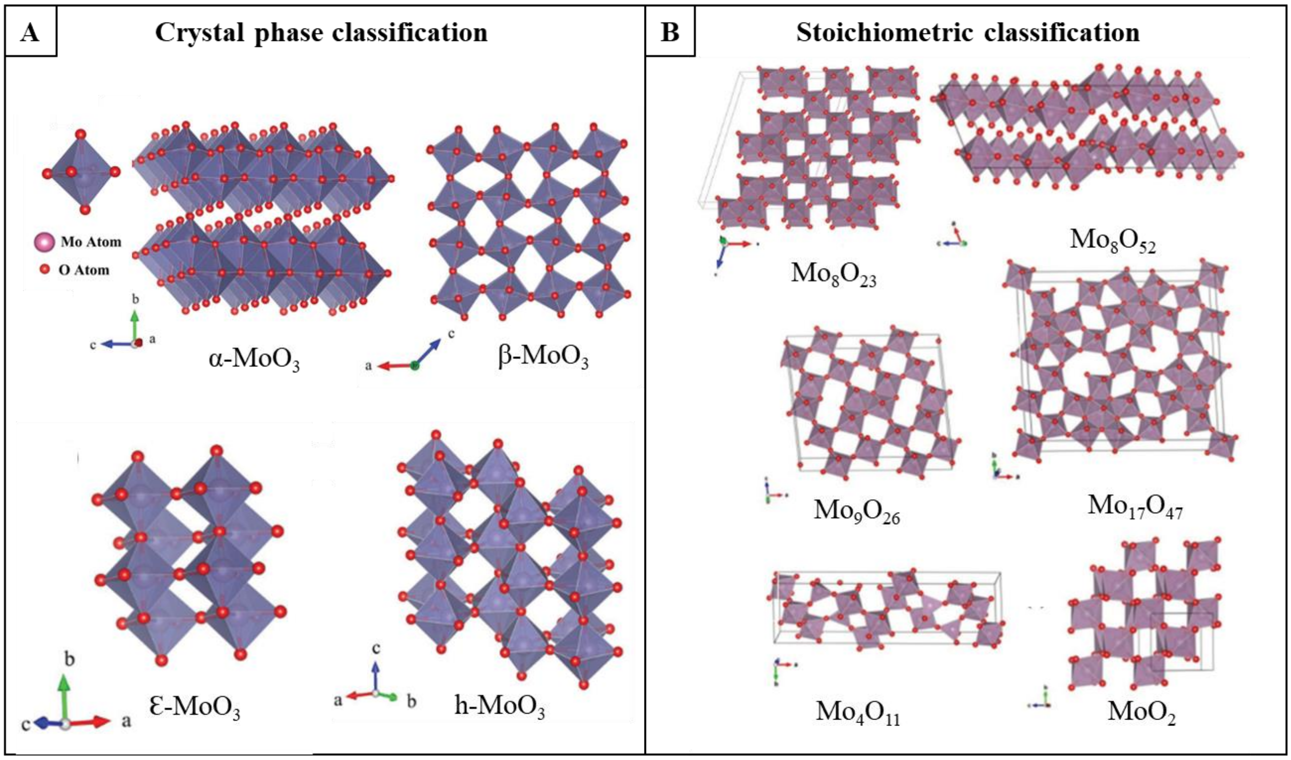

**Figure 1.6:** Classification of $MoO_3$ based on (A) Crystal phases and (B) Stoichiometry [Reprinted with permission from ref.[89], Copyright (2017), AIP Publishing].

Based on the octahedron building block of $MoO_6$, the two most common crystal phases of $MoO_3$ are the thermodynamically stable i.e., orthorhombic $\alpha$-phase and the metastable monoclinic $\beta$-phase.[90] Both of these phases possess distinctive physical and chemical properties, such as refractive indices, conductivity, bandgap energies, and mechanical hardness.[91] Another phase that has been observed is the metastable high-pressure phase $MoO_3$-II, also known as $\varepsilon$ -$MoO_3$, and the slightly more stable phase, hexagonal $h$-$MoO_3$ (refer figure 1.6 A).[89,92] Orthorhombic $\alpha$ -$MoO_3$, has a well-known layered crystal structure, which has the capability of creating two-dimensional (2D) morphologies.[93] They are formed from double layers of linked and distorted $MoO_6$ octahedra arranged in an atomically thin layer with a thickness of ≈0.7 nm.[93,94] A distance of 1.4 nm separates two layers of Mo atoms.[89] Double-layered sheets of distorted $MoO_6$ octahedra form edge-sharing zigzag rows along the [001] direction, while corner-sharing rows follow the [100] direction.[95] It is apparent that the distorted $MoO_6$ octahedra are held together by weak van der Waals forces, which result in stratification.[96] In contrast, the internal interactions between the octahedra are determined by strong covalent and ionic bonds.[97] Non-stoichiometric molybdenum with oxygen deficiency $MoO_x$ can form a number of well-defined sub-oxides with average valences between 6.0 ($MoO_3$) and 4.0 ($MoO_2$) (i.e., $Mo_{18}O_{52}$, $Mo_{17}O_{47}$, $Mo_9O_{26}$, $Mo_8O_{23}$, $Mo_5O_{14}$, and $Mo_4O_{11}$).[98] Figure 1.6 B shows some of the non-stoichiometric crystal structures of $MoO_{3-x}$.

## 1.7 ROLE OF ION INTERCALATION AND ELECTROCHEMICAL CHARGE STORAGE

Innovative technologies like hybrid vehicles, electronics, and storage technologies have significantly improved over the past couple of decades.[99] Tungsten and molybdenum oxides are especially good at storing charges and exhibiting electrochemical stability compared to other electrode materials.[100,101] In addition, they possess unique physico-chemical properties which are attributed to their modified crystal structures, as discussed earlier, making them highly effective electrode materials.[102] The oxidation state of W and Mo changes between 6+ and 5+ (sometimes 4+) at the surface of an electrode during an electrochemical process, which involves reversible redox reactions.[60,103] The charge transfer and storage processes that are responsible for $WO_3$ and $MoO_3$ electrode's supercapacitor properties can be explained by the following reversible chemical reaction:[53,77]

$$\mathrm{MO_3} + x\mathrm{A}^+ + xe^- \leftrightarrow \mathrm{A_xMO_3} \qquad (1)$$

*M* represents the metal atom (either W or Mo), the cation is represented by *A* (such as $H^+$, $Na^+$, $Li^+$, and $K^+$), *e* represents electrons, while the number of charged species is represented by *x*. The main factors that influence the charge storage properties of $WO_3$ and $MoO_3$ include; i) the current collector-electrolyte interface electron transport mechanism, ii) the charge transfer resistance of the W and Mo ions, iii) the insertion mechanism of $A^+$ ions into the metal oxide matrix.[104] These factors create an alteration in the oxidation state of W and Mo. Furthermore, their morphological characteristics, crystallinity, electroactive surface area, and conductivity all influence the charge storage properties of these oxides.[51] The intercalation-deintercalation process also causes chromaticity in these oxides.[105,106] As a result of the color change associated with these oxides, electrochromic supercapacitors are now a reality.[107,108] One example of this application has been demonstrated by Gao and Co-workers, who developed large-scale electrochromic energy storage devices based on $WO_3$ nanosheets.[109] The color-modulated charge storage device had high color efficiency, ultra-fast response times, and a long cycle life based on Li intercalation.

## 1.8 NANOSTRUCTURED $WO_3$ FOR SUPERCAPACITOR APPLICATIONS

As discussed in the previous sections, $WO_3$ is a well-suited material for energy storage systems due to its unique physical and chemical properties, which are primarily influenced by the nanostructure of the material.[102] Thus, tuning the nanostructure is paramount to maximizing the potential of $WO_3$ as a supercapacitor. There have been several reports on nanostructured $WO_3$ synthesized using different synthetic methodologies. This section describes some of the unique nanostructures of $WO_3$ synthesized using different synthesis routes and how they have been explored for their charge-storage properties. Table 1.1 presents an overview of some of the reported $WO_3$ morphologies for supercapacitors.

A widely accepted method for synthesizing $WO_3$ nanoparticles is the sol-gel method.[110] This method utilizes the unique chemistry of tungsten to form the tungstic acid sol and its subsequent conversion into the gel phase.[111] Sol-gel synthesis, for example, has been used in the production of $WO_3$ nanoparticles, an example of which is the work by Kusuma and co-workers.[112] They used graphite substrate and spin-coated it with $WO_3$ nanoparticles obtained by the sol-gel method and could obtain a specific capacitance of 233.6 F $g^{-1}$ at a scan rate of 2 mV $s^{-1}$. The wet chemical synthesis route is an alternative strategy for producing $WO_3$ nanostructures (mostly hydrated $WO_3$). An example of this is the wet chemical method followed by a post-annealing method used by Walke and co-workers to produce $WO_3$ nanoplates.[113] It was interesting to note that the $WO_3$ synthesized at the post-annealing temperature of 200°C exhibited remarkable specific capacitance of 606 F $g^{-1}$ at a current density of 1 A $g^{-1}$. Through wet-chemical synthesis, the same group also produced hierarchical flowers of hydrated $WO_3$ that yielded a specific capacitance of 457 F $g^{-1}$ at a scan rate of 2 mV $s^{-1}$.[114] Furthermore, they have also produced hydrated $WO_3$ 3D slabs that could provide a specific capacitance of 386 F $g^{-1}$ at a scan rate of 2 mV $s^{-1}$.[115]

Using chemical bath deposition technique which is another wet chemical method, Lokhande and co-workers created thin films consisting of disk-like $WO_3$.[116] At a current density of 7 mA $cm^{-2}$, the thin films demonstrated a high specific capacitance of 725 F $g^{-1}$. Lee and co-workers designed a mesoporous $WO_3$ material using KIT-6 which is a mesoporous molecular sieve template.[117] When tested at a current density of 1 mA $cm^{-2}$, the ordered $WO_3$ showed a specific capacitance of 199 F $g^{-1}$ along with good rate capabilities. The higher specific capacitance associated with $WO_3$ whenever the wet chemical method is utilized is associated mainly with confined water in the crystal structure of $WO_3$. Due to this confinement, van der Waals gaps develop in the layered crystal structure, allowing the easy insertion of ions and enhancing charge storage.

The electrodeposition and atomic layer deposition techniques are also very interesting techniques that have been largely used to synthesize 3D and ordered $WO_3$ architectures.[118,119] An example of this is the work by Mai and co-workers who used an electrodeposition technique to fabricate $WO_3$ nanoflowers.[120] Ti foil was used as a scaffold and substrate for the electrodeposition of $WO_3$. The nanoflowers demonstrated a specific capacitance of 196 F $g^{-1}$ at a scan rate of 10 mV $s^{-1}$. The $WO_3$ nanoflowers also exhibited an excellent energy density of 0.53 mW h $cm^{-3}$ and a power density of 229.3 mW $cm^{-3}$ when assembled into an asymmetric device (NFL-$WO_3$//$TiO_2$@C@PPy). Zhuiykov and co-workers developed 2D $WO_3$ electrodes using atomic layer deposition.[121] In their study, 0.7 nm thick films of 2D $WO_3$ were synthesized, which gave a specific capacitance of 650.3 F $g^{-1}$ at a current density of 1.5 A $g^{-1}$. However, their capacitance retention was limited (65.8%) to about 2000 cycles.

The hydro/solvothermal method is another widely used method for synthesizing $WO_3$ nanostructures. This technique uses high pressure and temperature conditions to promote nanostructured designs under closed systems.[122] Many reports have described the fabrication of nanostructured $WO_3$ electrodes using hydrothermal techniques for supercapacitor applications.[123] Lei and co-workers, for instance, synthesized $WO_3$ nanorod bundles that performed well as negative electrodes in an asymmetric device, demonstrating energy densities of 35.3 W h $kg^{-1}$ and power densities of 314 W $kg^{-1}$, respectively.[124] It was concluded in their study that the conductivity of the material and greater diffusion rates of ions were primary factors responsible for the device's performance. In another investigation, Walke and co-workers synthesized mixed-phase hydrated $WO_3$ nanorods with hexagonal tunnels aligned along the (020) plane that displayed a specific capacitance of 539 F $g^{-1}$ at a scanning rate of 2 mV $s^{-1}$.[125] Upon assembly into an asymmetric supercapacitor device, it could yield a power density of 800 W $kg^{-1}$ at an energy density of 43.7 W h $kg^{-1}$. They concluded that a combination of the $WO_3$ nanorod's morphological features which in turn allowed for improved wettability, and effective diffusion of protons into the $WO_3$ nanotunnels were responsible for the high electrochemical performance of the material.

A study by Wang and co-workers examined the impact of crystallinity on $WO_3$ supercapacitor performance. [126] They used hydrothermal synthesis to produce low-crystalline (LC) $WO_3$ nanorods. A comparison of the supercapacitor performance of low-crystalline $WO_3$ and highly-crystalline $WO_3$ was conducted. Electrochemical kinetic analysis revealed that LC-$WO_3$ exhibited a capacitive-dominated charge storage mechanism, resulting in enhanced rate capabilities. Therefore, the LC-$WO_3$ demonstrated superior supercapacitor performance with a specific capacitance of 474 F $g^{-1}$ at a current density of 0.1 A $g^{-1}$. Dai and co-workers used the hydrothermal technique and synthesized mesoporous $WO_3$ microspheres composed of self-assembly of nanofibers.[127] They demonstrated that the $WO_3$ microspheres were capable of delivering a specific capacitance of 797 F $g^{-1}$ at a current density of 0.5 A $g^{-1}$. The unsymmetric supercapacitor device assembled using these $WO_3$ microspheres exhibited an energy density of 97.61 W h $kg^{-1}$ at a power density of 28.01 kW $kg^{-1}$.

Li and co-workers synthesized hydrous hexagonal $WO_3$ using a hydrothermal technique and using it, developed a mixed protonic-electronic conductor.[128] They achieved excellent capacitance retention of 100% even after 50000 cycles with a specific capacitance of 496 F $g^{-1}$. The high capacitance retention attributed to a highly reversible proton insertion/desertion mechanism at the electrode. Additionally, in situ XRD was used to study the process, which revealed the dominance of (002) and (200) reflections for both charge and discharge processes. In addition to maintaining its "breathable" property, h-$WO_3$ did not show any phase transformations. In terms of material stability, this intern minimized mechanical and chemical stresses on the material. This gives the material a significant advantage over previously reported $WO_3$ nanostructures. Liu and co-workers also used the hydrothermal method to produce self-assembled pancake-like $WO_3$.[129] With a current density of 0.37 A $g^{-1}$, the pancake-like $WO_3$ exhibited a specific capacitance of 605.5 F $g^{-1}$, and capacitance retention of 100% after 4000 cycles. Zhi and co-workers synthesized hexagonal nanopillars made of $WO_3$ that demonstrated a specific capacitance of 421.8 F $g^{-1}$ at a current density of 0.5 A $g^{-1}$.[130]

The comparison between nanostructured WO3 electrodes and conventional nanoparticles has shown that the former is capable of demonstrating superior specific capacitance, which means that it can store more electrical energy per unit of mass compared to conventional nanoparticles. This is a promising finding that can lead to more efficient energy storage capabilities of supercapacitor devices. Furthermore, the research also revealed that the use of nanostructured WO3 electrodes led to improved electrochemical stability compared to the use of conventional nanoparticles. Electrochemical stability is crucial for the longevity of supercapacitor devices since it measures how well a material can withstand repeated charging and discharging cycles without degrading its performance. Despite these promising results, it is still necessary to improve the WO3 nanostructures to commercialize supercapacitor devices on a large scale. In particular, the electrical conductivity of the WO3 nanostructures needs to be improved, as this characteristic is critical for efficient electrical current flow in supercapacitor devices. Enhancing the electrical conductivity can lead to faster charging and discharging times, as well as higher overall efficiency of the supercapacitor. Another challenge that needs to be addressed to commercialize WO3 nanostructure-based supercapacitor devices is improving their electrochemical stability. While nanostructured WO3 electrodes exhibit better electrochemical stability than conventional nanoparticles, further improvements are necessary to ensure the long-term performance and reliability of the supercapacitor devices. Lastly, the surface area of the WO3 nanostructures also needs to be improved. The surface area of the electrode material is critical for energy storage in supercapacitors since it determines the amount of electrolyte that can come in contact with the electrode material. Increasing the surface area of the electrode material can, therefore, lead to a higher energy storage capacity of the supercapacitor devices.

| Morphology | Synthesis method | Synthesis Condition | Characterization (Particle size, Surface area) | Specific capacitance, Current density/Scan rate | Capacitance retention, cycle number | Energy Density (Wh $kg^{-1}$) | Power Density (W $kg^{-1}$) | Ref. |
|---|---|---|---|---|---|---|---|---|
| $WO_3$ nanoparticles | Sol-gel | $WCl_6$, Triton X-100 | 5.8 $m^2$ $g^{-1}$ | 233.6 F $g^{-1}$ at 2 mV $s^{-1}$ | - | - | - | 112 |
| $WO_3$ nanoplates | Wet chemical method | $Na_2WO_4.2H_2O$, $H_2SO_4$, 200 °C | 70-100 nm thickness and 400-500 nm width. | 471 F $g^{-1}$ at 2 mV $s^{-1}$ | 89%, 3000 cycles | - | - | 131 |
| $WO_3.H_2O$ nanoplates | Wet chemical method | $Na_2WO_4.2H_2O$, $H_2SO_4$, 110 °C | 124.7 $m^2$ $g^{-1}$ | 606 F $g^{-1}$ at 1 A $g^{-1}$ | 89%, 4000 cycles | - | - | 113 |
| Hydrated $WO_3$ slabs | Wet chemical method | $Na_2WO_4.2H_2O$, $H_2SO_4$, 110 °C | 68.8 $m^2$ $g^{-1}$ | 386 F $g^{-1}$ at 2 mV $s^{-1}$ | 96%, 3000 cycles | - | - | 115 |
| Hydrated $WO_3$ hierarchical | Wet chemical method | $Na_2WO_4.2H_2O$, $H_2SO_4$, 80 °C | 146.8 $m^2$ $g^{-1}$ | 457 F $g^{-1}$ at 2 mV $s^{-1}$ | 91%, 2000 cycles | 31 | 758 | 114 |
| $WO_3$ 2D film | Atomic layer deposition | $SiO_2$/Si , Tungsten source | 0.7 nm thick films | 650.3 F $g^{-1}$ at 1.5 A $g^{-1}$ | 65.8%, 2000 cycles | - | - | 121 |

**Table 1.1 (Part A) :** Analysis of the morphological modifications of nanostructured $WO_3$ and their supercapacitor performance based on the synthesis method.

| Morphology | Synthesis method | Synthesis Condition | Characterization (Particle size, Surface area) | Specific capacitance, Current density/Scan rate | Capacitance retention, cycle number | Energy Density (Wh $kg^{-1}$) | Power Density (W $kg^{-1}$) | Ref. |
|---|---|---|---|---|---|---|---|---|
| Ordered mesoporous $WO_3$ | Template method | $H_3PW_{12}O_{40}$, KIT-6 template, 550 °C | 54.3 $m^2$ $g^{-1}$ | 199 F $g^{-1}$ at 1 mA $cm^{-2}$ | 100%, 1200 cycles | - | - | 117 |
| $WO_3$ nanoflowers | Electrodeposition | $Na_2WO_4.2H_2O$, $H_2SO_4$, $H_2O_2$ | - | 196 F $g^{-1}$ at 10 mV $s^{-1}$ | 85%, 5000 cycles | 0.53 mWh $cm^{-3}$ | 229.3 mW $cm^{-3}$ | 120 |
| Disk like $WO_3$ | Chemical bath deposition | W powder, $H_2O_2$, 80 °C | 100-200 nm | 725 F $g^{-1}$ at 7 mA $cm^{-2}$ | 81%, 1000 cycles | 25.18 | 1166 | 116 |
| $WO_3$ nanorods | Hydrothermal | $Na_2WO_4.2H_2O$, $H_2SO_4$, autoclaved at 180 °C | 214.6 $m^2$ $g^{-1}$ | 539 F $g^{-1}$ at 2 mV $s^{-1}$ | 92%, 2000 cycles | 43.7 | 800 | 125 |
| $WO_3$ nanorod bundles | Hydrothermal | $Na_2WO_4.2H_2O$, NaCl, HCl, 180 °C | - | 254 F $g^{-1}$ at 0.5 A $g^{-1}$ | 88%, 1000 cycles | 35.3 | 314 | 124 |
| $WO_3$ nanorods | Hydrothermal | $(NH_4)_{10}W_{12}O_{41}.5H_2O$, $H_2SO_4$, $(NH_4)_2SO_4$, autoclaved at 120 °C | 19 $m^2$ $g^{-1}$ | 496 F $g^{-1}$ at 5 mV $s^{-1}$ | 100%, 50000 cycles | - | - | 128 |

**Table 1.1 (Part B) :** Analysis of the morphological modifications of nanostructured $WO_3$ and their supercapacitor performance based on the synthesis method.

| Morphology | Synthesis method | Synthesis Condition | Characterization (Particle size, Surface area) | Specific capacitance, Current density/Scan rate | Capacitance retention, cycle number | Energy Density (Wh kg$^{-1}$) | Power Density (W kg$^{-1}$) | Ref. |
|---|---|---|---|---|---|---|---|---|
| $WO_3$ nanorods | Hydrothermal | $(NH_4)_6H_2W_{12}O_{40}.x$ $H_2O$, autoclaved at 200 °C | 19 m$^2$ g$^{-1}$ | 474 F g$^{-1}$ at 0.1 A g$^{-1}$ | 92%, 10000 cycles | 7.6 mW h cm$^{-3}$ | 18.9 mW cm$^{-3}$ | 126 |
| Pancake like $WO_3$ | Hydrothermal | $Na_2WO_4.2H_2O$, $HNO_3$, autoclaved at 180 °C | 32.4 m$^2$ g$^{-1}$ | 605.5 F g$^{-1}$ at 0.37 A g$^{-1}$ | 100%, 4000 cycles | - | - | 129 |
| $WO_3$ microspheres | Hydrothermal | $K_2WO_4.H_2O$, HCl, $H_2O_2$, autoclaved at 160 °C | - | 797.1 F g$^{-1}$ at 0.5 A g$^{-1}$ | 100%, 2000 cycles | 97.6 | 28 | 127 |
| $WO_3$ nanopillars | Hydrothermal | HCl, $Na_2WO_4.2H_2O$, NaCl, autoclaved at 180 °C | 26.4 m$^2$g$^{-1}$ | 421.8 F g$^{-1}$ at 0.5 A g$^{-1}$ | 100%, 1000 cycles | 10 | 1000 | 132 |

**Table 1.1 (Part C) :** Analysis of the morphological modifications of nanostructured $WO_3$ and their supercapacitor performance based on the synthesis method.

## 1.9 NANOSTRUCTURED $MoO_3$ FOR SUPERCAPACITOR APPLICATIONS

Analogues to $WO_3$, $MoO_3$ has also gained much attention for being an excellent intercalating/ pseudocapacitive material.[133] The uniqueness of $MoO_3$ lies in its crystal structure which is formed from bilayer stacking which endows it with intercalation channels.[134] It has been thoroughly proven that weak van der Waals interactions link bilayers in $MoO_3$ with an interlayer spacing of 0.69 nm.[135] This large interlayer spacing offers sufficient diffusion path for intercalation-deintercalating a range of foreign ions, thus making it an interesting charge storage material.[136] $MoO_3$ as a supercapacitor has been reported with a variety of controlled morphologies and sizes ranging from nanoparticles to three-dimensional structures using an array of different synthesis approaches. It has been summarized in detail in table 1.2.

Among all the different approaches used to synthesize $MoO_3$, the hydrothermal technique is the most widely utilized one.[137] Using flexible temperature and pressure conditions, this method allows for the forced hydrolysis of the reactant precursor for crystallization. $MoO_3$ obtained from the hydrothermal route are known for their high phase purity along with morphological control.[138] Both of which are beneficial when it comes to charge storage. An example of this is the elm seed line mesoporous $MoO_{3-x}$ nanosheets synthesized by Nan and co-workers.[139] They demonstrated high pseudocapacitive performance of their material which could yield a specific capacitance of 1480 F $g^{-1}$ at a current density of 5 A $g^{-1}$. They also showcased that their material did not show any decay in the capacitance retention even after 10,000 cycles which was scanned at a scanning rate of 100 mV $s^{-1}$. When assembled into an asymmetric supercapacitor device, the $MoO_{3-x}$ nanosheets delivered an energy density of 143 W h $kg^{-1}$ at a power density of 2010 W $kg^{-1}$.

Along similar lines with a slight temperature modification to the synthesis protocol Cao and co-workers synthesized an oxygen vacancy enriched $MoO_{3-x}$ nanobelts via the hydrothermal method.[140] They developed asymmetric supercapacitors based on the nanobelts, utilized $H_2SO_4$ with ethylene glycol as a novel electrolyte, and could achieve a specific capacitance of 1220 F $g^{-1}$ at the current density of 50 A $g^{-1}$. When assembled into an asymmetric supercapacitor device the $MoO_{3-x}$ nanobelts delivered an energy density of 111 W h $kg^{-1}$ at a power density of 803 W $kg^{-1}$. In a recent investigation by Wang and co-workers, they synthesized $MoO_3$ nanorods and demonstrated them for dual, electrochromic, and capacitor performance.[141] They demonstrated that their $MoO_3$ nanorods alonwith excellent electrochromic performance with 67% high transmission contrast, also showed good capacitor performance with a specific capacitance of 650 F $g^{-1}$ at a current density of 1 A $g^{-1}$. Additionally, the material exhibited a capacitance retention of 98.5% even after 10,000 cycles. Warsi and co-workers used the hydrothermal technique to achieve in situ hydrogenation of $MoO_3$ nanowires which resulted in enhancement of its supercapacitor performance.[142] They demonstrated that the hydrogenation of $MoO_3$ nanowires could yield a specific capacitance of 168 F $g^{-1}$ at a current density of 0.5 A $g^{-1}$. The hydrogenated $MoO_3$ demonstrated a capacitance retention of 97% after 3000 cycles.

Nanostructured $MoO_3$ for supercapacitors have been synthesized using the chemical bath deposition method as well, which utilizes the process of heterogeneous nucleation in order to deposit thin films of $MoO_3$ onto a suitable substrate.[143] For instance, Lokhande and co-workers have reported hexagonal architectured $MoO_3$ thin films and demonstrated them for supercapacitor applications.[144] They could achieve a specific capacitance of 194 F $g^{-1}$ at a scanning rate of 5 mV $s^{-1}$ with capacitance retention of 100% after 1000 cycles. Recently, as a modification to the classical chemical bath deposition method, Tezel and co-workers have produced $MoO_3$ thin films through a bio-chemical bath deposition method.[145] This was achieved by mixed catalase and invertase enzymes in the chemical bath solution prior to deposition. The thin films synthesized using this technique exhibited a specific capacitance of 460 F $g^{-1}$ at a scanning rate of 50 mV $s^{-1}$.

Electrodeposition is another interesting technique reported in the literature for producing $MoO_3$ for supercapacitors.[146] For instance, Zhao and co-workers have recently produced a $MoO_3$ electrode using the electrodeposition technique which works within a widened electrochemical potential window.[147] The electrode exhibits a capacitance of 186 µAh $cm^2$ and has capacitance retention of only 65% after 100 cycles. When assembled as a symmetric supercapacitor device, the electrodeposited $MoO_3$ delivered an energy density of 22 W h $kg^{-1}$ at a power density of 301 W $kg^{-1}$. Spray pyrolysis is another technique largely utilized for synthesizing $MoO_3$ thin films for a variety of applications such as memory devices, gas sensing, and photochromics however, there are very few reports on supercapacitors. One such report is by Mane and co-workers, who deposited polycrystalline $MoO_3$ thin films over a fluorine-tin oxide (FTO) substrate at various deposition temperatures.[148] These films were then demonstrated for their charge storage performance and could exhibit a specific capacitance of 1249.2 F $g^{-1}$ at a current density of 6 A $g^{-1}$. Additionally, the $MoO_3$ thin films exhibited capacitance retention of 85% even after 5000 cycles.

However, since most of the methods employed for synthesis include methods such as hydrothermal, chemical bath deposition, electrodeposition, spray pyrolysis, etc. are not economically practicable for large-scale industrial production. In addition, the supercapacitor performance is also very limited in terms of long-term stability and energy delivery. Therefore, it has become imperative to develop a simple and scalable methodology by which nanostructured $WO_3$ and $MoO_3$ with high conductivity and improved electrochemical cycling stability can be made for application in supercapacitors.

The motivation for this thesis was provided by the need to improve energy storage technology and find alternatives to traditional fossil fuel-based power sources. The focus of the thesis was on designing nanostructured $WO_3$ and $MoO_3$ materials for supercapacitor applications, which are promising candidates for energy storage due to their high power density, fast charging times, and long cycle lives. The design of several nanostructured $WO_3$ and $MoO_3$ materials for supercapacitor applications was the core objective of this thesis. The major aims of this thesis are listed in section 1.10 in light of the literature review above. The outcome of the systematic research methodology employed to achieve the above objectives is discussed in detail in individual chapters 2-4. Finally, chapter 5 provides an overall summary of the findings of these investigations. The research presented in this thesis provides a valuable contribution to the field of energy storage technology and highlights the potential of nanostructured $WO_3$ and $MoO_3$ materials for supercapacitor applications. By demonstrating the importance of specific design parameters in optimizing the electrochemical performance of these materials, this thesis provides a framework for future research and development in the field of energy storage.

| Morphology | Synthesis method | Synthesis Condition | Characterization (Particle size, Surface area) | Specific capacitance, Current density/Scan rate | Capacitance retention, cycle number | Energy Density (Wh $kg^{-1}$) | Power Density (W $kg^{-1}$) | Ref. |
|---|---|---|---|---|---|---|---|---|
| Elm seed like $MoO_{3-x}$ | Hydrothermal | Mo powder, $H_2O_2$, Ethanol, Autoclaved at 180 °C. | - | 1480 F $g^{-1}$ at 5 A $g^{-1}$. | 100% at 10000 cycles. | 143 | 2010 | [139] |
| $MoO_{3-x}$ nanobelts | Hydrothermal | Mo powder, $H_2O_2$, Ethanol, Autoclaved at 140 °C. | 18.5 $m^2$ $g^{-1}$ | 1220 F $g^{-1}$ at 50 A $g^{-1}$ | 100% at 38000 cycles | 111 | 803 | [140] |
| $MoO_3$ nanorods | Hydrothermal | Sodium molybdate, $HNO_3$, autoclave | - | 650 F $g^{-1}$ at 1 A $g^{-1}$ | 98.5 % at 10000 cycles | - | - | [141] |
| $MoO_3$ nanorods | Hydrothermal | Ammonium heptamolybdare, SDA, autoclave | 389 F $g^{-1}$ at 1 mA $g^{-1}$ | 411 F $g^{-1}$ at 5 mV $s^{-1}$ | 82.4% at 1000 cycles | - | - | [149] |
| $MoO_3$ nanowires | Hydrothermal | $MoO_2$, $H_2O_2$, HCl, Autoclave | 100 nm | 168 F $g^{-1}$ at 0.5 A $g^{-1}$ | 97% at 3000 cycles | - | - | [142] |

**Table 1.2 (Part A):** Analysis of the morphological modifications of nanostructured $MoO_3$ and their supercapacitor performance based on the synthesis method.

| **Morphology** | **Synthesis method** | **Synthesis Condition** | **Characterization (Particle size, Surface area)** | **Specific capacitance, Current density/Scan rate** | **Capacitance retention, cycle number** | **Device configeration** | **Energy Density (Wh kg$^{-1}$)** | **Power Density (W kg$^{-1}$** | **Ref.** |
|---|---|---|---|---|---|---|---|---|---|
| $MoO_3$ nanobelts | Hydrothermal | Ammonium heptamolybdare tetrahydrate, CTAB, $HNO_3$, | 59.3 m$^2$ g$^{-1}$ | 256.8 F g$^{-1}$ at 5 mV s$^{-1}$. | 100% at 200 cycles | - | - | - | 150 |
| $MoO_3$ microrods | Chemical bath deposition | Ammonium, molybdate, $HNO_3$ | - | 194 F g$^{-1}$ at 5 mV s$^{-1}$ | 100% at 1000 cycles | - | 7.33 | 1200 | 144 |
| $MoO_3$ film | Bio chemical bath deposition | Sodium molybdate, enzymes, $H_2SO_4$, $H_2O_2$ | - | 460 F g$^{-1}$ at 50 mV s$^{-1}$ | - | - | - | - | 145 |
| $MoO_3$ film | Electrodeposition | Graphite foil, Ammonium heptamolybdare tetrahydrate | - | 186 µAh cm$^2$ | 65% at 100 cycles | $MoO_3$// $MoO_3$ | 22 | 301 | 147 |
| $MoO_3$ film | Spray pyrolysis | $MoO_3$ powder, $NH_4OH$, FTO | - | 1249.2 F g$^{-1}$ at 6 A g$^{-1}$ | 85% at 5000 cycles | - | - | - | 148 |

**Table 1.2 (Part B):** Analysis of the morphological modifications of nanostructured $MoO_3$ and their supercapacitor performance based on the synthesis method.

## 1.10 THESIS OBJECTIVES

- To synthesize nanostructures of $WO_{3-x}$ and perform their detailed material characterization.
- To synthesize $WO_{3-x}$/C microfibers and perform their detailed material characterization.
- To synthesize 2D $MoO_{3-x}$ microplates and microdisks and perform their detailed material characterization.
- To synthesize 3D $MoO_{3-x}$ microflowers and perform their detailed material characterization.
- To evaluate the synthesized materials for their charge storage performance.

## 1.11 REFERENCES

(1) Abdel Maksoud, M. I. A.; Fahim, R. A.; Shalan, A. E.; Abd Elkodous, M.; Olojede, S. O.; Osman, A. I.; Farrell, C.; Al-Muhtaseb, A. H.; Awed, A. S.; Ashour, A. H.; Rooney, D. W. Advanced Materials and Technologies for Supercapacitors Used in Energy Conversion and Storage: A Review. *Environ. Chem. Lett.* **2021**, *19* (1), 375–439.

(2) Kennedy, C.; Steinberger, J.; Gasson, B.; Hansen, Y.; Hillman, T.; Havránek, M.; Pataki, D.; Phdungsilp, A.; Ramaswami, A.; Mendez, G. V. Greenhouse Gas Emissions from Global Cities. *Environ. Sci. Technol.* **2009**, *43* (19), 7297–7302.

(3) Wang, F.; Harindintwali, J. D.; Yuan, Z.; Wang, M.; Wang, F.; Li, S.; Yin, Z.; Huang, L.; Fu, Y.; Li, L.; Chang, S. X.; Zhang, L.; Rinklebe, J.; Yuan, Z.; Zhu, Q.; Xiang, L.; Tsang, D. C. W.; Xu, L.; Jiang, X.; Liu, J.; Wei, N.; Kästner, M.; Zou, Y.; Ok, Y. S.; Shen, J.; Peng, D.; Zhang, W.; Barceló, D.; Zhou, Y.; Bai, Z.; Li, B.; Zhang, B.; Wei, K.; Cao, H.; Tan, Z.; Zhao, L. bin; He, X.; Zheng, J.; Bolan, N.; Liu, X.; Huang, C.; Dietmann, S.; Luo, M.; Sun, N.; Gong, J.; Gong, Y.; Brahushi, F.; Zhang, T.; Xiao, C.; Li, X.; Chen, W.; Jiao, N.; Lehmann, J.; Zhu, Y. G.; Jin, H.; Schäffer, A.; Tiedje, J. M.; Chen, J. M. Technologies and Perspectives for Achieving Carbon Neutrality. *Innov.* **2021**, *2* (4), 100180.

(4) Gielen, D.; Boshell, F.; Saygin, D.; Bazilian, M. D.; Wagner, N.; Gorini, R. The Role of Renewable Energy in the Global Energy Transformation. *Energy Strateg. Rev.* **2019**, *24*, 38–50.

(5) Daiyan, R.; MacGill, I.; Amal, R. Opportunities and Challenges for Renewable Power-to-X. *ACS Energy Lett.* **2020**, *5* (12), 3843–3847.

(6) Blanco, H.; Faaij, A. A Review at the Role of Storage in Energy Systems with a Focus on Power to Gas and Long-Term Storage. *Renew. Sustain. Energy Rev.* **2018**, *81*, 1049–1086.

(7) Duffy, P.; Fitzpatrick, C.; Conway, T.; Lynch, R. P. Energy Sources and Supply Grids – The Growing Need for Storage. In *Energy Storage Options and Their Environmental Impact*; The Royal Society of Chemistry, 2019; pp 1–41.

(8) Shao, Y.; El-Kady, M. F.; Sun, J.; Li, Y.; Zhang, Q.; Zhu, M.; Wang, H.; Dunn, B.; Kaner, R. B. Design and Mechanisms of Asymmetric Supercapacitors. *Chem. Rev.* **2018**, *118* (18), 9233–9280.

(9) Zhou, R.; Wei, S.; Liu, Y.; Gao, N.; Wang, G.; Lian, J.; Jiang, Q. Charge Storage by Electrochemical Reaction of Water Bilayers Absorbed on $MoS_2$ Monolayers. *Sci. Rep.* **2019**, *9* (1), 3980.

(10) Manthiram, A. An Outlook on Lithium Ion Battery Technology. *ACS Cent. Sci.* **2017**, *3* (10), 1063–1069.

(11) Ma, S.; Jiang, M.; Tao, P.; Song, C.; Wu, J.; Wang, J.; Deng, T.; Shang, W. Temperature Effect and Thermal Impact in Lithium-Ion Batteries: A Review. *Prog. Nat. Sci. Mater. Int.* **2018**, *28* (6), 653–666.

(12) Wood, K. N.; Kazyak, E.; Chadwick, A. F.; Chen, K.-H.; Zhang, J.-G.; Thornton, K.; Dasgupta, N. P. Dendrites and Pits: Untangling the Complex Behavior of Lithium Metal Anodes through Operando Video Microscopy. *ACS Cent. Sci.* **2016**, *2* (11), 790–801.

(13) Castro-Gutiérrez, J.; Celzard, A.; Fierro, V. Energy Storage in Supercapacitors: Focus on Tannin-Derived Carbon Electrodes. *Front. Mater.* **2020**, *7*.

(14) Chatterjee, D. P.; Nandi, A. K. A Review on the Recent Advances in Hybrid Supercapacitors. *J. Mater. Chem. A* **2021**, *9* (29), 15880–15918.

(15) Rehman, J.; Eid, K.; Ali, R.; Fan, X.; Murtaza, G.; Faizan, M.; Laref, A.; Zheng, W.; Varma, R. S. Engineering of Transition Metal Sulfide Nanostructures as Efficient Electrodes for High-Performance Supercapacitors. *ACS Appl. Energy Mater.* **2022**.

(16) Kandasamy, M.; Sahoo, S.; Nayak, S. K.; Chakraborty, B.; Rout, C. S. Recent Advances in Engineered Metal Oxide Nanostructures for Supercapacitor Applications: Experimental and Theoretical Aspects. *J. Mater. Chem. A* **2021**, *9* (33), 17643–17700.

(17) Huang, S.; Zhu, X.; Sarkar, S.; Zhao, Y. Challenges and Opportunities for Supercapacitors. *APL Mater.* **2019**, *7* (10), 100901.

(18) Natarajan, S.; Ulaganathan, M.; Aravindan, V. Building Next-Generation Supercapacitors with Battery Type $Ni(OH)_2$. *J. Mater. Chem. A* **2021**, *9* (28), 15542–15585.

(19) Hellström, S. The Discovery of Static Electricity and Its Manifestation. In *ESD - The Scourge of Electronics*; Springer Berlin Heidelberg: Berlin, Heidelberg, 1998; pp 1–20.

(20) Sarma, D. D.; Shukla, A. K. Building Better Batteries: A Travel Back in Time. *ACS Energy Lett.* **2018**, *3* (11), 2841–2845.

(21) Kurra, N.; Jiang, Q. 18 - Supercapacitors. In *Storing Energy (Second Edition)*; Letcher, T. M., Ed.; Elsevier, 2022; pp 383–417.

(22) Sun, J.; Luo, B.; Li, H. A Review on the Conventional Capacitors, Supercapacitors, and Emerging Hybrid Ion Capacitors: Past, Present, and Future. *Adv. Energy Sustain. Res.* **2022**, *3* (6), 2100191.

(23) Brown, M. A.; Bossa, G. V.; May, S. Emergence of a Stern Layer from the Incorporation of Hydration Interactions into the Gouy–Chapman Model of the Electrical Double Layer. *Langmuir* **2015**, *31* (42), 11477–11483.

(24) Yassine, M.; Fabris, D. Performance of Commercially Available Supercapacitors.

*Energies* **2017**, *10* (9).

(25) Miller, J. R.; Burke, A. Electrochemical Capacitors: Challenges and Opportunities for Real-World Applications. *Electrochem. Soc. Interface* **2008**, *17* (1), 53–57.

(26) Yoshida, N.; Yamada, Y.; Nishimura, S.; Oba, Y.; Ohnuma, M.; Yamada, A. Unveiling the Origin of Unusual Pseudocapacitance of $RuO_2{\cdot}nH_2O$ from Its Hierarchical Nanostructure by Small-Angle X-Ray Scattering. *J. Phys. Chem. C* **2013**, *117* (23), 12003–12009.

(27) Rehman, Z. U.; Bilal, M.; Hou, J.; Ahmad, J.; Ullah, S.; Wang, X.; Hussain, A. 6 - Metal Oxide–Carbon Composites for Supercapacitor Applications. In *Metal Oxide-Carbon Hybrid Materials*; Chaudhry, M. A., Hussain, R., Butt, F. K., Eds.; Metal Oxides; Elsevier, 2022; pp 133–177.

(28) Jalal, N. I.; Ibrahim, R. I.; Oudah, M. K. A Review on Supercapacitors: Types and Components. *J. Phys. Conf. Ser.* **2021**, *1973* (1), 12015.

(29) Winter, M.; Brodd, R. J. What Are Batteries, Fuel Cells, and Supercapacitors? *Chem. Rev.* **2004**, *104* (10), 4245–4270.

(30) Azaïs, P. Manufacturing of Industrial Supercapacitors. In *Supercapacitors*; John Wiley & Sons, Ltd, 2013; pp 307–371.

(31) Xu, B.; Wu, F.; Chen, R.; Cao, G.; Chen, S.; Zhou, Z.; Yang, Y. Highly Mesoporous and High Surface Area Carbon: A High Capacitance Electrode Material for EDLCs with Various Electrolytes. *Electrochem. commun.* **2008**, *10* (5), 795–797.

(32) Şahin, M. E.; Blaabjerg, F.; Sangwongwanich, A. A Comprehensive Review on Supercapacitor Applications and Developments. *Energies* **2022**, *15* (3).

(33) Lee, S. P.; Ali, G. A. M.; Hegazy, H. H.; Lim, H. N.; Chong, K. F. Optimizing Reduced Graphene Oxide Aerogel for a Supercapacitor. *Energy & Fuels* **2021**, *35* (5), 4559–4569.

(34) Komatsubara, K.; Suzuki, H.; Inoue, H.; Kishibuchi, M.; Takahashi, S.; Marui, T.; Umezawa, S.; Nakagawa, T.; Nasu, K.; Maetani, M.; Tanaka, Y.; Yamada, M.;

Nishikawa, T.; Yamashita, Y.; Hada, M.; Hayashi, Y. Highly Oriented Carbon Nanotube Supercapacitors. *ACS Appl. Nano Mater.* **2022**, *5* (1), 1521–1532.

(35) Korenblit, Y.; Rose, M.; Kockrick, E.; Borchardt, L.; Kvit, A.; Kaskel, S.; Yushin, G. High-Rate Electrochemical Capacitors Based on Ordered Mesoporous Silicon Carbide-Derived Carbon. *ACS Nano* **2010**, *4* (3), 1337–1344.

(36) Down, M. P.; Rowley-Neale, S. J.; Smith, G. C.; Banks, C. E. Fabrication of Graphene Oxide Supercapacitor Devices. *ACS Appl. Energy Mater.* **2018**, *1* (2), 707–714.

(37) Béguin, F.; Presser, V.; Balducci, A.; Frackowiak, E. Carbons and Electrolytes for Advanced Supercapacitors. *Adv. Mater.* **2014**, *26* (14), 2219–2251.

(38) You, X.; Misra, M.; Gregori, S.; Mohanty, A. K. Preparation of an Electric Double Layer Capacitor (EDLC) Using Miscanthus-Derived Biocarbon. *ACS Sustain. Chem. Eng.* **2018**, *6* (1), 318–324.

(39) Liu, Y.; Jiang, S. P.; Shao, Z. Intercalation Pseudocapacitance in Electrochemical Energy Storage: Recent Advances in Fundamental Understanding and Materials Development. *Mater. Today Adv.* **2020**, *7*, 100072.

(40) Sahoo, S.; Kumar, R.; Joanni, E.; Singh, R. K.; Shim, J.-J. Advances in Pseudocapacitive and Battery-like Electrode Materials for High Performance Supercapacitors. *J. Mater. Chem. A* **2022**, *10* (25), 13190–13240.

(41) Balasubramaniam, S.; Mohanty, A.; Balasingam, S. K.; Kim, S. J.; Ramadoss, A. Comprehensive Insight into the Mechanism, Material Selection and Performance Evaluation of Supercapatteries. *Nano-Micro Lett.* **2020**, *12* (1), 85.

(42) Lokhande, P. E.; Chavan, U. S.; Pandey, A. Materials and Fabrication Methods for Electrochemical Supercapacitors: Overview. *Electrochem. Energy Rev.* **2020**, *3* (1), 155–186.

(43) Jiang, Y.; Liu, J. Definitions of Pseudocapacitive Materials: A Brief Review. *ENERGY \& Environ. Mater.* **2019**, *2* (1), 30–37.

(44) Majumdar, D.; Maiyalagan, T.; Jiang, Z. Recent Progress in Ruthenium Oxide-Based

Composites for Supercapacitor Applications. *ChemElectroChem* **2019**, *6* (17), 4343–4372.

(45) Zhou, Y.; Guo, W.; Li, T. A Review on Transition Metal Nitrides as Electrode Materials for Supercapacitors. *Ceram. Int.* **2019**, *45* (17, Part A), 21062–21076.

(46) Snook, G. A.; Kao, P.; Best, A. S. Conducting-Polymer-Based Supercapacitor Devices and Electrodes. *J. Power Sources* **2011**, *196* (1), 1–12.

(47) Lokhande, V.; Lokhande, A.; Namkoong, G.; Kim, J. H.; Ji, T. Charge Storage in $WO_3$ Polymorphs and Their Application as Supercapacitor Electrode Material. *Results Phys.* **2019**, *12* (February 2019), 2012–2020.

(48) Gao, L.; Wang, X.; Xie, Z.; Song, W.; Wang, L.; Wu, X.; Qu, F.; Chen, D.; Shen, G. High-Performance Energy-Storage Devices Based on $WO_3$ Nanowire Arrays/Carbon Cloth Integrated Electrodes. *J. Mater. Chem. A* **2013**, *1* (24), 7167–7173.

(49) Naik, A. P.; Salkar, A. V.; Peña, G. D. J. G. J. G.; Sawant, J. V.; Bharath, G.; Banat, F.; Bhosale, S. V.; Morajkar, P. P. Facile Synthesis of Fibrous, Mesoporous $Ni_{1-x}O$ Nanosponge Supported on Ni Foam for Enhanced Pseudocapacitor Applications. *J. Mater. Sci.* **2020**, *55* (26), 12232–12248.

(50) Fleischmann, S.; Mitchell, J. B.; Wang, R.; Zhan, C.; Jiang, D.; Presser, V.; Augustyn, V. Pseudocapacitance: From Fundamental Understanding to High Power Energy Storage Materials. *Chem. Rev.* **2020**, *120* (14), 6738–6782.

(51) Shinde, P. A.; Jun, S. C. Review on Recent Progress in the Development of Tungsten Oxide Based Electrodes for Electrochemical Energy Storage. *ChemSusChem* **2020**, *13* (1), 11–38.

(52) S, K.; A, S.; K, H. Performance of Tungsten Oxide/Polypyrrole Composite as Cathode Catalyst in Single Chamber Microbial Fuel Cell. *J. Environ. Chem. Eng.* **2020**, *8* (6), 104520.

(53) Salkar, A. V; Fernandes, R. X.; Bhosale, S. V; Morajkar, P. P. NH- and CH-Substituted Ureas as Self-Assembly Directing Motifs for Facile Synthesis and Electrocapacitive Applications of Advanced $WO_{3-x}$ One-Dimensional Nanorods. *ACS*

*Appl. Energy Mater.* **2019**, *2* (12), 8724–8736.

(54) Smeaton, W. A. Carl Wilhelm Scheele (1742–1786). *Endeavour* **1986**, *10* (1), 28–30.

(55) Schufle, J. A. Juan Jose D'Elhuyar, Discoverer of Tungsten. *J. Chem. Educ.* **1975**, *52* (5), 325.

(56) Zheng, H.; Tachibana, Y.; Kalantar-zadeh, K. Dye-Sensitized Solar Cells Based on WO3. *Langmuir* **2010**, *26* (24), 19148–19152.

(57) Staerz, A.; Somacescu, S.; Epifani, M.; Kida, T.; Weimar, U.; Barsan, N. $WO_3$-Based Gas Sensors: Identifying Inherent Qualities and Understanding the Sensing Mechanism. *ACS Sensors* **2020**, *5* (6), 1624–1633.

(58) Jelinska, A.; Bienkowski, K.; Jadwiszczak, M.; Pisarek, M.; Strawski, M.; Kurzydlowski, D.; Solarska, R.; Augustynski, J. Enhanced Photocatalytic Water Splitting on Very Thin $WO_3$ Films Activated by High-Temperature Annealing. *ACS Catal.* **2018**, *8* (11), 10573–10580.

(59) Li, Y.; A. McMaster, W.; Wei, H.; Chen, D.; A. Caruso, R. Enhanced Electrochromic Properties of WO3 Nanotree-like Structures Synthesized via a Two-Step Solvothermal Process Showing Promise for Electrochromic Window Application. *ACS Appl. Nano Mater.* **2018**, *1* (6), 2552–2558.

(60) Salkar, A. V.; Naik, A. P.; Bhosale, S. V.; Morajkar, P. P. Designing a Rare DNA-Like Double Helical Microfiber Superstructure via Self-Assembly of In Situ Carbon Fiber-Encapsulated $WO_{3-x}$ Nanorods as an Advanced Supercapacitor Material. *ACS Appl. Mater. Interfaces* **2021**, *13* (1), 1288–1300.

(61) Chatten, R.; Chadwick, A. V; Rougier, A.; Lindan, P. J. D. The Oxygen Vacancy in Crystal Phases of $WO_3$. *J. Phys. Chem. B* **2005**, *109* (8), 3146–3156.

(62) Gerosa, M.; Di Valentin, C.; Onida, G.; Bottani, C. E.; Pacchioni, G. Anisotropic Effects of Oxygen Vacancies on Electrochromic Properties and Conductivity of γ-Monoclinic $WO_3$. *J. Phys. Chem. C* **2016**, *120* (21), 11716–11726.

(63) Constable, E. C. Evolution and Understanding of the D-Block Elements in the

Periodic Table. *Dalt. Trans.* **2019**, *48* (26), 9408–9421.

(64) Gong, Y.; Dong, Y.; Zhao, B.; Yu, R.; Hu, S.; Tan, Z. Diverse Applications of $MoO_3$ for High Performance Organic Photovoltaics: Fundamentals- Processes and Optimization Strategies. *J. Mater. Chem. A* **2020**, *8* (3), 978–1009.

(65) Mai, L.; Yang, F.; Zhao, Y.; Xu, X.; Xu, L.; Hu, B.; Luo, Y.; Liu, H. Molybdenum Oxide Nanowires: Synthesis & Properties. *Mater. Today* **2011**, *14* (7), 346–353.

(66) Zhu, Y.; Yao, Y.; Luo, Z.; Pan, C.; Yang, J.; Fang, Y.; Deng, H.; Liu, C.; Tan, Q.; Liu, F.; Guo, Y. Nanostructured $MoO_3$ for Efficient Energy and Environmental Catalysis. *Molecules* **2020**, *25* (1).

(67) de Castro, I. A.; Datta, R. S.; Ou, J. Z.; Castellanos-Gomez, A.; Sriram, S.; Daeneke, T.; Kalantar-zadeh, K. Molybdenum Oxides – From Fundamentals to Functionality. *Adv. Mater.* **2017**, *29* (40), 1701619.

(68) Noby, S. Z.; Fakharuddin, A.; Schupp, S.; Sultan, M.; Krumova, M.; Drescher, M.; Azarkh, M.; Boldt, K.; Schmidt-Mende, L. Oxygen Vacancies in Oxidized and Reduced Vertically Aligned $\alpha$-$MoO_3$ Nanoblades. *Mater. Adv.* **2022**, 3571–3581.

(69) Ren, H.; Sun, S.; Cui, J.; Li, X. Synthesis, Functional Modifications, and Diversified Applications of Molybdenum Oxides Micro/Nanocrystals: A Review. *Cryst. Growth Des.* **2018**, *18* (10), 6326–6369.

(70) Achadu, O. J.; Abe, F.; Li, T.-C.; Khoris, I. M.; Lee, D.; Lee, J.; Suzuki, T.; Park, E. Y. Molybdenum Trioxide Quantum Dot-Encapsulated Nanogels for Virus Detection by Surface-Enhanced Raman Scattering on a 2D Substrate. *ACS Appl. Mater. Interfaces* **2021**, *13* (24), 27836–27844.

(71) Chen, J. S.; Cheah, Y. L.; Madhavi, S.; Lou, X. W. Fast Synthesis of $\alpha$-$MoO_3$ Nanorods with Controlled Aspect Ratios and Their Enhanced Lithium Storage Capabilities. *J. Phys. Chem. C* **2010**, *114* (18), 8675–8678.

(72) Morita, M.; Toyoda, S.; Kiuchi, H.; Abe, T.; Kumagai, K.; Saida, T.; Fukuda, K. Chromogenic Amorphous $MoO_{3-x}$ Nanosheets and Their Nanostructured Films for Smart Window Applications. *ACS Appl. Nano Mater.* **2021**, *4* (9), 8781–8788.

(73) Sajadi, M.; Ranjbar, M.; Rasuli, R. Two-Step Synthesis of Ag-Decorated $MoO_3$ Nanotubes, and the Effect of Hydrogen Doping. *Appl. Surf. Sci.* **2020**, *527*, 146675.

(74) Chithambararaj, A.; Rajeswari Yogamalar, N.; Bose, A. C. Hydrothermally Synthesized h-$MoO_3$ and α-$MoO_3$ Nanocrystals: New Findings on Crystal-Structure-Dependent Charge Transport. *Cryst. Growth Des.* **2016**, *16* (4), 1984–1995.

(75) Lupan, O.; Cretu, V.; Deng, M.; Gedamu, D.; Paulowicz, I.; Kaps, S.; Mishra, Y. K.; Polonskyi, O.; Zamponi, C.; Kienle, L.; Trofim, V.; Tiginyanu, I.; Adelung, R. Versatile Growth of Freestanding Orthorhombic α-Molybdenum Trioxide Nano- and Microstructures by Rapid Thermal Processing for Gas Nanosensors. *J. Phys. Chem. C* **2014**, *118* (27), 15068–15078.

(76) Bandi, S.; Srivastav, A. K. Unveiling the Crystallographic Origin of Mechanochemically Induced Monoclinic to Triclinic Phase Transformation in $WO_3$. *CrystEngComm* **2021**, *23* (8), 1821–1827.

(77) Mardare, C. C.; Hassel, A. W. Review on the Versatility of Tungsten Oxide Coatings. *Phys. status solidi* **2019**, *216* (12), 1900047.

(78) Pirker, L.; Višić, B.; Škapin, S. D.; Dražić, G.; Kovač, J.; Remškar, M. Multi-Stoichiometric Quasi-Two-Dimensional W:$NO_{3(n -1)}$ tungsten Oxides. *Nanoscale* **2020**, *12* (28), 15102–15114.

(79) Migas, D. B.; Shaposhnikov, V. L.; Rodin, V. N.; Borisenko, V. E. Tungsten Oxides. I. Effects of Oxygen Vacancies and Doping on Electronic and Optical Properties of Different Phases of $WO_3$. *J. Appl. Phys.* **2010**, *108* (9).

(80) Migas, D. B.; Shaposhnikov, V. L.; Borisenko, V. E. Tungsten Oxides. II. the Metallic Nature of Magńli Phases. *J. Appl. Phys.* **2010**, *108* (9).

(81) Glember, O.; Saurr, H. Über Wolframoxyde. *Zeitschrift für Anorg. Chemie* **1943**, *252* (3-4), 144–159.

(82) Cong, S.; Geng, F.; Zhao, Z. Tungsten Oxide Materials for Optoelectronic Applications. *Adv. Mater.* **2016**, *28* (47), 10518–10528.

(83) Al Mohammad, A.; Gillet, M. Phase Transformations in WO3 Thin Films during Annealing. *Thin Solid Films* **2002**, *408* (1–2), 302–309.

(84) Imran, M.; Alenezy, E.; Sabri, Y.; Wang, T.; Motta, N.; Tesfamichael, T.; Sonar, P.; Shafiei, M. Enhanced Amperometric Acetone Sensing Using Electrospun Non-Stoichiometric $WO_{3-x}$ nanofibers. *J. Mater. Chem. C* **2021**, *9* (2), 671–678.

(85) Wang, W.; Janotti, A.; de Walle, C. G.; Van De Walle, C. G. Role of Oxygen Vacancies in Crystalline $WO_3$. *J. Mater. Chem. C* **2016**, *4* (27), 6641–6648. \

(86) Vasilopoulou, M.; Douvas, A. M.; Georgiadou, D. G.; Palilis, L. C.; Kennou, S.; Sygellou, L.; Soultati, A.; Kostis, I.; Papadimitropoulos, G.; Davazoglou, D.; Argitis, P. The Influence of Hydrogenation and Oxygen Vacancies on Molybdenum Oxides Work Function and Gap States for Application in Organic Optoelectronics. *J. Am. Chem. Soc.* **2012**, *134* (39), 16178–16187.

(87) Salkar, A. V.; Naik, A. P.; Joshi, V. S.; Haram, S. K.; Morajkar, P. P. Designing a 3D Nanoporous Network: Via Self-Assembly of $WO_3$ Nanorods for Improved Electrocapacitive Performance. *CrystEngComm* **2018**, *20* (42), 6683–6694.

(88) Zheng, H.; Ou, J. Z.; Strano, M. S.; Kaner, R. B.; Mitchell, A.; Kalantar-Zadeh, K. Nanostructured Tungsten Oxide - Properties, Synthesis, and Applications. *Adv. Funct. Mater.* **2011**, *21* (12), 2175–2196.

(89) de Castro, I. A.; Datta, R. S.; Ou, J. Z.; Castellanos-Gomez, A.; Sriram, S.; Daeneke, T.; Kalantar-zadeh, K. Molybdenum Oxides – From Fundamentals to Functionality. *Adv. Mater.* **2017**, *29* (40), 1–31.

(90) Noby, S. Z.; Wong, K. K.; Ramadoss, A.; Siroky, S.; Hagner, M.; Boldt, K.; Schmidt-Mende, L. Rapid Synthesis of Vertically Aligned $\alpha$-$MoO_3$ nanostructures on Substrates. *RSC Adv.* **2020**, *10* (40), 24119–24126.

(91) Kumar, V. V.; Gayathri, K.; Anthony, S. P. Synthesis of $\alpha$-$MoO_3$ Nanoplates Using Organic Aliphatic Acids and Investigation of Sunlight Enhanced Photodegradation of Organic Dyes. *Mater. Res. Bull.* **2016**, *76*, 147–154.

(92) Kumar, V.; Sumboja, A.; Wang, J.; Bhavanasi, V.; Nguyen, V. C.; Lee, P. S.

Topotactic Phase Transformation of Hexagonal $MoO_3$ to Layered $MoO_3$-II and Its Two-Dimensional (2D) Nanosheets. *Chem. Mater.* **2014**, *26* (19), 5533–5539.

(93) Martín-Ramos, P.; Fernández-Coppel, I. A.; Avella, M.; Martín-Gil, J. α-$MoO_3$ Crystals with a Multilayer Stack Structure Obtained by Annealing from a Lamellar $MoS_2$/g-$C_3N_4$ Nanohybrid. *Nanomaterials* **2018**, *8* (7).

(94) Cai, L.; McClellan, C. J.; Koh, A. L.; Li, H.; Yalon, E.; Pop, E.; Zheng, X. Rapid Flame Synthesis of Atomically Thin $MoO_3$ down to Monolayer Thickness for Effective Hole Doping of $WSe_2$. *Nano Lett.* **2017**, *17* (6), 3854–3861.

(95) Ou, J. Z.; Campbell, J. L.; Yao, D.; Wlodarski, W.; Kalantar-zadeh, K. In Situ Raman Spectroscopy of $H_2$ Gas Interaction with Layered $MoO_3$. *J. Phys. Chem. C* **2011**, *115* (21), 10757–10763.

(96) Timmerman, M. A.; Xia, R.; Le, P. T. P.; Wang, Y.; Ten Elshof, J. E. Metal Oxide Nanosheets as 2D Building Blocks for the Design of Novel Materials. *Chemistry* **2020**, *26* (42), 9084–9098.

(97) Martín-Ramos, P.; Fernández-Coppel, I. A.; Avella, M.; Martín-Gil, J. α-$MoO_3$ Crystals with a Multilayer Stack Structure Obtained by Annealing from a Lamellar $MoS_2$/g-$C_3N_4$ Nanohybrid. *Nanomater. (Basel, Switzerland)* **2018**, *8* (7), 559.

(98) Ressler, T.; Jentoft, R. E.; Wienold, J.; Günter, M. M.; Timpe, O. In Situ XAS and XRD Studies on the Formation of Mo Suboxides during Reduction of $MoO_3$. *J. Phys. Chem. B* **2000**, *104* (27), 6360–6370.

(99) Sanguesa, J. A.; Torres-Sanz, V.; Garrido, P.; Martinez, F. J.; Marquez-Barja, J. M. A Review on Electric Vehicles: Technologies and Challenges. *Smart Cities* **2021**, *4* (1), 372–404.

(100) Lokhande, V.; Lokhande, A.; Namkoong, G.; Kim, J. H.; Ji, T. Charge Storage in WO3 Polymorphs and Their Application as Supercapacitor Electrode Material. *Results Phys.* **2019**, *12*, 2012–2020.

(101) Elkholy, A. E.; Duignan, T. T.; Hussain, T.; Knibbe, R.; Zhao, X. S. Charge Storage Behaviour of α-$MoO_3$ in Aqueous Electrolytes – Effect of Charge Density of

Electrolyte Cations. *ChemElectroChem* **2022**, *9* (3), e202101449.

(102) Yao, Y.; Sang, D.; Zou, L.; Wang, Q.; Liu, C. A Review on the Properties and Applications of WO(3) Nanostructure-Based Optical and Electronic Devices. *Nanomater. (Basel, Switzerland)* **2021**, *11* (8), 2136.

(103) Freitas, A. P.; André, R. F.; Poucin, C.; Le, T. K.-C.; Imbao, J.; Lassalle-Kaiser, B.; Carenco, S. Guidelines for the Molybdenum Oxidation State and Geometry from X-Ray Absorption Spectroscopy at the Mo L2,3-Edges. *J. Phys. Chem. C* **2021**, *125* (32), 17761–17773.

(104) Forouzandeh, P.; Kumaravel, V.; Pillai, S. C. Electrode Materials for Supercapacitors: A Review of Recent Advances. *Catalysts* **2020**, *10* (9), 1–73.

(105) Arvizu, M. A.; Qu, H.-Y.; Cindemir, U.; Qiu, Z.; Rojas-González, E. A.; Primetzhofer, D.; Granqvist, C. G.; Österlund, L.; Niklasson, G. A. Electrochromic $WO_3$ Thin Films Attain Unprecedented Durability by Potentiostatic Pretreatment. *J. Mater. Chem. A* **2019**, *7* (6), 2908–2918.

(106) Hsu, C.-S.; Chan, C.-C.; Huang, H.-T.; Peng, C.-H.; Hsu, W.-C. Electrochromic Properties of Nanocrystalline $MoO_3$ Thin Films. *Thin Solid Films* **2008**, *516* (15), 4839–4844.

(107) Kim, K.-W.; Yun, T. Y.; You, S.-H.; Tang, X.; Lee, J.; Seo, Y.; Kim, Y.-T.; Kim, S. H.; Moon, H. C.; Kim, J. K. Extremely Fast Electrochromic Supercapacitors Based on Mesoporous $WO_3$ Prepared by an Evaporation-Induced Self-Assembly. *NPG Asia Mater.* **2020**, *12* (1), 84.

(108) Guo, Q.; Zhao, X.; Li, Z.; Wang, D.; Nie, G. A Novel Solid-State Electrochromic Supercapacitor with High Energy Storage Capacity and Cycle Stability Based on Poly(5-Formylindole)/$WO_3$ Honeycombed Porous Nanocomposites. *Chem. Eng. J.* **2020**, *384*, 123370.

(109) Bi, Z.; Li, X.; Chen, Y.; He, X.; Xu, X.; Gao, X. Large-Scale Multifunctional Electrochromic-Energy Storage Device Based on Tungsten Trioxide Monohydrate Nanosheets and Prussian White. *ACS Appl. Mater. Interfaces* **2017**, *9* (35), 29872–

29880.

(110) Susanti, D.; Diputra, A. A. G. P.; Tananta, L.; Purwaningsih, H.; Kusuma, G. E.; Wang, C.; Shih, S.; Huang, Y. $WO_3$ Nanomaterials Synthesized via a Sol-Gel Method and Calcination for use as a CO Gas Sensor. *Front. Chem. Sci. Eng.* **2014**, *8* (2), 179–187.

(111) Breedon, M.; Spizzirri, P.; Taylor, M.; du Plessis, J.; McCulloch, D.; Zhu, J.; Yu, L.; Hu, Z.; Rix, C.; Wlodarski, W.; Kalantar-zadeh, K. Synthesis of Nanostructured Tungsten Oxide Thin Films: A Simple, Controllable, Inexpensive, Aqueous Sol−Gel Method. *Cryst. Growth Des.* **2010**, *10* (1), 430–439.

(112) Susanti, D.; Wibawa, R. N. D.; Tananta, L.; Purwaningsih, H.; Fajarin, R.; Kusuma, G. E. The Effect of Calcination Temperature on the Capacitive Properties of $WO_3$-Based Electrochemical Capacitors Synthesized via a Sol-Gel Method. *Front. Mater. Sci.* **2013**, *7* (4), 370–378.

(113) Gupta, S. P.; Nishad, H. H.; Chakane, S. D.; Gosavi, S. W.; Late, D. J.; Walke, P. S. Phase Transformation in Tungsten Oxide Nanoplates as a Function of Post-Annealing Temperature and Its Electrochemical Influence on Energy Storage. *Nanoscale Adv.* **2020**, *2* (10), 4689–4701.

(114) Gupta, S. P.; More, M. A.; Late, D. J.; Walke, P. S. High-Rate Quasi-Solid-State Hybrid Supercapacitor of Hierarchical Flowers of Hydrated Tungsten Oxide Nanosheets. *Electrochim. Acta* **2021**, *366*.

(115) Gupta, S. P.; Nishad, H. H.; Patil, V. B.; Chakane, S. D.; More, M. A.; Late, D. J.; Walke, P. S. Morphology and Crystal Structure Dependent Pseudocapacitor Performance of Hydrated $WO_3$ Nanostructures . *Mater. Adv.* **2020**, *1* (7), 2492–2500.

(116) Shinde, P. A.; Lokhande, V. C.; Chodankar, N. R.; Ji, T.; Kim, J. H.; Lokhande, C. D. Enhanced Electrochemical Performance of Monoclinic $WO_3$ Thin Film with Redox Additive Aqueous Electrolyte. *J. Colloid Interface Sci.* **2016**, *483*, 261–267.

(117) Yoon, S.; Kang, E.; Kim, J. K.; Lee, C. W.; Lee, J.; Kon Kim, J.; Wee Lee, C.; Lee, J. Development of High-Performance Supercapacitor Electrodes Using Novel Ordered

Mesoporous Tungsten Oxide Materials with High Electrical Conductivity. *Chem. Commun.* **2011**, *47* (3), 1021–1023.

(118) Poongodi, S.; Kumar, P. S.; Mangalaraj, D.; Ponpandian, N.; Meena, P.; Masuda, Y.; Lee, C. Electrodeposition of $WO_3$ Nanostructured Thin Films for Electrochromic and $H_2S$ Gas Sensor Applications. *J. Alloys Compd.* **2017**, *719*, 71–81.

(119) Nandi, D. K.; Sarkar, S. K. Atomic Layer Deposition of Tungsten Oxide for Solar Cell Application. *Energy Procedia* **2014**, *54*, 782–788.

(120) Qiu, M.; Sun, P.; Shen, L.; Wang, K.; Song, S.; Yu, X.; Tan, S.; Zhao, C.; Mai, W. WO 3 Nanoflowers with Excellent Pseudo-Capacitive Performance and the Capacitance Contribution Analysis. *J. Mater. Chem. A* **2016**, *4* (19), 7266–7273.

(121) Hai, Z.; Karbalaei Akbari, M.; Wei, Z.; Xue, C.; Xu, H.; Hu, J.; Zhuiykov, S. Nano-Thickness Dependence of Supercapacitor Performance of the ALD-Fabricated Two-Dimensional $WO_3$. *Electrochim. Acta* **2017**, *246*, 625–633.

(122) Feng, S.; Xu, R. New Materials in Hydrothermal Synthesis. *Acc. Chem. Res.* **2001**, *34* (3), 239–247.

(123) Li, J.; Guo, C.; Li, L.; Gu, Y.; Kim, B.-H.; Huang, J. Synthesis of Vertical $WO_3$ Nanoarrays with Different Morphologies Using the Same Protocol for Enhanced Photocatalytic and Photoelectrocatalytic Performances. *RSC Adv.* **2021**, *11* (38), 23700–23706.

(124) Peng, H.; Ma, G.; Sun, K.; Mu, J.; Luo, M.; Lei, Z. High-Performance Aqueous Asymmetric Supercapacitor Based on Carbon Nanofibers Network and Tungsten Trioxide Nanorod Bundles Electrodes. *Electrochim. Acta* **2014**, *147*, 54–61.

(125) Gupta, S. P.; More, M. A.; Late, D. J.; Walke, P. S. Highly Ordered Nano-Tunnel Structure of Hydrated Tungsten Oxide Nanorods for Superior Flexible Quasi-Solid-State Hybrid Supercapacitor. *Appl. Surf. Sci.* **2021**, *545* (December 2020), 149044.

(126) Chen, J.; Wang, H.; Deng, J.; Xu, C.; Wang, Y. Low-Crystalline Tungsten Trioxide Anode with Superior Electrochemical Performance for Flexible Solid-State Asymmetry Supercapacitor. *J. Mater. Chem. A* **2018**, *6* (19), 8986–8991.

(127) Xu, J.; Ding, T.; Wang, J.; Zhang, J.; Wang, S.; Chen, C.; Fang, Y.; Wu, Z.; Huo, K.; Dai, J. Tungsten Oxide Nanofibers Self-Assembled Mesoscopic Microspheres as High-Performance Electrodes for Supercapacitor. *Electrochim. Acta* **2015**, *174*, 728–734.

(128) Chen, Z.; Peng, Y.; Liu, F.; Le, Z.; Zhu, J.; Shen, G.; Zhang, D.; Wen, M.; Xiao, S.; Liu, C. P.; Lu, Y.; Li, H. Hierarchical Nanostructured $WO_3$ with Biomimetic Proton Channels and Mixed Ionic-Electronic Conductivity for Electrochemical Energy Storage. *Nano Lett.* **2015**, *15* (10), 6802–6808.

(129) Jia, J.; Liu, X.; Mi, R.; Liu, N.; Xiong, Z.; Yuan, L.; Wang, C.; Sheng, G.; Cao, L.; Zhou, X.; Liu, X. Self-Assembled Pancake-like Hexagonal Tungsten Oxide with Ordered Mesopores for Supercapacitors. *J. Mater. Chem. A* **2018**, *6* (31), 15330–15339.

(130) Zhu, M.; Meng, W.; Huang, Y.; Huang, Y.; Zhi, C. Proton-Insertion-Enhanced Pseudocapacitance Based on the Assembly Structure of Tungsten Oxide. *ACS Appl. Mater. Interfaces* **2014**, *6* (21), 18901–18910.

(131) Gupta, S. P.; Nishad, H.; Magdum, V.; Walke, P. S. High-Performance Supercapacitor Electrode and Photocatalytic Dye Degradation of Mixed-Phase $WO_3$ Nanoplates. *Mater. Lett.* **2020**, *281*, 128639.

(132) Zhu, M.; Meng, W.; Huang, Y.; Huang, Y.; Zhi, C. Proton-Insertion-Enhanced Pseudocapacitance Based on the Assembly Structure of Tungsten Oxide. *ACS Appl. Mater. Interfaces* **2014**, *6* (21), 18901–18910.

(133) Liang, R.; Cao, H.; Qian, D. $MoO_3$ Nanowires as Electrochemical Pseudocapacitor Materials. *Chem. Commun.* **2011**, *47* (37), 10305–10307.

(134) Światowska-Mrowiecka, J.; de Diesbach, S.; Maurice, V.; Zanna, S.; Klein, L.; Briand, E.; Vickridge, I.; Marcus, P. Li-Ion Intercalation in Thermal Oxide Thin Films of $MoO_3$ as Studied by XPS, RBS, and NRA. *J. Phys. Chem. C* **2008**, *112* (29), 11050–11058.

(135) Xu, J.; Zhang, J.; Zhang, W.; Lee, C. S. Interlayer Nanoarchitectonics of Two-

Dimensional Transition-Metal Dichalcogenides Nanosheets for Energy Storage and Conversion Applications. *Adv. Energy Mater.* **2017**, *7* (23), 1–30.

(136) Yu, M.; Shao, H.; Wang, G.; Yang, F.; Liang, C.; Rozier, P.; Wang, C.-Z.; Lu, X.; Simon, P.; Feng, X. Interlayer Gap Widened α-Phase Molybdenum Trioxide as High-Rate Anodes for Dual-Ion-Intercalation Energy Storage Devices. *Nat. Commun.* **2020**, *11* (1), 1348.

(137) Chithambararaj, A.; Bose, A. C. Hydrothermal Synthesis of Hexagonal and Orthorhombic $MoO_3$ Nanoparticles. *J. Alloys Compd.* **2011**, *509* (31), 8105–8110.

(138) Chithambararaj, A.; Bose, A. C. Hydrothermal Synthesis of Molybdenum Oxide Microbelts. *AIP Conf. Proc.* **2012**, *1447* (1), 311–312.

(139) Lu, Q.-L.; Zhao, S.-X.; Chen, C.-K.; Wang, X.; Deng, Y.-F.; Nan, C.-W. A Novel Pseudocapacitance Mechanism of Elm Seed-like Mesoporous $MoO_{3-x}$ Nanosheets as Electrodes for Supercapacitors. *J. Mater. Chem. A* **2016**, *4* (38), 14560–14566.

(140) Wu, Q.-L.; Zhao, S.-X.; Yu, L.; Zheng, X.-X.; Wang, Y.-F.; Yu, L.-Q.; Nan, C.-W.; Cao, G. Oxygen Vacancy-Enriched $MoO_{3-x}$ Nanobelts for Asymmetric Supercapacitors with Excellent Room/Low Temperature Performance. *J. Mater. Chem. A* **2019**, *7* (21), 13205–13214.

(141) Duan, Y.; Wang, C.; Hao, J.; Jiao, Y.; Xu, Y.; Wang, J. Electrochromic Performance and Capacitor Performance of α-$Moo_3$ Nanorods Fabricated by a One-Step Procedure. *Coatings* **2021**, *11* (7).

(142) Shakir, I.; Shahid, M.; Rana, U. A.; Warsi, M. F. In Situ Hydrogenation of Molybdenum Oxide Nanowires for Enhanced Supercapacitors. *RSC Adv.* **2014**, *4* (17), 8741–8745.

(143) Dhara, A.; Hodes, G.; Sarkar, S. K. Two Stage Chemical Bath Deposition of $MoO_3$ Nanorod Films. *RSC Adv.* **2014**, *4* (96), 53694–53700.

(144) Pujari, R. B.; Lokhande, V. C; Kumbhar, V. S; Chodankar, N. R; Chandrakant, Lokhande, D. Hexagonal Microrods Architectured $MoO_3$ Thin Film for Supercapacitor Application. J. Mat. Sci: Mater Electron. **2016**, 27, 3312-3317.

(145) Kariper, A.; Meydaneri Tezel, F. Producing $MoO_3$ Thin Film Supercapacitor through Bio-Chemical Bath Deposition. *Ceram. Int.* **2019**, *45* (3), 3478–3482.

(146) Zhao, N.; Fan, H.; Zhang, M.; Ma, J.; Du, Z.; Yan, B.; Li, H.; Jiang, X. Simple Electrodeposition of $MoO_3$ Film on Carbon Cloth for High-Performance Aqueous Symmetric Supercapacitors. *Chem. Eng. J.* **2020**, *390* (December 2019), 124477.

(147) Elkholy, A. E.; Duignan, T. T.; Sun, X.; Zhao, X. S. Stable $\alpha$-$MoO_3$ Electrode with a Widened Electrochemical Potential Window for Aqueous Electrochemical Capacitors. *ACS Appl. Energy Mater.* **2021**, *4* (4), 3210–3220.

(148) Deokate, R. J.; Kate, R.; Shinde, N. M.; Mane, R. S. Energy Storage Potential of Sprayed $\alpha$-$MoO_3$ Thin Films. *New J. Chem.* **2021**, *45* (2), 582–589.

(149) Kiran Kumar Reddy, R.; Kailasa, S.; Geetha Rani, B.; Jayarambabu, N.; Yasuhiko, H.; Venkata Ramana, G.; Venkateswara Rao, K. Hydrothermal Approached 1-D Molybdenum Oxide Nanostructures for High-Performance Supercapacitor Application. *SN Appl. Sci.* **2019**, 1, 1365.

(150) Pal, S.; Kumar Chattopadhyay, K. Fabrication of Molybdenum Trioxide Nanobelts as High Performance Supercapacitor. *Mater. Today Proc.* **2018**, *5* (3), 9776–9782.

# CHAPTER II:

# EXPERIMENTATION

## 2.1 CHEMICALS USED

Sodium tungstate dihydrate ($Na_2WO_4.2H_2O$, 99%), Ammonium heptamolybdate ($(NH_4)_6Mo_7O_{24}.4H_2O$, 99%), Urea ($CH_4N_2O$, 99%), Citric acid monohydrate ($C_6H_8O_7.H_2O$, 99%) were purchased from Spectrochem Pvt. Ltd. Hydrochloric acid (HCl), and Sulphuric acid ($H_2SO_4$) were purchased from Fisher Scientific, India. N-Methylurea ($C_2H_6N_2O$, 97%), and Tetramethylurea ($C_5H_{12}N_2O$) were acquired from Sigma-Aldrich. Carbohydrazide ($CH_6N_4O$, 97%), Semicarbazide hydrochloride ($CH_5N_3O.HCl$, 99%), Toray Carbon paper (TGP-H-60), Acetylene black, Poly (vinylidene fluoride) $[-CH_2CF_2-]_n$ and Polyvinyl alcohol $[-CH_2CH(OH)-]_n$ were purchased from Alfa Aesar and N-Methyl-2-pyrrolidone ($C_5H_9NO$) was purchased from S D Fine chemicals limited. All the chemicals used in this study were of reagent grade and were used as received from commercial sources without further purification.

## 2.2 EXPERIMENTAL: SYNTHESES STRATEGIES & PROCEDURES

### 2.2.1 Synthesis of $WO_3$ nanoparticles

Sodium tungstate dihydrate (2.84 g) was added to 20 mL of deionized water with stirring for 10 minutes to form a clear solution. 30 mL of 2M HCl was added dropwise to this solution in order to form a colloidal gel of tungstic acid at a constant stirring speed of 1200 RPM. This gel was washed to remove $Na^+$ and $Cl^-$ ions by centrifugal filtration. The tungstic acid gel was digested on an oil bath at 90°C for 6 h. The obtained semi-solid precipitate was calcined in air using a preheated muffle furnace at a temperature of 550°C for 2 h.

### 2.2.2 Synthesis of 1D $WO_{3-x}$ nanorods

Tungsten acid gel free from $Na^+$ and $Cl^-$ was prepared using similar procedure mentioned in 2.2.1. Urea (14.27 g) was dissolved separately in 20 mL of deionized water. The urea solution was added dropwise to the tungstic acid gel under constant stirring at 1200 RPM, in order to form the colloidal tungstic acid-urea hybrid gel precursor. The pH of the hybrid gel was maintained at 2 using 2 M HCl. The hybrid gel was digested on an oil bath at 90°C for 3 h. The obtained semi-solid precipitate was calcined in air using a preheated muffle furnace at a temperature of 550°C for 2 h.

### 2.2.3 Synthesis of 2D $WO_{3-x}$ microsheets

In the process of synthesizing 2D $WO_{3-x}$ microsheets, the methodology described in section 2.2.2 was followed with all other experimental parameters being kept the same. However, the only variation made in the process was that the calcination temperature was changed to 650°C. This alteration in the calcination temperature was performed in order to study the effect of sintering on the properties of the resulting $WO_{3-x}$.

### 2.2.4 Synthesis of 3D $WO_{3-x}$ microstructures

The synthesis of the 3D $WO_{3-x}$ microstructures was performed by following the methodology described in section 2.2.2, with all other experimental parameters being kept constant. After the digestion stage, the obtained semi-solid precipitate was subjected to calcination in air, which was performed using a preheated muffle furnace. The calcination was carried out at a specific temperature of 450°C for a duration of 4 to 6 hours, which was necessary for the transformation of the semi-solid precipitate into 3D $WO_{3-x}$ microstructures.

### 2.2.5 Effect of synthesis pH and calcination temperature on the growth of 1D $WO_{3-x}$ nanorods

The synthesis involved keeping all other parameters constant, as detailed in section 2.2.2, while varying the pH of the hybrid gel using either 2 M HCl or 2 M $NH_4OH$ in the range of 1 to 10. The calcination temperature was also varied between 150°C to 650°C. The resulting materials were then analyzed to determine the effects of these variations on their morphological characteristics.

### 2.2.6 Effect of metal to SDA ratio on the $WO_{3-x}$ morphologies

The synthesis was performed by keeping all other experimental parameters similar to the methodology described in section 2.2.2 and only varying the metal : urea ratio from 1:1 to 1:10.

### 2.2.7 Effect of substituted ureas on the morphology of $WO_{3-x}$

The process of synthesis of $WO_3$ was carried out using a methodology described in section 2.2.2, while making sure to maintain all other experimental parameters constant. However, the only modification made was the substitution of urea with one of the following substituted ureas: N-methylurea, tetramethylurea, carbohydrazide or semicarbazide. This alteration in the synthesis process was performed in order to investigate the effect of these different substituted ureas on the morphology of $WO_{3-x}$.

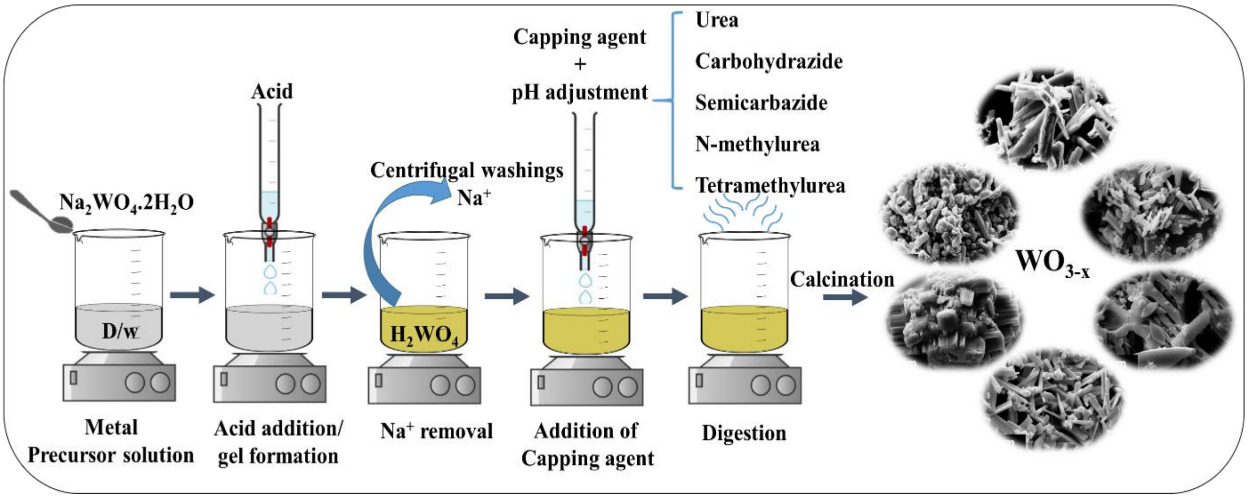

**Figure 2.1:** General synthesis scheme for preparing nanostructured $WO_{3-x}$.

### 2.2.8 Synthesis of 3D $WO_{3-x}$/C microfibers using citric acid

Tungsten acid gel free from $Na^+$ and $Cl^-$ was prepared using similar procedure mentioned in 2.2.1. Citric acid monohydrate (9.52 g) was dissolved separately in 20 mL of deionized water. The citric acid solution was added dropwise to the tungstic acid gel under constant stirring at 1200 RPM, in order to form the colloidal tungstic acid-citric acid hybrid gel precursor. The pH of the hybrid gel was maintained at 2 using 2 M HCl. The hybrid gel was refluxed on an oil bath at 100°C for 6 h. The obtained semi solid precipitate was calcined in air using a preheated muffle furnace at a temperature of 450°C for 2 h.

### 2.2.9 pH dependent synthesis of 3D $WO_{3-x}$/C microfibers

The synthesis was performed by keeping all other experimental parameters similar to the methodology described in section 2.2.8 and only varying the pH. The pH was varied in range of 1-10 using either 2 M HCl or 2 M $NH_4OH$. After digestion the obtained semi solid precipitate was calcined in air using a preheated muffle furnace at a temperature of 450°C for 2 h.

### 2.2.10 Temperature dependent synthesis of 3D $WO_{3-x}$/C microfibers

The synthesis was performed by keeping all other experimental parameters similar to the methodology described in section 2.2.8 and only varying the calcination temperature from 150 to 550°C.

### 2.2.11 Effect of metal to SDA ratio on the growth of 3D $WO_{3-x}$/C microfibers

The synthesis was performed by keeping all other experimental parameters similar to the methodology described in section 2.2.8 and only varying the metal : citric acid ratio from 1:1 to 1:10.

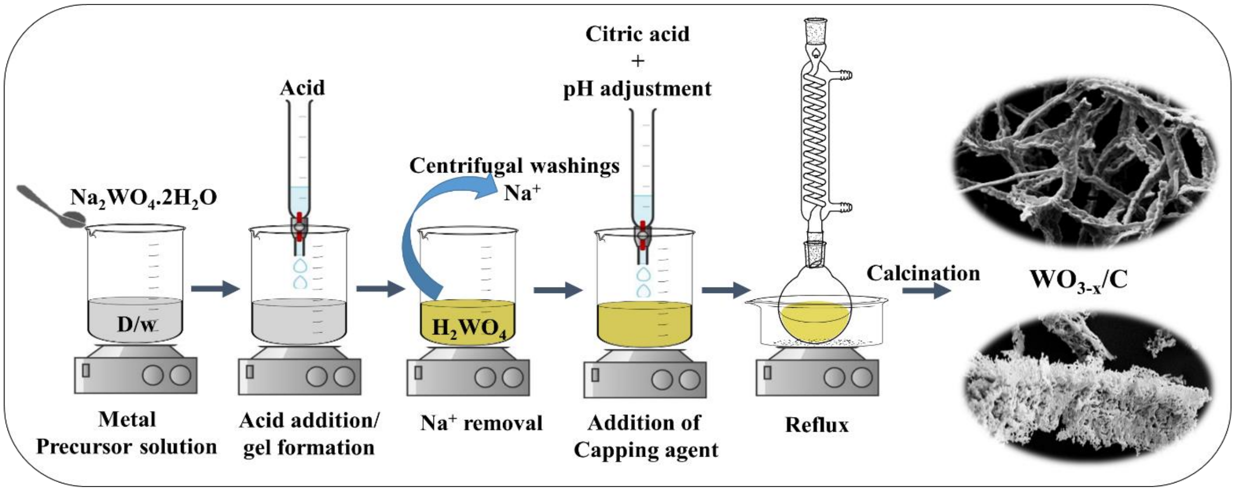

**Figure 2.2:** General synthesis scheme for preparing $WO_{3-x}$/C microfibers and hierarchical structures.

### 2.2.12 Synthesis of $MoO_{3-x}$ nanoparticles

Ammonium heptamolybdate (1.22 g) was dissolved in 10 mL of deionized water with stirring for 15 minutes. Then, 15 mL of 2 M hydrochloric acid was added dropwise to the above solution while stirring constantly at a speed of 1200 RPM. The pH of the solution was adjusted to 2 using 2 M HCl. The resulting mixture was digested on an oil bath at a temperature of 90°C for 8 hours. After the digestion process, a semi-solid precipitate was obtained, which was subsequently calcined in air using a preheated muffle furnace at a temperature of 550°C for 2 hours.

### 2.2.13 Synthesis of 2D $MoO_{3-x}$ microplates

Ammonium heptamolybdate (1.22 g) was dissolved in 10 mL of deionized water with stirring for 15 minutes. 15 mL of 2 M HCl was added dropwise to the above solution at a constant stirring speed of 1200 RPM. 7.99 g of urea was dissolved separately in 20 mL of deionized water. The urea solution was added dropwise to the ammonium heptamolybdate solution. The pH of the mixture was maintained at 3 using 2 M HCl throughout the synthesis and the solution mixture was digested on an oil bath at 90°C for 8 h. The obtained semi-solid precipitate was calcined in air at temperatures ranging from 150 to 650°C for 2 hours using a preheated muffle furnace.

### 2.2.14 Synthesis of 2D $MoO_{3-x}$ microdisks

The synthesis was performed by keeping all other experimental parameters similar to the methodology described in section 2.2.13 and only changing the synthesis pH to 5.

### 2.2.15 Influence of synthesis pH on $MoO_{3-x}$ morphologies

The synthesis was performed by keeping all other experimental parameters similar to the methodology described in section 2.2.13 and only varying the synthesis pH from 1 to 10 using either 2 M HCl or 2 M $NH_4OH$.

### 2.2.16 Influence of calcination temperature on $MoO_{3-x}$ morphologies

The synthesis was performed by keeping all other experimental parameters similar to the methodology described in section 2.2.13 and only varying the calcination temperature from 150 to 650°C.

### 2.2.17 Effect of metal to SDA ratio on $MoO_{3-x}$ morphologies

The synthesis was performed by keeping all other experimental parameters similar to the methodology described in section 2.2.13 and only varying the metal : urea ratio from 1:1 to 1:10.

### 2.2.18 Effect of using substituted ureas as structure directing agents on the morphology of $MoO_{3-x}$

The synthesis was performed by keeping all other experimental parameters similar to the methodology described in section 2.2.13 and replacing urea with substituted ureas (N-methylurea, tetramethylurea, carbohydrazide or semicarbazide).

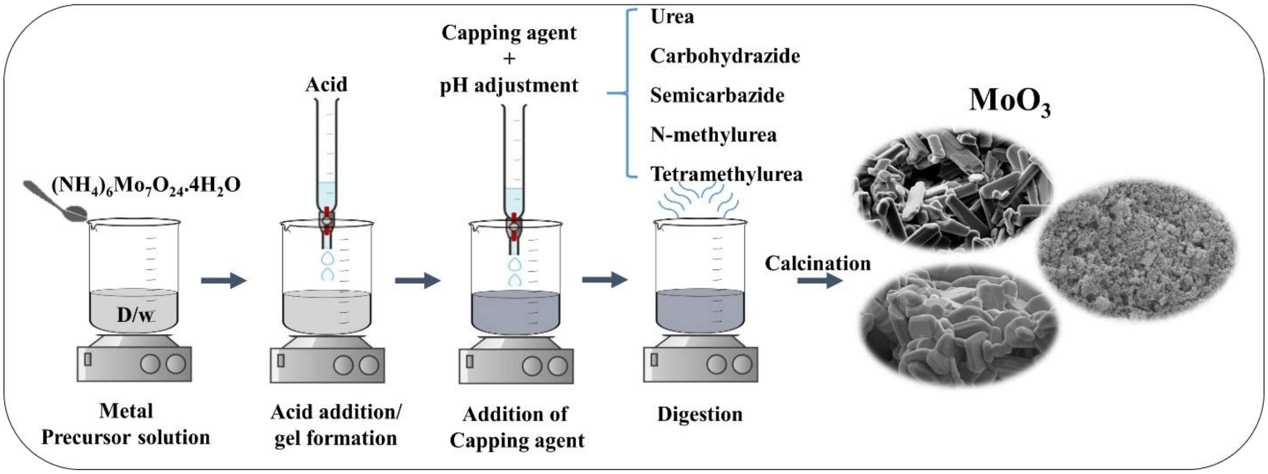

**Figure 2.3:** General synthesis scheme for preparing $MoO_{3-x}$ microstructures.

### 2.2.19 Synthesis of 3D $MoO_{3-x}$ microflowers using citric acid

Ammonium heptamolybdate (1.22 g) was dissolved in 10 mL of deionized water with stirring for 15 minutes. 15 mL of 2 M HCl was added dropwise to the above solution at a constant stirring speed of 1200 RPM. Furthermore, citric acid monohydrate (7.99 g) was dissolved separately in 20 mL of deionised water. The citric acid solution was dropwise added to the ammonium heptamolybdate solution under vigorous stirring at 1200 RPM. The pH of the mixture was maintained at 2 throughout the synthesis using 2M HCl and the solution mixture was refluxed on an oil bath at 100°C for 8 h. The obtained semi-solid precipitate was calcined in air at 550°C for 2 hours using a preheated muffle furnace.

### 2.2.20 pH dependent synthesis of 3D $MoO_{3-x}$ microflowers

The synthesis was performed by keeping all other experimental parameters similar to the methodology described in section 2.2.19 and only varying the synthesis pH from 1 to 10 using either 2 M HCl or 2 M $NH_4OH$.

### 2.2.21 Temperature dependent synthesis of 3D $MoO_{3-x}$ microflowers

The synthesis was performed by keeping all other experimental parameters similar to the methodology described in section 2.2.19 and only varying the calcination temperature from 150 to 650°C.

### 2.2.22 Effect of Mo to SDA ratio on the morphology of 3D $MoO_{3-x}$ microflowers

The synthesis was performed by keeping all other experimental parameters similar to the methodology described in section 2.2.19 and only varying the metal : citric acid ratio from 1:1 to 1:10.

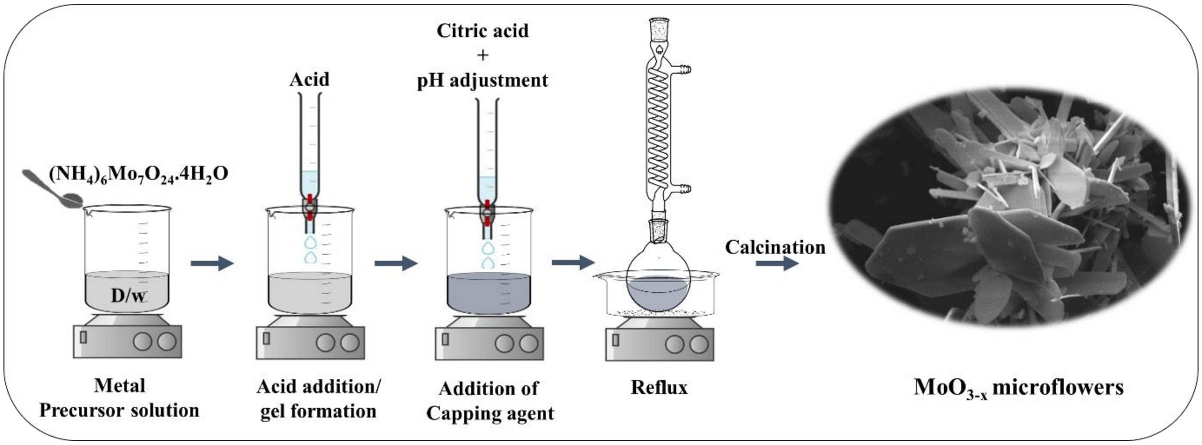

**Figure 2.4:** General synthesis scheme for preparing $MoO_{3-x}$ microflowers**.**

## 2.3 INSTRUMENTATION

The principles of different instrumental techniques used in this thesis have been presented in brief in this section.

### 2.3.1 Characterization techniques

In order to fully understand the properties and potential applications of the synthesized nano and microstructured catalysts, a range of characterization techniques were utilized to analyze the physical and chemical properties of the materials. These techniques included Thermogravimetric-Differential Thermal Analysis (TG-DTA), Infrared Spectroscopy (IR), Powder X-ray Diffraction (XRD), Scanning Electron Microscopy (SEM), Energy-Dispersive X-ray Spectroscopy (EDS), High Resolution-Transmission Electron Microscopy (HR-TEM),

$N_2$-adsorption-desorption isotherm studies (BET), CHNS analysis, Raman spectroscopy, Electron Paramagnetic Resonance spectroscopy (EPR), and X-ray Photoelectron Spectroscopy (XPS). In order to provide a comprehensive overview of the methods and techniques utilized in this study, the principles and associated equations of each technique have been summarized and presented below.

#### 2.3.1.1 Thermogravimetric Differential Thermal Analysis (TG-DTA)

TG/DTA analysis is a method of thermal analysis in which the mass and the temperature changes associated with the sample are measured over time as the temperature is increased with a fixed heating rate and under a controlled gaseous environment.[1] A TG/DTA analyzer is capable of characterizing multiple thermal properties simultaneously of a sample. In the TG component, temperatures at which substances decompose, reduce, or oxidize are measured. The TG technique can accurately measure the weight losses associated to decomposition, oxidation, or any other physical or chemical changes in the material. While the differential thermal analysis also referred to as "DTA" identifies whether or not the decomposition process is endothermic or exothermic.

In DTA, the difference between the sample temperature (Ts) and the reference temperature (Tr), usually alpha alumina is measured.[2] Thermal events are mapped by a plot of Ts – Tr over a programmed temperature range that shows peaks or step changes. Furthermore, the DTA can measure temperatures related to phase changes where no mass loss is involved, such as melting, crystallization, or glass transitions. In the present study a hyphenated TG-DTA instrument was used for performing the thermal analysis. The instrument used was a thermogravimetric analyzer (NETZSCH STA 409PC-LUXX) operated in an air atmosphere at a fixed heating rate of 5 °C $min^{-1}$.

#### 2.3.1.2 Infrared Spectroscopy (IR)

Infrared spectroscopy measures a sample's vibrational spectrum by passing IR radiation through it and measuring the wavelengths absorbed.[3] Chemical compounds such as metal precursors, oxides and also other chemical compounds can be studied and identified for their functional groups using this technique. When a beam of infrared light is passed through a sample to record its infrared spectrum, absorption occurs when the IR frequency matches the vibrational frequency of a chemical bond which is associated with a change in dipole moment of a molecule. Only those molecules that undergo a change in dipole moment when interacting with IR radiations are termed as IR active.

At each frequency (or wavelength), the transmitted light shows how much energy has been absorbed. The collected data is processed using fourier transformation, and then a transmittance or absorbance spectrum is generated.[5] Infrared spectrums are represented as graphs charting infrared radiation absorbance (or transmittance) on the y-axis versus wavelength, frequency, or wavenumber on the x-axis.[4] In the present study SHIMADZU FTIR Prestige-21 spectrophotometer was used for the analysis. For all the IR analysis the samples were first finely ground with KBr and then mounted on the sample holder for the analysis. The IR spectra were recorded in the vibrational frequency regime of 4000-400 $cm^{-1}$.

### 2.3.1.3 Powder X-ray Diffraction (XRD)

X-ray diffraction (XRD) is a very useful analytical technique that is primarily used to identify phases of crystalline materials and can also provide information about phase purity, average crystallite size, crystal structure, etc.[6] In XRD, a material is irradiated with incident X-rays, and then the X-rays that leave it are measured for intensity and scattering angle. It is based on the constructive interference of monochromatic X-rays with crystalline samples. By using a cathode ray tube, monochromatic X-rays are generated, filtered, collimated, and directed at the sample. A sample interacting with incident rays produces constructive interference when Bragg's Law is satisfied:

$$n\lambda = 2dsin\theta \qquad (2.1)$$

In the above equation $n$ is an integer, $\lambda$ is the wavelength of X-rays, $d$ is the inter planner spacing and $\theta$ is the diffraction angle. According to this law, electromagnetic radiation wavelength is related to the diffraction angle and the lattice spacing in an crystalline samples.[7] By scanning the sample through a range of 2θ angles, diffracted X-rays are detected, processed, and counted. In the present study the phase and structure of the samples were investigated using a RIGAKU ULTIMA IV X-Ray diffractometer using Cu Kα as target source having $\lambda$=1.5418 nm and using a Ni filter. The samples were recorded from the angles 20 to 80° with the scanning step speed of 0.02.

### 2.3.1.4 Scanning Electron Microscopy (SEM) & Energy Dispersive X-ray spectroscopy (EDS)

The scanning electron microscope (SEM) is a popular tool for studying or analyzing surface morphology of the samples.[8] A SEM produces high resolution images of a sample by detecting high energy electrons emitted from a sample surface after an electron gun shoots a highly focused beam of electrons at it. A SEM objective lens focuses the electron beam onto a small spot on the sample surface. In order to achieve the best quality images, variables such as accelerating voltage, aperture size, and working distance between sample and electron gun can be optimized. Different types of electron detection enable different types of imaging and analysis, each providing valuable information. A contrast can be generated based on the backscattered electrons. Whereas, secondary electron emission can provide information about the surface topography of the sample.[9]

Energy-dispersive X-ray spectroscopy (EDS) is an analytical technique that is widely used to characterize and quantify materials in terms of their chemical and elemental composition.[10] The technique involves the use of an electron beam with an energy of 10-20 keV that strikes the surface of a conducting sample, which then emits X-rays whose energy depends on the composition of the sample. Electrons are focused into the specimen in order to stimulate the emission of characteristic X-rays. In an atom at rest, electrons are bound to the nucleus at discrete energy levels. When an electron in an inner shell is excited by the incident beam, it may be ejected from the shell, creating an electron hole. When an electron from an outer shell fills the hole, the difference in energy between the shell with higher energy and the one with lower energy is released as an X-ray.

An energy-dispersive spectrometer is used to measure the number and energy of the emitted X-rays from the specimen. Since the energy of X-rays is determined by the difference in energy between the two shells and by the atomic structure of the emitting element, EDS can be used to determine the elemental composition of the sample. In the present work, the morphologies of the nano and microstructured catalysts were observed using scanning electron microscopy (SEM) with the Carl-Zeiss JSM-5800LV instrument, which was coupled with the Ametek edx PV6500 EDS system to enable the determination of the elemental composition of the catalysts.

### 2.3.1.5 High Resolution Transmission Electron Microscopy (HRTEM) and Selected Area Electron Diffraction (SAED) analysis

In transmission electron microscopy electrons are transmitted through a specimen and as the beam passes through the sample, electrons interact with the sample to form an image. After amplification, the electron transmission pattern is focused onto an imaging device, such as a fluorescent screen, photographic film, or a charge-coupled device with a scintillator attached. It is possible to see morphology, size distribution, crystal structure, strain, defects in materials down to the atomic level through TEM. Electron-sample interaction is the source of all information derived from TEM. The TEM sample must be thin enough to allow electrons to transmit through it (usually less than 200 nm, depending on the sample composition and TEM characterization information expected).[11] There are two basic modes of operation for TEM imaging systems, namely diffraction mode and imaging mode. The SAED method is produced through the diffraction mode of TEM and it creates diffraction patterns by virtually selecting an area aperture from the sample to insert into the image plane. It is possible to identify crystal structures, nanostructure growth direction, and crystallinity by using SAED.[12] In the present study the TEM analysis were performed using a transmission electron microscope (TEM -Tecnai 200 kV). A Lacey carbon 400 mesh Cu TEM grid was coated with all samples after they were sonicated in acetone for 15 minutes and subsequently dried under an IR lamp.

### 2.3.1.6 X-ray Photoelectron Spectroscopy (XPS)

X-ray Photoelectron Spectroscopy is based on the photoelectric effect. XPS is a surface-sensitive quantitative spectroscopic technique.[13] It identifies the elements present in a material (elemental composition) as well as their chemical state and can also provide information on their overall electronic structure and density of electronic states. It is a form of photoemission spectroscopy in which X-rays are used to obtain electron population spectra of materials. In this technique electrons emitted from the top 1-10 nm of a solid surface are measured by irradiating it with X-rays and measuring their kinetic energy. Electrons ejected from a target are counted over a range of kinetic energies to generate a photoelectron spectrum. It is possible to identify and quantify all surface elements (except hydrogen) by measuring the energies and intensities of the photoelectron peaks.[14] In the present thesis a

Kratos Axis Supra DLD XPS spectrometer having an Al Kα X-ray source (hν = 1486.6 eV) operated at 150 W was used to evaluate the oxidation states of elements in the samples. A multi-channel plate and delay line detector at a vacuum of ≈ $10^{-9}$ mbar was used for sample analysis. The instrument was calibrated at 284.8 eV using adventitious carbon C1s.

### 2.3.1.7 BET Surface area analysis

In Brunauer-Emmett-Teller (BET) surface area analysis, an inert gas, such as nitrogen, is continuously flowed over a solid sample, or the solid sample is suspended in a defined gaseous volume at extremely low temperatures, to measure analyte surface area ($m^2/g$). The adsorbed gas forms a monolayer on the solid substrate and its porous structures due to weak van der Waals forces. A $N_2$ adsorption - desorption isotherm was constructed by measuring the adsorbed volume at different adsorption pressures. In addition to calculating the specific surface area of a solid sample, one can also determine the porous geometry of the solid based on the monomolecular layer and the rate of adsorption.[15,16] In the present work the $N_2$ sorption studies were performed using a QUANTACHROME AUTOSORB iQ-MP-C instrument at liquid nitrogen temperature. The samples were degassed at 200 °C for 2h prior to the surface area measurements.

### 2.3.1.8 Raman Spectroscopy

Raman spectroscopy is a class of vibrational spectroscopy and it provides information about molecular interaction and material properties such as crystallinity, phase, and polymorphism.[17] The technique involves the scattering of incident light or photons from a high intensity laser light source and its subsequent measurement. As most of the scattered photons are at the same wavelength as the laser source, it does not provide useful information. This phenomenon is known as Rayleigh scattering. However, approximately one in ten million of these photons will scatter at a different frequency than the incident photon. This effect is also known as Raman scattering or inelastic scattering, which is unique for different chemical systems and it forms the basis of chemical characterization of materials through Raman spectroscopy.[18] In the present thesis a Raman spectrometer (Witech Alpha 300 RAS) consisting of a 532 nm laser source along with a dual-purpose 50× objective lens was used to analyze the nature of samples.

### 2.3.1.9 Electron Paramagnetic Resonance Spectroscopy

Electron paramagnetic resonance (EPR) is a spectroscopic technique for determining the structure and dynamics of systems containing unpaired electrons (paramagnetic systems).[19] A magnetic field is applied to the sample during the EPR experiment, which removes the degeneracy of the paramagnetic center's spin states. Microwave irradiation can then induce transitions between the different spin states. EPR spectra are obtained by registering the absorption of microwaves by the sample. As a result, this spectrum is particularly useful for characterization of paramagnetic centers due to its high sensitivity to their physical and chemical environments.[20] In the present thesis the EPR measurements were carried out using a JEOL Model JES FA200 instrument operated at room temperature (300 K).

### 2.3.2 Electrochemical charge storage measurements

The supercapacitor (SC), or ultracapacitor (UC), is a high-capacity capacitor, also known as a high performance capacitor, that bridges the gap between electrolytic capacitors and rechargeable batteries.[21] As shown in Figure 2.5, a supercapacitor (SC) consists of two electrodes separated by a separator and is immersed in an electrolyte. Supercapacitors store charges using electrode materials, so the choice of electrode materials directly affects their performance. In order to understand how different electrode materials work, it is necessary to investigate their working mechanisms. As discussed in section 1.3 it is possible to categorize SCs into two types, that is, electric double-layer capacitors (EDLCs) and pseudocapacitors.[22]

Typically, charge storage electrochemical measurements are performed in a classical three-electrode configuration which provide the inputs for a two-electrode device scale applications. Active materials can then be investigated using a three-electrode system, which includes the active materials as the working electrode, $Ag/AgCl_{(sat\ KCl)}$ as a reference electrode, and a Pt wire as a counter electrode. To investigate the electrochemical charge storage performance of asymmetric supercapacitors, a two-electrode system comprising an active material on one electrode and active carbon on the other is employed. The techniques used to evaluate the SC performance in both these configurations include cyclic voltammetry (CV), galvanostatic charge-discharge (GCD), and electrochemical impedance spectroscopy (EIS). As a result of the above measurement techniques, three basic parameters can be measured: voltage, current, and time. Additional performance indicators can be further derived from this measurements which include the operating voltage, electroactive area, diffusion coefficients, specific capacitance, equivalent series resistance, cycling stability as well as energy and power densities.

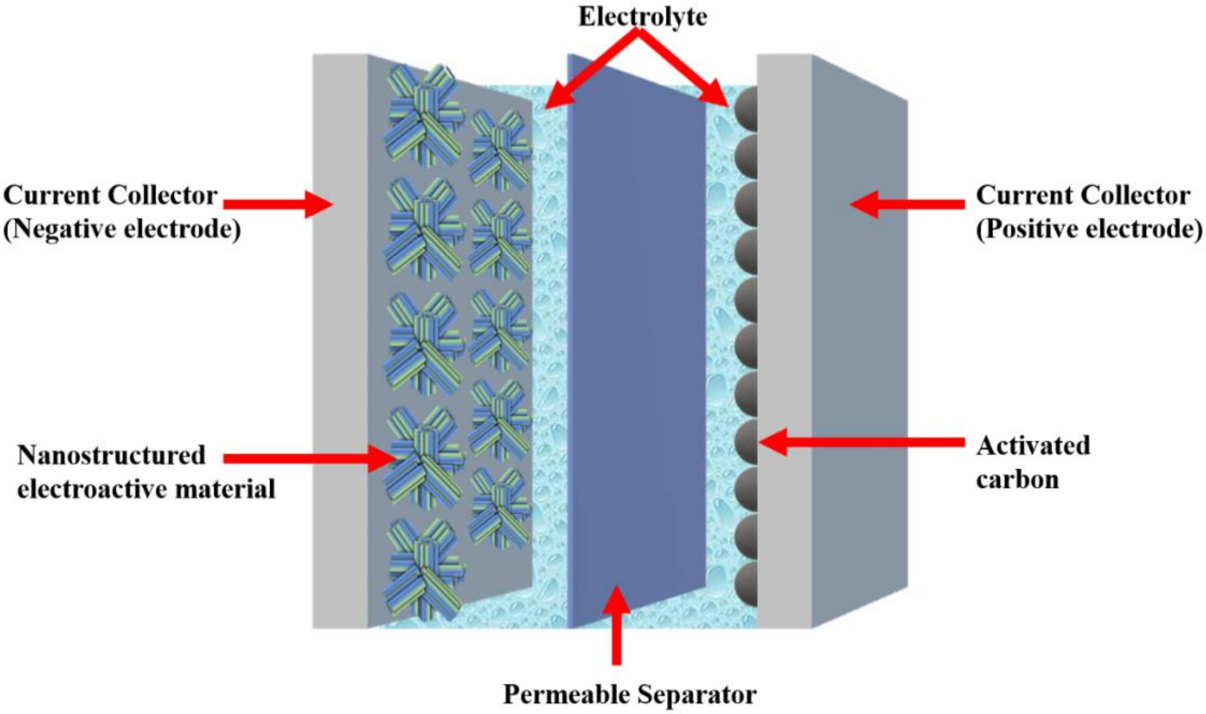

**Figure 2.5:** Schematic of a two-electrode supercapacitor device.

### 2.3.2.1 Electrode preparation

Prior to device scale measurements, a standard three electrode system was used to evaluate the electrochemical performance using a CHI 660 E series potentiostat. A uniform film slurry was prepared of the nanostructured metal oxide by making use of acetylene black as a conducting agent and Polyvinylidene fluoride as a binder. The three components were mixed thoroughly by grinding in the weight ratio of 70:20:10, i.e. (14:4:2 mg). From the finely ground mixture, 10 mg was taken and dispersed in N-methyl pyrrolidone (NMP) solvent and sonicated for 1 hour to obtain a uniform homogenous slurry. 0.05 mL (mass loading of 0.7 mg) of this slurry was uniformly dropped on a Toray carbon paper TGP-H-60 with a dimension of 1 × 1 $cm^2$ followed by drying the electrode in an oven at 100 ℃ for 6h. The electrodes electrochemical performance was then studied in a three-electrode cell configuration. The prepared electrode was used as a working electrode, Ag/AgCl$_{(sat\ KCl)}$ and platinum electrodes were used as reference and counter electrodes respectively. 1 M $H_2SO_4$ was used as an electrolyte for all the measurements and all the tests were performed at room temperature.

To understand the device performance of the different nanostructured metal oxides, an asymmetric supercapacitor device was assembled. The current collectors comprised of Toray carbon paper TGP-H-60 with a dimension of 1 × 1 $cm^2$. The cathode was prepared using the same procedure as above. For preparing the anode, the active material was replaced with active carbon (AC). The electrolyte was prepared by adding 1 g of polyvinyl alcohol in 8 mL of distilled water, followed by 2 mL of 1 M $H_2SO_4$ and stirred at 85 ℃ until a clear gel was obtained. This gel was saturated onto a Whatman glass microfiber separator and was coated in-between the two current collectors and dried till the device solidified.[23,24]

#### 2.3.2.2 Optimizing the electrode mass loading percentages

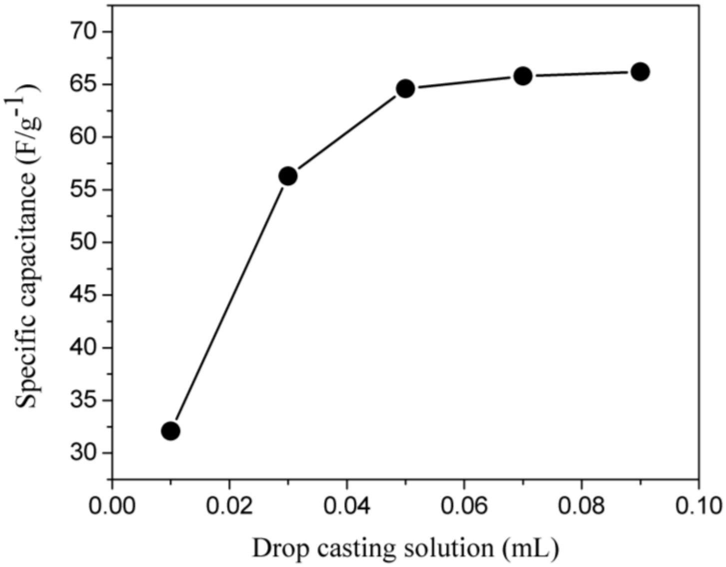

**Figure 2.6:** Electrode drop casting solution optimization.

To optimize the electrode preparation process, the mass loading percentages of a drop casting solution consisting of WO3 nanoparticles were varied by loading different amounts of drop casting solutions. The drop casting volumes of 0.01, 0.03, 0.05, 0.07, and 0.09 mL corresponded to mass loadings of 0.14, 0.42, 0.7, 0.98, and 1.26 mg, respectively. A gradual increase in specific capacitance was observed with increasing mass loading up to 0.7 mg. Beyond this point, the specific capacitance remained almost constant. This phenomenon could be attributed to the increasing thickness of the electrode layer, which hindered the intercalation process at higher mass loading percentages. Therefore, it was concluded that a mass loading of 0.7 mg was ideal for making electrodes.

#### 2.3.2.3 Cyclic Voltammetry (CV)

Cyclic voltammetry (CV) is a potentiodynamic electrochemical measurement technique.[25] In this technique, a linearly cycled potential sweep between two or more set values is used to measure the current response of a redox active solution. It is a valuable technique which can be used for determining the kinetics of electronic-transfer reactions, as well as the thermodynamics of redox processes. A working electrode, a reference electrode, and a counter electrode are used in cyclic voltammetry, as in other types of voltammetry.[26] A cyclic voltammetry experiment is performed by using an electrochemical cell with three electrodes and the electrolyte solution. Using a potentiostat, the potential between the working electrode and reference electrode is linearly swept until it reaches a pre-set limit, at which point it is reversed. It repeats this process multiple times during a scan, and the device measures real-time the changing current between the counter electrode and the working electrode. This yields a characteristic duck-shaped current vs potential plot called a cyclic voltammogram.

#### 2.3.2.4 Galvanostatic charge-discharge analysis (GCD)

The Galvanostatic charge-discharge (GCD) analysis is one of the most important methods for studying electrode material electrochemical performance.[27] Galvanostatic measurements are used for electrochemical analysis or for determining kinetics and mechanisms of electrode reactions using a current control. In GCD analysis the working electrodes are successively charged and discharged at constant current density without or with dwelling periods (in which the peak voltage remains constant between charging and discharging).[28] Charge and discharge times and potential windows can be determined from the GCD curves. Subsequently, the charge-discharge curves can be used to calculate the specific capacitance

($C_{sp}$) of electroactive materials, and the charge-discharge performance analysis at different current densities can be used to measure the rate performance of electrodes. In addition, the charge and discharge tests performed in this thesis were used to determine the cycling stability of electrode materials.

### 2.3.2.5 Electrochemical Impedance Spectroscopy (EIS)

An electrochemical impedance spectrometer (EIS) measures a system's resistance in frequency domain by applying a sinusoidal voltage perturbation.[29] It is possible to analyze the electrode reaction kinetics and the charge transfer between electrode materials at the electrode/electrolyte interface with EIS. A single perturbation amplitude is used to sweep through a wide range of frequencies in EIS in order to obtain a graph called as the Nyquist plot. Typically, Nyquist plots reveal a depressed semicircle at high-to-medium frequencies due to charge transfer and a straight line at low frequencies caused by ion diffusion. By simulating an equivalent circuit, it is possible to estimate the internal resistance of the solution, the charge transfer resistance, the double layer capacitance of the electrode, and the diffusion mass transfer process.[30] In the present thesis the EIS measurements were performed at an open circuit potential, an amplitude of 5 mV, and a frequency range of 1 mHz - 1 MHz.

## 2.4 FORMULAS USED FOR CALCULATING ELECTROCHEMICAL METRICES

### 2.4.1 Specific capacitance calculations

In the formulas for specific capacitance, $C_{sp}$ represents the specific capacitance (F $g^{-1}$), $I$ represents the response current (A), $v$ represents the scan rate (V $s^{-1}$), $m$ represents the average mass of the electro-active material (g), $\Delta t$ represents the discharge time (s), $\Delta V$ represents the voltage window (V).

### 2.4.1.1 Three electrode CV measurements

$$C_{sp} = \frac{\int I \, dV}{2 \times v \times m \times \Delta V} \qquad (2.2)$$

### 2.4.1.2 Three electrode GCD measurements

$$C_{sp} = \frac{\int I \times \Delta t}{m \times \Delta V} \qquad (2.3)$$

### 2.4.1.3 Two electrode CV measurements

$$C_{sp} = \frac{\int I \, dV}{v \times m \times \Delta V} \qquad (2.4)$$

### 2.4.1.4 Two electrode GCD measurements

$$C_{sp} = \frac{\int 2I \times \Delta t}{m \times \Delta V} \qquad (2.5)$$

### 2.4.2 Energy and power densities from two electrode GCD studies

*C* represents the specific capacitance (F $g^{-1}$), *ΔV* represents the voltage window (V), *Δt* represents the discharge time (s), *E* represents the energy density (W h $kg^{-1}$) and *P* represents the power density (W $kg^{-1}$).

$$\boldsymbol{E} = \frac{1}{2} C (\Delta V)^2 \qquad (2.6)$$

$$P = \frac{E}{\Delta t} \qquad (2.7)$$

### 2.4.3 Electroactive area

The electroactive areas of the materials were estimated by the Cottrell equation using a ferrocyanide reversible redox system.[31]

$$(i)_t = \frac{nFAD_0^{1/2} C^*}{\Pi^{1/2} t^{1/2}} \qquad (2.8)$$

where $(i)_t$ is the peak current (in A), *n* denotes the number of electrons, *F* = 96,485 C $mol^{-1}$ is the Faraday constant, *A* represents the electroactive surface area of the electrode ($cm^2$), $C^*$ represents bulk concentration of the analyte (mol $cm^{-3}$) and *t* denotes the time (s).

### 2.4.4 Diffusion coefficient

From CV measurements at different scan rates, the values of anodic peak current ($I_p$) were obtained. From the slope of square root of scan rate ($v^{1/2}$) versus the anodic peak current ($I_p$) graph, the diffusion coefficient of $H^+$ ions is calculated using the Randles-Sevcik equation at 298 K.[32]

$$I_p = 2.69 \times 10^5 A C_0 D_0^{1/2} n^{3/2} v^{1/2} \qquad (2.9)$$

In the above equation 2.69 × $10^5$ is a constant, *A* is the area of electrode, $C_0$ is the electrolyte concentration and *n* is the amount of electrons transferred during the reaction.

Based on the innovative synthesis strategies as discussed in this chapter, this thesis presents a plethora of nano and microstructured $WO_{3-x}$ and $MoO_{3-x}$ alongwith their detailed characterization. These materials have also been evaluated for their charge storage performance, and the detailed results have been discussed in the next chapters III and IV.

## 2.5 REFERENCES

(1) Ashby, E. C.; Claudy, P.; Bousquet, J.; Etienne, J. High Vacuum DTA-TGA Instrumentation for Air-Sensitive Compounds. *J. Chem. Educ.* **1975**, *52* (9), 618.

(2) Campbell, P. F.; Ortner, M. H.; Anderson, C. J. Differential Thermal Analysis and Thermogravimetric Analysis of Fission Product Oxides and Nitrates to 1500° C. *Anal. Chem.* **1961**, *33* (1), 58–61.

(3) Pimentel, G. C. Infrared Spectroscopy: A Chemist's Tool. *J. Chem. Educ.* **1960**, *37* (12), 651.

(4) Barnes, R. B.; Gore, R. C. Infrared Spectroscopy. *Anal. Chem.* **1949**, *21* (1), 7–12.

(5) Perkins, W. D. Fourier Transform-Infrared Spectroscopy: Part l. Instrumentation. *J. Chem. Educ.* **1986**, *63* (1), 5.

(6) Leonardi, A.; Bish, D. L. Understanding Powder X-Ray Diffraction Profiles from Layered Minerals: The Case of Kaolinite Nanocrystals. *Inorg. Chem.* **2020**, *59* (8), 5357–5367.

(7) Holder, C. F.; Schaak, R. E. Tutorial on Powder X-Ray Diffraction for Characterizing Nanoscale Materials. *ACS Nano* **2019**, *13* (7), 7359–7365.

(8) Reimschuessel, A. C. Scanning Electron Microscopy - Part I. *J. Chem. Educ.* **1972**, *49* (8), A413.

(9) Srinivasan, C.; Mullen, T. J.; Hohman, J. N.; Anderson, M. E.; Dameron, A. A.; Andrews, A. M.; Dickey, E. C.; Horn, M. W.; Weiss, P. S. Scanning Electron Microscopy of Nanoscale Chemical Patterns. *ACS Nano* **2007**, *1* (3), 191–201.

(10) Scimeca, M.; Bischetti, S.; Lamsira, H. K.; Bonfiglio, R.; Bonanno, E. Energy Dispersive X-Ray (EDX) Microanalysis: A Powerful Tool in Biomedical Research and Diagnosis. *Eur. J. Histochem.* **2018**, *62* (1), 2841.

(11) Wan, W.; Su, J.; Zou, X. D.; Willhammar, T. TEM as an Important Tool for Characterization of Zeolite Structures. *Inorg. Chem. Front.* **2018**, *5* (11), 2836–2855.

(12) Ponce, A.; Aguilar, J. A.; Tate, J.; Yacamán, M. J. Advances in the Electron Diffraction Characterization of Atomic Clusters and Nanoparticles. *Nanoscale Adv.* **2021**, *3* (2), 311–325.

(13) Korin, E.; Froumin, N.; Cohen, S. Surface Analysis of Nanocomplexes by X-Ray Photoelectron Spectroscopy (XPS). *ACS Biomater. Sci. Eng.* **2017**, *3* (6), 882–889.

(14) Gardella, J. A. Recent Developments in Instrumentation for X-Ray Photoelectron Spectroscopy. *Anal. Chem.* **1989**, *61* (9), 589A-600A.

(15) Walton, K. S.; Snurr, R. Q. Applicability of the BET Method for Determining Surface Areas of Microporous Metal−Organic Frameworks. *J. Am. Chem. Soc.* **2007**, *129* (27), 8552–8556.

(16) Bae, Y.-S.; Yazaydın, A. Ö.; Snurr, R. Q. Evaluation of the BET Method for Determining Surface Areas of MOFs and Zeolites That Contain Ultra-Micropores. *Langmuir* **2010**, *26* (8), 5475–5483.

(17) Sarycheva, A.; Gogotsi, Y. Raman Spectroscopy Analysis of the Structure and Surface Chemistry of $Ti_3C_2T_x$ MXene. *Chem. Mater.* **2020**, *32* (8), 3480–3488.

(18) Stamm, R. F. Raman Spectroscopy. *Anal. Chem.* **1954**, *26* (1), 49–53.

(19) Basu, P. Use of EPR Spectroscopy in Elucidating Electronic Structures of Paramagnetic Transition Metal Complexes. *J. Chem. Educ.* **2001**, *78* (5), 666.

(20) Reeves, L. W. NMR and EPR Spectroscopy. *J. Am. Chem. Soc.* **1961**, *83* (18), 3924.

(21) Winter, M.; Brodd, R. J. What Are Batteries, Fuel Cells, and Supercapacitors? *Chem. Rev.* **2004**, *104* (10), 4245–4270.

(22) Jalal, N. I.; Ibrahim, R. I.; Oudah, M. K. A Review on Supercapacitors: Types and Components. *J. Phys. Conf. Ser.* **2021**, *1973* (1), 12015.

(23) Ishita, I.; Singhal, R. Porous Multi-Channel Carbon Nanofiber Electrodes Using Discarded Polystyrene Foam as Sacrificial Material for High-Performance Supercapacitors. *J. Appl. Electrochem.* **2020**, *50* (8), 809–820.

(24) Ma, G.; Li, J.; Sun, K.; Peng, H.; Mu, J.; Lei, Z. High Performance Solid-State Supercapacitor with PVA–KOH–$K_3[Fe(CN)_6]$ Gel Polymer as Electrolyte and Separator. *J. Power Sources* **2014**, *256*, 281–287.

(25) Kissinger, P. T.; Heineman, W. R. Cyclic Voltammetry. *J. Chem. Educ.* **1983**, *60* (9), 702.

(26) Elgrishi, N.; Rountree, K. J.; McCarthy, B. D.; Rountree, E. S.; Eisenhart, T. T.; Dempsey, J. L. A Practical Beginner's Guide to Cyclic Voltammetry. *J. Chem. Educ.* **2018**, *95* (2), 197–206.

(27) Zeng, L.; Wu, T.; Ye, T.; Mo, T.; Qiao, R.; Feng, G. Modeling Galvanostatic Charge–Discharge of Nanoporous Supercapacitors. *Nat. Comput. Sci.* **2021**, *1* (11), 725–731.

(28) Yun, C.; Hwang, S. Analysis of the Charging Current in Cyclic Voltammetry and Supercapacitor's Galvanostatic Charging Profile Based on a Constant-Phase Element. *ACS Omega* **2021**, *6* (1), 367–373.

(29) Zardalidis, G.; Chatzogiannakis, D.; Glynos, E.; Farmakis, F. Electrochemical Impedance Spectroscopy Study of Surface Film Formation on Lithium Anodes and the Role of Chain Termination on Poly(Ethylene Oxide) Electrolytes. *ACS Appl. Energy Mater.* **2021**, *4* (7), 6815–6823.

(30) Bredar, A. R. C.; Chown, A. L.; Burton, A. R.; Farnum, B. H. Electrochemical Impedance Spectroscopy of Metal Oxide Electrodes for Energy Applications. *ACS Appl. Energy Mater.* **2020**, *3* (1), 66–98.

(31) Suroviec, A. H.; Suroviec, A. H. Determining Surface Coverage of Self-Assembled Monolayers on Gold Electrodes. **2012**, *4171* (12), 83–85.

(32) Xiao, L.; Lv, Y.; Dong, W.; Zhang, N.; Liu, X. Dual-Functional $WO_3$ Nanocolumns with Broadband Antireflective and High-Performance Flexible Electrochromic Properties. *ACS Appl. Mater. Interfaces* **2016**, *8* (40), 27107–27114.

# CHAPTER III:

## WO$_{3-x}$ NANO AND MICROSTRUCTURES AS CHARGE STORAGE ELECTRODE MATERIALS

## 3.1 PROLOGUE

Tungsten trioxide ($WO_3$) is a semiconductor material that has aroused a great deal of attention for being used in various industrial applications such as electrochemical supercapacitors, water splitting, photocatalysis, photoluminescence, gas sensing, photochromic, electrochromic devices, etc.[1,2] $WO_3$ due to its inherent characteristics such as high theoretical specific capacitance, good electrochemical stability, high conductivity, environmental friendliness, and low cost, is considered to be a promising candidate for high energy supercapacitors. This provides a scope of interest towards morphology and size-controlled synthesis of nanostructured $WO_3$ to enhance its activity when targeted towards a specific application such as the ones discussed above.

Numerous nanostructured $WO_3$ with unique morphologies are listed in the literature and presented in detail in section 1.5. The major drawback of all these techniques is the cost inefficiency and the hazards/safety issues that come with handling high-pressure instruments, along with the associated problems of bulk synthesis. While the research on developing $WO_3$ nanostructures using hydrothermal conditions and organic templates has gained a lot of interest, less focus has been channelled towards the scalable synthesis of nanostructures using simple precipitation or gelation methods.

Thus in the present chapter, various nano and microstructures of $WO_{3-x}$ have been presented that are synthesized using a modified sol-gel method. The synthesis were performed using various structure directing agents such as urea, carbohydrazide, semicarbazide, N-methylurea, tetramethylurea, and citric acid. The details of chemicals used and synthesis procedures are presented in sections 2.1 and 2.2, respectively. The effect of various synthesis parameters such as solution pH, calcination temperature, reaction time, metal to SDA ratio on the morphology of $WO_{3-x}$ was investigated in detail. The synthesized $WO_{3-x}$ were characterized using the different characterization techniques listed in section 2.3. All synthesized WO3-x nano and microstructures were utilized in the fabrication of electrodes, and their charge-storage performance was assessed. The results and discussion of this investigation are presented in detail in section 3.2, while the conclusions of this study which provides a concise and critical reflection on the significance of the results can be found in section 3.9.

## 3.2 RESULTS AND DISCUSSIONS

### 3.2.1 TG-DTA studies

Using the methodology described in section 2.2 the $WO_{3-x}$ nanorods were synthesized. Prior to calcination, the as-synthesized tungstic acid-urea hybrid gel was subjected to TG-DTA analysis in the temperature range of 30-600 °C at a constant heating rate of 5 °C $min^{-1}$. Analysis of TG-DTA data as presented in figure 3.1 (A) indicated an initial weight loss below 150°C (10%) corresponding to an endothermic peak at 102°C in DTA and was attributed to the loss of physically adsorbed water. At temperatures from 150°C to 280°C, the exothermic peak centering at 257°C (accounting for a further weight loss of 47%) was attributed to the combustion of excess urea leading to the formation of CO/$CO_2$ and $NO_x$ gases. The weight loss from 280°C to 500°C (≈10%) was attributed to the oxidation of urea coordinated with tungstic acid molecules, which required relatively higher temperatures for complete removal. Based on the TG data, the calcination temperature was fixed at 550°C. On the contrary, the tungstic acid gel without urea synthesized as per the procedure mentioned in section 2.2.1, showed an overall weight loss of only 30%, which was due to the loss of water of crystallization. The $WO_{3-x}$ samples obtained after calcination at different temperatures were subjected to IR and XRD analysis.

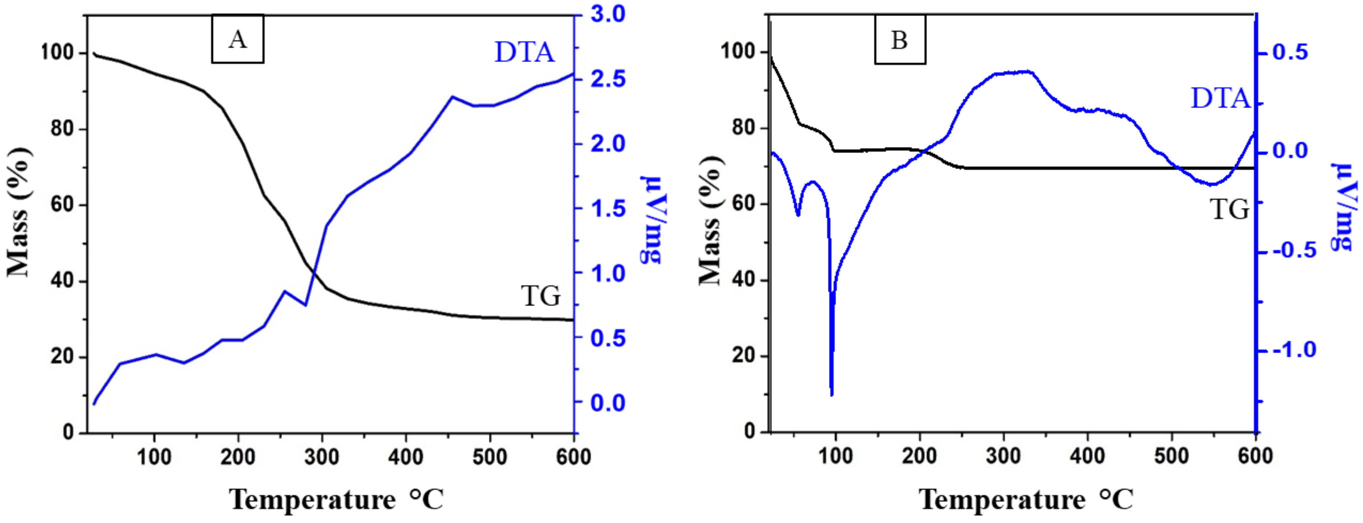

**Figure 3.1:** TG-DTA analysis of (A) Tungstic acid-urea hybrid gel and (B) Tungstic acid (without urea).

### 3.2.2 IR studies

The IR spectra of the as-synthesized tungstic acid-urea hybrid dry gel, calcined at different calcination temperatures of 250°C, 350°C, 450°C, 550°C, and 650°C, respectively, are presented in Figure 3.2 (A). At 250°C, the peak appearing at 1676 cm$^{-1}$ can be assigned to C=O stretching frequency. A broad peak that appears at 3455 cm$^{-1}$ can be assigned to O-H stretching and N-H stretching frequencies. The C-N stretching frequency appears at 1447 cm$^{-1}$. All these peaks indicate the presence of urea in the sample. As the temperature increases to 450°C, bands at 672 cm$^{-1}$ and 837 cm$^{-1}$ begin to appear and can be assigned to the O-W-O and W=O vibrations, indicating the formation of tungsten oxide. These peaks due to the metal oxide persist as the temperature is increased to 550°C and 650°C. However, the peaks at 3455 cm$^{-1}$, 1676 cm$^{-1}$, and 1447 cm$^{-1}$ disappear due to the combustion of urea into $NO_x$(g) and $CO_2$(g).

### 3.2.3 XRD studies

Figure 3.2 (B) represents the XRD pattern of $WO_{3-x}$ samples obtained after drying and calcination at different temperatures ranging from 250°C to 650°C. $WO_{3-x}$ samples dried at 250°C exhibits an orthorhombic phase (Fmm2, JCPDS # 35-0270). A phase change from orthorhombic to anhydrous hexagonal phase (P6/mmm, JCPDS # 75-2187) is observed at 350°C.[3–5] Further increase in the annealing temperature ≥ 450°C produces a stable monoclinic phase, with peaks appearing at 2θ value of 22.7, 23.5, 24.2, 26.5, 28.8, 32.8, 33.6, 34.1, 35.2, 41.2, 41.8, 45.1, 47.1, 49.8, 50.1 and 55.4 having miller indices (002), (020), (200), (120), (-112), (022), (-202), (202), (122), (-222), (222), (004), (040), (140), (-114) and (420) respectively (P21/n, JCPDS # 43-1035).[6–8]

A comparative analysis of the ratio of major peaks with miller indices (002) : (020) : (200) at 450°C and 550°C are observed to be similar (i.e. 1 : 0.85 : 0.65). However, a major shift in the ratio of the corresponding peak intensities is observed at 650°C (i.e., 1: 0.94 : 0.98), thus indicating morphological transformation in the synthesized $WO_{3-x}$ at elevated temperatures. Additionally, the observed peaks were strong, sharp, and narrow, with no peaks of secondary phases present. Thus, it can be concluded that the synthesized $WO_{3-x}$ were of high phase purity and crystallinity.

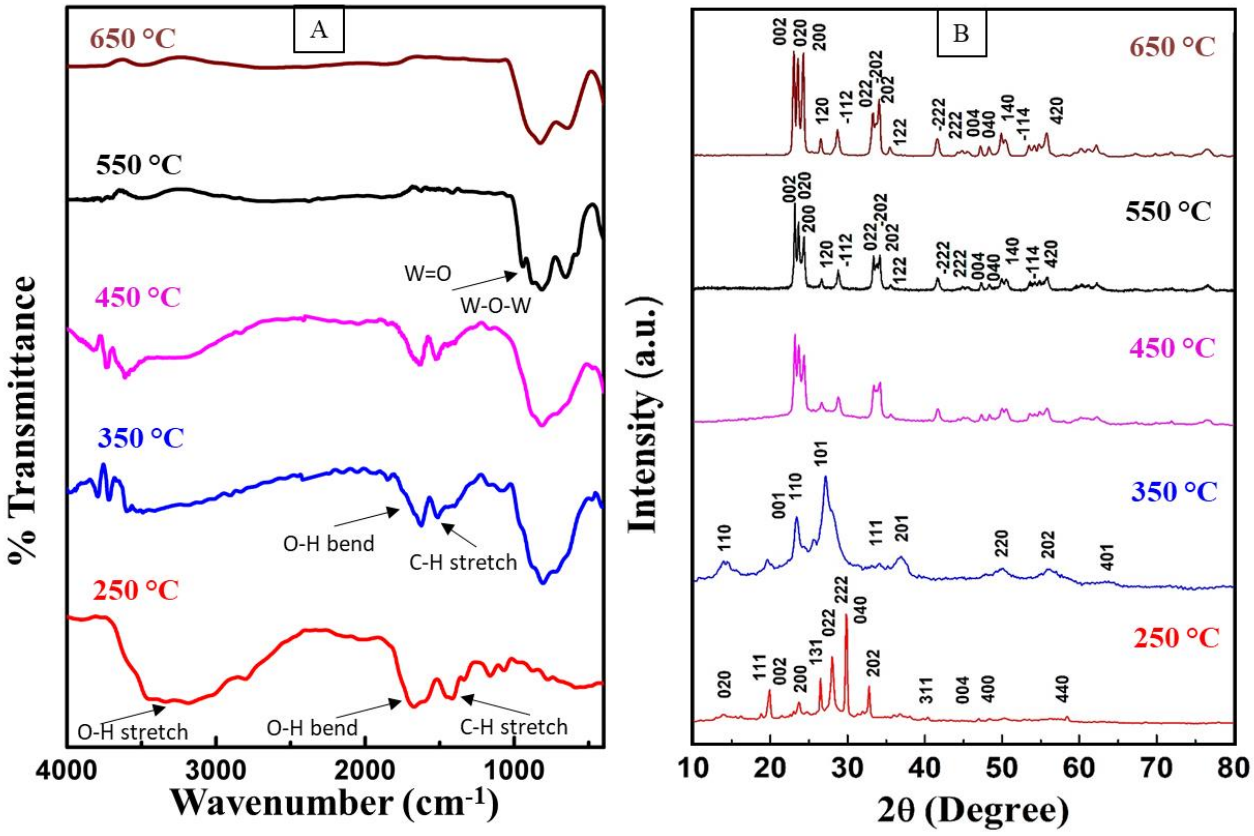

**Figure 3.2: (A)** IR spectra and (B) X-ray diffractograms of synthesized tungstic acid-urea hybrid gels dried/calcined at different temperatures.

### 3.2.4 Morphological studies

To understand the influence of experimental conditions such as solution pH, urea concentration, calcination temperature, and calcination time on the formation of $WO_{3-x}$, several control experiments were carried out by varying each of the above synthesis parameter one at a time.

#### 3.2.4.1 Effect of synthesis pH

In the first set of experiments, the pH of the tungstic acid colloidal gel was varied in the range of 1-10 by adding HCl or $NH_4OH$ solution. In a parallel experiment, the pH of the tungstic acid-urea hybrid gel was also varied similarly as above before subjecting the two sets to digestion at 100 °C and calcination in air at 550 °C for 2 h. The effect of pH on

$WO_{3-x}$ morphology with and without urea was monitored by SEM analysis. Figure 3.3 shows the SEM micrographs of the two sets of experiments.

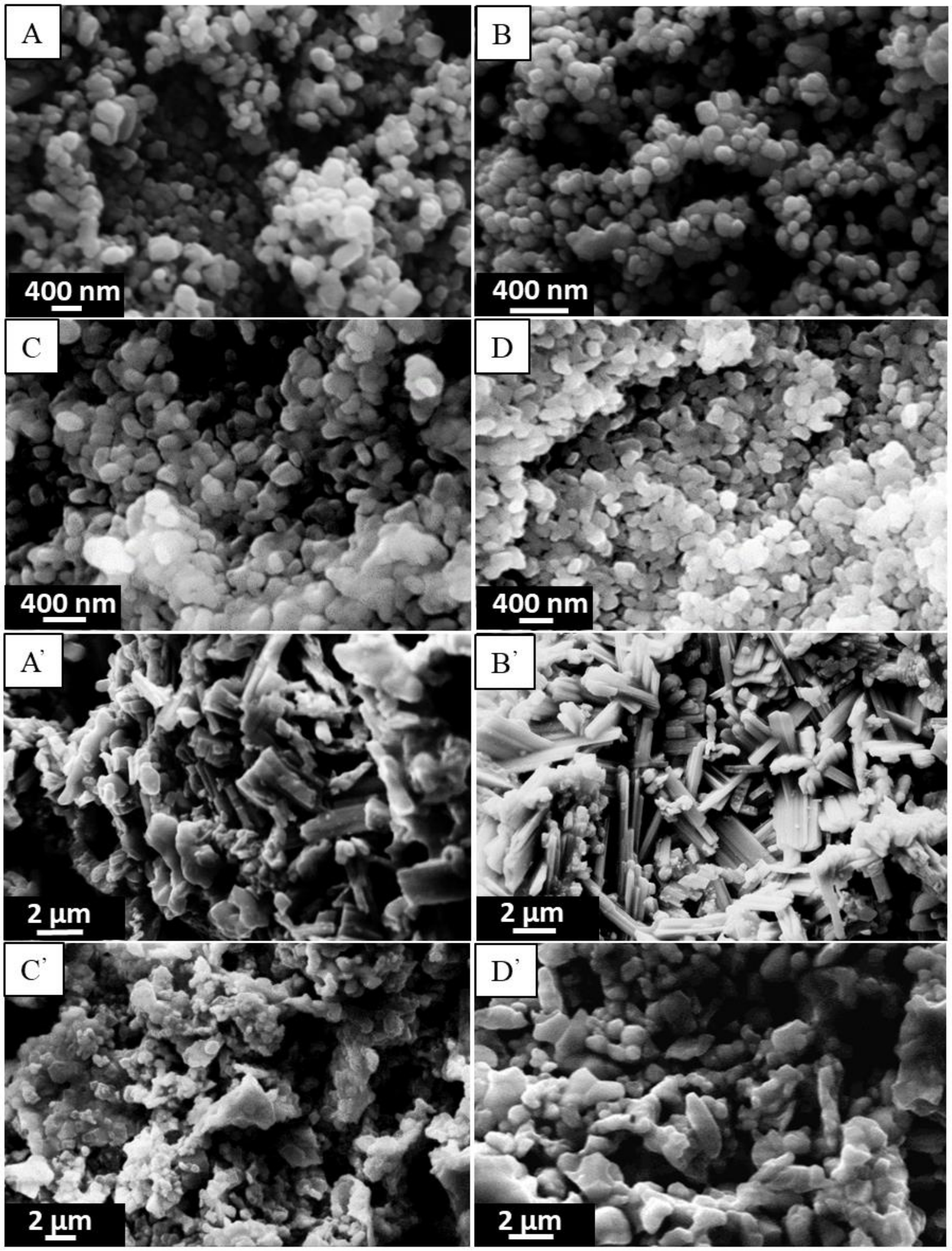

**Figure 3.3:** Effect of variation in pH on the morphology of synthesized $WO_{3-x}$ at 550°C; SEM images of $WO_{3-x}$ in A,B,C, and D correspond to pH values of 1, 2.5, 5, and 10, respectively, synthesized without urea and A', B', C', and D' synthesized with urea.

It was observed that variation in pH of the tungstic acid gel without urea did not induce any significant changes in the shape of $WO_{3-x}$ particles (henceforth labelled as WP). The overall morphology of the obtained nanoparticles was more or less spherical, with an observed relative increase in the tendency for agglomeration as the pH of the solution increases. On the contrary, when urea is added to the colloidal tungstic acid gel, the lower pH conditions tend to favor nanorod formation, as can be seen in figure 3.3 A' and B', with best results obtained in the pH range of 2-3. At pH < 2, the obtained $WO_{3-x}$ demonstrated irregular formation of rod-like structures densely packed together as agglomerates. The high pH of the solution (pH=5-10) did not yield nanorods and only increased the tendency for the formation of aggregates of $WO_{3-x}$ nanoparticles, having no specific morphology.

#### 3.2.4.2 Effect of W to urea ratio on the growth of 1D $WO_{3-x}$ nanorods

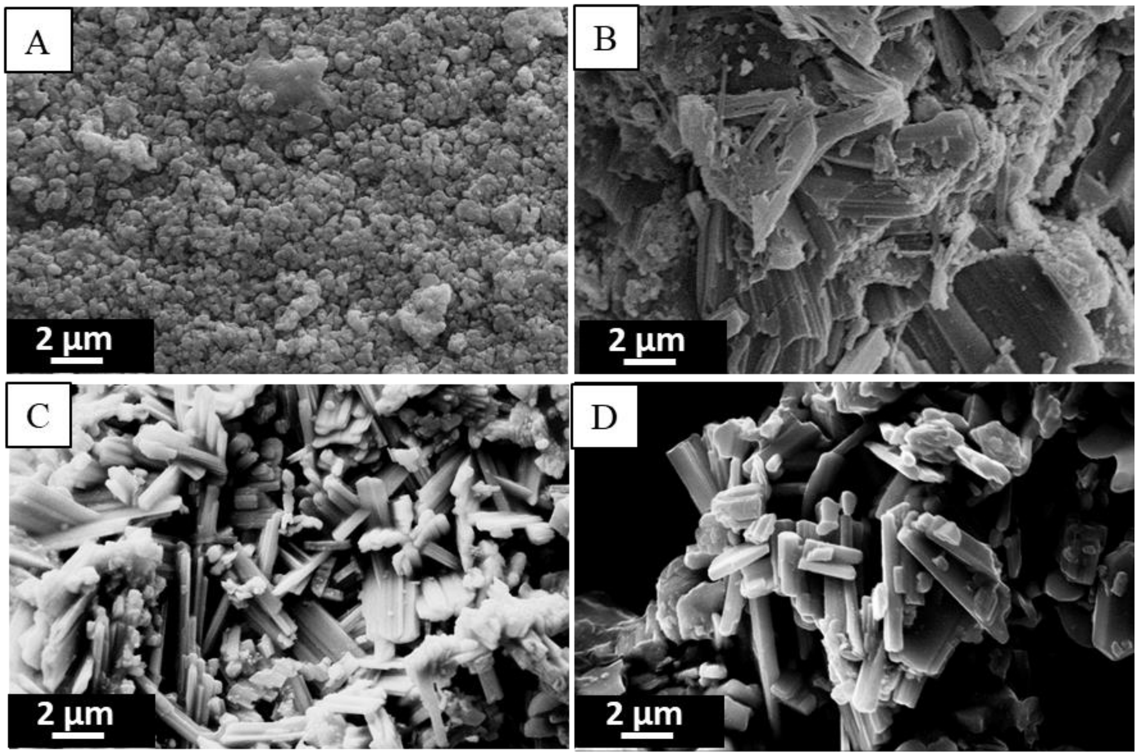

**Figure 3.4:** Effect of W to urea ratio on the morphology of $WO_{3-x}$ (A) 1:1, (B) 1:3, (C) 1:6, and (D) 1:9.

When experiments were performed by varying the W to urea ratio in the order 1:1, 1:3, 1:6, and 1:9, it was observed that with W to urea ratio ≤ 1:6, mixed aggregates of $WO_{3-x}$ nanoparticles and nanorods were formed while ratios ≥1:6 were necessary for better growth of nanorods, with best results obtained when the ratio was maintained at 1:6 as shown in figure 3.4 C (henceforth labeled as WN).

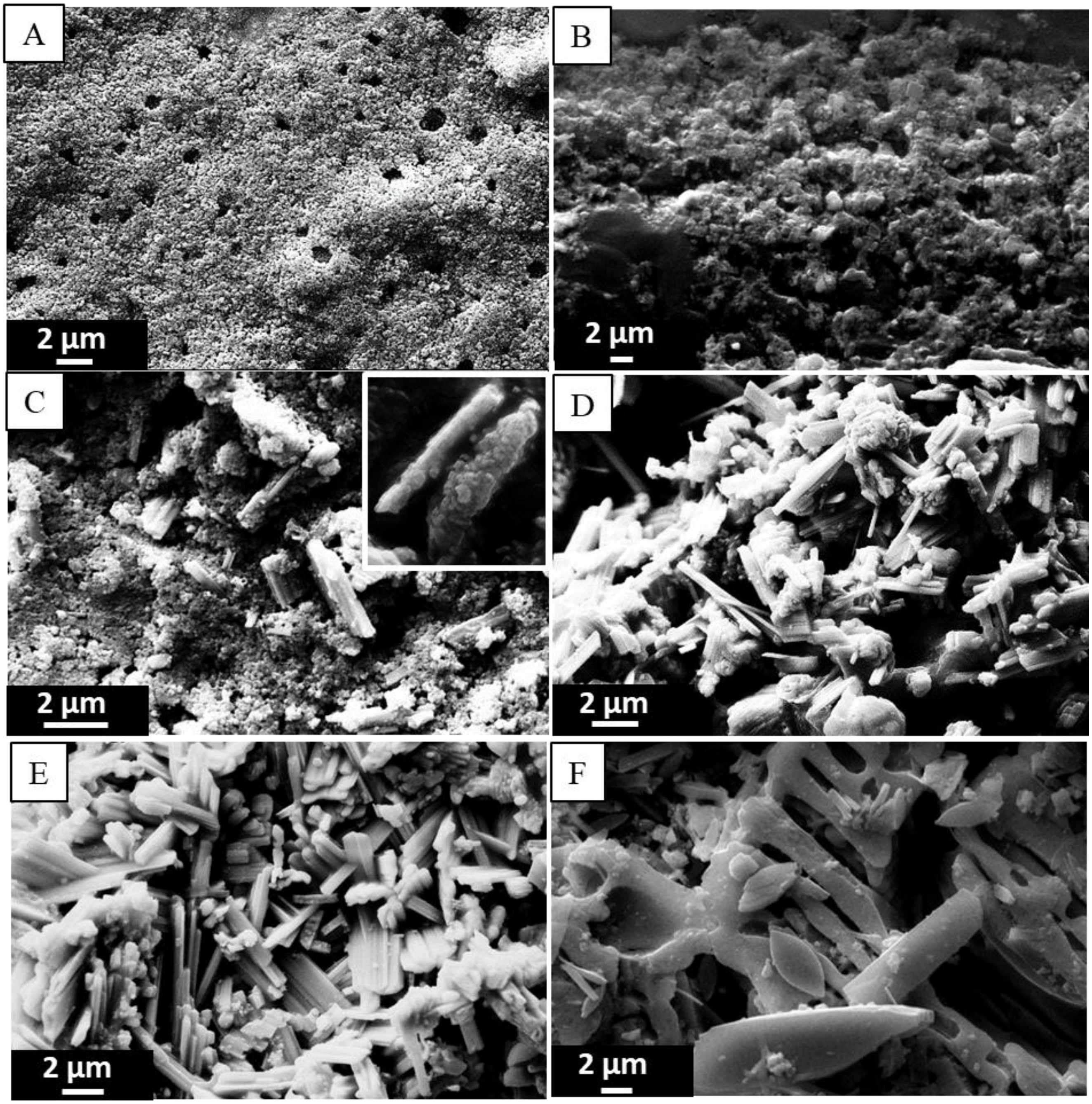

**Figure 3.5:** Temperature dependent morphological transformation of $WO_{3-x}$ at (A) 150 °C, (B) 250 °C, (C) 350 °C, (D) 450 °C, (E) 550 °C, and (F) 650 °C at pH = 2.5 and calcination time = 2h.

### 3.2.4.3 Effect of calcination temperature on the growth of 1D $WO_{3-x}$ nanorods

To get a better insight into the process of transformation of colloidal tungstic acid-urea hybrid gel into $WO_{3-x}$ nanorods, the hybrid gels were subjected to calcination in air at different temperatures of 150°C, 250°C, 350°C, 450°C, 550°C, and 650°C for 2 hours. The temperature-dependent morphological transformation of the calcined product was monitored by SEM (Figure 3.5). At a low temperature of 150-250°C, the tungstic acid-urea dry gel appears as aggregates of densely packed particles composed of both tungstic acid and urea (presented in figures 3.5 A, B). A further rise in calcination temperature initiates the decomposition of urea into $NH_{3(g)}$ and $CO_{2(g)}$, and at 350°C, the nanorods begin to appear (refer to figure 3.5 C, inset). Further increase in temperature (450 – 550°C, figure 3.5 D and E) leads to the complete removal of urea and transformation of $WO_{3-x}$ particles into bundles of $WO_{3-x}$ nanorods. Temperatures > 600°C lead to the sintering of $WO_{3-x}$ nanorods, wherein the nanorods appear to stack together and grow into lamellar sheet-like structures (henceforth labeled as 2DW). This observation is consistent with the XRD data wherein the preferential growth is observed along the (200) plane due to an increase in calcination temperature from 550°C to 650°C.

### 3.2.4.4 Effect of calcination time on the morphology of 1D $WO_{3-x}$ nanorods

When subjected to longer calcination times of $> 2$ to $\leq 4$h at 550°C, the initially formed nanorods self-assemble into complex 3D microstructures. It is evident from figure 3.6 A-F that the nanorods stack together in the form of bundles. These bundles grow in three dimensions to form a complex surface heterostructure, full of edges and kink sites which are crucial for catalytic performance. Another unique feature of these nanostructures is that the empty spaces created within a given stack of nanorod bundle results in the formation of well-aligned porous structures, similar to a stack of hollow vertical columns, which not only increases the available surface area but also could serve as passages for easy diffusion of ions or molecules through it. However, longer calcination time $\geq 6$ h results in excessive fusion of nanorod bundles resulting in loss of both the 3D nanostructure morphology and the collapse of nanoporous structure (refer figure SF1 in Annexure-1). The growth mechanism of the synthesized nanorods and their subsequent self-assembly into microstructures is further discussed in detail in section 3.2.7.

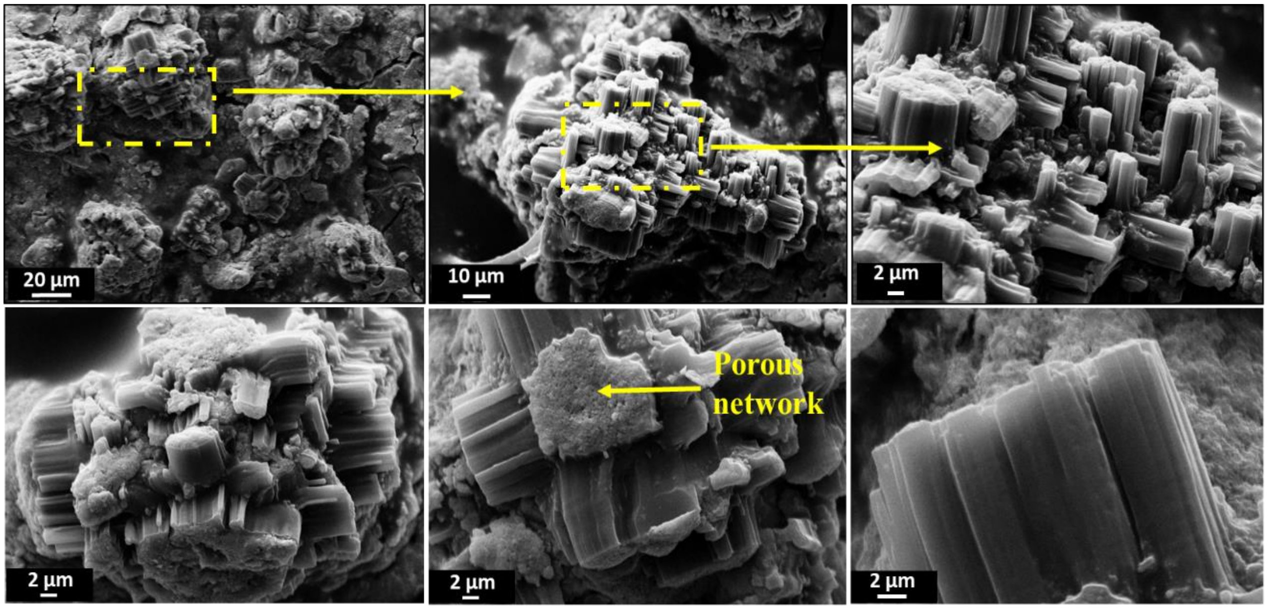

**Figure 3.6:** SEM images depicting self-assembly of $WO_{3-x}$ nanorod bundles into 3D nanoporous structure. A-C= represents the 3D growth of nanostructure, D = the side view of a stack of vertically aligned nanorod bundles, and E-F= top and complete view of the 3D porous structure.

### 3.2.5 HRTEM studies

To understand the detailed structural and morphological characteristics of the synthesized $WO_{3-x}$ nanorods, low and high-resolution TEM images were recorded. A typical image of a single nanorod bundle is shown in figure 3.7 A. The analyzed nanorods have an average diameter of ~115 nm and a length of ~5 μm, in good agreement with SEM analysis. The HRTEM image shown in figure 3.7 B reveals lattice fringes with a d-spacing of 0.386 nm, which matches with the (002) plane of monoclinic $WO_3$. Selected-area electron diffraction (SAED) pattern, figure 3.7 C, also reveals the 002 plane and can be indexed with a monoclinic phase of $WO_3$ (JCPDS No. 43-1035). The regular intensities of bright spots in the SAED pattern confirm the monocrystalline nature of synthesized monoclinic $WO_{3-x}$. The HRTEM and SAED analysis were in good agreement with the XRD analysis, establishing the formation of stable monoclinic $WO_{3-x}$ nanorods, preferentially growing along the (002) plane at temperature $\leq 550°C$.

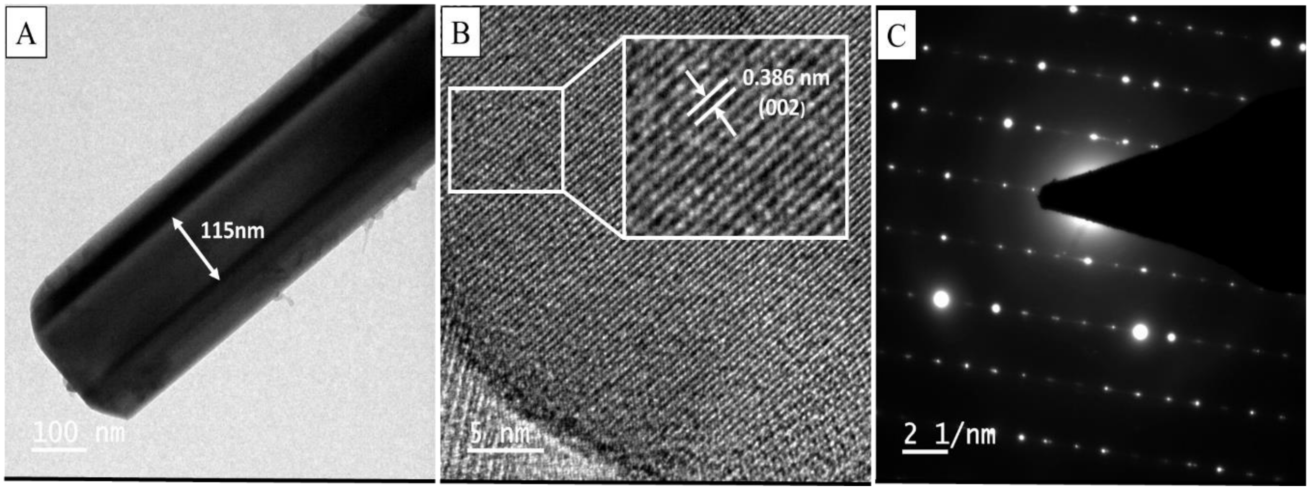

**Figure 3.7:** (A) TEM image of synthesized $WO_{3-x}$ nanorod bundle, (B) HRTEM image of $WO_{3-x}$ nanorod, and (C) SAED pattern of $WO_{3-x}$ nanorod.

### 3.2.6 XPS studies

To obtain more information on the chemical composition and relative distribution of oxidation states of the synthesized $WO_{3-x}$ nanostructures, X-ray photoelectron spectroscopy (XPS) was employed (refer figure 3.8). All the $WO_{3-x}$ samples display the characteristic W4f peaks located at 35.53 eV and 37.82 eV, which can be attributed to $W4f_{7/2}$ and $W4f_{5/2}$, respectively. These peaks result from the spin-orbital splitting of $4f_{7/2}$ with $4f_{5/2}$.[9] These two peaks are well separated, and the peak fitting reveals the presence of a majority of bulk tungsten in $W^{6+}$ while ~ 5-25 % was in $W^{5+}$ oxidation state, which was present mostly on the surface of the material, in agreement with the observations of Tu et al.[10] and Qiu et al.[11]

The O1s peak located at 530.36 eV, can be ascribed to the W-O peak, and a shoulder peak at 532.62 eV is due to the oxygen in water molecules intercalated in the $WO_{3-x}$ crystal structure.[48,] The percentage composition analysis of $W^{6+}$, $W^{5+}$, and O1s peaks are presented in Table 3.1. The W4f analysis of XPS spectra reveals that the ratio of $W^{5+}/W^{6+}$ is the highest for WN (0.15) and 3DW (0.21), which confirms that the nanostructured surface has a greater magnitude of surface oxygen defects compared to particle agglomerates (0.04). Moreover, the relative distribution of the interstitial water is also greater in WN and 3DW compared to WP. The lower value of $W^{5+}/W^{6+}$ in the case of 2DW is due to the high-temperature sintering the material.

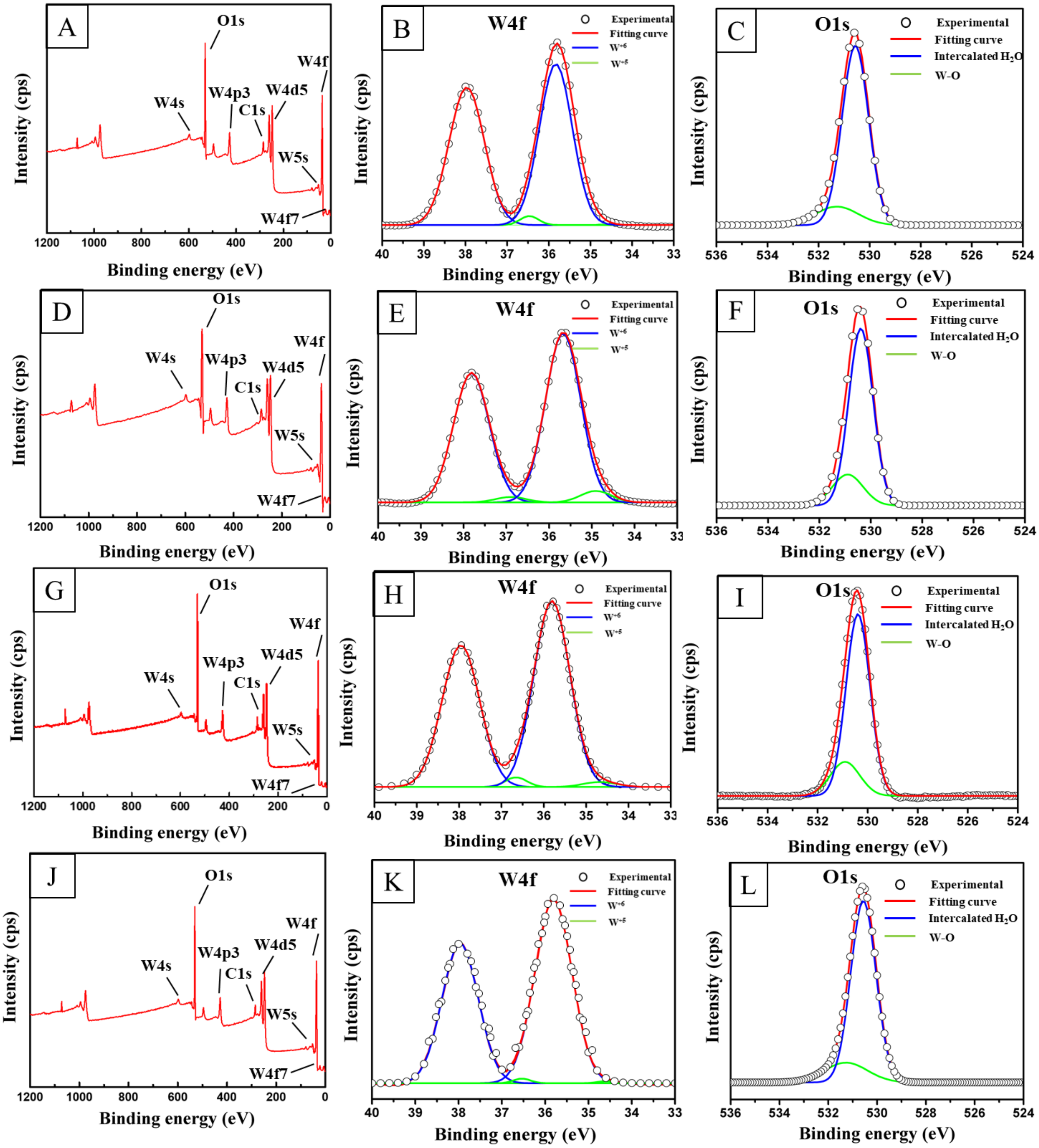

**Figure 3.8:** XPS spectra of (A-C) WP, (D-F) WN, (G-I) 3DW, and (J-L) 2DW.

| Material | Narrow scan | Tungsten species | XPS area integration (%) | Area ratio $W^{5+}$ / $W^{6+}$ |
|---|---|---|---|---|
| WP | W 4f | $W^{6+}$ | 95.77 | 0.04 |
| | | $W^{5+}$ | 4.23 | |
| | O 1s | W-O | 81.88 | |
| | | Intercalated $H_2O$ | 18.12 | |
| WN | W 4f | $W^{6+}$ | 86.58 | 0.15 |
| | | $W^{5+}$ | 13.41 | |
| | O 1s | W-O | 78.45 | |
| | | Intercalated $H_2O$ | 21.55 | |
| 3DW | W 4f | $W^{6+}$ | 82.77 | 0.21 |
| | | $W^{5+}$ | 17.23 | |
| | O 1s | W-O | 76.48 | |
| | | Intercalated $H_2O$ | 23.52 | |
| 2DW | W 4f | $W^{6+}$ | 94.15 | 0.06 |
| | | $W^{5+}$ | 5.85 | |
| | O 1s | W-O | 82.75 | |
| | | Intercalated $H_2O$ | 17.25 | |

**Table 3.1:** The percentage of species obtained from the XPS peak area integration of narrow scan spectra.

### 3.2.7 Growth Mechanism of $WO_{3-x}$ nanostructures

In the presence of urea, the growth mechanism of 3D $WO_{3-x}$ microstructures at low pH can be explained according to the crystal nucleation-growth–assembly mechanism.[12–14] As explained earlier, the formation of colloidal tungstic acid gel and its interaction with protonated urea, plays a significant role in crystal growth of $WO_{3-x}$ nanorods and microstructures. It is well established that, the crystal growth mechanism consists of two main stages: nucleation and subsequent growth. The nucleation stage comprises of rapid formation of small colloidal particles of tungstic acid, which are driven by the supersaturation force of the acidic medium.[13] These small particles subsequently enter the growth phase in order to form larger crystals of $WO_{3-x}$ particles.

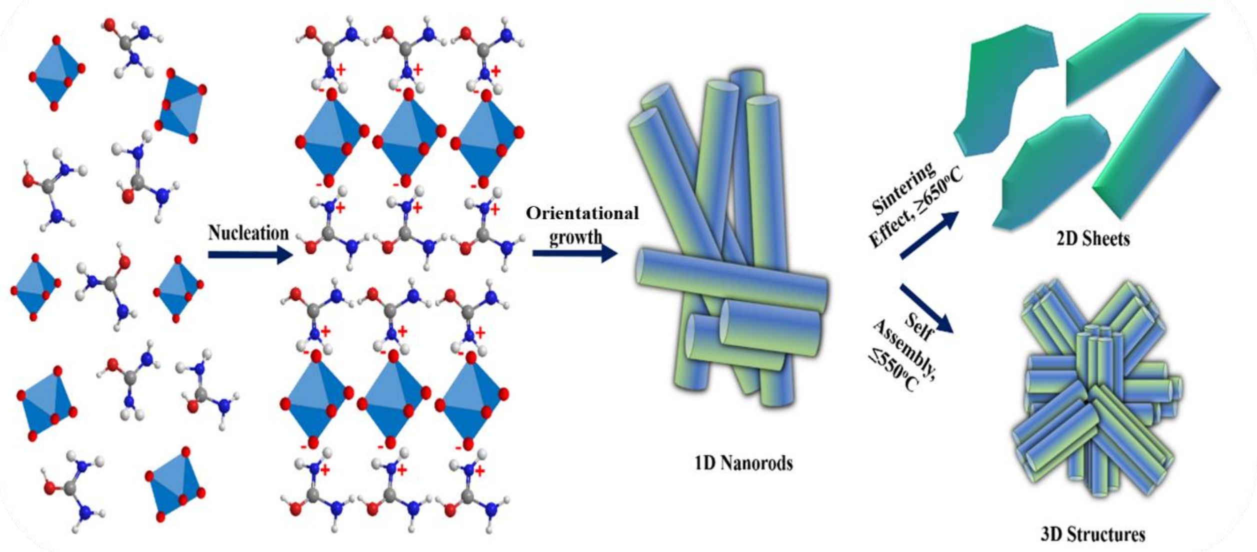

**Figure 3.9:** Schematic illustration of the growth mechanism of $WO_{3-x}$ nanorods and subsequent transformation into sheets and microstructures.

The addition of protonated urea in an appropriate amount at this stage becomes crucial, as it acts as a capping agent under acidic conditions to orient the growth of nanorods (see figure 3.9). Under acidic conditions, mono-protonation of urea occurs at the carbonyl oxygen, resulting in the formation of iminium cation ($-C=NH_2^+$).[15,16] In an investigation by Bortoluzzi et al., these imminum cation salts were isolated by reacting $WCl_6$, $WCl_5$, and $WOCl_4$ with alkylated ureas in ratios ≥ 1:2.[17,18] They isolated corresponding O-monoprotonated dimeric (figure 3.10 A) and monomeric salts (figure 3.10 B) in approximately 50% yield. In our synthesis method presented here, a similar effect could occur wherein, ionic interaction of protonated urea would serve as a charge stabilizer by the interaction of positively charged iminium ions with oxygen atoms of $WO_6$ octahedra, thus avoiding agglomeration of particles and directing the growth mechanism of $WO_{3-x}$ nanorods. This was also comfirmed by performing an control experiment in which urea was replaced with thiourea and it was observed that no nanorod formation took place. (refer figure SF2 in Annexure-I) The lower yields of iminium salt formation in the work of Bortoluzzi et al. could also explain the need for a high W to urea ratio (1:6) for the effective growth of nanorods, as observed in the present study. At pH < 2 (high concentration of $H^+$ ions), the nucleation rate of tungstic acid particles could be so fast that, it could kinetically dominate over urea protonation and its subsequent rearrangement around the $WO_6$ octahedral units. This would explain the incomplete formation of nanorod-like aggregates seen in SEM micrograph at pH ~1 (figure 3.3 A').

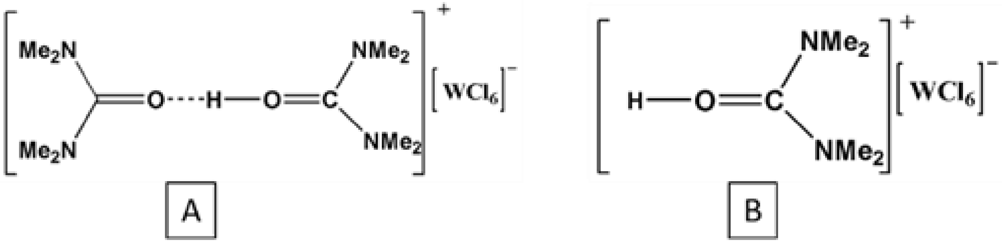

**Figure 3.10:** (A) O-monoprotonated dimeric salt (B) O-monoprotonated monomeric salt obtained by reacting tetramethyl urea with tungsten hexachloride.[15,16]

On the contrary, at high pH (5-10), the significant difference in the nucleation and the growth phase can be attributed to the fact that the nucleation rate is too slow due to the lack of $H^+$ ions. Moreover, the $WO_6$ units are not stable in the basic medium, and urea protonation may not occur in these conditions. Therefore, the basic conditions become entirely unfavorable to the growth of nanorods, which ultimately results in the formation of densely aggregated, irregular-shaped nanoparticles. At the optimized conditions of pH =2.5 and W: urea ratio of 1:6, which are ideal for nanorod formation, the thermodynamic requirements of nanorod growth is satisfied by the exothermic decomposition of urea into $NH_3$ and $CO_2$, providing sufficient energy for directional growth and transformation of $WO_6$ units into $WO_{3-x}$ nanorods. At calcination temperatures of 450°C-550°C, complete removal of the capping agent leads to fully grown $WO_3$ nanorods within a short calcination time of 2 h.

At higher calcination temperatures above ≥ 600°C, the obtained lamellar sheet-like aggregates (refer figure 3.5 F) can be explained based on the fact that such high pyrolysis conditions lack the time for structural orientation of individual nanorods and rapid burst of heat energy due to urea decomposition possibly resulting in sintering of $WO_{3-x}$ nanorods, thus resulting in sheet like morphology. On the contrary, if the nanorods are allowed to grow at lower temperature and for longer time (up to 6 h), the nanorods self-assemble into 3D $WO_{3-x}$ microstructures as explained earlier (refer figure 3.6).

Comparing the above results with that of literature such as the work published by Chen et al.[19], striking advantages of our synthesis method over the cited literature can be revealed. The rapid combustion synthesis of Chen et al. utilizes ammonium paratungstate as a precursor and large excess of fuels such as glycine or citric acid-urea co-fuel mixtures (W to fuel ratio of >1:20) and ammonium nitrate as oxidizer. The authors stress on the importance of the presence of amino group and carboxylic groups in fuels such as glycine and urea-citric acid co-fuel mixture wherein the amino group needs to undergo hydration polymerization reaction with carboxylic groups, in order to form a cross-linked network structure, which is filled with high volumes of reducing gases ($CO/NH_3$), resulting in the formation of reduced $W_{18}O_{49}$. The oxidizer, ammonium nitrate/$O_2$ converts $W_{18}O_{49}$ into $WO_3$ nanorods during the combustion process. It was interesting to note that, since urea has only amino groups and no carboxylic groups, urea alone could not form such a network structure as mentioned above and hence essentially produces only nanoparticles of $WO_3$.[19]

On the contrary to the above literature, our method used urea under protonated conditions in significantly lower amounts (W to urea ratio of 1:6, which is required for complete formation of nanorods), as an efficient and cost-effective structure directing agent, thus eliminating the need of additional co-fuel and oxidizer, making the synthesis process more simple and cost-efficient. This is also an additional highlight of the present method over traditional nanostructure synthesis methods reported in literature, which requires co-fuels, oxidizers under hydrothermal/solvothermal conditions, in high pressure autoclaves, which limit their bulk scale industrial production.The synthesized $WO_{3-x}$ nanostructures were tested for their charge storage performance and the results obtained are discussed in the next section.

## 3.3 Evaluation of the charge storage properties of nanostructured $WO_{3-x}$ synthesized using urea

### 3.3.1 Three electrode charge storage studies

The investigation of the charge storage properties of $WO_{3-x}$ nanostructures, namely 3DW, WN, WP, and 2DW were performed using cyclic voltammetry (CV), galvanostatic charge-discharge (GCD), and electrochemical impedance spectroscopic (EIS) measurements. Figure 3.11 A shows an overlay of CV measurements in a three-electrode system with 0.5 M $H_2SO_4$ as an electrolyte and recorded at a fixed scan rate of 50 mV $s^{-1}$ in a potential window between -0.2 to 1.0 V (vs. Ag/AgCl) at 28°C ± 1°C. The shape of the voltammogram if typical of $WO_{3-x}$ and its nature can be understood as per the following reaction 3.1.

$$\mathrm{WO_{3-x(bleached)}} + n\mathrm{H}^+ + ne^- \leftrightarrow \mathrm{H_nWO_{3-x(colored)}} \qquad (3.1)$$

When protons are intercalated in the $WO_{3-x}$ lattice, the metal is reduced from $W^{+6}$ to $W^{+5}$, and the reverse reaction occurs during deintercalation. This property was investigated by studying $H^+$ intercalation using cyclic voltammetry with three-electrode system. The typical cyclic voltammogram (as shown in figure 3.11 A and figure SF3 in Annexure-I), shows an anodic peak at ~ -0.1 V vs. Ag/AgCl due to the deintercalation of $H^+$ ions from the $WO_{3-x}$ matrix.[20,21] However, as the electrode approaches more negative potentials, it can be observed that there is a steep drop in current. This is a result of excess polarization of the electrode, which is caused by the formation of solid electrolyte interphase layers on the electrode surface. This layer can slow down or completely block the intercalation of $H^+$ ions into the electrode, resulting in a decrease in current response. This drop in current is seen as a steep decline in the CV curve at around -0.2 V.

The largest area under the CV were observed for 3DW and WN. The area under the CV curve is an important parameter in evaluating the electrochemical performance of materials. The CV curve represents the relationship between the potential and charge in a system, and the area under the curve provides a measure of the amount of charge stored in the material. A large area under the CV curve suggests that the material can store a significant amount of charge, which is critical for its use as a supercapacitor. In the case of 3DW and WN, the large area under the CV curve indicates that their nanostructure has a positive impact on the charge storage performance, leading to improved electrochemical performance. This observation also highlights the importance of nanostructuring in the design and optimization of supercapacitor materials.

Furthermore, the diffusion coefficient ($D_0$) for $H^+$ ions were estimated by performing scan rate-dependent study of the different $WO_{3-x}$ nanostructured electrodes and using the Randles-

Sevciks method described in section 2.4.4 (refer figure SF3 in Annexure-I). The calculated results show that, the $D_0$ value of WP is $2.4 \times 10^{-9}$ cm$^2$ s$^{-1}$, was ~ 2 times smaller than that of WN, $4.1 \times 10^{-9}$ cm$^2$ s$^{-1}$. Moreover, $D_0$ values for the 3DW nanostructured films were found to be $5.9 \times 10^{-9}$ cm$^2$ s$^{-1}$. On the contrary, the calculated $D_o$ value for 2DW is 1.1 x $10^{-9}$ cm$^2$ s$^{-1}$, which are almost 6 times lower compared to 3DW due to the heavy sintering in the former case. This suggests that 3D nanostructures with porous channels allowed greater mobility and enhanced diffusion of $H^+$ ions compared to the rest of the catalysts.

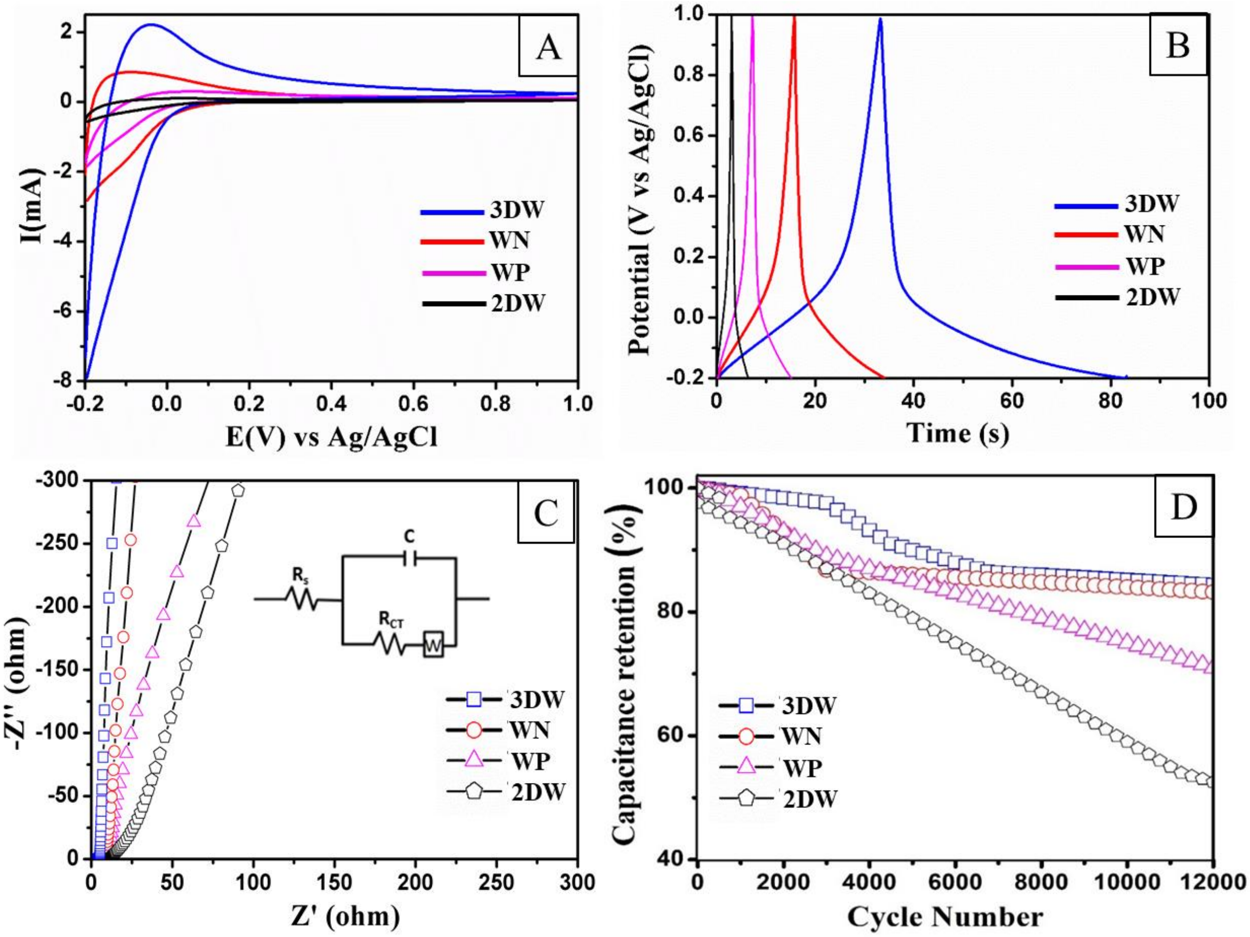

**Figure 3.11:** Supercapacitor performance investigated via (A) CV analysis at a scan rate of 10 mV s$^{-1}$; (B) GCD analysis at the current density of 2 A g$^{-1}$ ; (C) Nyquist plots in the frequency range of 1 mHz to 1 MHz; and (D) cycling stability performance evaluated at a constant current density of 8 A g$^{-1}$.

To further investigate the role of surface morphology on improved electrochemical activity of $WO_{3-x}$ nanostructures, chronoamperometric measurements were performed to estimate the electroactive surface area using the method described in section 2.4.3. The obtained areas are summarized in Table 3.2 along with a comparison to their BET surface area results (presented as SF4 in Annexure-I). As evident from Table 3.2, the presence of 3D nanoporous network in 3DW results in an electroactive surface area of 0.87 $cm^2$ and a greater BET surface area of 8.3 $m^2$ $g^{-1}$ compared to the rest of the synthesized catalysts. The 3D nanoporous network enables active sites of the material to be readily exposed to diffusing $H^+$ ions, thus improving intercalation efficiency and hence an increase in the electroactive area of the material. Due to the increased diffusion coefficient and greater electroactive surface area, the 3DW and WN also show enhancement in charge storage capacity (i.e., specific capacitance).

| **Material code** | **Electroactive surface area ($cm^2$)** | **BET surface area ($m^2g^{-1}$)** |
|---|---|---|
| 3DW | 0.87 | 8.3 |
| WN | 0.32 | 7.3 |
| WP | 0.11 | 4.0 |
| 2DW | 0.07 | 1.8 |

**Table 3.2:** Summary of the electroactive and BET surface area for the different $WO_{3-x}$ nanostructures.

The values of specific capacitance for synthesized nanostructures were calculated from cyclic voltammograms as well as galvanostatic charge-discharge analysis using the formulas described in section 2.4.1. The values of specific capacitance at various scanning rates have been tabulated in table 3.3. The highest specific capacitance of 310.8 $Fg^{-1}$ was observed for 3DW, followed by WN (270.3 F $g^{-1}$), while WP and 2DW gave lower values of 84.3 and 39.2 F $g^{-1}$. The lower values of $D_o$, electroactive area, and specific capacitance as observed in the case of 2DW could well be due to the sintering effect of particles resulting in decreased surface area, in good agreement with the SEM and BET $N_2$ adsorption-desorption studies.

| Scan rate (mV s$^{-1}$) | Specific capacitance (F g$^{-1}$) (Error bar ± 2%) | | | | | | | |
|---|---|---|---|---|---|---|---|---|
| | 3DW | | WN | | WP | | 2DW | |
| | 3 Elec. | 2 Elec. | 3 Elec. | 2 Elec. | 3 Elec. | 2 Elec. | 3 Elec. | 2 Elec. |
| 5 | 310.8 | 163.4 | 270.3 | 142.3 | 84.3 | 78.3 | 39.2 | 31.2 |
| 10 | 296.4 | 129.2 | 256.2 | 128.8 | 79.7 | 61.5 | 30.9 | 25.6 |
| 20 | 175.2 | 105.3 | 162.3 | 102.5 | 61.1 | 53.6 | 21.5 | 18.3 |
| 50 | 152.9 | 92.8 | 132.5 | 82.6 | 52.6 | 42.8 | 17.3 | 14.2 |
| 100 | 120.6 | 81.1 | 105.9 | 72.2 | 40.3 | 32.6 | 12.8 | 6.5 |

**Table 3.3:** Summary of specific capacitance values calculated from CV curves obtained for the different $WO_{3-x}$ nanostructures.

Furthermore, these observations were confirmed by performing galvanostatic charge-discharge analysis at various current densities from 2 to 10 A g$^{-1}$. A typical overlay of the charge-discharge curve recorded at a current density of 2 A g$^{-1}$ is shown in figure 3.11 B. Specific capacitance calculated from the charge-discharge curve at various current densities (refer figure SF5 in Annexure-I) and their values are tabulated in table 3.4. The values for specific capacitance at the current density of 2 A g$^{-1}$ are observed to be 240.4 F g$^{-1}$, 210.9 F g$^{-1}$, 64.6 F g$^{-1}$, and 28.1 F g$^{-1}$ for 3DW, WN, WP, and 2DW, respectively. In order to better understand the observed order of specific capacitance, electrochemical impedance measurements at open circuit potential values within the frequency region of 1 mHz to 1 MHz were recorded and are presented in figure 3.11 C. The Nyquist plots comprised of two regions wherein a linear dependence was observed in the low-frequency region, which can be attributed to the solution resistance (Rs), whereas a semicircle was observed in the high-frequency region, which could be ascribed to the charge transfer resistance.[22] A representative circuit diagram which best describes the system is presented as an inset in figure 3.11 C. The circuit diagram comprises of a charge transfer resistor ($R_{CT}$) that is connected with a capacitor and a Warburg resistor (W) in parallel and solution resistor ($R_S$) in series. The solution resistance values of 12.1, 18.3, 23.2, and 26.6 Ω were observed for

3DW, WN, WP, and 2DW, respectively, indicating greater conductivity of nanostructured $WO_{3-x}$ along with easy access to the electrolytic phase which can be correlated to the presence of oxygen vacancies in the materials.[23]

| Current density (A $g^{-1}$) | Specific capacitance (F $g^{-1}$) (Error bar ± 2%) | | | | | | | |
|---|---|---|---|---|---|---|---|---|
| | 3DW | | WN | | WP | | 2DW | |
| | 3 Elec. | 2 Elec. | 3 Elec. | 2 Elec. | 3 Elec. | 2 Elec. | 3 Elec. | 2 Elec. |
| 2 | 240.4 | 138.2 | 210.9 | 125.5 | 64.6 | 51.6 | 28.1 | 56.2 |
| 4 | 202.9 | 103.7 | 191.3 | 96.3 | 52.7 | 39.2 | 21.1 | 40.6 |
| 6 | 170.3 | 79.2 | 162.7 | 62.9 | 41.3 | 30.3 | 15.3 | 32.7 |
| 8 | 149.5 | 56.3 | 138.3 | 51.1 | 29.6 | 25.1 | 9.4 | 23.4 |
| 10 | 127.6 | 42.9 | 117.2 | 33.8 | 19.3 | 15.2 | 6.5 | 16.3 |

**Table 3.4:** Summary of specific capacitance values calculated from GCD curves obtained for the different $WO_{3-x}$ nanostructures.

Electrode stability is also an important parameter for evaluating the performance of a charge storage electrode materials.[24] We observed that the morphology of the electrode material had an impact on its stability. The stability of the modified electrodes were investigated by performing continuous galvanostatic charge-discharge measurements at a constant current density of 8 A $g^{-1}$. 3DW and WN demonstrated excellent stability with capacitance retention of 89.2 % (133.3 F $g^{-1}$) and 85.5 % (118.2 F $g^{-1}$), respectively. Whereas WP and 2DW demonstrated relatively lower capacitance retention of 70.2 % (20.7 F $g^{-1}$) and 49.1 % (4.6 F $g^{-1}$), respectively, after over 12,000 continuous GCD cycles, compared to their initial specific capacitance as reported in table 3.4. The excellent stability demonstrated by 3DW and WN indicate their potential for device scale applications and have been evaluated for the same in the next section 3.3.2.

### 3.3.2 Electrochemical performance of the $WO_{3-x}$//AC asymmetric supercapacitor device

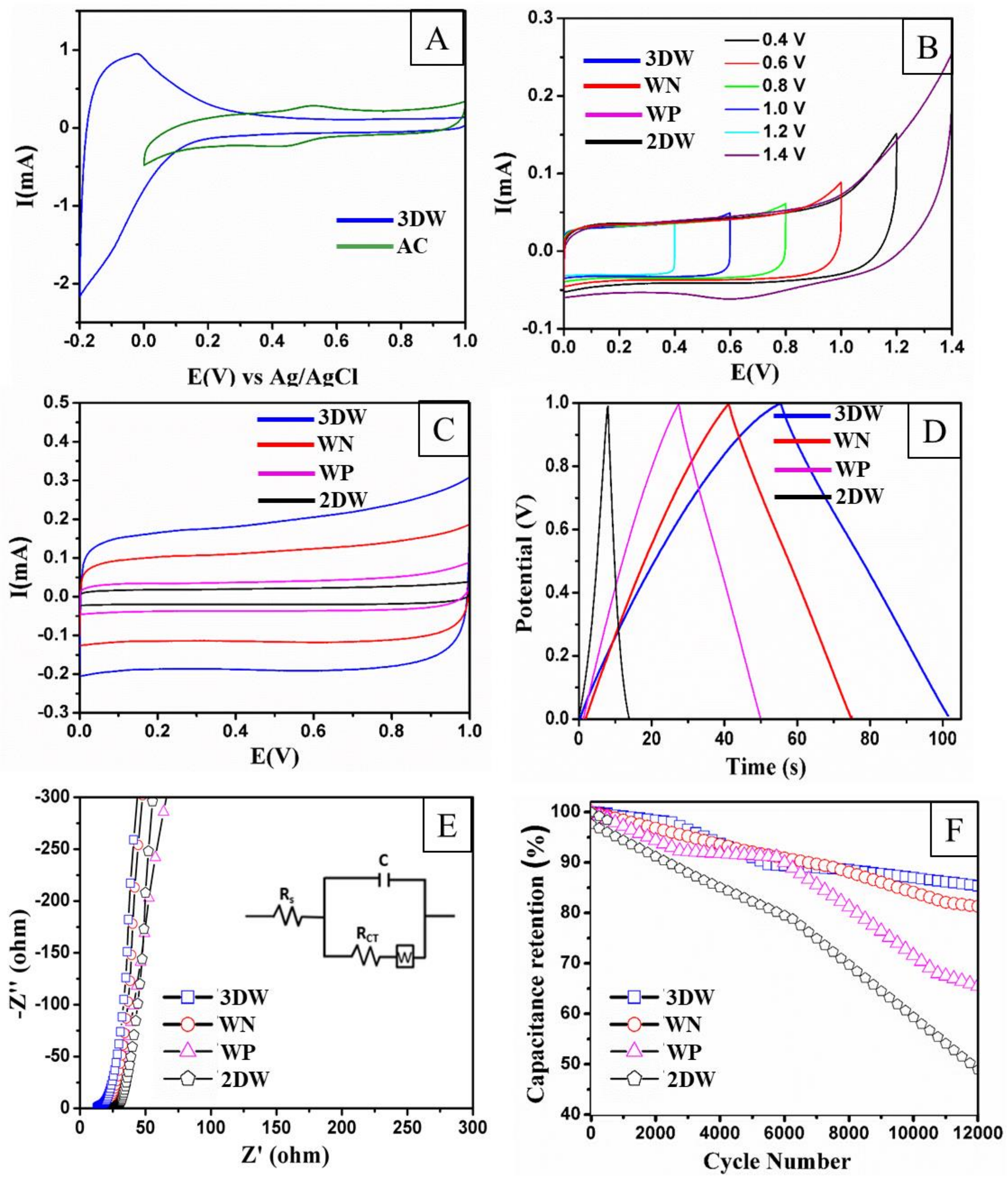

**Figure 3.12:** (A) CV curves of 3DW and AC recorded at a scan rate of 10 mV $s^{-1}$, (B) CV curves of 3DW//AC at variable voltage windows, (C) overlay of CV curves recorded at a scan rate of 5 mV $s^{-1}$, (D) overlay of GCD analysis recorded at the current density of 2 A $g^{-1}$, (E) overlays of Nyquist plots in the frequency range of 1 mHz to 1 MHz ,and (F) overlays of cycling stability performance measured in a two-electrode asymmetric setup evaluated at 8 A $g^{-1}$.

To evaluate the practical applicability of the synthesized $WO_{3-x}$ nanostructures, an asymmetric supercapacitor device was assembled using $WO_{3-x}$ nanostructures fabricated onto carbon paper as the anode and activated carbon (AC) fabricated onto another carbon paper as a cathode using the methodology described in section 2.3.2.1. Figure 3.12 A shows the CV curves of 3DW and AC electrodes at a fixed scan rate of 5 mV $s^{-1}$, from which it was observed that the faradaic pseudocapacitance of 3DW was almost double than the double-layer capacitance of the AC fabricated electrode. The material loading onto the $WO_{3-x}$ coated electrode was modified accordingly. The voltage window of the asymmetric supercapacitor device was also extended effectively while avoiding excess polarization, as shown in figure 3.12 B, and was evaluated from 0.4 to 1.4 V. The testing of the asymmetric supercapacitor device was performed at the optimum voltage window of 1.0 V. An overlay of the cyclic voltammograms at a fixed scan rate of 5 mV $s^{-1}$ and galvanostatic charge-discharge studies at a constant current density of 2 A $g^{-1}$ has been shown in figure 3.12 C and D respectively, which indicates both greater voltammogram area and longer discharge time for 3DW and WN electrodes in comparison to WP and 2DW. Scan rate dependent CV and current density-dependent GCD studies were also performed (see figures SF6 and SF7 in Annexure-I), and the specific capacitance thus obtained has been tabulated in tables 3.3 and 3.4 (Equations 2.4and 2.5).

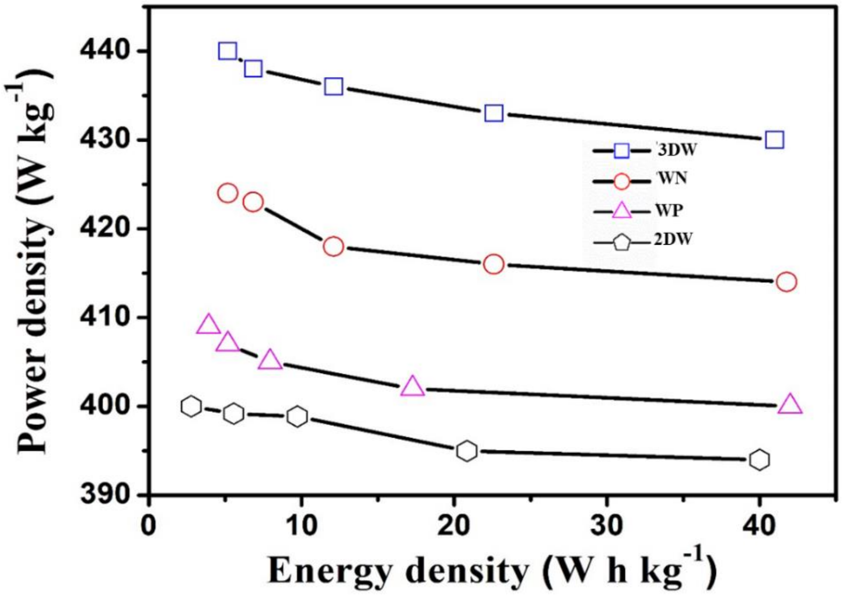

**Figure 3.13:** Ragone plot demonstrating the device performance of $WO_{3-x}$ nanostructures.

The highest specific capacitance of 163.4 F $g^{-1}$ at a scan rate of 5 mV $s^{-1}$ and 138.2 F $g^{-1}$ at a current density of 2 A $g^{-1}$ was demonstrated by 3DW. The observed results of specific capacitance measurements were in line with the results of three-electrode studies. A representative circuit diagram which best describes the system is presented as an inset in figure 3.12 E. The circuit diagram comprises of a charge transfer resistor ($R_{CT}$) that is connected with a capacitor and a Warburg resistor (W) in parallel and solution resistor ($R_S$) in series. The EIS studies showed the Rs values of 3.2, 8.5, 10.1, and 12.3 Ω by 3DW, WN, WP, and 2DW, respectively. Additionally, exceptional cycling stability was also observed for the 3DW and WN when testing over 12000 continuous charge-discharge cycles. Capacitance retention of 90.1 (50.7 F $g^{-1}$), 88.4 (45.1 F $g^{-1}$), 79.2 (19.8 F $g^{-1}$), and 58.4 % (13.6 F $g^{-1}$) were observed for 3DW, WN, WP, and 2DW electrodes, compared to their initial specific capacitance as reported in table 3.4.

As power density and energy density are the most important parameters of supercapacitors, figure 3.13 displays the Ragone plot of the assembled asymmetric supercapacitors. (Equation 2.6 and 2.7). The highest power density of 437.3 W $kg^{-1}$ and energy density of 11.6 W h $kg^{-1}$ were demonstrated by the 3DW, followed by the performance of WN, which displayed a power density of 418.2 W $kg^{-1}$ and energy density of 11.8 W h $kg^{-1}$. In contrast, the WP, due to the only particle like morphology and 2DW due to heavy sintering, demonstrated the least performance. The exceptional capacitance performance and high electrochemical stability of the $WO_{3-x}$ nanostructures can be considered as a cumulative outcome of the presence of a greater number of oxygen vacancies accompanied by surface redox states and nanostructured features which facilitate the diffusion of $H^+$ ions through the $WO_{3-x}$ matrix.

## 3.4 Effect of substituted ureas on growth characteristics of $WO_{3-x}$ nanorods.

Multifunctional organic molecules, which can act as structure-directing motifs and energy-rich fuels in combustion synthesis, play a vital role in tailoring the surface morphologies of a variety of transition metal nanostructures.[25–27] Urea is one such organic compound that can form persistent hydrogen-bonded chains in various environments and has been investigated as an efficient nanostructure-inducing fuel in the present thesis. The characteristic hydrogen bonding feature of urea has made it an attractive candidate for supramolecular chemistry as well.[28] The nature of the substituents on the nitrogen atom in urea has a direct effect on its hydrogen bonding attributes, thus making it a robust and tunable building block.[29]

A wide variety of building blocks can be produced by substitution in urea which can be applied as assembly directing motifs towards the construction of nanostructured materials.[30,31] Urea has a unique feature wherein it can act both as a hydrogen donor through its NH protons as well as an acceptor through the lone pair of the C=O group. Elucidating this mechanism becomes crucial since the good complementarity between the two groups can result in self-association into robust hydrogen-bonded chains, which can be further applied to produce nanostructured materials.[29,32] This property has been explored in the present thesis to produce $WO_{3-x}$ nanostructures described in detail in the previous sections.

In comparison to urea, substituted ureas have been far less explored for the rational design of nanomaterials, despite the fact that they can also form relatively strong hydrogen-bonded motifs. Understanding urea's fundamental chemistry becomes crucial to identify what makes urea a nanostructure growth promoter. In the previous sections, we demonstrated two critical parameters i.e., 1) the mono-protonation of urea at the carbonyl oxygen, which resulted in the formation of an iminium cation ($-C=NH_2^+$) which facilitates the kinetics of one-dimensional growth and 2) the exothermic decomposition of urea could satisfy the thermodynamic requirements for transforming particles of $WO_{3-x}$ into stable solid-state nanostructures.[33] However, urea being a sluggish fuel, there exists a significant scope to improve upon its exothermic decomposition efficiency.

Several research groups have utilized hydrazine as an alternative fuel to urea in combustion synthesis due to its ability to undergo rapid exothermic decomposition.[26,34] However, the lack of an O-protonation center, inability to act as an assembly directing motif, and excessive particle sintering induced by the explosive nature of its exothermic decomposition have severely restricted its use in designing nanostructured materials. On the contrary, NH-substituted ureas such as semicarbazide and carbohydrazide which are traditionally prepared in the laboratory by combining hydrazine and urea, could prove to be the perfect balance of nanostructure directing ability with improved exothermicity and can further promote the growth of $WO_{3-x}$ nanostructures.

On the contrary, if the NH- substitution is replaced by CH- substitution in urea, this could have detrimental effects on its nanostructuring ability to direct the growth of nanorods. More importantly, by altering the degree of NH- substitution in urea, its decomposition pattern in the metal-precursor hybrid gels can be tuned to achieve controlled in situ reduction of $WO_3$ surface to synthesize advanced $WO_{3-x}$ nanostructures. This in turn could have a direct effect on its electrochemical charge-storage characteristics. Therefore, in the present section, we put the above hypothesis to test by utilizing NH- and CH- substituted, O-protonated ureas in a dual role, i.e., to act as a fuel and a cost-effective nanostructure directing motif, for synthesizing 1D $WO_{3-x}$ nanorods. The resulting effect of NH- and CH- substitution on the decomposition pattern of metal precursor, $WO_{3-x}$ nanorod morphology, percentage distribution of redox states, and corresponding influence on the charge-storage performance have also been investigated.

### 3.4.1 SEM studies

Figure 3.14 A-F presents the SEM images of synthesized $WO_{3-x}$ using carbohydrazide, urea, semicarbazide, N-methylurea, and tetramethylurea, and shall be referred to as WC, WN, WSC, WM, and WT respectively and have been synthesized using the methodologies described in section 2.2.7. The SEM images presented in Figure 3.14 provide important insights into the morphological characteristics of the different WO3-x nanostructures synthesized using various carbonyl compounds. Among these, the SEM results clearly show that calcination of tungstic acid gels with carbohydrazide and urea resulted in the formation of fully grown nanorods with diameters in the range of 100-200 nm and lengths of 2-7 µm. Notably, WC demonstrated a more robust growth and homogeneous distribution of nanorods compared to WN. On the other hand, moving in the direction of NH- substitution, the WSC yielded relatively poor nanorod characteristics, as evidenced by the SEM image presented in Figure 3.14 D. Furthermore, from Figures 3.14 E and F, it is observed that CH-substituted ureas such as N-methylurea lead to only partial or incomplete growth of rod-like morphologies, while tetramethylurea largely produced mixed rod-particle aggregates with incompletely formed or deformed rod-like structures visible in the mixture. These observations highlight the crucial role of substituted ureas used in the synthesis process in determining the morphological characteristics of the resulting $WO_{3-x}$ nanostructures.

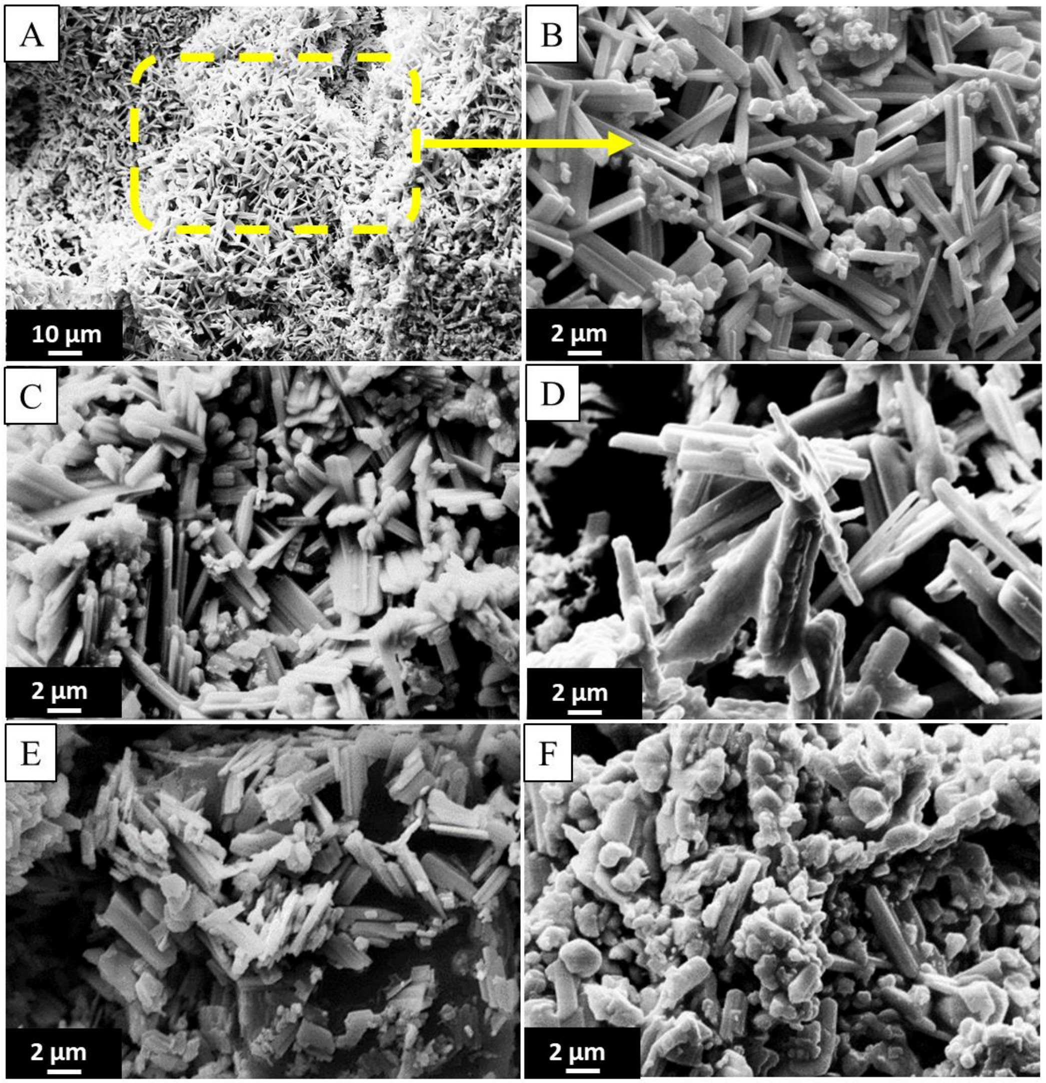

**Figure 3.14:** SEM images of $WO_{3-x}$ synthesized by calcining tungstic acid gels with (A, B) carbohydrazide, (C) urea, (D) semicarbazide (E) N-methylurea, and (F) tetramethylurea.

### 3.4.2 HRTEM studies

To investigate the detailed morphological and structural characteristics, the synthesized $WO_{3-x}$ samples were subjected to HRTEM and SAED analysis. The typical representative results, one containing fully grown nanorods (WC) and the second with a mixture of rod-like and particle agglomerates (WT) are presented in figure 3.15. Figure 3.15 A revealed that the average diameter of nanorods in WC was 115 nm with an average length of 500 nm, measured through TEM analysis which was in good agreement with the results of SEM analysis. The HRTEM images of fully formed nanorod morphologies shown in figure 3.15 B revealed the lattice fringes with a d-spacing of 0.382 nm, which matches with the (002) plane of monoclinic $WO_{3-x}$ in agreement with the literature reports.[35,36] The Selected-Area Electron Diffraction (SAED) pattern (Figure 3.15 C) also reveals the (002) plane, which could be indexed to a monoclinic phase of $WO_3$ (JCPDS No. 43-1035) for WC. However, the incompletely formed rod-like/particle aggregates showed the presence of mixed fringes of both (002) and (020) planes. The particle agglomerates had fringes with a d-spacing of 0.371 nm, which matched with the (020) plane of monoclinic $WO_3$ as reported in the literature.[35,37] The regular intensities of bright spots in the SAED pattern and the monocrystalline surface character were both profound in the case of WC compared to WT.

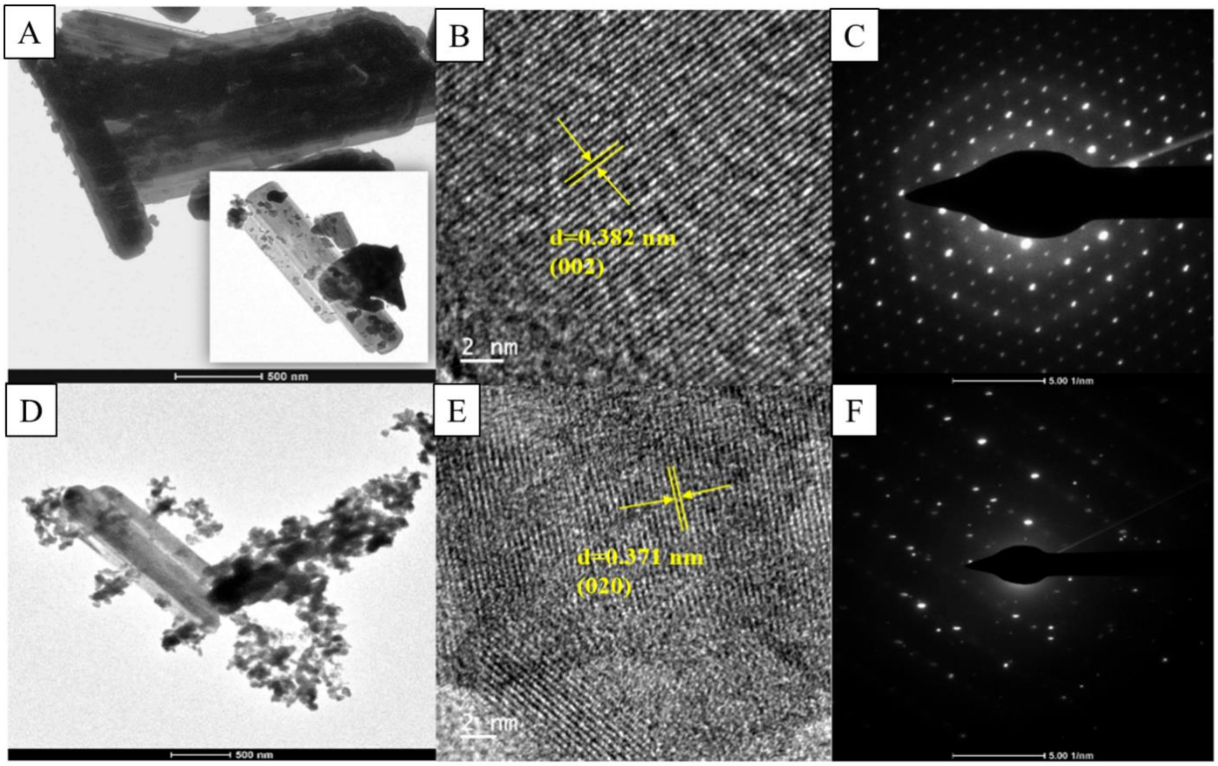

**Figure 3.15:** The TEM, HRTEM, and SAED analysis (A-C) for WC and (D-F) for WT, respectively.

### 3.4.3 XRD studies

Further analysis of the surface crystal structure and growth patterns of different planes in the synthesized $WO_{3-x}$ morphologies were performed using an X-ray powder diffractometer. Figure 3.16 A-E represents the XRD pattern of all the synthesized $WO_{3-x}$ morphologies. All the $WO_{3-x}$ samples indicate the formation of a stable monoclinic phase, with peaks appearing at 2θ values of 22.7, 23.5, 24.2, 26.5, 28.8, 32.8, 33.6, 34.1, 35.2, 41.2, 41.8, 45.1, 47.1, 49.8, 50.1 and 55.4 having miller indices (002), (020), (200), (120), (-112), (022), (-202), (202), (122), (-222), (222), (004), (040), (140), (-114) and (420) respectively (P21/n, JCPDS # 43-1035) and as reported in.[6,8,38] Since, the observed peaks were intense, sharp and of narrow width with no peaks of secondary phases present, it could be concluded that the synthesized $WO_{3-x}$were of high phase purity and crystallinity.

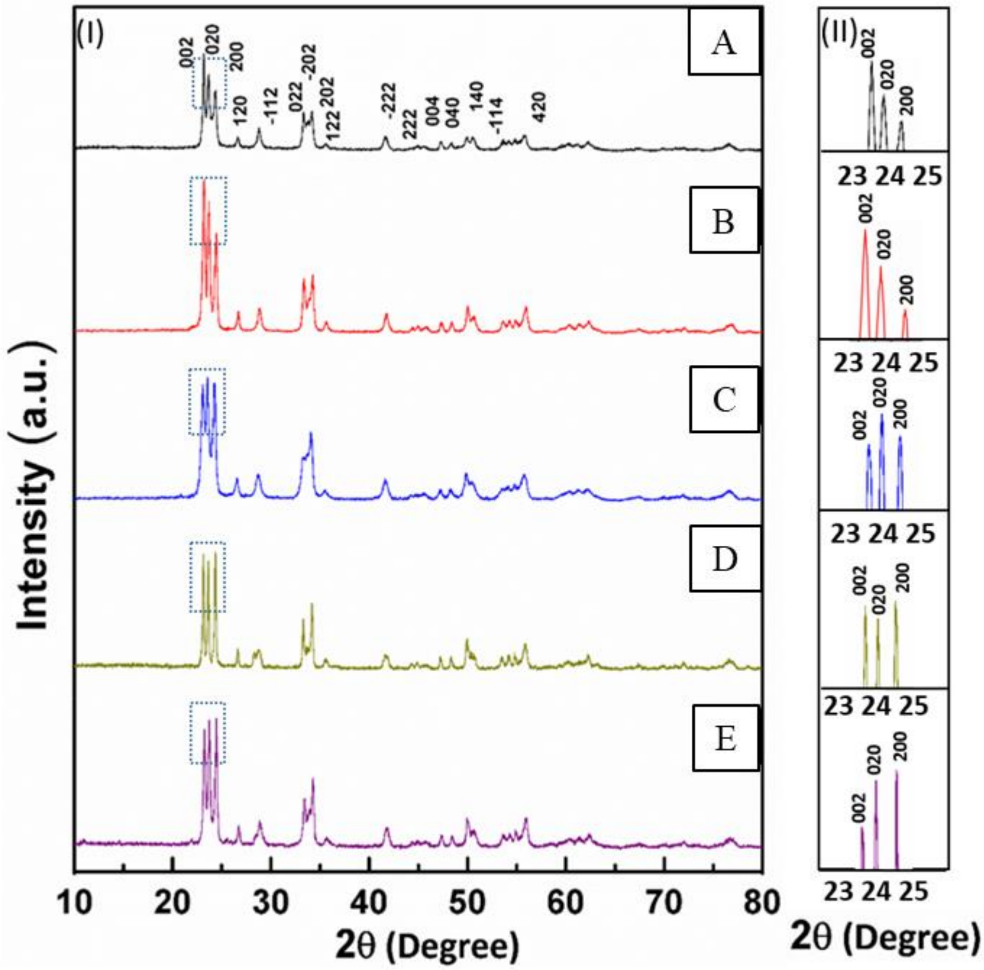

**Figure 3.16:** XRD patterns of (A) WN, (B) WC, (C) WSC, (D) WM, and (WT). (I) overlay of XRD patterns, and (II) is a magnified subset of the rectangular area in (I).

It was interesting to note that the obtained $WO_{3-x}$ morphologies had significant differences in the relative percentage distribution of (002), (200), and (020) facets (shown as a separate subset at R.H.S in figure 3.16). A comparative analysis of the ratio of major peaks with miller indices (002) : (020) : (200) are as follows: WN (1.5 : 1.26 : 1), WC (1.59 : 1.31 : 1), WSC (0.99 : 1.05 : 1), WM (0.95 : 0.92 : 1), and WT (0.92 : 0.99 : 1). It was evident that both urea and carbohydrazide had the highest intensity ratio of (002) plane which was indicative of the fact that, the profound growth of $WO_{3-x}$ nanorods as observed in SEM and TEM, was facilitated by the systematic tailored growth of $WO_{3-x}$ particles along the (002) plane, leading to a highly monocrystalline nanorod surface. On the contrary, XRD pattern of $WO_{3-x}$ obtained using CH- substituted ureas showed a significant decrease in the (002) plane intensity with an increase in the degree of CH- substitution from N-methylurea to tetramethylurea. It was evident that with the increase in the number of bulky methyl groups, the steric effect also increased, which facilitates the growth of $WO_{3-x}$ particles along the (020) and (200) plane instead of (002). These (020) and (200) planes possibly lack in the flexibility for tailored growth into one-dimensional structure, resulting in incompletely formed nanorods or nanoparticle agglomerates. The (002) plane is not only important for building 1D $WO_{3-x}$ nanostructures as observed above but is even more significant in improving the electrochemical charge-storage characteristics of $WO_{3-x,}$ which have been confirmed through charge storage measurements and shall be discussed later in detail in section 3.5.

### 3.4.4 XPS studies

It is possible that structural defects could accompany such a transformation from 0D particles into 1D rods during solid-state crystal growth of $WO_{3-x}$ nanorods. Such defects could also result in induced partial non-stoichiometry in molecular composition leading to the formation of $WO_{3-x}$. To obtain more information on the chemical composition and relative distribution of oxidation states of the synthesized $WO_{3-x}$ nanostructures, X-ray photoelectron spectroscopy (XPS) was employed to analyze representative samples of fully grown nanorods (WC) and mixed rod-particles agglomerates (WT). The XPS spectra (Figure 3.17, A-C) is of WC while that of WT is presented in figure 3.17 D-F. Both $WO_{3-x}$ samples display the characteristic W4f peaks located at 35.53 eV and 37.68 eV, which can be attributed to W $4f_{7/2}$ and W $4f_{5/2}$, respectively, these peaks result from the spin-orbit splitting of $4f_{7/2}$ with $4f_{5/2}$.[9] These two peaks were well separated, and the peak fitting revealed the presence of the majority of bulk tungsten in $W^{6+}$ while ~ 15-20 % in $W^{5+}$ oxidation state, mostly on the surface of the material. The O1s peak was located at 530.36 eV, which could be ascribed to the W-O peak, and a shoulder peak at 532.62 eV was due to the oxygen in water molecules intercalated in the $WO_{3-x}$ crystal structure.[48,50] A minor C1s peak was observed at 284.92 eV due to the presence of adventitious carbon species from the instrument.

Similar peaks were observed in case of WT as shown in figure 3.17 D-F. The energy separations and the peak positions are in good agreement with the NIST XPS database.[39] The percentage composition analysis of $W^{6+}$, $W^{5+,}$ and O1s peaks as presented in Table 3.5. The W4f analysis of XPS spectra reveals that the ratio of $W^{5+}/W^{6+}$ was 0.17 for WC and 0.13 for WT which confirmed that the nanorod surface has a greater magnitude of surface oxygen defects compared to particle agglomerates. Moreover, the relative distribution of the interstitial water was also greater in WC compared to WT. Therefore, the above findings clearly suggested that the NH- substitution in urea enhanced the presence of surface oxygen defects during the growth of nanorod structures, which could serve as active centers that promote the electrochemical charge-storage processes.[40] On the contrary, the inefficiency of CH- substituted ureas in forming nanorod structures, thus resulted in the retention of the agglomerated particle morphologies with relatively lesser oxygen defects.

| **Material** | **Narrow scan** | **Tungsten species** | **XPS area integration (%)** | **Area ratio $W^{5+}$ / $W^{6+}$** |
|---|---|---|---|---|
| WC | W 4f | $W^{6+}$ | 85.66 | 0.17 |
| | | $W^{5+}$ | 14.34 | |
| | O 1s | W-O | 74.55 | |
| | | Intercalated $H_2O$ | 25.45 | |
| WT | W 4f | $W^{6+}$ | 88.47 | 0.13 |
| | | $W^{5+}$ | 11.53 | |
| | O 1s | W-O | 78.88 | |
| | | Intercalated $H_2O$ | 21.01 | |

**Table 3.5:** The percentage of species obtained from the XPS peak area integration of narrow scan spectra of WC and WT.

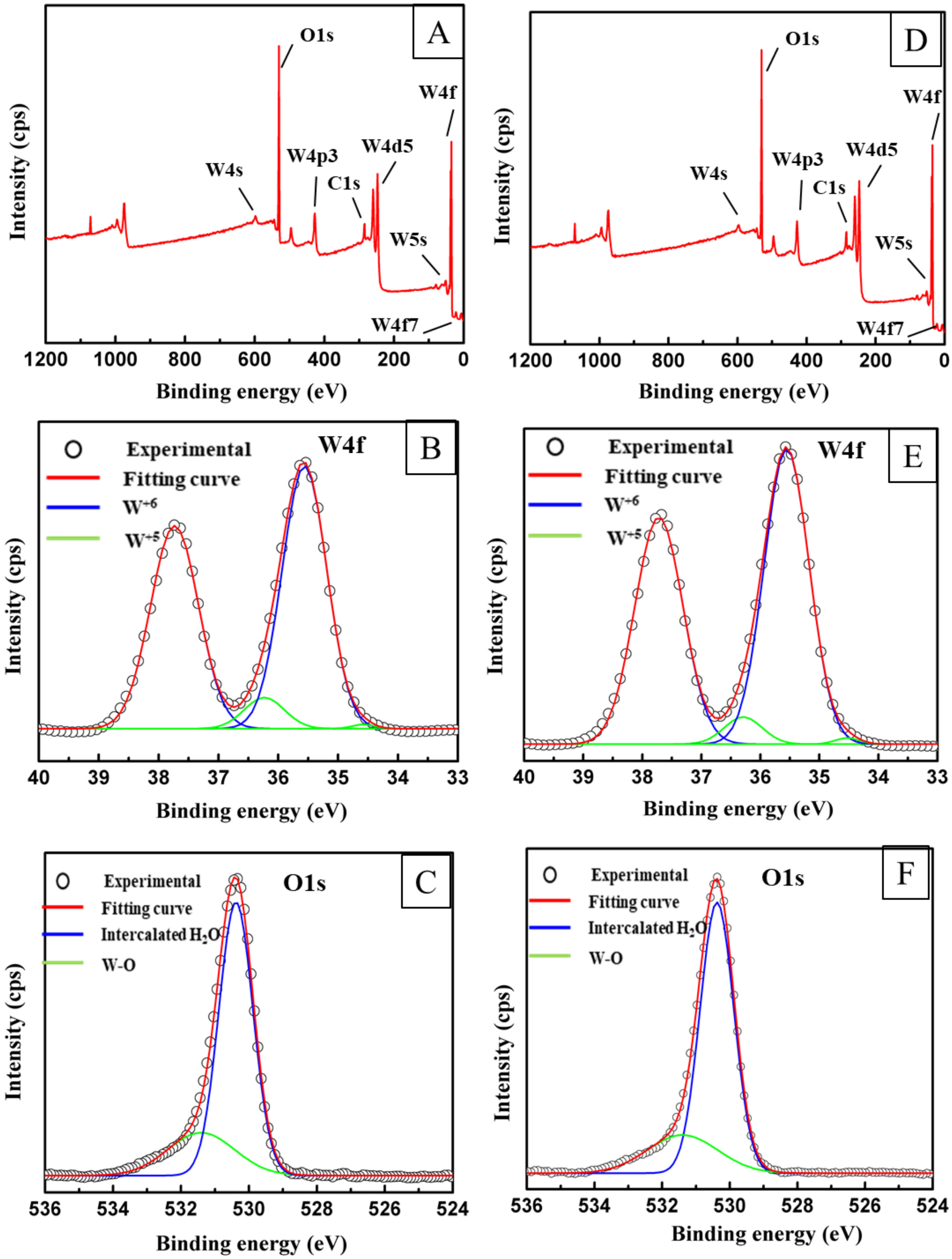

**Figure 3.17:** XPS spectra of (A-C) WC and (D-F) WT.

### 3.4.5 TG-DTA and IR studies

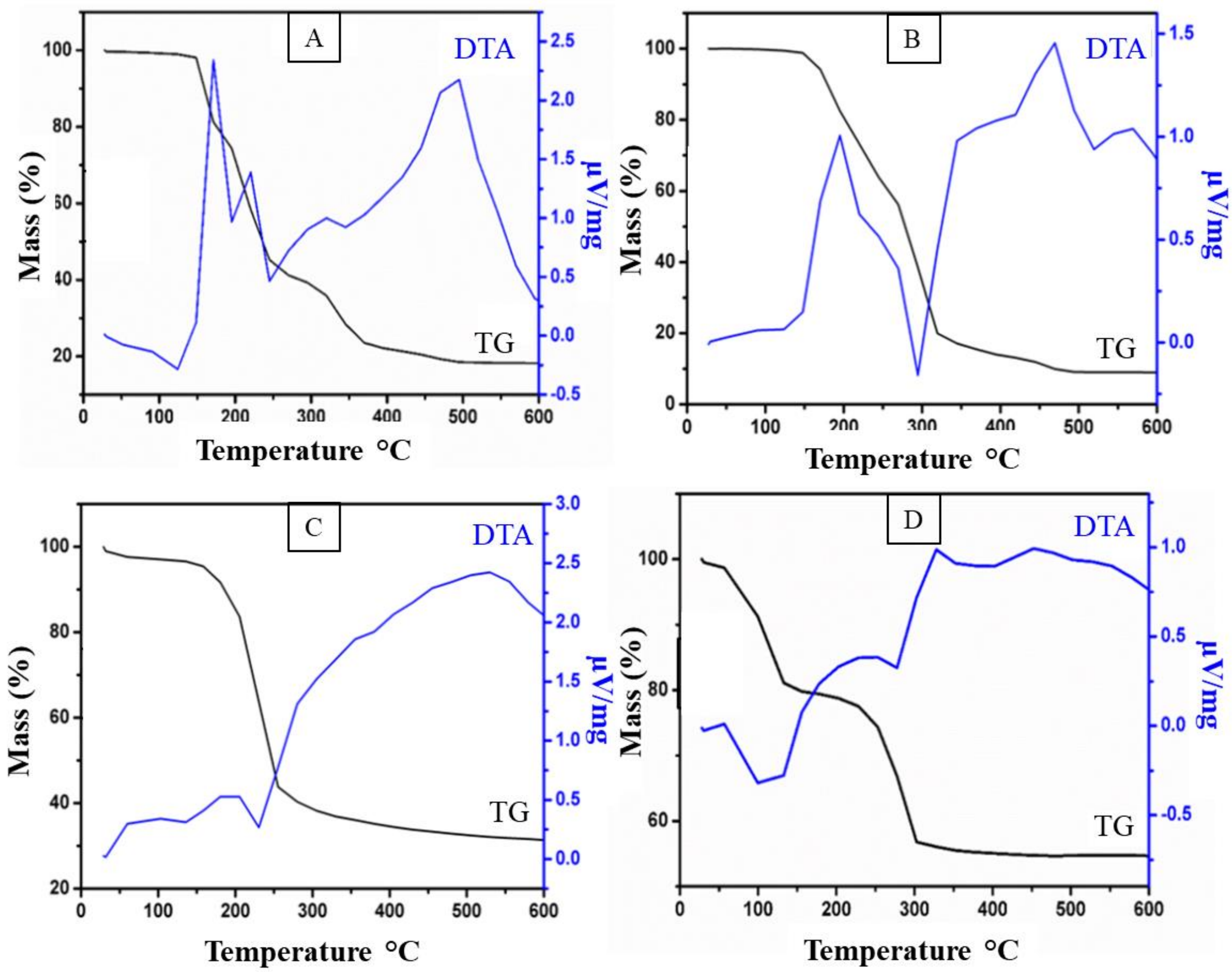

**Figure 3.18:** TG-DTA curve of the as-synthesized mixture of (A) tungstic acid–carbohydrazide, (B) tungstic acid-semicarbazide (C) tungstic acid–N-methylurea and (D) tungstic acid–tetramethylurea hybrid gels.

All the above findings and trends of SEM, HRTEM, XRD, and XPS studies confirm that the type of NH- and CH- substitution in urea significantly alters the growth mechanism of $WO_{3-x}$ nanorods. This alteration in the growth mechanism could arise from the differences in the thermal decomposition processes of CH- and NH- substituted ureas. Therefore, thermogravimetric analysis were performed on the as-synthesized metal precursor -CH/-NH substituted urea-hybrid gels to obtain greater insight into the oxidation process. Figure 3.18 A-D represents the TG-DTA curve of the as-synthesized tungstic acid-substituted urea hybrid gels. The initial weight loss observed below 150 ℃, corresponding to an endothermic peak around 100-110 ℃ in DTA, is attributed to the loss of physically adsorbed water and is common in all the four samples. However, striking differences were observed in the subsequent decomposition rate of hybrid gels based on the type of substitution in urea. For instance, in case of NH- substituted carbohydrazide and semicarbazide modified precursor gels, decomposition started during its melting process i.e.,~159 ℃ for carbohydrazide and ~ 170 ℃ for semicarbazide. Upon further heating, a major weight loss was observed, which could be attributed to the combustion of, at first, the excess uncoordinated carbohydrazide/semicarbazide, followed by the combustion of those molecules coordinated with tungstic acid gel, which required relatively higher temperatures for complete removal.[33] The decomposition of carbohydrazide in particular, is known to facilitate the in situ formation of hydrazine.[41] This step-wise release of in situ generated hydrazine (which is an efficient fuel) and its subsequent exothermic decomposition into $NO_x$ and $CO_2$ would allow controlled release of excess energy for complete and profound crystal growth of $WO_{3-x}$ nanorods. This controlled combustion of in situ generated hydrazine also avoids the unwanted nanoparticle sintering effect observed by several research groups when hydrazine is added ex-situ as a fuel.[26] More importantly, the in situ reducing atmosphere so created could also facilitate partial reduction of the $W^{6+}$ to $W^{5+}$ on the nanorod surface resulting in the formation of $WO_{3-x}$ surface oxide as confirmed by XPS studies. A similar effect can be observed in urea modified precursor gels, with urea decomposition producing $NH_3$ and CO.[19]

On the contrary, the corresponding decomposition patterns of metal precursor gels modified with CH-substituted ureas are relatively rapid and reach a stable weight loss at around 400 ºC compared to 500 ºC in the case of NH-substituted urea-modified precursor gels. Such a rapid decomposition possibly does not provide sufficient kinetic energy for controlled reduction of $W^{6+}$ and complete growth of nanorod structure. Moreover, it induces sintering and agglomeration of nanoparticles as observed in SEM and TEM analysis, thus reducing the number of accessible active redox centers. The FTIR analysis were also performed wherein characteristic peaks due to C-H, C-N, N-H, N-N, C=O, and O-H, stretching frequencies of the corresponding substituted urea modified hybrid gels were observed (refer figure SF 8 in Annexure-I). These peaks get eliminated upon calcination at 550 ºC in air, giving rise to O-

W-O and W=O vibrations at 672 cm$^{-1}$ and 837 cm$^{-1}$ leading to the formation of $WO_{3-x}$ in agreement with XRD and XPS studies.

### 3.4.6 Influence of urea substitution on the growth characteristics of 1D $WO_{3-x}$ nanorods.

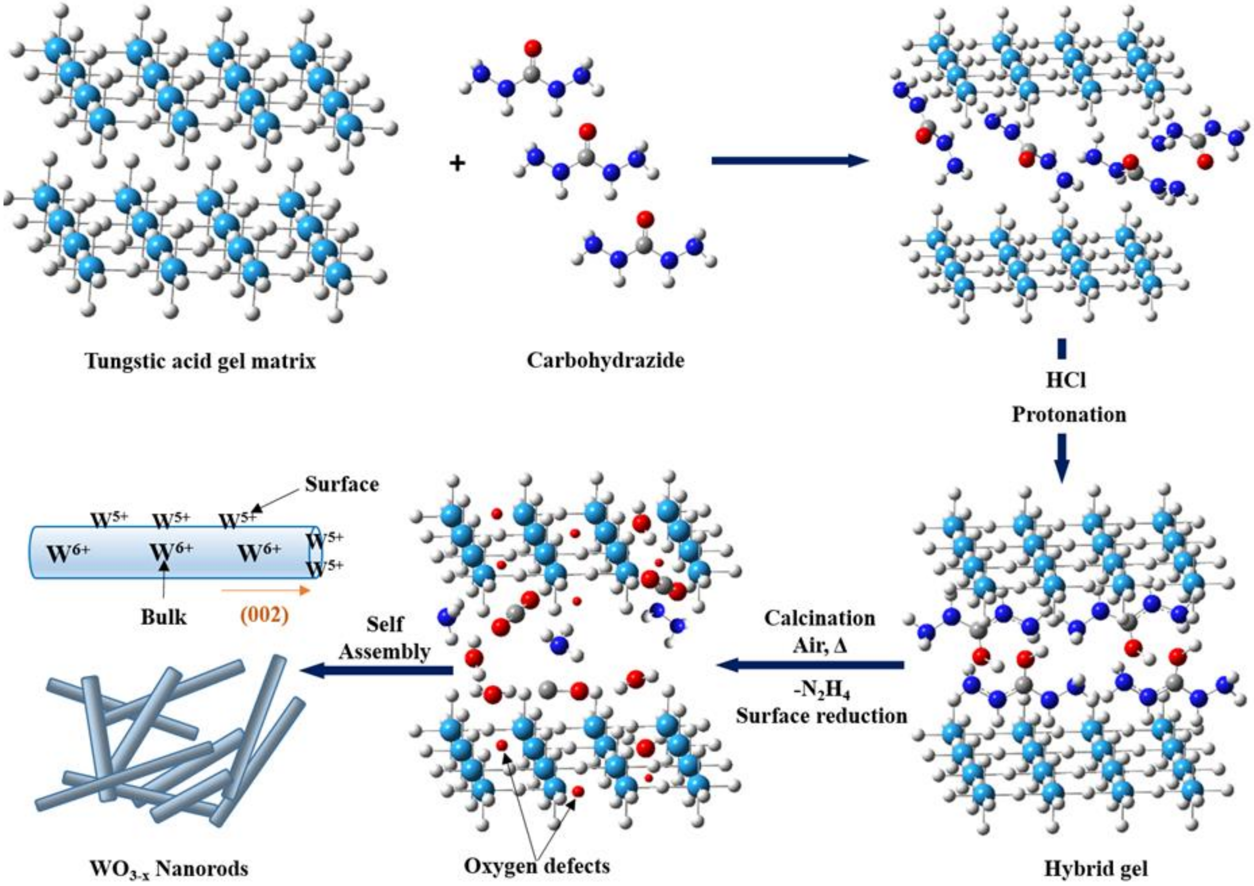

**Figure 3.19:** Schematic illustration of the plausible $WO_{3-x}$ nanorod growth mechanism with in situ induction of partial surface oxygen vacancies during the calcination of tungstic acid-carbohydrazide precursor gels in air at 550 °C.

The detailed growth mechanism of protonated urea-induced transformation of nanoparticles into 1D $WO_{3-x}$ nanorods using the nucleation-growth-assembly route has already been explained in section 3.2.7. As explained earlier, the key factors for the generation of nanorods is the formation of colloidal tungstic acid gel particles and its subsequent interaction with NH-substituted, O-protonated urea. The supersaturation force of the acidic medium acts as the driving force at the nucleation step, forming larger crystals of $WO_3$

nanoparticles.[33] The capping tendency of O-protonated, NH-substituted ureas becomes crucial at this stage as it serves as a structure-directing motif to force one-dimensional growth of $WO_{3-x}$ crystallites.[33] Moreover, the tailoring of nanocrystallites into 1D nanorods requires a greater activation energy along with other kinetic and thermodynamic requirements. The relative differences in the combustion energies of substituted ureas vary in the order carbohydrazide>semicarbohydrazide> urea> N-methylurea> tetramethylurea.[42–45] Therefore, their differential combustion rates as observed in TG-DTA, induces variation in the percentage distribution of (002):(020):(200) surface planes in the nanocrystallites. This possibly results in the variation in the number of nanocrystallites being stitched into 1D nanorods along the preferred (002) plane. The in situ formation of hydrazine in case of NH-substituted ureas, possibly allow controlled release of excess energy to effectively overcome these requirements, which are accompanied by induction of partial surface oxygen vacancies in the lattices during the growth of nanorods.

The extent of $W^{6+}$ partial reduction tendency is in the order of carbohydrazide > semicarbazide > urea > N-methylurea > tetramethylurea which was in good agreement with the XPS results. In a recent study by Tu et al.[10] a series of $WO_{3-x}$ nanorods with surface oxygen vacancies were obtained via thermally treating pre-synthesized nanorods in $H_2$ atmosphere.[10] The chemical reactions leading to the production of $WO_{3-x}$ nanorods in the present work can be described as follows:

$$\mathrm{Na_2WO_4} + \mathrm{2HCl} + \mathrm{nH_2O} \rightarrow \mathrm{H_2WO_4.nH_2O} + \mathrm{2NaCl} \qquad (3.2)$$

$$\mathrm{H_2WO_4.nH_2O} + \mathrm{m(-C=NH_2^+)(iminium\ cation)} \overset{\Delta}{\rightarrow} \mathrm{WO_{3-x}} + \mathrm{mNH_3} + \mathrm{mCO_2} + \mathrm{(n+m)H_2O} \quad (3.3)$$

The second crucial factor to be considered here is the requirement of self-association of one-dimensional hydrogen-bonded chains of the building units, which are the prerequisites for designing one-dimensional nanostructures. In order to form these one-dimensional hydrogen-bonded chains, a good complementarity must be maintained between both the protonated carbonyl oxygen as well as, at the NH groups. The increase in the degree of methylation from N-methylurea to tetramethylurea, therefore, decreases this synergy and is unable to produce $WO_{3-x}$ nanorods. On the contrary, as observed in SEM and TEM studies, carbohydrazide satisfies both the thermodynamic requirements of energy and nucleation growth kinetics for the complete growth of nanorods. The schematic illustration of the above plausible mechanism is presented in figure 3.19. The effect of all the above morphological and chemical changes induced in $WO_{3-x}$ nanostructures due to the CH- and NH- substitution in ureas, on the interfacial processes such as reversible $H^+$ ion intercalation in $WO_{3-x}$ with reference to supercapacitor application, has been further investigated and shall be discussed in the next section 3.5.

## 3.5 Evaluation of the charge storage properties of nanostructured $WO_{3-x}$ synthesized using substituted ureas

### 3.5.1 Three electrode charge storage studies

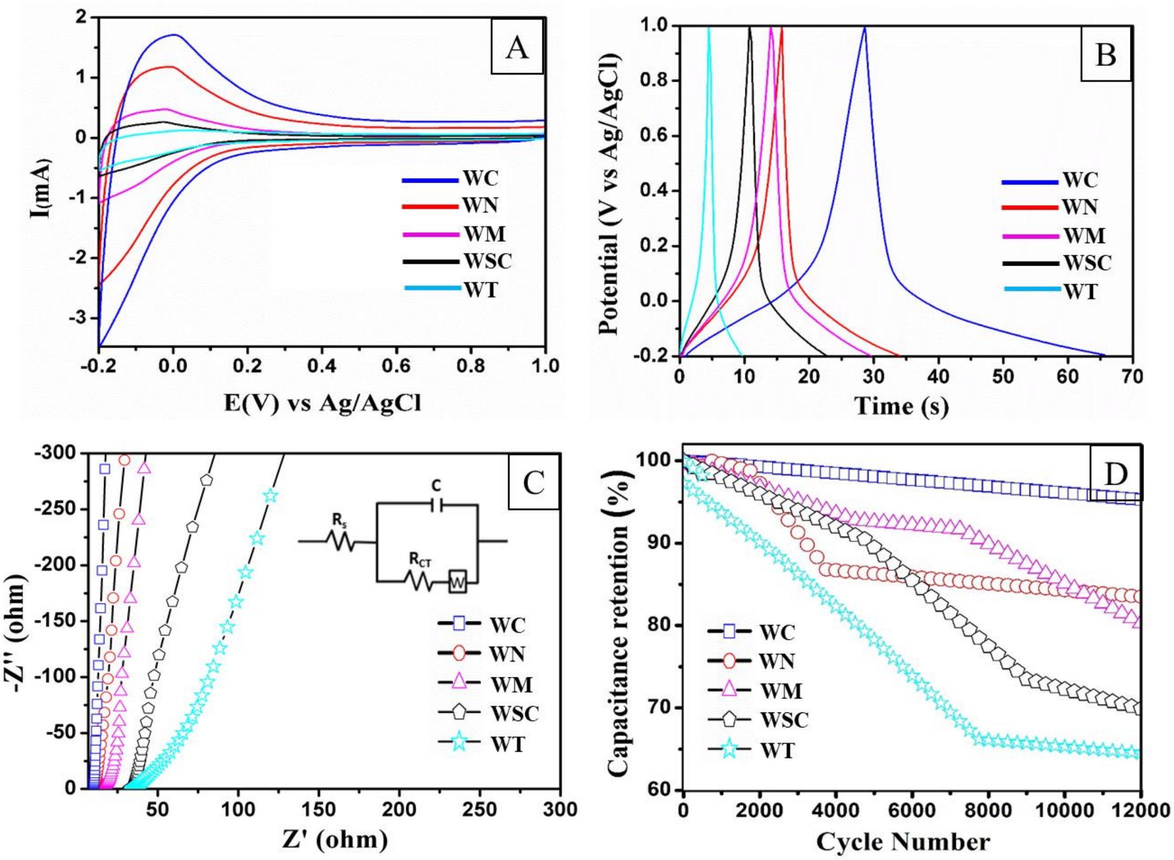

**Figure 3.20:** Supercapacitor performance investigated via (A) CV analysis at a scan rate of 10 mV $s^{-1}$; (B) GCD analysis at the current density of 2 A $g^{-1}$ ; (C) Nyquist plots in thefrequency range of 1 mHz to 1 MHz; and (D) cycling stability performance evaluated at a constant current density of 8 A $g^{-1}$.

The investigation of charge storage properties in order to highlight the merits of NH- and CH- substitution in urea to generate $WO_{3-x}$ architectures was carried out using cyclic voltammetry (CV), galvanostatic charge-discharge (GCD), and electrochemical impedance spectroscopy (EIS) tests. Figure 3.20 A shows an overlay of cyclic voltammograms of $WO_{3-z}$ synthesized using the different substituted ureas at a scan rate of 50 mV $s^{-1}$ in a potential window between -0.2 to 1.0 V (vs. Ag/AgCl) at 28°C ± 1°C. It is observed that the highest area under the voltammograms is shown by the $WO_{3-x}$ nanorods (WC and WP), indicative of their large charge storage characteristics. As observed from our XRD analysis (Figure 3.16 A and B) both WC and WN nanorods have the dominance of (002) plane. The (002) plane of $WO_{3-x}$ has been reported several times as being the reason for improved electro-catalytic activity.[46] Valdés et al., using density functional theory (DFT) calculations, has reported that the photo-oxidation of water on gamma $WO_3$ surfaces requires an overpotential of 1.10 V for (020) and 1.05 V for (002) plane.[47] Xie et al. and Zheng et al. have established the surface energy order in $WO_3$ as (002) (1.56 J $m^{-2}$) > (020) (1.54 J $m^{-2}$) > (200) (1.43 J $m^{-2}$), which indicates that (200) being the most stable and (002) as the least stable and thereby making it the most reactive plane.[48,49] Guo et al. reported that in nanoporous $WO_{3,}$ the preferential orientation of the (002) planes helps in improving electrode kinetics by providing better conditions for the adsorption and redox reaction of pollutants compared to the (020) planes.[50] To understand the improved kinetics associated with the (002) surface dominant $WO_{3-x,}$ the diffusion coefficient ($D_0$) for $H^+$ ions was estimated by performing a scan rate-dependent study of the different $WO_{3-x}$ modified electrodes. (refer figure SF-9 in Annexure I)

Figure SF-9 shows the CVs of the synthesized $WO_{3-x}$ nanorods at scan rates from 25 to 250 mV $s^{-1}$. The oxidation current increases with increasing scan rate. Inset shows the graph of oxidation peak current vs square root of scan rate, which exhibits a linear regression with $R^2$ value of 0.99, which is an indication that there is no surface poisoning of the electrode surface. Furthermore, the diffusion coefficient ($D_0$) for $H^+$ ions were estimated using the Randles-Sevciks method described in section 2.4.4. The calculated $D_0$ value obtained for WC was $5.2 \times 10^{-9}$ $cm^2$ $s^{-1}$ and WN was $4.1 \times 10^{-9}$ $cm^2$ $s^{-1}$, while that of WM was $3.4 \times 10^{-9}$ $cm^2$ $s^{-1}$, WSC was $2.8 \times 10^{-9}$ $cm^2$ $s^{-1}$ and WT was $1.9 \times 10^{-10}$ $cm^2$ $s^{-1}$ which were almost identical within the error limits. It is to be noted here that, the $D_0$ values of fully grown nanorods (WC and WP) are relatively greater compared to partially formed rod-particles agglomerates (WM, WSC, and WT) as listed above. The greater $D_0$ values for WC and WN indicate the ease with which the $H^+$ ions can diffuse in as well as out of the $WO_{3-x}$ matrix. The $D_0$ values are comparable to work of Xiao et al.[66] wherein a value of $1.91 \times 10^{-9}$ $cm^2$ $s^{-1}$ has been reported for porous $WO_3$ electrode and to the work of Ghosh et al.[16] who have reported a value of $2.27 \times 10^{-10}$ $cm^2$ $s^{-1}$ for hexagonal $WO_3$. To understand the reason behind the difference in $D_0$ values between the morphologies, the electroactive areas of the materials were estimated using the method described in section 2.4.3.

WC resulted in the highest electroactive area of 0.45 $cm^2$ followed by WN (0.32 $cm^2$) while WM, WSC had relatively lower electroactive areas of 0.29 $cm^2$, 0.21 $cm^2$ respectively with WT (0.17 $cm^2$) being the lowest electroactive surface. The BET surface area analysis results were in trend with the electroactive area results and were observed to be 7.0, 5.3, 4.0, 3.9, and 3.5 $m^2$ $g^{-1}$ for WC, WN, WM, WSC, and WT respectively. (refer figure SF 10 in Annexure-I) The decrease in the electroactive areas from the nanorods (WC with $W^{5+}/W^{6+}$ = 0.17) to particle agglomerates (WT with $W^{5+}/W^{6+}$ = 0.13) can be understood as a consequence of the reduction in surface oxygen defects and decreased presence of intercalated $H_2O$ as observed from the XPS analysis (Table 3.5).

| **Material code** | **Electroactive surface area ($cm^2$)** | **BET surface area ($m^2g^{-1}$)** |
|---|---|---|
| WC | 0.45 | 7.0 |
| WN | 0.32 | 5.3 |
| WM | 0.29 | 4.0 |
| WSC | 0.21 | 3.9 |
| WT | 0.17 | 3.5 |

**Table 3.6:** Summary of the electroactive and BET surface area for the different $WO_{3-x}$ synthesized using substituted ureas.

The values of specific capacitance for synthesized nanostructures were calculated from cyclic voltammograms as well as galvanostatic charge-discharge analysis using the formulas described in section 2.4.1. A typical overlay of the cyclic voltammograms recorded at a scan rate of 10 mV $s^{-1}$ is shown in figure 3.20 B. The values of specific capacitance at various scanning rates have been tabulated in table 3.7. The highest specific capacitance of 285.4 F $g^{-1}$ was observed for WC, followed by WN (270.3 F $g^{-1}$), while WM, WSC, and WT produced relatively lower values of 196.3, 180.2, and 162.7 F $g^{-1}$.

| Scan rate (mV $s^{-1}$) | Specific capacitance (F $g^{-1}$) (Error bar ± 2%) | | | | | | | |
|---|---|---|---|---|---|---|---|---|
| | WC | | WM | | WSC | | WT | |
| | 3 Elec. | 2 Elec. | 3 Elec. | 2 Elec. | 3 Elec. | 2 Elec. | 3 Elec. | 2 Elec. |
| 5 | 285.4 | 156.8 | 196.3 | 125.2 | 180.2 | 115.3 | 162.7 | 101.2 |
| 10 | 260.7 | 142.3 | 172.7 | 116.2 | 165.8 | 102.6 | 152.9 | 96.7 |
| 20 | 212.5 | 116.2 | 160.3 | 91.6 | 158.2 | 85.9 | 147.3 | 73.9 |
| 50 | 175.6 | 92.0 | 146.8 | 80.1 | 140.1 | 71.8 | 129.5 | 62.2 |
| 100 | 150.2 | 75.3 | 130.9 | 65.3 | 118.3 | 58.4 | 102.3 | 41.6 |

**Table 3.7:** Summary of specific capacitance values calculated from CV curves obtained for $WO_{3-x}$ synthesized using substituted ureas.

Furthermore, these observations were confirmed by performing galvanostatic charge-discharge analysis at various current densities from 2 to 10 A $g^{-1}$ (refer figure SF 11 in Annexure-I). A typical overlay of the charge-discharge curve recorded at a current density of 2 A $g^{-1}$ is shown in figure 3.20 C. Specific capacitance was calculated from charge-discharge curves at various current densities and their values are tabulated in table 3.8. The values for specific capacitance at the current density of 2 A $g^{-1}$ are observed to be 231.3 F $g^{-1}$, 210.9 F $g^{-1}$, 198.3 F $g^{-1}$, 150.2 F $g^{-1}$, and 111.2 F $g^{-1}$ for WC, WN, WM, WSC, and WT respectively. In order to better understand the observed order of specific capacitance, electrochemical impedance measurements at open circuit potential values within the frequency region of 1 mHz to 1 MHz were recorded and are presented in figure 3.20 D. The

Nyquist plots comprised of two regions wherein a linear dependence was observed in the low-frequency region, which can be attributed to the solution resistance (Rs), whereas a semicircle was observed in the high-frequency region, which could be ascribed to the charge transfer resistance.[22] A representative circuit diagram which best describes the system is presented as an inset in figure 3.20 C. The circuit diagram comprises of a charge transfer resistor ($R_{CT}$) that is connected with a capacitor and a Warburg resistor (W) in parallel and solution resistor ($R_S$) in series. The solution resistance values of 6.5, 8.0, 18.1, 25.2, and 30.6 Ω were observed for WC, WN, WM, WSC, and WT, respectively, indicating greater conductivity of $WO_{3-x}$ nanorods along with easy access to the electrolytic phase which can be correlated to the presence of oxygen vacancies in the materials.[23]

| Current density (A $g^{-1}$) | Specific capacitance (F $g^{-1}$) (Error bar ± 2%) | | | | | | | |
|---|---|---|---|---|---|---|---|---|
| | WC | | WM | | WSC | | WT | |
| | 3 Elec. | 2 Elec. | 3 Elec. | 2 Elec. | 3 Elec. | 2 Elec. | 3 Elec. | 2 Elec. |
| 2 | 231.3 | 135.2 | 198.3 | 120.3 | 170.2 | 111.1 | 152.2 | 89.2 |
| 4 | 215.7 | 121.3 | 172.3 | 106.3 | 163.2 | 98.3 | 151..2 | 81.7 |
| 6 | 193.6 | 106.8 | 156.7 | 90.1 | 147.7 | 79.3 | 135.8 | 70.3 |
| 8 | 172.3 | 94.6 | 140.3 | 81.6 | 131.3 | 67.3 | 121.7 | 52.3 |
| 10 | 156.8 | 87.3 | 129.9 | 72.3 | 102..3 | 58.4 | 92.6 | 40.5 |

**Table 3.8:** Summary of specific capacitance values calculated from GCD analysis obtained for $WO_{3-x}$ synthesized using substituted ureas.

Electrode stability is also an important parameter for evaluating the performance of capacitor electrode materials.[24]It was observed that the morphology of the electrode material had an impact on its stability. The stability of the modified electrodes was studied by performing continuous galvanostatic charge-discharge measurements and has been presented in Figure 3.20 D. It was observed that the electrode films prepared from fully grown nanorod morphologies were significantly more stable than those prepared with rod-particle agglomerates. The order of capacitance retention was WC (95.8 %) (169.7 F $g^{-1}$) > WN (84.2 %) (118.2 F $g^{-1}$) > WSC (81.3 %) (114.1 F $g^{-1}$) > WM (104.7 %) (104.7 F $g^{-1}$) > WT (64.3 %) (78.2 F $g^{-1}$), compared to their initial specific capacitance as reported in table 3.8. The excellent stability demonstrated by WC and WM indicated their potential for device scale applications and have been evaluated for the same in the next section 3.5.2.

### 3.5.2 Electrochemical performance of the $WO_{3-x}$//AC asymmetric supercapacitor device

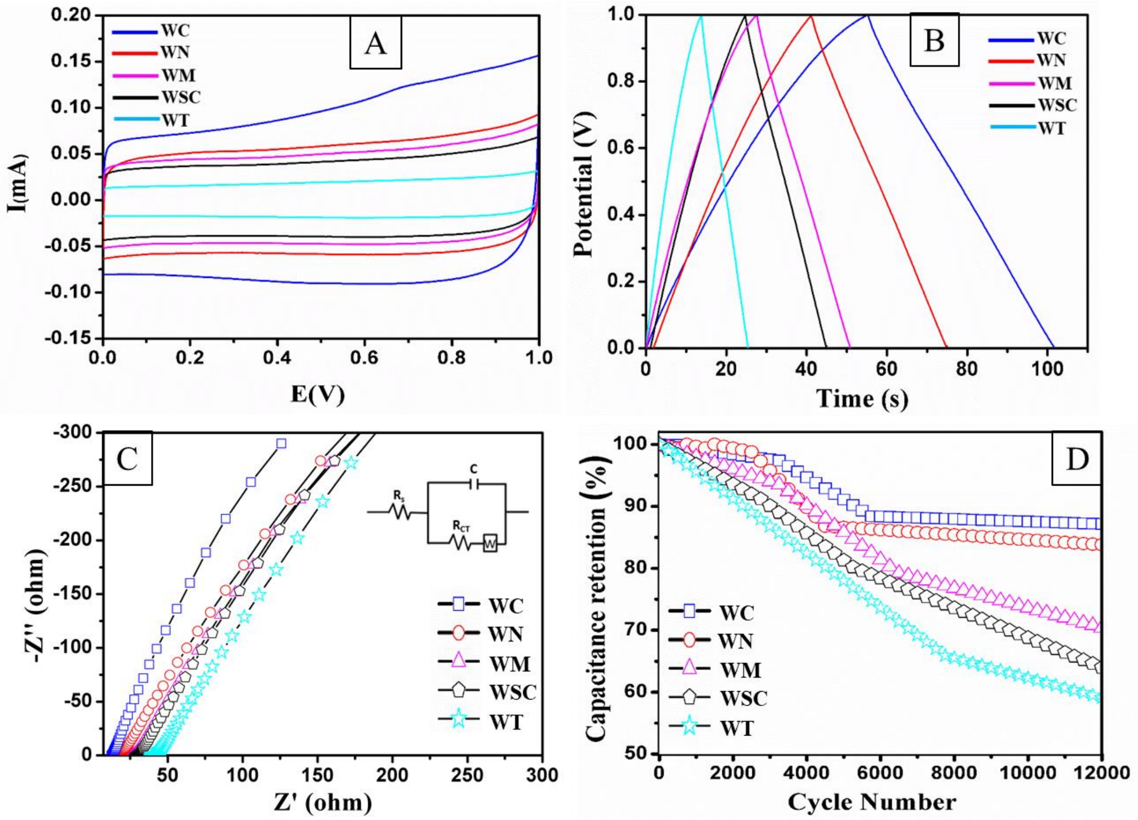

**Figure 3.21:** (A) Overlay of CV curves recorded at a scan rate of 5 mV $s^{-1}$ (B) Overlay of GCD analysis recorded at the current density of 2 A $g^{-1}$ (C) Overlays of Nyquist plots in the frequency range of 1 mHz to 1 MHz and (D) Overlays of cycling stability performance measured in a two-electrode asymmetric setup evaluated at 8 A $g^{-1}$.

To evaluate the influence of substituted urea towards the charge storage characteristics of $WO_{3-x}$ nanostructures and to evaluate their practical applicability, asymmetric supercapacitor devices were assembled using $WO_{3-x}$ nanostructures fabricated onto carbon paper as the anode and activated carbon (AC) fabricated onto another carbon paper as an cathode using the methodology described in section 2.3.2.1. Figure 3.21 A displays an overlay of the cyclic voltammograms at a fixed scan rate of 5 mV $s^{-1}$ and galvanostatic charge-discharge studies at a constant current density of 2 A $g^{-1}$ has been presented as figure 3.21 B. The two figures indicates both greater voltammogram area and longer discharge time for WC and WN electrodes in comparison to WM, WSC and WT. Scan rate dependent CV and current density-dependent GCD studies were also performed (see figures SF12 and SF13 in Annexure-I), and the specific capacitance thus obtained has been tabulated in tables 3.7 and 3.8 (Equations 2.4 and 2.5).

The highest specific capacitance of 156.8 F $g^{-1}$ at a scan rate of 5 mV $s^{-1}$ and 138.2 F $g^{-1}$ at a current density of 2 A $g^{-1}$ was demonstrated by WC. The observed results of specific capacitance measurements were in line with the results of three-electrode studies. The EIS studies showed the Rs values of 12.5, 14.2, 25.1, 28.5, and 39.3 Ω by WC, WN, WM, WSC, and WT, respectively. A representative circuit diagram which best describes the system is presented as an inset in figure 3.21 C. The circuit diagram comprises of a charge transfer resistor ($R_{CT}$) that is connected with a capacitor and a Warburg resistor (W) in parallel and solution resistor ($R_S$) in series. Additionally, exceptional cycling stability was also demonstrated by WC and WN when tested over 12,000 continuous charge-discharge cycles. Capacitance retention of 87.2 (82.4 F $g^{-1}$), 83.9 (45.1 F $g^{-1}$), 70.3 (57.3 F $g^{-1}$), 64.2 (43.2 F $g^{-1}$), and 59.1 (30.9 F $g^{-1}$) % were observed for WC, WN, WM, WSC, and WT electrodes, compared to their initial specific capacitance as reported in table 3.8.

Power density and energy density are the most significant parameters of any supercapacitor device. The Ragone plot displaying the performance of the assembled asymmetric supercapacitors has been presented as figure 3.22 (Equations 2.6 and 2.7). The highest power density of 436.2 W $kg^{-1}$ and energy density of 11.4 W h $kg^{-1}$ were demonstrated by WC, followed by the performance of WN, which displayed a power density of 418.2 W $kg^{-1}$ and energy density of 11.8 W h $kg^{-1}$. In contrast, the WM, WSC, and WT, due to poor morphological features, demonstrated the least performance. The exceptional capacitance performance and high electrochemical stability of the $WO_{3-x}$ nanostructures can be considered as a cumulative outcome of the presence of a greater number of oxygen vacancies accompanied by surface redox states and nanostructured features which facilitate the diffusion of $H^+$ ions through the $WO_{3-x}$ matrix. The overall results thus indicate the remarkable performance of nano and microstructured $WO_{3-x}$. However, they can still be improved further if assembled into even higher dimensional microstructures. This motivation has led to the synthesis of $WO_{3-x}$/C microfibers, which are presented in the next section 3.6.

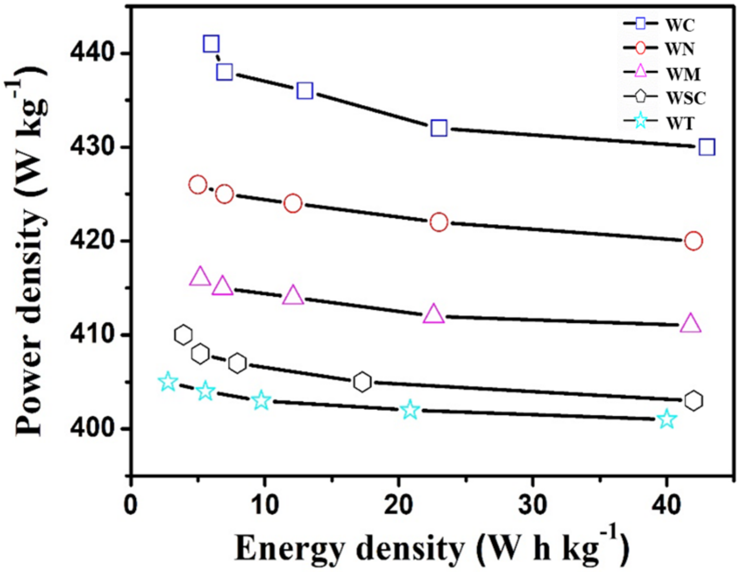

**Figure 3.22:** Ragone plot demonstrating the device performance of $WO_{3-x}$ nanostructures.

## 3.6 Designing 3D $WO_{3-x}$/C microfibers using citric acid

3D fibrous nanostructures have immense potential applications in the field of bioengineering, energy harvesting, optical diagnostics, drug delivery etc.[51–53] The revolutionary discovery of double helical DNA (deoxyribonucleic acid) structure in 1953, led to the fundamental understanding that helical structures impart special properties such as, enhanced stability, cellular replication, signal processing, catalysis, etc.[53–55] The fibrous structure is, therefore, of paramount importance to unravel the mystery about the origin of life itself.[56] The curiosity and fascination towards this unique architecture has led material chemists worldwide to synthesize fibrous structures using organic and inorganic molecules and gain insight into nature’s construction rules, study material properties, and its utilization in potential applications.

Tuning the nanomaterial design into fibrous structures is extremely difficult as the nanoparticles are too small for lithographic fabrication and too big for molecular synthesis.

Recently, Suzuki *et al.*[57] utilized L/D-cysteine moieties functionalized to the edges of graphene quantum dots (GQDs), causing single helical buckling at the "crowded" edges of GQDs. Hou *et al.*[58] designed helical fibers via co-pyrolysis of $Fe(CO)_5$ and toluene/pyridine mixture as carbon source. Micro-ribbons of ZnO have been reported via the solid-vapor phase deposition method by Wang *et al.*.[59] Wu *et al.*[60] reported the synthesis of double helical silica fibers using tetraethyl orthosilicate (TEOS), sodium dodecyl sulfate as a chiral surfactant, and N-trimethoxysilylpropyl-N,N,N-trimethylammonium chloride as the co-structure-directing agent. Jung *et al.*[61] utilized a predesigned helical template, *p*-dodecanoyl-aminophenyl-β-D-glucopyranoside, to functionalize TEOS to produce $SiO_2$ microfibers. Sharma *et al.*[62] performed Au functionalization of DNA itself to produce double helical gold nanostructures. Although these methods produce fibrous structures, the use of expensive templates and post-separation complexities limit their large-scale production. Therefore, a great deal of further research is required to develop simple and scalable methods for preparing double helical structures of semiconductor oxides, especially with reference to their utilization in energy and environmental applications.

Therefore, this section presents a facile citric acid-assisted synthetic route for producing $WO_{3-x}/C$ microfibers. The design strategy utilizes citric acid-tungstic acid hybrid gel precursor, controlled pH, and calcination treatment in order to generate $WO_{3-x}$ nanorod in a similar manner as described in previous sections. Furthermore, their in situ carbon fiber encapsulation into a core-shell structure and subsequent self-assembly into a microfibers-like structure is presented and further evaluated for its charge-storage performance.

### 3.6.1 SEM studies

Figure 3.23 A-E presents the temperature-dependent morphological transformation and growth of $WO_{3-x}/C$ microfibers (hereafter referred to as WF) from 250°C to 550°C. Calcination of tungstic acid-citric acid hybrid gel initiates the formation of a tripodal-shaped intermediate structure (refer figure 3.23, A-C), which transforms into WF at 450°C (refer figure 3.23, (D,E)). The EDX elemental mapping of D confirmed the homogeneous surface distribution of W, O with carbon encapsulation of rod-like morphologies (refer figure 3.23, F-H). Further increase in temperature > 550 °C, resulted in collapse of the microfiber-like structure due to the removal of carbon fibers, leaving behind a randomly oriented hierarchical assembly made of $WO_{3-x}$ nanorods separated by hollow cavities (refer figure 3.23 E), henceforth labeled as WH.

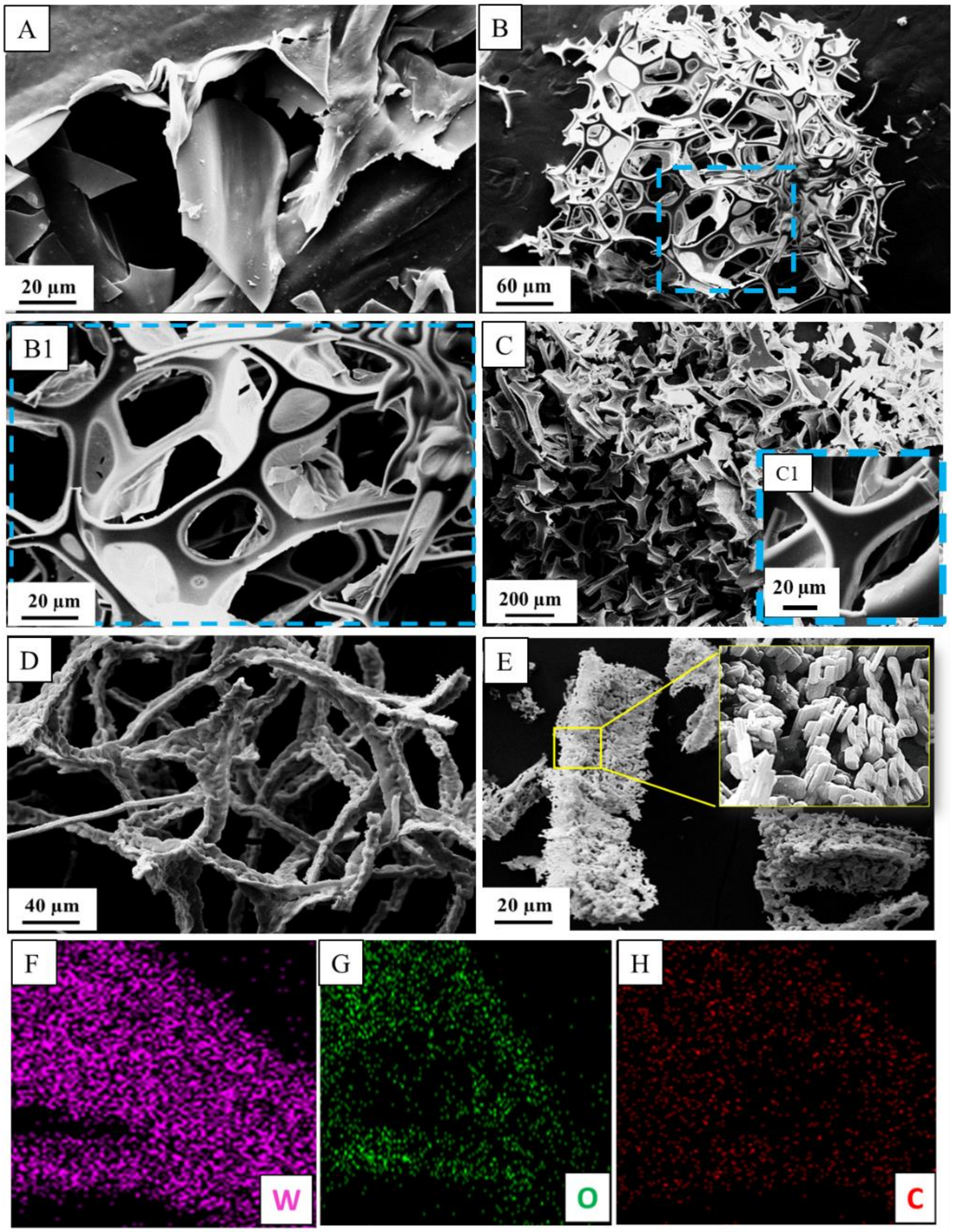

**Figure 3.23:** (A-E) SEM micrograph of temperature-dependent morphological transformation of tungstic acid-citric acid hybrid gel (A) 250 °C, (B) 300 °C, (B1) Inset of B (C) 350 °C, (C1) Inset of C, (D) 450 °C and (E) 550°C. (F-H) Elemental mapping of D.

### 3.6.2 HRTEM studies

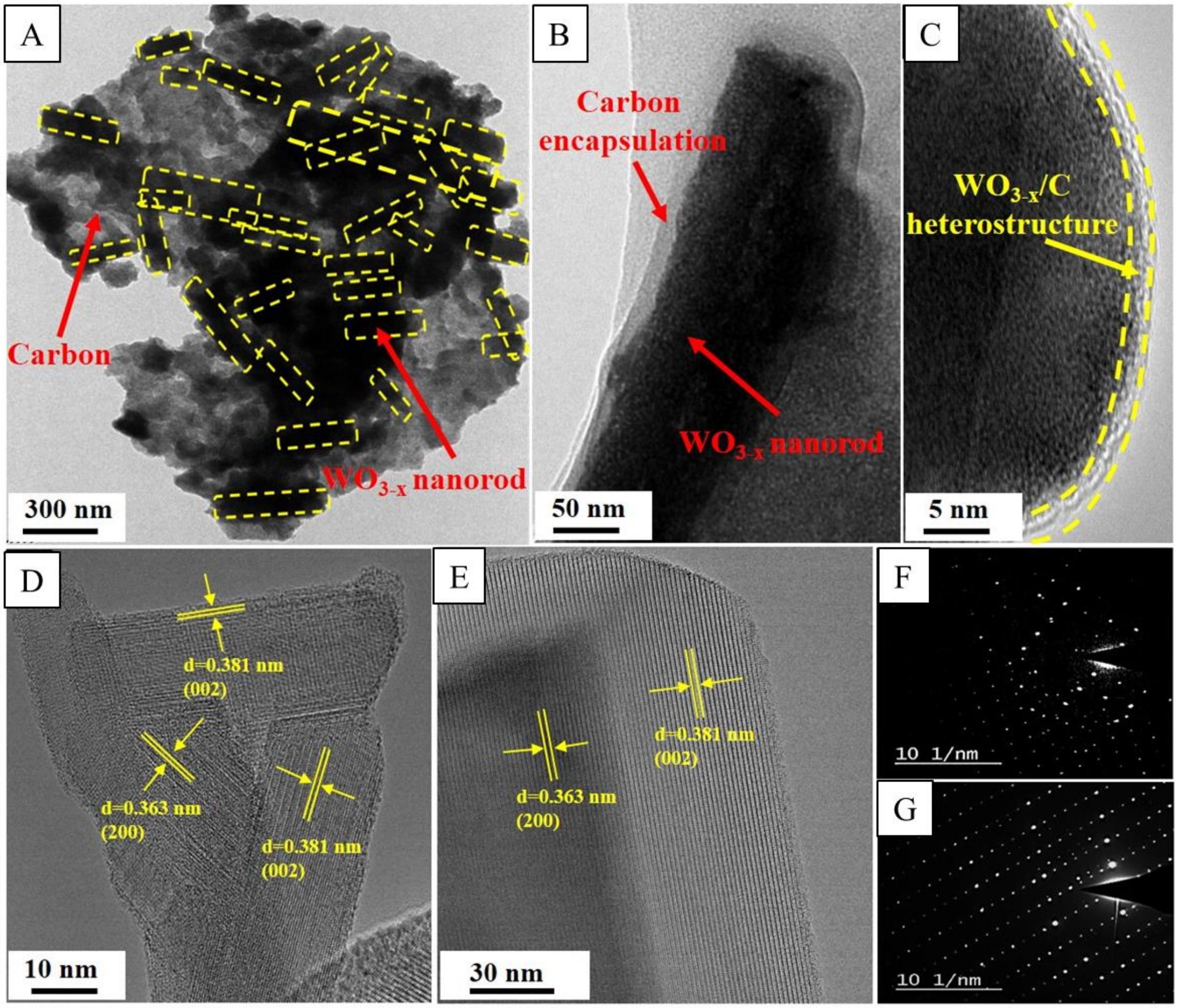

**Figure 3.24:** (A-D and F) represent the HRTEM and SAED analysis of WF, and (E and G) represent the HRTEM and SAED analysis of WH, respectively.

The HRTEM and SAED analysis (refer figure 3.24) of WF and WH revealed that the WF consisted of a random arrangement of a number of carbon encapsulated $WO_{3-x}$ nanorods. These $WO_{3-x}$ rods were held together by a double helical arrangement, which grows along the three directions in close contact with each other, within the initially formed tripodal geometry. Two types of carbon encapsulated $WO_{3-x}$ nanorods are observed (refer figure 3.24 A and B). The bigger microrods of size < 200 nm in diameter comprises the fibrous chains while relatively smaller nanorods of size < 50 nm which get randomly trapped in between the adjacent fibrous chains, somewhat mimicking a DNA-like structure. The carbon fiber encapsulation of $WO_{3-x}$ nanorods was confirmed using HRTEM analysis, as depicted in figure 3.24 A and B. The calculated lattice fringe spacing of ~0.381 nm and ~0.363 nm matched with the (002) and (200) planes of monoclinic $WO_{3-x}$.[35,36] WH consisted of relatively bigger nanorods (refer figure 3.24 E). The SAED pattern (refer figure 3.24 F and G), displayed bright spots due to monocrystalline surface character, both of which were more profound in WF compared to WH due to the removal of excess surface carbon.

### 3.6.3 TG-DTA and elemental studies

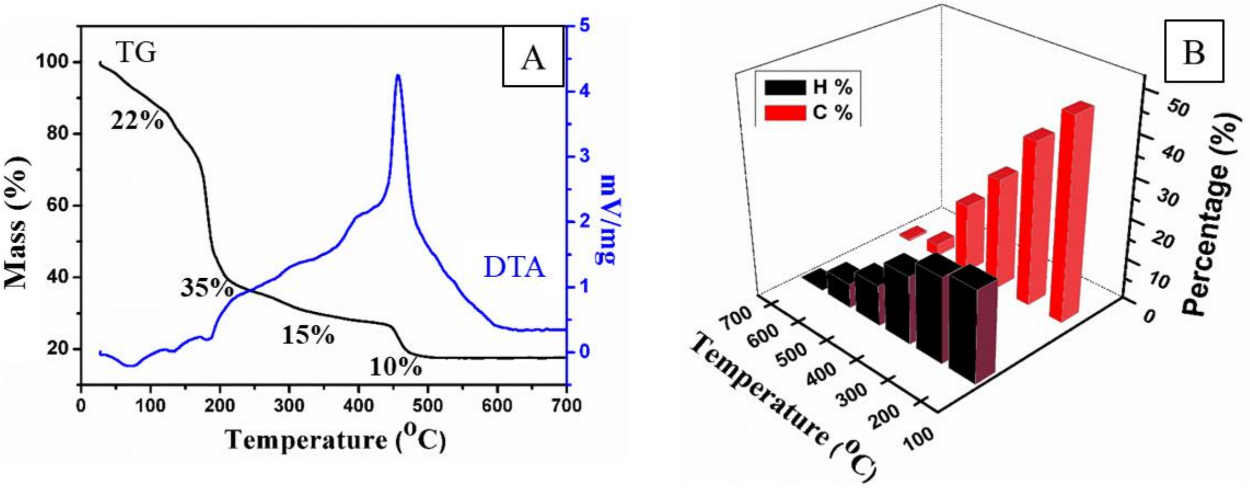

**Figure 3.25:** (A) TG-DTA of the as-synthesized tungstic acid-citric acid gel and (B) histogram of the C and H distribution.

In the TG analysis of the hybrid gel (Figure 3.25 A), four distinct weight losses and their corresponding DTA peaks were evident. i) At ≤ 150 °C, loss of adsorbed water was observed. ii) In the temperature range of 150 °C - 200 °C, rapid combustion of the excess citric acid was observed. Subsequently, iii) a gradual weight loss of around 15% within a temperature range of 200 °C - 450 °C occurred. This could result from partial oxidative carbonization of citric acid into its pyrolysis products which could further transform it into reduced graphene oxide (rGO)-like carbon fibers catalyzed by the growing $WO_{3-x}$ nanorods. Further heating, iv) > 550°C resulted in the increased oxidative removal of carbon fibers causing loss of structural integrity of WF and collapse of the fibrous structure. Elemental analysis of C and H of the post calcination products (refer figure 3.25 B) revealed that nearly

17 % carbon content was present in the WF which reduced to ~ 4 % when the fibrous structure collapsed, forming WH, which was in good agreement with the TG results.

### 3.6.4 IR and XRD studies

IR analysis (refer figure 3.26 A) revealed the presence of a broad peak within 3600 to 2300 cm$^{-1}$, which could be a combination of O-H and C-H stretching vibrations. The O-H bending vibration was observed at 1660 cm$^{-1}$. The C=O and C-O stretching frequencies of citric acid present in the gel mixture were observed at the characteristic wavenumbers of 1722 and 1207 cm$^{-1}$at 150 °C, respectively. A slight shift in the C=O stretching vibration from 1722 to 1731 and 1735 cm$^{-1}$ was observed with an increase in temperature to 250 and 350 °C, respectively. The C-O stretching vibration also showed a similar trend wherein the stretching vibrations shifted to 1225 and 1233 cm$^{-1}$ at temperatures of 250 and 350 °C. Such a shift towards a high wavenumber is indicative of stronger bonding interaction between the metal and carboxylic groups. The above shifts in the C=O and C-O stretching frequencies was accompanied by the morphological transformation of tungstic acid-citric acid hybrid gel into tripodal shaped intermediate structures as observed in the SEM analysis (refer figure 3.23). All the above signals were eliminated at higher temperatures >350 °C confirming the decomposition of citric acid. A broad peak corresponding to the presence of O-W-O and W=O vibration within 1020 to 535 cm$^{-1}$ was indicative of the oxide formation in the temperature range of 450 °C - 650 °C.[35]

Figure 3.26 B presents the XRD patterns depicting gradual transformation of the tungstic acid-citric acid gels into monoclinic phase of $WO_{3-x}$. Peaks are observed at 2θ value of 22.6, 23.5, 24.1, 26.5, 28.7, 32.7, 33.5, 34.1, 35.1, 41.2, 41.7, 45.1, 47.1, 49.7, 50.1 and 55.3. Corresponding miller indices of (002), (020), (200), (120), (-112), (022), (-202), (202), (122), (-222), (222), (004), (040), (140), (-114) and (420) for the above peaks were matched with P21/n, JCPDS # 43-1035 and were in agreement with the literature reports.[6,38] The low intensity carbon peaks possibly overlapped with that of high intensity $WO_3$ peaks at 2θ values of 26.5 and 45.1 and hence were not evident from the XRD plot, in agreement with the observations of Wang *et al*. [63] It was interesting to note that, WF and WH exhibited significant differences in the relative peak percentage distribution of the (002), (020) and (200) facets. Intensity ratio comparison of the major peaks having miller indices (002): (020):

(200) gave values of 1.6 : 0.9 : 1 for WF and 0.9 : 0.7 : 1 for WH. The surface dominance of (002) plane was in agreement with the HRTEM results. The (002) plane is crucial for building 1D $WO_{3-x}$ nanostructures and is reported to significantly enhance electrochemical performance of $WO_{3-x}$, [46,48,49]

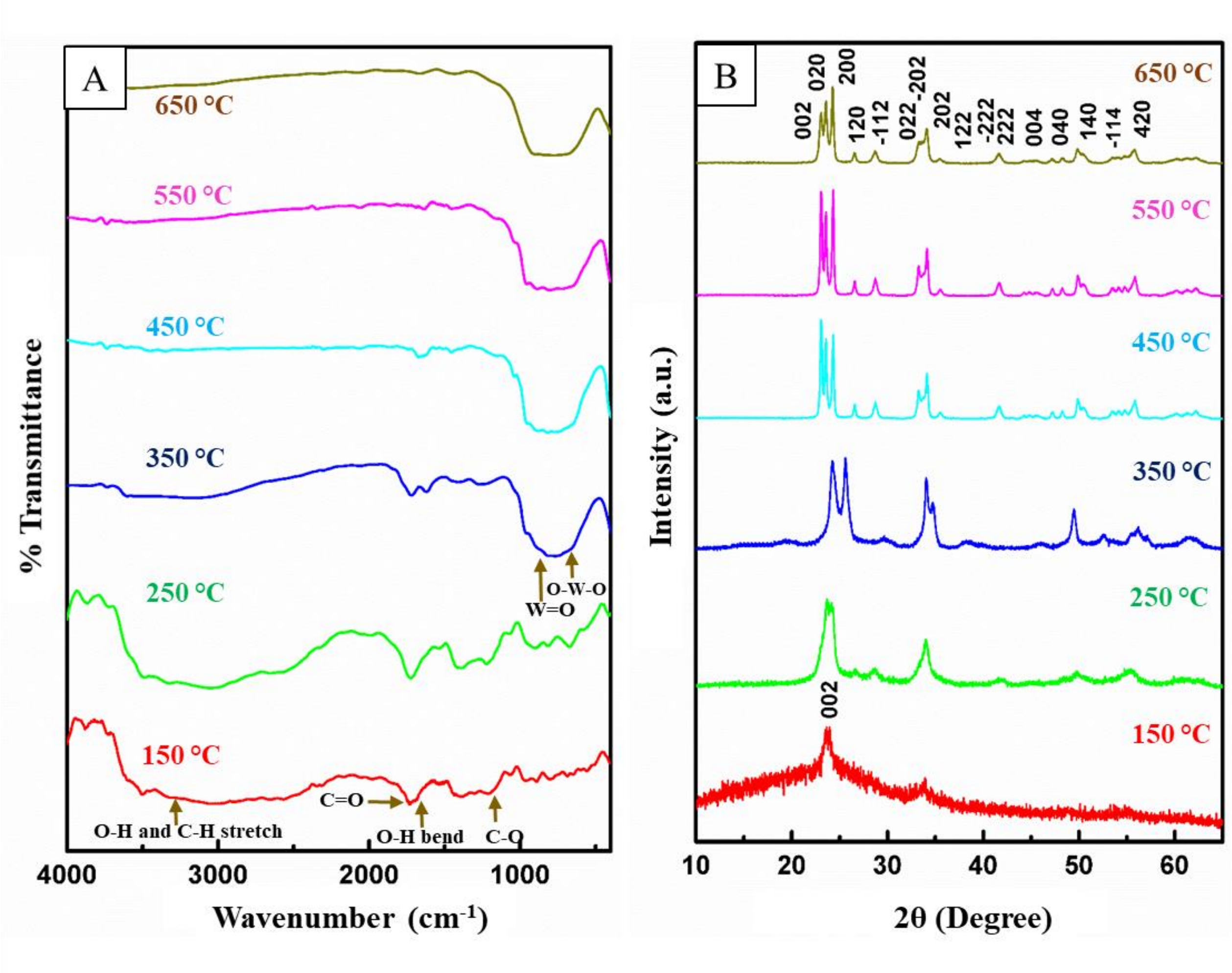

**Figure 3.26:** (A) IR spectra and (B) XRD patterns depicting the transformation of tungstic acid-citric acid gel mixture at various temperatures from 150 to 650 °C.

### 3.6.5 Raman and EPR studies

The nature of carbon encapsulation plays a crucial role in tailoring the nanorods of $WO_{3-x}$ into the complex fibrous structure. Therefore, Raman analysis were performed to elucidate the carbon structure (refer figure 3.27 A and B). Besides the bands due to $WO_{3-x}$ at 710 and 804 $cm^{-1}$ ascribed to the stretching modes of W-O vibrations, the characteristic first order Raman bands at 1350 $cm^{-1}$ and 1600 $cm^{-1}$ were identified, typical of reduced graphene oxide (rGO)-like carbon fibers.[64–67] The Raman bands of rGO like carbon fibers were deconvoluted via a five peak fit model using the Voigt function. This has been a standard method used over decades to explain the types of disorders in carbon soot, and more recently, it has been adopted to analyze GO.[68] The corresponding fitted peaks are denoted as D1 = 1353 cm$^{-1}$, D2 = 1560 cm$^{-1}$, D3 = 1445 cm$^{-1}$, D4 = 1150-1250 cm$^{-1}$, and G =1610 cm$^{-1}$.[69]

The D bands represent the defects and disorder of carbon structure, while the G band represents the graphitic carbon layers.[70] The ratio of peak intensities ($I_{D1}/I_G$) is a good measure of the crystal structure disorder induced due to strong chemical interactions of GO with $WO_{3-x}$. From the values of intensity ratios of the D1 and G bands, the $I_{D1}/I_G$ values of 1.13 and 1.45 were obtained for WF and WH, respectively. The D4 peak represents the crystal edge disorder due to the presence of sp$^3$ bonded oxygen species present at the edges of GO, while the D3 is an indicator of the amorphous carbon surface structure.

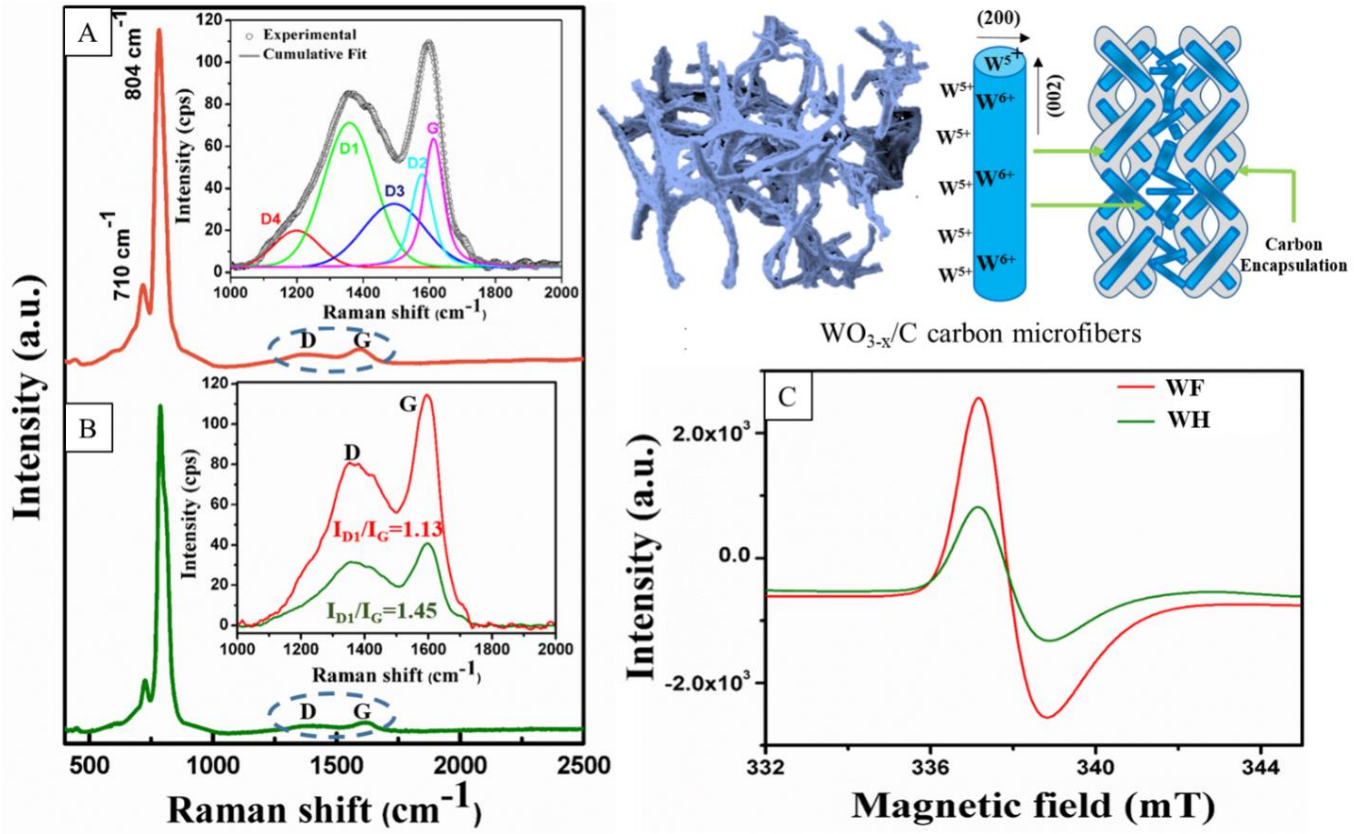

**Figure 3.27:** (A-B) Raman spectra of WF and WH, respectively, and (C) Overlay EPR spectra of WF and WH, respectively.

The relative decrease in $I_{D4}/I_G$ peak intensity is more pronounced in the case of WF (0.25) compared to WH (0.31). This confirms the reduction in surface or edge oxygen functionalities due to the chemical bonding of GO with $WO_{3-x}$ resulting in the formation of reduced graphene oxide (rGO) like encapsulation over $WO_{3-x}$ nanorods. This is understandable as the calcination temperature was lower in the case of WF compared to the WH and agrees with the C, H, N, and TGA studies as well. Such a heterostructure formation could induce variations in surface oxygen vacancies resulting in changes in the surface redox states of $WO_{3-x}$ nanorods as illustrated in the schematic in figure 3.29. Therefore, EPR spectroscopic analysis of WF and WH were performed.

The EPR analysis (refer figure 3.27 C) gave a resonance signal at g = 2.001, confirming the presence of oxygen vacancies on the $WO_{3-x}$ nanorod surface.[63,71] Furthermore, the peak intensity comparison of the EPR spectrum of WF and WH revealed greater oxygen vacancies in the former case. The presence of redox states and types of oxygen functionalities in rGO fiber encapsulated $WO_{3-x}$ nanorods were investigated further using X-ray photoelectron spectroscopy (XPS).

### 3.6.6 XPS studies

The XPS spectra shown in Figure 3.28 A-D are of WF, while that of WH are presented as figure 3.28 E-H. The typical W4f peaks (at 35.53 eV and 37.68 eV) ascribed to W $4f_{7/2}$ and W $4f_{5/2}$, respectively, were observed in case of both WF and WH, as a result of spin orbital splitting (refer figure 3.28 B and F). Analysis confirmed that majority of surface tungsten is in $W^{6+}$ state while < 20 % is in $W^{5+}$, distributed throughout the nanorod surface.[10,11,72] The 530.36 eV peak of O1s was ascribed to the W-O species while the shoulder peak at 532.62 eV was a result of oxygen in intercalated water (refer figure 3.28 C and G).

The C1s band at 284.92 eV was from the carbon species (figure 3.28 D and H), which upon deconvolution revealed three peaks at 285.0, 286.6, and 288.3 eV due to C-C, C-O, and C=O groups of rGO-like carbon fibers respectively.[73,74] The possibility of carbon doping in $WO_3$ matrix was thus ruled out, since no peaks around 281-282 eV were observed in XPS spectrum.[73] Therefore, it was concluded that the carbon was largely distributed over the surface of $WO_{3-x}$ nanorods as also observed from the HRTEM (refer figure 3.28 B) and EDX map (refer figure 3.23 F-H).

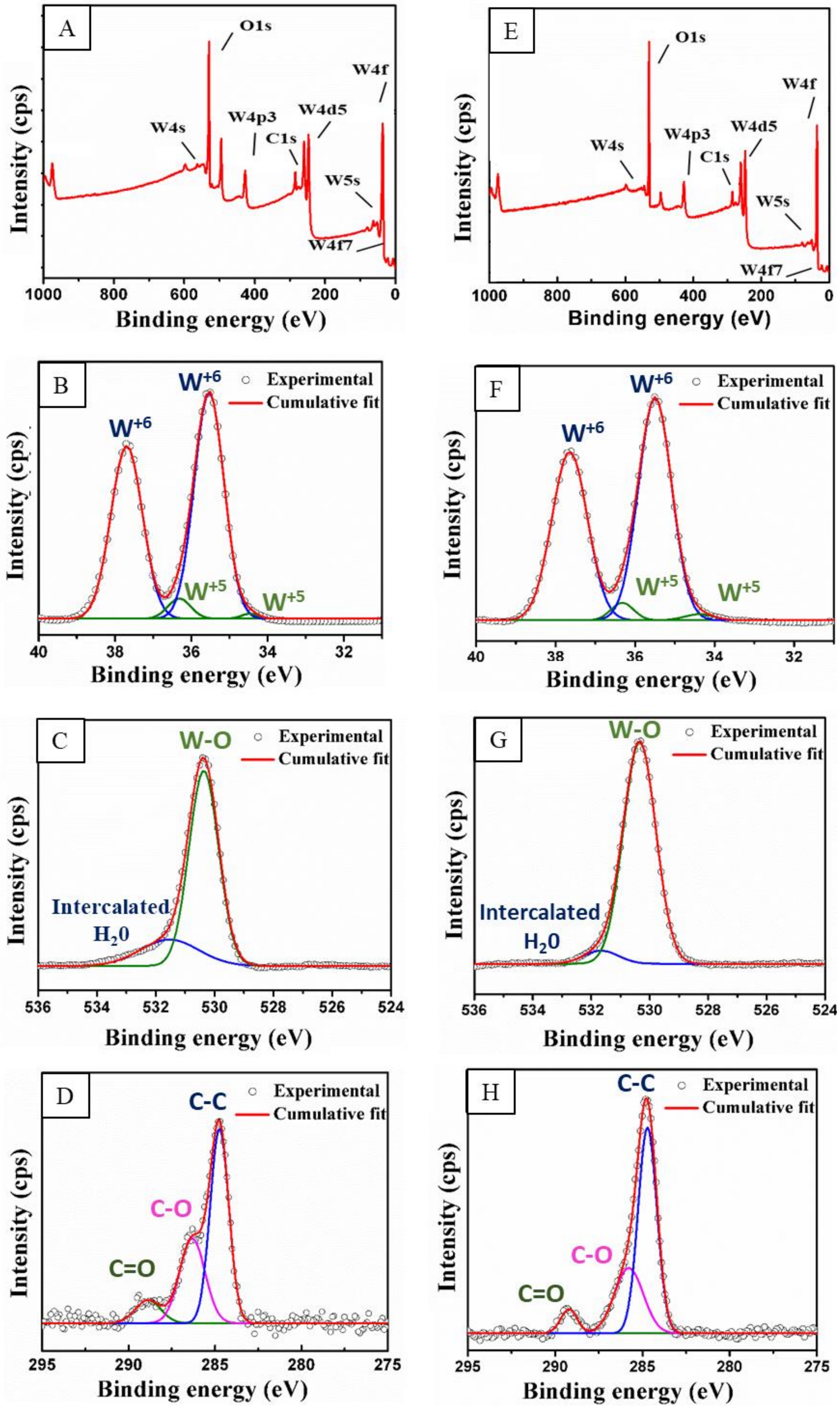

**Figure 3.28:** XPS spectra of (A-D) WF and (E-H) WH.

The percentage compositional analysis from the W4f, O1s and C1s narrow scan spectrums are presented in table 3.9. The W4f analysis of XPS spectrum revealed that the ratio of $W^{5+}/W^{6+}$ was 0.18 for WF while for WH was only 0.07 which confirmed that WF had a greater magnitude of surface oxygen defects in agreement with EPR results. The peak due to the intercalated water in the O1s spectra were due to the oxygen from the hydroxyl ions and is an direct indicative for oxygen vacancies on the surface.[75] The relative distribution of the intercalated water was also greater in WF reconfirming the greater magnitude of oxygen defects. The increased distribution of oxygen vacancies is also known to exhibit improved electrochemical performance and has been demonstrated in section 3.7 by performing charge storage measurements.[70,76,77]

| **Material** | **Narrow scan** | **Tungsten species** | **XPS area integration (%)** | **Area ratio $W^{5+}$ / $W^{6+}$** |
|---|---|---|---|---|
| WF | W 4f | $W^{6+}$ | 84.61 | 0.18 |
| | | $W^{5+}$ | 15.39 | |
| | O 1s | W-O | 78.88 | |
| | | Intercalated $H_2O$ | 21.12 | |
| | C 1s | C-C | 56.36 | |
| | | C-O | 33.74 | |
| | | C=O | 9.9 | |
| WH | W 4f | $W^{6+}$ | 93.46 | 0.07 |
| | | $W^{5+}$ | 6.54 | |
| | O 1s | W-O | 97.61 | |
| | | Intercalated $H_2O$ | 2.39 | |
| | C 1s | C-C | 67.73 | |
| | | C-O | 30.03 | |
| | | C=O | 2.24 | |

**Table 3.9:** The percentage of species obtained from the XPS peak area integration of narrow scan spectra of WF and WH.

### 3.6.7 Growth mechanism of 3D $WO_{3-x}$/C microfibers

The schematic representation of the plausible growth mechanism of WF and WH is illustrated in figure 3.29. Citric acid is a well-known naturally available organic surface modifier, used in nanomaterial synthesis. Being a weak triprotic acid with three carboxylic groups that are able to cap metal ions under controlled pH conditions, allows synthetic tunability for designing nanostructures. The hydrolysis of sodium tungstate forms tungstic acid sol which upon subsequent polycondensation results in the formation of tungstic acid gel. The presence of citric acid at this stage serves as a capping agent to induce anisotropic, directional growth of $WO_3$ particles. These interactions between citric acid and $WO_4^{2-}$ were observed in IR measurements as well (refer figure 3.26 A). Moreover, the oxidative pyrolysis (incomplete combustion) of citric acid is reported to produce polymeric graphene oxide-like quantum dots and fibers especially when catalyzed by alkali metals.[78,79] While majority of unreacted citric acid would decompose into CO/$CO_2$ upon heating, it is speculated that, the dominant (002) surface plane of the growing $WO_{3-x}$ nanorods may serve as an active surface for catalyzing the growth of rGO-like carbon fibers in the temperature range of 200-450$^oC$. Since, varied size distribution of $WO_{3-x}$ nanorods were observed in TEM analysis, it is likely that the carbon encapsulation rate could compete with $WO_{3-x}$ nanorod growth kinetics.[80,81] This may result in the termination of the nanorod growth to a restricted size and leads to the formation of $WO_{3-x}$/C heterostructures.

Elucidating the helicity induction mechanism in such carbon fibers still remains a challenge till date. Several mechanisms attempting to explain the growth of helical structures can be found in the literature. For instance, the crystallization of a double helical superstructure from a macrocyclic dimer that exhibits two diastereoisomeric conformations was reported by Stoddart and coworkers.[82] These double helical structures were stabilized by intermolecular [C-H$\cdots$O] interactions across the functional groups of the diastereoisomers. Furthermore, duplex formation through base pair specific hydrogen bonding interactions in nucleic acids[83,84], Van der Waals interactions in self-assembled fibers[85] and interaction of organic ligands with metal surfaces have also been reported to produce double, triple and quadrapole helices.[86] Computational studies by Suzuki et al.[57] on L/D-cysteine moieties functionalized to the crowded edges of graphene were found to undergo “buckling effect” across the functional groups inducing helicity in GO.

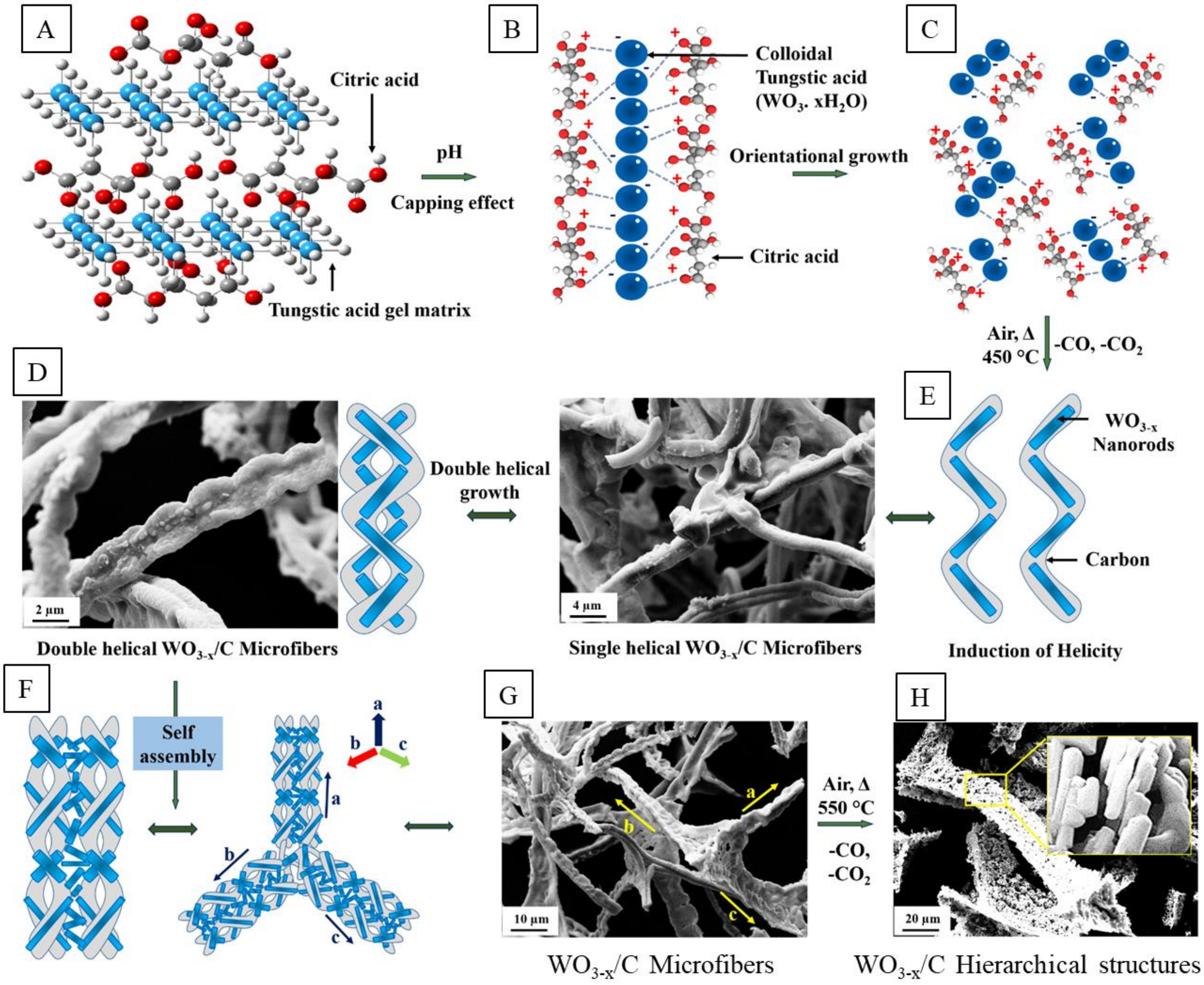

**Figure 3.29:** Schematic illustration of the plausible growth mechanism of WF and WH. (A) depicts tungstic acid-citric acid hybrid gel, (B) capping effect induced by citric acid, (C) orientational growth of citric acid particles, (D) growth of carbon fiber encapsulated $WO_{3-x}$ single helices, (E) formation of $WO_{3-x}$/C double helical fibers, (F-G) self-assembled WF tripodal superstructures and (H) transformation of WF into WH.

Considering the above observations, it can be speculated that such a hydrogen bonding or Van der Waals interaction across carbon fiber encapsulated $WO_{3-x}$ nanorods may produce helical fibers via self-assembly process. The trapping of $WO_{3-x}$ nanorods in between the growing helical strands along the three directions (refer figure 3.29 F) may thus result in the formation of the double helical tripodal superstructure. It is to be noted here that the actual mechanism of inducing helicity in carbon fiber encapsulated $WO_{3-x}$/C nanorods could be much more complex than the one speculated in figure 3.29. Furthermore, subsequent heating of these superstructures to > 450$^{o}$C, results in removal of carbon encapsulation via CO/$CO_2$ loss (as observed in TG). This lead to collapse of the double helical structure, leaving behind a hierarchical assembly of $WO_{3-x}$ nanorods (refer figure 3.29 H). The WF structure with redox surface states, enhanced oxygen vacancies is also expected to exhibit enhanced electrical conductivity and electrode-electrolyte interfacial kinetics due to the rGO-like carbon fiber-$WO_{3-x}$ heterostructure formation. Therefore, the synthesized WF and WH microstructures were subjected to charge-storage measurements.

## 3.7 Evaluation of the charge storage properties of microstructured 3D $WO_{3-x}$/C microfibers and hierarchical structures

### 3.7.1 Three electrode charge storage studies

Cyclic voltammetry (CV), galvanostatic charge discharge (GCD), and electrochemical impedance spectroscopic (EIS) measurements were conducted to evaluate the electrochemical performance of WF and WH. The comparative CVs for WF and WH are presented in figure 3.30 A. The cyclic voltammograms exhibits an anodic peak at ~ -0.1 V due to the $H^+$ ions deintercalation from the $WO_{3-x}$/C matrix as per the reaction 3.1. WF displayed a highest area coverage under the CV curve compared to WH demonstrating significant improvement in electrochemical performance due to its fibrous morphology assisted by the presence of rGO-like fiber encapsulation, which provides facile diffusion pathways for $H^+$ ions across the $WO_{3-x}$ matrix. Therefore, scan rate dependent CV measurement were performed to calculate the diffusion coefficients ($D_0$) using the Randles-Sevciks method described in section 2.4.4 (refer figure SF14 in Annexure-I).[87,88] The WF electrodes exhibited the highest $D_0$ value of $5.6 \times 10^{-9}$ cm$^2$ s$^{-1}$ compared to the $D_0$ value of WH ($4.7 \times 10^{-9}$ cm$^2$ s$^{-1}$).

The 3D arrangement of $WO_{3-x}$ nanorods and its fibrous nature provide preferential orientation of a greater number of electroactive centers to participate in the electrochemical reaction. Therefore, the electroactive area of each material was determined using the Cottrell equation using the methodology described in section 2.4.3. The highest electroactive area of 0.78 $cm^2$ was obtained for WF while WH displayed a relatively lower electroactive area of 0.54 $cm^2$, which were in trends with the results of BET surface area analysis as well (refer figure SF 15 in Annexure-1). The decrease in the electroactive areas from the WF to WH can be understood as a result of reduction in surface oxygen defects and decreased intercalated $H_2O$ as observed from the XPS analysis.

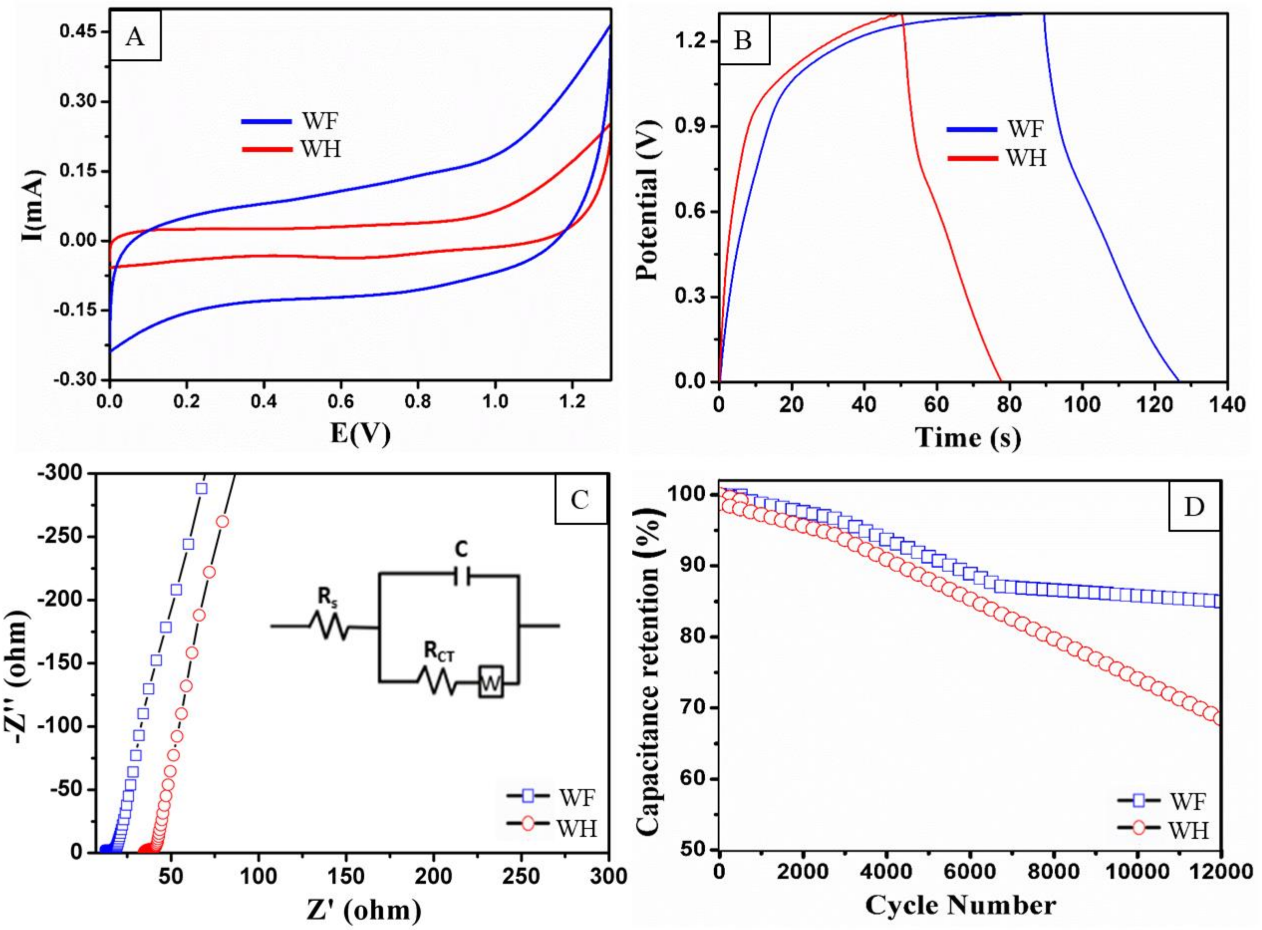

**Figure 3.30:** Supercapacitor performance investigated via (A) CV analysis at a scan rate of 10 mV $s^{-1}$; (B) GCD analysis at the current density of 2 A $g^{-1}$ ; (C) Nyquist plots in the frequency range of 1 mHz to 1 MHz; and (D) cycling stability performance evaluated at a constant current density of 8 A $g^{-1}$.

The values of specific capacitance for synthesized nanostructures were calculated from cyclic voltammograms as well as galvanostatic charge-discharge analysis using the formulas described in section 2.4.1. The values of specific capacitance at various scanning rates have been tabulated in table 3.11. The highest specific capacitance of 315.2 $Fg^{-1}$ was observed for WF while WH gave a lower values of 216.6 F $g^{-1}$. The lower values of $D_o$, electroactive area and specific capacitance as observed in case of WH could well be due to the loss of fibrous nature of the material resulting in decreased surface area and was in good agreement with the SEM and BET $N_2$ adsorption-desorption studies as well.

| Scan rate (mV $s^{-1}$) | Specific capacitance (F $g^{-1}$) (Error bar ± 2%) | | | |
|---|---|---|---|---|
| | WF | | WH | |
| | 3 Elec. | 2 Elec. | 3 Elec. | 2 Elec. |
| 5 | 402.3 | 196.3 | 352.8 | 170.1 |
| 10 | 375.1 | 165.6 | 361.9 | 149.4 |
| 20 | 332.7 | 146.7 | 311.3 | 128.3 |
| 50 | 292.3 | 125.1 | 271.6 | 116.9 |
| 100 | 248.3 | 101.8 | 228.1 | 91.2 |

**Table 3.10:** Summary of specific capacitance values calculated from CV curves obtained for WF and WH.

Furthermore, these observations were confirmed by performing galvanostatic charge-discharge analysis at various current densities from 2 to 10 A $g^{-1}$ (refer figure SF 16 in Annexure-I). A typical overlay of the charge-discharge curve recorded at a current density of 2 A $g^{-1}$ is shown in figure 3.30 B. Specific capacitance was calculated from charge-discharge curve at various current densities and their values are tabulated in table 3.12. The values for specific capacitance at the current density of 2 A $g^{-1}$ are observed to be 161.6 F $g^{-1}$ for WF and 146.2 F $g^{-1}$ for WF and WH, respectively. The obtained capacitance of WF showed improvement in comparison to other reported microfiber-like $WO_3$ morphologies. For instance, Wang *et al.* [89] reported $WO_3$-polypyrrole core shell nanowire arrays grown on carbon fibers using an electrodeposition technique and exhibited capacitance of 253 mF $cm^{-2}$

at a current density of 0.67 mA $cm^{-2}$. Gao *et al.* [90] made use of hydrothermal technique to produce $WO_3$ nanowire arrays/carbon cloth integrated electrodes with the specific capacitance of 32.6 mF $cm^{-2}$ at 1.2 mA $cm^{-2}$. Tian *et al.* [91]produced $W_{18}O_{49}$ nanofibers with polyaniline using electro-deposition technique, yielding specific capacitance of 20 mF $cm^{-2}$ at 0.5 mA $cm^{-2}$. This suggests that the double helical superstructure significantly improves the supercapacitor performance of $WO_3$.

| Current density ($Ag^{-1}$) | Specific capacitance ($F\ g^{-1}$) (Error bar ± 2%) | | | |
|---|---|---|---|---|
| | WF | | WH | |
| | 3 Elec. | 2 Elec. | 3 Elec. | 2 Elec. |
| 2 | 315.2 | 161.6 | 216.6 | 121.2 |
| 4 | 289.6 | 142.3 | 182.3 | 105.5 |
| 6 | 262.3 | 129.5 | 163.9 | 95.4 |
| 8 | 226.5 | 102.4 | 149.8 | 78.3 |
| 10 | 199.6 | 81.5 | 119.4 | 58.6 |

**Table 3.11:** Summary of specific capacitance values calculated from GCD analysis obtained for WF and WH.

In order to better understand the observed order of specific capacitance, electrochemical impedance measurements at open circuit potential values within the frequency region of 1 mHz to 1 MHz were recorded and are presented in figure 3.30 C. The Nyquist plots from the EIS studies of low frequency region showed linear dependence while a small semicircle form was observed in the high frequency region.[92,93] A representative circuit diagram which best describes the system is presented as an inset in figure 3.30 C. The circuit diagram comprises of a charge transfer resistor ($R_{CT}$) that is connected with a capacitor and a Warburg resistor (W) in parallel and solution resistor ($R_S$) in series. The solution resistance ($R_s$) for WF (8.2 **Ω**) was almost 4 times lower than WH (32.1.2 **Ω**). The lowest $R_s$ values suggested better conductivity of WF compared to WH. Electrode stability is also an important parameter for evaluating the performance of capacitor electrode materials.[24] It was observed that the morphology of the electrode material had an impact on its stability. The stability of the modified electrodes was studied by performing continuous galvanostatic charge-discharge measurements and has been presented in Figure 3.30 D. It was observed that the electrode films prepared from WF were significantly more stable (92 %) (208.3 F $g^{-1}$) than those prepared with WH (87 %) (130.3 F $g^{-1}$), compared to their initial specific capacitance as reported in table 3.11. The excellent stability demonstrated by WF and WH indicated their potential for device scale applications and have been evaluated for the same in the next section 3.7.2.

### 3.7.2 Electrochemical performance of the $WO_{3-x}$/C//AC asymmetric supercapacitor devices

To evaluate the practical applicability of the synthesized WF and WH microstructures, an asymmetric supercapacitor device was assembled using $WO_{3-x}$ microstructures fabricated onto carbon paper as the anode and activated carbon (AC) fabricated onto another carbon paper as an cathode using the methodology described in section 2.3.2.1. Figure 3.31 A displays an overlay of the cyclic voltammograms at a fixed scan rate of 5 mV $s^{-1}$ and galvanostatic charge-discharge studies at a constant current density of 2 A $g^{-1}$ has been presented as figure 3.31 B. The two figures indicate both greater voltammogram area and longer discharge time for WF in comparison to WH. Scan rate-dependent CV and current density-dependent GCD studies were also performed (see figures SF16 and SF17 in Annexure-I), and the specific capacitance thus obtained has been tabulated in tables 3.10 and 3.11, respectively (Equations 2.4 and 2.5).

The highest specific capacitance of 165.6 F $g^{-1}$ at a scan rate of 5 mV $s^{-1}$ and 161.6 F $g^{-1}$ at a current density of 2 A $g^{-1}$ was demonstrated by WF. The observed results of specific capacitance measurements were in line with the results of three-electrode studies. However, low coulombic efficiency (~ 55 %) was observed in the GCD curves for the asymmetric supercapacitor. This may be due to irreversible peristatic reactions that occur during the charging and discharging of the supercapacitor. The low coulombic efficiency could be a result of the properties of the solid electrolyte material itself, such as its ionic conductivity, electrochemical stability, and chemical compatibility with the cathode and anode materials. It is also possible that the efficiency is limited by the interface between the solid electrolyte and the electrodes, as well as by the thickness of the solid electrolyte layer. The low coulombic efficiency observed in our study also presents an opportunity for future research to improve the performance of asymmetric supercapacitor devices. The EIS studies showed the Rs values of 21.2 and 31.9 Ω by WF and WH, respectively. A representative circuit diagram which best describes the system is presented as an inset in figure 3.31 C. The circuit diagram comprises of a charge transfer resistor ($R_{CT}$) that is connected with a capacitor and a Warburg resistor (W) in parallel and solution resistor ($R_S$) in series. Additionally, exceptional cycling stability was also demonstrated by WF when tested over 12000 continuous charge-discharge cycles. Capacitance retention of 87.6 (89.7 F $g^{-1}$) and 71.9 % (56.2 F $g^{-1}$) were observed for WF and WH electrodes, compared to their initial specific capacitance as reported in table 3.11.

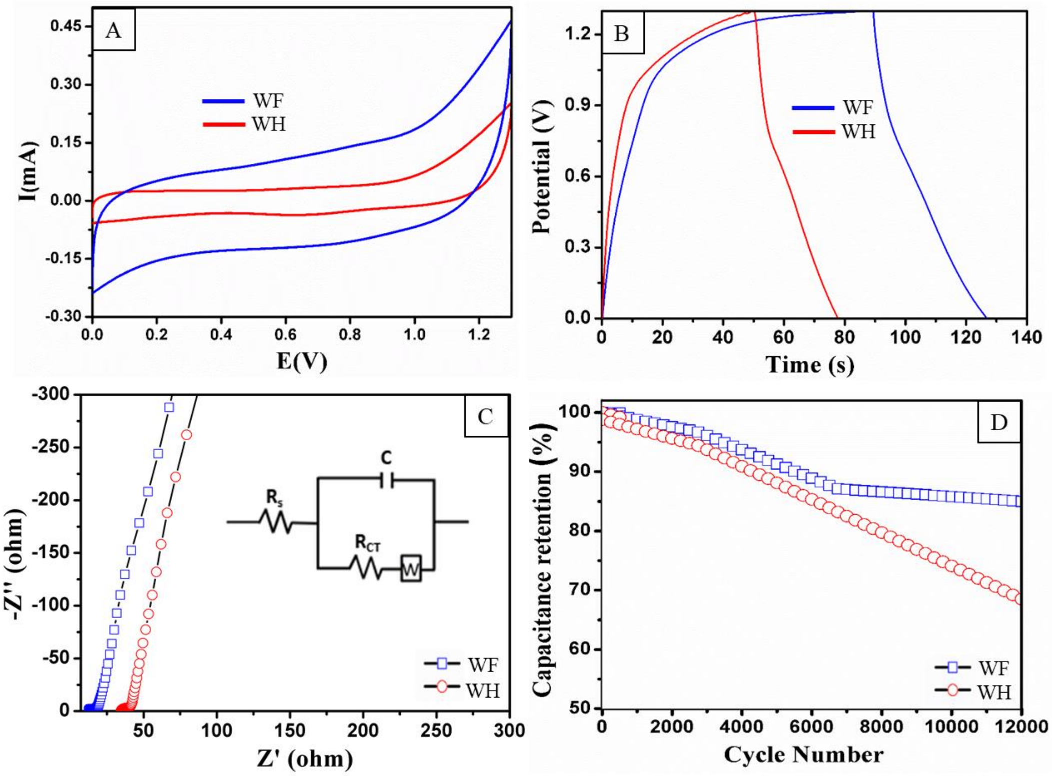

**Figure 3.31:** (A) Overlay of CV curves recorded at a scan rate of 5 mV $s^{-1}$ (B) Overlay of GCD analysis recorded at the current density of 2 A $g^{-1}$ (C) Overlays of Nyquist plots in the frequency range of 1 mHz to 1 MHz and (D) Overlays of cycling stability performance measured in a two-electrode asymmetric setup evaluated at 8 A $g^{-1}$.

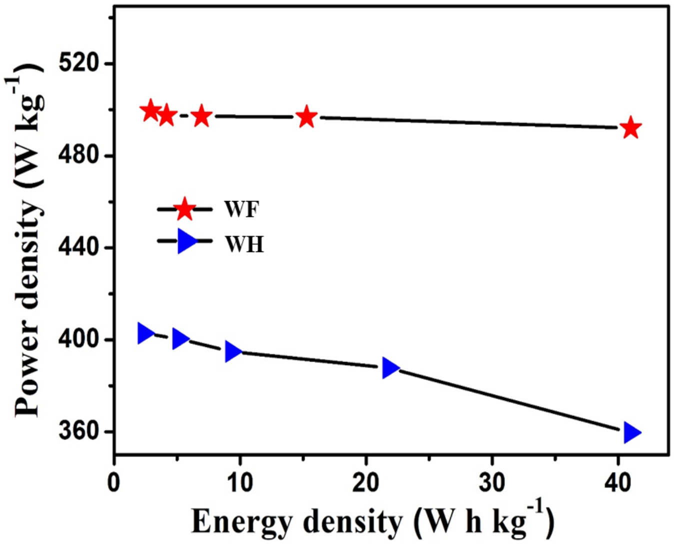

**Figure 3.32:** Ragone plot demonstrating the device performance of WF and WH microstructures

Power density and energy density are the most significant parameters of any supercapacitor device. The Ragone plot displaying the performance of the assembled asymmetric supercapacitors has been presented as figure 3.32 (Equation 2.6 and 2.7). The highest power density of 489.3 W kg$^{-1}$ and energy density of 15.3 W h kg$^{-1}$ were demonstrated by the WF, while WH displayed a power density of 400.3 W kg$^{-1}$ and energy density of 8.2 W h kg$^{-1}$. The exceptional capacitance performance and high electrochemical stability of the WF can be considered as a cumulative outcome of the presence of a greater number of oxygen vacancies accompanied by surface redox states and nanofibrous features, which facilitate the enhanced charge performance of the material.

## 3.8 The impact of nanostructuring in $WO_{3-x}$ on the charge storage performance

It is known through literature that nanostructuring provides several catalytic advantages to materials, such as generation of kink sites, exposure of catalytically active facets, enhanced material stability, larger surface area, improvements in the long-range anisotropy, etc.[99] Introspecting the charge storage performance of all the synthesized nano and microstructures of $WO_{3-x}$ in the present thesis, it appears that WP being the simplest nanostructure, displayed the least charge storage performance with the specific capacitance of 51.6 F g$^{-1}$ along with the energy and power density values of 8.1 W h $kg^{-1}$ and 405.2 W $kg^{-1}$. When the dimensionality was increased from 0D to 1D $WO_{3-x}$, improvement in the charge storage performance was observed, with the specific capacitance being doubled to 125.5 F $g^{-1}$ with the energy and power density values of 11.8 W h $kg^{-1}$ and 418.2 W $kg^{-1}$. When WN was utilized in constructing 3D $WO_{3-x}$ microstructures, further performance improvements were observed. 3DW displayed a specific capacitance of 138.2 F $g^{-1}$ with energy and power density values of 9.1 W h $kg^{-1}$ and 435.2 W $kg^{-1,}$ respectively. Remarkably higher performance was observed in WF, which has added advantage of being fibrous in nature along with the presence of graphitized carbon. This allowed WF to produce a specific capacitance of 161.2 F $g^{-1}$ along with energy and power density values of 15.3 W h $kg^{-1}$ and 489.3 W $kg^{-1}$ respectively. These results were on par or in some cases even better than the complex nanostructures of $WO_{3-x}$ reported in literature as presented in figure 3.33.

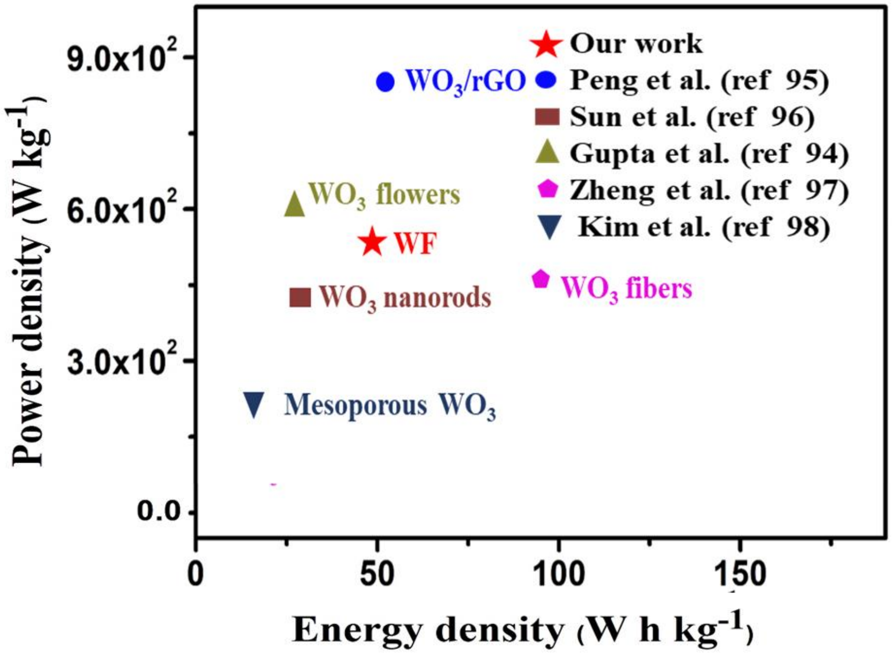

**Figure 3.33:** Comparative analysis of our synthesized $WO_{3-x}$ with some literature reports.[94–98]

On the other hand, sintering had a detrimental effect on the properties of $WO_{3-x}$. This was evident from the decrease in the charge storage performance of WH, which was formed by the sintering of WF. The sintering decreased the electroactive area from 0.78 $cm^2$ (WF) to

0.07 $cm^2$ (WH). Thus WH resulted in a lower specific capacitance of 131.2 F $g^{-1}$ with energy and power density values of 131.2 W h $kg^{-1}$ and 400.3 W $kg^{-1}$ respectively. Similarly, 2DW, which was produced through sintering of WN has the least performance with the specific capacitance of 136.2 F $g^{-1}$ with energy and power density values of 8.3 W h $kg^{-1}$ and 398.3 W $kg^{-1}$. The sintering effect which has a detrimental influence on the 2D morphology of $WO_{3-x}$ is an exception to the properties of 2D nanomaterials as they are expected to have higher charge storage performance due to the presence of long-range anisotropy in the material. The observed effect in the present case arises due to a number of factors such as lower $W^{+5}$ and the lowering of the electroactive area caused by the temperature-induced destruction of active centers, etc. Nonetheless, the merits of 2D nano and microstructures have been highlighted by constructing a number of novel microstructures of $MoO_{3-x}$ in the next chapter.

## 3.9 CONCLUSIONS

The study demonstrates the synthesis $WO_{3-x}$ nano and microstructures such as nanorods, microplates, 3D hierarchical structures, microfibers, etc. Fuels such as urea, N-methylurea, tetramethylurea, carbohydrazide, semicarbazide, and citric acid were utilized in a dual role of a structure-directing agent and also as fuel to transform $WO_3$ nanoparticles into complex nanostructures. It was confirmed that the SDA, when utilized under protonated conditions and in a tungsten to SDA ratio of ≈1:6, could produce $WO_{3-x}$ nano/microstructures. A detailed investigation into the growth mechanism by perturbing different synthesis conditions of pH, temperature, time, and ratio were carried out. By carefully tuning the calcination time of the $WO_{3-x}$ nanorods, they could be transformed into 3D hierarchical structures, whereas if the calcination temperature was increased to more the 550 °C, as an influence of the sintering effect, the nanorods transformed into 2D $WO_{3-x}$ microsheets. Additionally, to further evaluate the nanorod promoting effect of urea, –NH substituted (Carbohydrazide and Semicarbazide) and –CH substituted (N-methylurea and tetramethylurea) urea was also studied. It was observed that -NH substitution promoted the nano/microstructing whereas -CH substitution had a detrimental effect. Furthermore, when thiourea was used in place of urea, no nanostructuring was observed. This observation further supported our theory of requirement of protonation center in urea which plays a important role in directing the growth of nano/microstructures.

Meanwhile, a citric acid-assisted reflux method was developed to synthesize $WO_{3-x}/C$ microfibers, which collapsed when subjected to temperatures ≥ 550 °C and transformed into hierarchical structures. The synthesized nano and microstructured materials were characterized using IR, XRD, TG-DTA, SEM, EDX, HRTEM, SAED, CHNS, EPR, XPS, etc. Detailed spectroscopic analysis revealed that nanostructuring enabled effective induction and distribution of oxygen vacancies along with $W^{5+}/W^{6+}$ and also led to the preferential orientation of the (002) surface plane, which was beneficial for the charge storage performance of nanostructured $WO_{3-x}$. Furthermore, all the nano and microstructured $WO_{3-x}$ were evaluated for their charge-storage performance. $WO_{3-x}/C$ microfibers demonstrated the highest performance of all nanostructured tungsten electrodes with an energy density of 15.3 $W\ h\ kg^{-1}$ at a power density of 489.3 $W\ kg^{-1}$. It has also been concluded that nanostructuring enabled faster electrode-electrolyte interfacial kinetics, improving the material's electrical conductivity and electrochemical cycling stability. These nanostructured $WO_{3-x}$ electrodes with improved charge storage performance could have significant potential for commercial-scale applications.

## 3.10 REFERENCES

(1) Kida, T.; Nishiyama, A.; Hua, Z.; Suematsu, K.; Yuasa, M.; Shimanoe, K. $WO_3$ Nanolamella Gas Sensor: Porosity Control Using $SnO_2$ Nanoparticles for Enhanced $NO_2$ Sensing. *Langmuir* **2014**, *30* (9), 2571–2579.

(2) Van Dang, T.; Duc Hoa, N.; Van Duy, N.; Van Hieu, N. Chlorine Gas Sensing Performance of On-Chip Grown ZnO, $WO_3$, and $SnO_2$ Nanowire Sensors. *ACS Appl. Mater. Interfaces* **2016**, *8* (7), 4828–4837.

(3) Yang, C.; Zhu, Q.; Lei, T.; Li, H.; Xie, C. The Coupled Effect of Oxygen Vacancies and Pt on the Photoelectric Response of Tungsten Trioxide Films. *J. Mater. Chem. C* **2014**, *2* (44), 9467–9477.

(4) Zhu, M.; Meng, W.; Huang, Y.; Huang, Y.; Zhi, C. Proton-Insertion-Enhanced Pseudocapacitance Based on the Assembly Structure of Tungsten Oxide. *ACS Appl. Mater. Interfaces* **2014**, *6* (21), 18901–18910.

(5) Shirke, Y. M.; Porel Mukherjee, S. Selective Synthesis of $WO_3$ and $W_{18}O_{49}$ Nanostructures: Ligand-Free pH-Dependent Morphology-Controlled Self-Assembly of

Hierarchical Architectures from 1D Nanostructure and Sunlight-Driven Photocatalytic Degradation. *CrystEngComm* **2017**, *19* (15), 2096–2105.

(6) Li, N.; Zheng, Y.; Wei, L.; Teng, H.; Zhou, J. Metal Nanoparticles Supported on $WO_3$ Nanosheets for Highly Selective Hydrogenolysis of Cellulose to Ethylene Glycol. *Green Chem.* **2017**, *19* (3), 682–691.

(7) Ghosh, S.; Acharyya, S. S.; Kumar, M.; Bal, R. Chloride Promoted Room Temperature Preparation of Silver Nanoparticles on Two Dimensional Tungsten Oxide Nanoarchitectures for the Catalytic Oxidation of Tertiary N-Compounds to N-Oxides. *Nanoscale* **2015**, *7* (37), 15197–15208.

(8) Nagy, D.; Nagy, D.; Szilagyi, I. M.; Fan, X. Effect of the Morphology and Phases of $WO_3$ Nanocrystals on Their Photocatalytic Efficiency. *RSC Adv.* **2016**, *6* (40), 33743–33754.

(9) Park, C. Y.; Seo, J. M.; Jo, H.; Park, J.; Ok, K. M.; Park, T. J. Hexagonal Tungsten Oxide Nanoflowers as Enzymatic Mimetics and Electrocatalysts. *Sci. Rep.* **2017**, *7* (January), 40928.

(10) Tu, J.; Lei, H.; Yu, Z.; Jiao, S. Ordered WO3−x Nanorods: Facile Synthesis and Their Electrochemical Properties for Aluminum-Ion Batteries. *Chem. Commun.* **2018**, *54* (11), 1343–1346.

(11) Qiu, M.; Sun, P.; Shen, L.; Wang, K.; Song, S.; Yu, X.; Tan, S.; Zhao, C.; Mai, W. WO 3 Nanoflowers with Excellent Pseudo-Capacitive Performance and the Capacitance Contribution Analysis. *J. Mater. Chem. A* **2016**, *4* (19), 7266–7273.

(12) Chem, J. M.; Yin, J.; Cao, H.; Lu, Y. Self-Assembly into Magnetic $Co_3O_4$ Complex Nanostructures as Peroxidase †. **2012**, 527–534.

(13) Cao, H.; Zheng, H.; Liu, K.; Warner, J. H. Bioinspired Peony-Like b-$Ni(OH)_2$ Nanostructures with Enhanced Electrochemical Activity and Superhydrophobicity. **2010**, 489–494.

(14) Cao, H.; Zheng, H.; Yin, J.; Lu, Y.; Wu, S.; Wu, X. $Mg(OH)_2$ Complex Nanostructures with Superhydrophobicity and Flame Retardant Effects. **2010**, 17362–17368.

(15) Ireland, N.; Utrecht, O. C. /P 1 : **1961**, *555* (1957), 475–485.

(16) Wen, N.; Brooker, M. H. Urea Protonation: Raman and Theoretical. **1993**, *2*, 8608–

8616.

(17) Bortoluzzi, M.; Evangelisti, C.; Marchetti, F.; Pampaloni, G.; Piccinelli, F.; Zacchini, S. Synthesis of a Highly Reactive Form of $WO_2Cl_2$, Its Conversion into Nanocrystalline Mono-Hydrated $WO_3$ and Coordination Compounds with Tetramethylurea. *Dalt. Trans.* **2016**, *45* (1), 15342–15349.

(18) Bortoluzzi, M.; Marchetti, F.; Pampaloni, G.; Zacchini, S. The Chemistry of High Valent Tungsten Chlorides with: N -Substituted Ureas, Including Urea Self-Protonation Reactions Triggered by $WCl_6$. *New J. Chem.* **2016**, *40* (10), 8271–8281.

(19) Chen, P.; Qin, M.; Chen, Z.; Jia, B.; Qu, X. Solution Combustion Synthesis of Nanosized $WO_x$: Characterization, Mechanism and Excellent Photocatalytic Properties. *RSC Adv.* **2016**, *6* (86), 83101–83109.

(20) De Ribamar Martins Neto, J.; Torresi, R. M.; Cordoba De Torresi, S. I. Electrochromic Behavior of $WO_3$ Nanoplate Thin Films in Acid Aqueous Solution and a Protic Ionic Liquid. *J. Electroanal. Chem.* **2016**, *765*, 111–117.

(21) Kattouf, B.; Ein-Eli, Y.; Siegmann, A.; Frey, G. L. Hybrid Mesostructured Electrodes for Fast-Switching Proton-Based Solid State Electrochromic Devices. *J. Mater. Chem. C* **2013**, *1* (1), 151.

(22) Nagaraju, P.; Arivanandhan, M.; Alsalme, A.; Alghamdi, A.; Jayavel, R. Enhanced Electrochemical Performance of α-$MoO_3$/Graphene Nanocomposites Prepared by an in Situ Microwave Irradiation Technique for Energy Storage Applications. *RSC Adv.* **2020**, *10* (38), 22836–22847.

(23) Wu, Q.-L.; Zhao, S.-X.; Yu, L.; Zheng, X.-X.; Wang, Y.-F.; Yu, L.-Q.; Nan, C.-W.; Cao, G. Oxygen Vacancy-Enriched $MoO_{3-x}$ Nanobelts for Asymmetric Supercapacitors with Excellent Room/Low Temperature Performance. *J. Mater. Chem. A* **2019**, *7* (21), 13205–13214.

(24) Lokhande, V.; Lokhande, A.; Namkoong, G.; Kim, J. H.; Ji, T. Charge Storage in $WO_3$ Polymorphs and Their Application as Supercapacitor Electrode Material. *Results Phys.* **2019**, *12* (February 2019), 2012–2020.

(25) Bignozzi, C. A.; Caramori, S.; Cristino, V.; Argazzi, R.; Meda, L.; Tacca, A. Nanostructured Photoelectrodes Based on $WO_3$: Applications to Photooxidation of Aqueous Electrolytes. *Chem. Soc. Rev. Chem. Soc. Rev* **2013**, *42* (6), 2228–2246.

(26) Li, F.; Ran, J.; Jaroniec, M.; Qiao, S. Z. Solution Combustion Synthesis of Metal Oxide Nanomaterials for Energy Storage and Conversion. *Nanoscale* **2015**, *7* (42), 17590–17610.

(27) Naik, A. P.; Salkar, A. V.; Majik, M. S.; Morajkar, P. P. Enhanced Photocatalytic Degradation of Amaranth Dye on Mesoporous Anatase TiO$_2$ : Evidence of C–N, N□N Bond Cleavage and Identification of New Intermediates. *Photochem. Photobiol. Sci.* **2017**, *16* (7), 1126–1138.

(28) Simic, V.; Bouteiller, L.; Jalabert, M. Highly Cooperative Formation of Bis-Urea Based Supramolecular Polymers. *J. Am. Chem. Soc.* **2003**, *125* (43), 13148–13154.

(29) Custelcean, R. Crystal Engineering with Urea and Thiourea Hydrogen-Bonding Groups. *Chem. Commun.* **2008**, No. 3, 295–307.

(30) Koshti, V. S.; Thorat, S. H.; Gote, R. P.; Chikkali, S. H.; Gonnade, R. G. The Impact of Modular Substitution on Crystal Packing: The Tale of Two Ureas. *CrystEngComm* **2016**, *18* (37), 7078–7094.

(31) Sindt, A. J.; Smith, M. D.; Pellechia, P. J.; Shimizu, L. S. Thioureas and Squaramides: Comparison with Ureas as Assembly Directing Motifs for m -Xylene Macrocycles. *Cryst. Growth Des.* **2018**, *18* (3), 1605–1612.

(32) Morajkar, P. P.; B. Fernandes, J.; Fernandes, J. B. A New Facile Method to Synthesize Mesoporous γ-Al$_2$O$_3$ of High Surface Area and Catalytic Activity. *Catal. Commun.* **2010**, *11* (5), 414–418.

(33) Salkar, A. V.; Naik, A. P.; Joshi, V. S.; Haram, S. K.; Morajkar, P. P. Designing a 3D Nanoporous Network: Via Self-Assembly of WO$_3$ Nanorods for Improved Electrocapacitive Performance. *CrystEngComm* **2018**, *20* (42), 6683–6694.

(34) Varma, A.; Mukasyan, A. S.; Rogachev, A. S.; Manukyan, K. V. Solution Combustion Synthesis of Nanoscale Materials. *Chem. Rev.* **2016**, *116* (23), 14493–14586.

(35) Yin, J.; Cao, H.; Zhang, J.; Qu, M.; Zhou, Z. Synthesis and Applications of γ-Tungsten Oxide Hierarchical Nanostructures. *Cryst. Growth Des.* **2013**, *13* (2), 759–769.

(36) Nayak, A. K.; Verma, M.; Sohn, Y.; Deshpande, P. A.; Pradhan, D. Highly Active Tungsten Oxide Nanoplate Electrocatalysts for the Hydrogen Evolution Reaction in Acidic and near Neutral Electrolytes. *ACS Omega* **2017**, *2* (10), 7039–7047.

(37) Pokhrel, S.; Birkenstock, J.; Schowalter, M.; Rosenauer, A.; Mädler, L. Growth of

Ultrafine Single Crystalline $WO_3$ Nanoparticles Using Flame Spray Pyrolysis. *Cryst. Growth Des.* **2010**, *10* (2), 632–639.

(38) Kalanur, S. S.; Hwang, Y. J.; Chae, S. Y.; Joo, O. S. Facile Growth of Aligned $WO_3$ Nanorods on FTO Substrate for Enhanced Photoanodic Water Oxidation Activity. *J. Mater. Chem. A* **2013**, *1* (10), 3479.

(39) Arvizu, M. A.; Qu, H. Y.; Cindemir, U.; Qiu, Z.; Rojas-González, E. A.; Primetzhofer, D.; Granqvist, C. G.; Österlund, L.; Niklasson, G. A. Electrochromic $WO_3$ Thin Films Attain Unprecedented Durability by Potentiostatic Pretreatment. *J. Mater. Chem. A* **2019**, *7* (6), 2908–2918.

(40) Song, J.; Huang, Z. F.; Pan, L.; Zou, J. J.; Zhang, X.; Wang, L. Oxygen-Deficient Tungsten Oxide as Versatile and Efficient Hydrogenation Catalyst. *ACS Catal.* **2015**, *5* (11), 6594–6599.

(41) Shea, L. E.; Collins, M.; Hirschfel, D. Combustion Synthesis and Effects of Processing Parameters on Physical Properties of A-Alumina. *Am. Ceram. Soc.* **2000**.

(42) Yan, Q.-L.; Yang, Z.; Zhang, X.-X.; Lyu, J.-Y.; He, W.; Huang, S.; Liu, P.-J.; Zhang, C.; Zhang, Q.-H.; He, G.-Q.; Nie, F.-D. High Density Assembly of Energetic Molecules under the Constraint of Defected 2D Materials. *J. Mater. Chem. A* **2019**, *7* (30), 17806–17814.

(43) Kabo, G. Y.; Miroshnichenko, E. A.; Frenkel, M. L.; Kozyro, A. A.; Simirskii, V. V; Krasulin, A. P.; Vorob'eva, V. P.; Lebedev, Y. A. Thermochemistry of Alkyl Derivatives of Urea. *Bull. Acad. Sci. USSR, Div. Chem. Sci.* **1990**, *39* (4), 662–667.

(44) Tischer, S.; Börnhorst, M.; Amsler, J.; Schoch, G.; Deutschmann, O. Thermodynamics and Reaction Mechanism of Urea Decomposition. *Phys. Chem. Chem. Phys.* **2019**, *21* (30), 16785–16797.

(45) Dorofeeva, O. V.; Ryzhova, O. N.; Suchkova, T. A. Enthalpies of Formation of Hydrazine and Its Derivatives. *J. Phys. Chem. A* **2017**, *121* (28), 5361–5370.

(46) Kwong, W. L.; Koshy, P.; Hart, J. N.; Xu, W.; Sorrell, C. C. Critical Role of {002} Preferred Orientation on Electronic Band Structure of Electrodeposited Monoclinic $WO_3$ Thin Films. *Sustain. Energy Fuels* **2018**, *2* (10), 2224–2236.

(47) Valdś, Á.; Kroes, G. J. First Principles Study of the Photo-Oxidation of Water on Tungsten Trioxide ($WO_3$). *J. Chem. Phys.* **2009**, *130* (11).

(48) Xie, Y. P.; Liu, G.; Yin, L.; Cheng, H.-M. M. Crystal Facet-Dependent Photocatalytic Oxidation and Reduction Reactivity of Monoclinic $WO_3$ for Solar Energy Conversion. *J. Mater. Chem.* **2012**, *22* (14), 6746–6751.

(49) Zheng, J. Y.; Haider, Z.; Van, T. K.; Pawar, A. U.; Kang, M. J.; Kim, C. W.; Kang, Y. S. Tuning of the Crystal Engineering and Photoelectrochemical Properties of Crystalline Tungsten Oxide for Optoelectronic Device Applications. *CrystEngComm* **2015**, *17* (32), 6070–6093.

(50) Guo, Y.; Quan, X.; Lu, N.; Zhao, H.; Chen, S. High Photocatalytic Capability of Self-Assembled Nanoporous $WO_3$ with Preferential Orientation of (002) Planes. *Environ. Sci. Technol.* **2007**, *41* (12), 4422–4427.

(51) Malyshev, D. A.; Dhami, K.; Lavergne, T.; Chen, T.; Dai, N.; Foster, J. M.; Corrêa, I. R.; Romesberg, F. E. A Semi-Synthetic Organism with an Expanded Genetic Alphabet. *Nature* **2014**, *509* (7500), 385–388.

(52) Nielsen, P. E. Peptide Nucleic Acid: A Versatile Tool in Genetic Diagnostics and Molecular Biology. *Curr. Opin. Biotechnol.* **2001**, *12* (1), 16–20.

(53) Zhao, M.-Q.; Zhang, Q.; Tian, G.-L.; Wei, F. Emerging Double Helical Nanostructures. *Nanoscale* **2014**, *6* (16), 9339–9354.

(54) Saleh, L. M. A.; Dziedzic, R.; Spokoyny, A. M. An Inorganic Twist in Nanomaterials: Making an Atomically Precise Double Helix. *ACS Cent. Sci.* **2016**, *2* (10), 685–686.

(55) Abendroth, J. M.; Nakatsuka, N.; Ye, M.; Kim, D.; Fullerton, E. E.; Andrews, A. M.; Weiss, P. S. Analyzing Spin Selectivity in DNA-Mediated Charge Transfer via Fluorescence Microscopy. *ACS Nano* **2017**, *11* (7), 7516–7526.

(56) Xu, X.; Winterwerber, P.; Ng, D.; Wu, Y. DNA-Programmed Chemical Synthesis of Polymers and Inorganic Nanomaterials. *Top. Curr. Chem.* **2020**, *378* (2), 31.

(57) Suzuki, N.; Wang, Y.; Elvati, P.; Qu, Z.-B.; Kim, K.; Jiang, S.; Baumeister, E.; Lee, J.; Yeom, B.; Bahng, J. H.; Lee, J.; Violi, A.; Kotov, N. A. Chiral Graphene Quantum Dots. *ACS Nano* **2016**, *10* (2), 1744–1755.

(58) Hou, H.; Jun, Z.; Weller, F.; Greiner, A. Large-Scale Synthesis and Characterization of Helically Coiled Carbon Nanotubes by Use of $Fe(CO)_5$ as Floating Catalyst Precursor. *Chem. Mater.* **2003**, *15* (16), 3170–3175.

(59) Gao, P. X.; Ding, Y.; Mai, W.; Hughes, W. L.; Lao, C.; Wang, Z. L. Conversion of

Zinc Oxide Nanobelts into Superlattice-Structured Nanohelices. *Science (80).* **2005**, *309* (5741), 1700 LP – 1704.

(60) Wu, X.; Jin, H.; Liu, Z.; Ohsuna, T.; Terasaki, O.; Sakamoto, K.; Che, S. Racemic Helical Mesoporous Silica Formation by Achiral Anionic Surfactant. *Chem. Mater.* **2006**, *18* (2), 241–243.

(61) Jung, J. H.; Yoshida, K.; Shimizu, T. Creation of Novel Double-Helical Silica Nanotubes Using Binary Gel System. *Langmuir* **2002**, *18* (23), 8724–8727.

(62) Sharma, J.; Chhabra, R.; Cheng, A.; Brownell, J.; Liu, Y.; Yan, H. Control of Self-Assembly of DNA Tubules Through Integration of Gold Nanoparticles. *Science (80).* **2009**, *323* (5910), 112 LP – 116.

(63) Wang, L.; Xu, X.; Wu, S.; Cao, F. Nonstoichiometric Tungsten Oxide Residing in a 3D Nitrogen Doped Carbon Matrix a Composite Photocatalyst for Oxygen Vacancy Induced VOC Degradation and $H_2$ Production. *Catal. Sci. Technol.* **2018**, *8* (5), 1366–1374.

(64) Khan, Q. A.; Shaur, A.; Khan, T. A.; Joya, Y. F.; Awan, M. S.; Ali, Q.; Shaur, A.; Khan, T. A.; Joya, Y. F.; Awan, M. S. Characterization of Reduced Graphene Oxide Produced through a Modified Hoffman Method Characterization of Reduced Graphene Oxide Produced through a Modified Hoffman Method. *Cogent Chem.* **2017**, *3*, 1298980.

(65) Wang, M.; Yang, J.; Liu, S.; Li, M.; Hu, C.; Qiu, J. Nitrogen-Doped Hierarchically Porous Carbon Nanosheets Derived from Polymer/Graphene Oxide Hydrogels for High-Performance Supercapacitors. *J. Colloid Interface Sci.* **2020**, *560,* 69–76.

(66) He, X.; Xie, X.; Wang, J.; Ma, X.; Xie, Y.; Gu, J.; Xiao, N.; Qiu, J. From Fluorene Molecules to Ultrathin Carbon Nanonets with an Enhanced Charge Transfer Capability for Supercapacitors. *Nanoscale* **2019**, *11* (14), 6610–6619.

(67) Wei, F.; He, X.; Zhang, H.; Liu, Z.; Xiao, N.; Qiu, J. Crumpled Carbon Nanonets Derived from Anthracene Oil for High Energy Density Supercapacitor. *J. Power Sources* **2019**, *428,* 8–12.

(68) Claramunt, S.; Varea, A.; López-Díaz, D.; Velázquez, M. M.; Cornet, A.; Cirera, A. The Importance of Interbands on the Interpretation of the Raman Spectrum of Graphene Oxide. *J. Phys. Chem. C* **2015**, *119* (18), 10123–10129.

(69) Morajkar, P. P.; Guerrero, G. D. J.; Raj, A.; Elkadi, M.; Rahman, R. K.; Salkar, A. V; Pillay, A.; Anjana, T.; Cha, M. S.; Guerrero Peña, G. D. J.; Raj, A.; Elkadi, M.; Rahman, R. K.; Salkar, A. V; Pillay, A.; Anjana, T.; Cha, M. S. Effects of Camphor Oil Addition to Diesel on the Nanostructures and Oxidative Reactivity of Combustion-Generated Soot. *Energy & Fuels* **2019**, *33* (12), 12852–12864.

(70) Xu, J.; Li, C.; Chen, L.; Li, Z.; Bing, P. Anchoring Carbon Layers and Oxygen Vacancies Endow $WO_{3-x}$/C Electrode with High Specific Capacity and Rate Performance for Supercapacitors. *RSC Adv.* **2019**, *9* (49), 28793–28798.

(71) Meng, J.; Lin, Q.; Chen, T.; Wei, X.; Li, J.; Zhang, Z. Oxygen Vacancy Regulation on Tungsten Oxides with Specific Exposed Facets for Enhanced Visible-Light-Driven Photocatalytic Oxidation. *Nanoscale* **2018**, *10* (6), 2908–2915.

(72) Zhao, Y.; Balasubramanyam, S.; Sinha, R.; Lavrijsen, R.; Verheijen, M. A.; Bol, A. A.; Bieberle-Hütter, A. Physical and Chemical Defects in $WO_3$ Thin Films and Their Impact on Photoelectrochemical Water Splitting. *ACS Appl. Energy Mater.* **2018**, *1* (11), 5887–5895.

(73) Shi, W.; Zhang, X.; Brillet, J.; Huang, D.; Li, M.; Wang, M.; Shen, Y. Significant Enhancement of the Photoelectrochemical Activity of $WO_3$ Nanoflakes by Carbon Quantum Dots Decoration. *Carbon N. Y.* **2016**, *105*, 387–393.

(74) Liu, S.-J.; Yuan, Y.; Zheng, S.-L.; Zhang, J.-H.; Wang, Y. Fabrication of C-Doped $WO_3$ Nanoparticle Cluster Arrays from PS-b-P4VP for Room Temperature H2 Sensing. *Dalt. Trans.* **2015**, *44* (25), 11360–11367.

(75) Castillero, P.; Rico-Gavira, V.; López-Santos, C.; Barranco, A.; Pérez-Dieste, V.; Escudero, C.; Espinós, J. P.; González-Elipe, A. R. Formation of Subsurface $W^{5+}$ Species in Gasochromic Pt/$WO_3$ Thin Films Exposed to Hydrogen. *J. Phys. Chem. C* **2017**, *121* (29), 15719–15727.

(76) Li, Y.; Tang, Z.; Zhang, J.; Zhang, Z. Defect Engineering of Air-Treated $WO_3$ and Its Enhanced Visible-Light-Driven Photocatalytic and Electrochemical Performance. *J. Phys. Chem. C* **2016**, *120* (18), 9750–9763.

(77) Kim, H. S.; Cook, J. B.; Lin, H.; Ko, J. S.; Tolbert, S. H.; Ozolins, V.; Dunn, B. Oxygen Vacancies Enhance Pseudocapacitive Charge Storage Properties of $MoO_{3-x}$. *Nat. Mater.* **2017**, *16* (4), 454–462.

(78) Dong, Y.; Shao, J.; Chen, C.; Li, H.; Wang, R.; Chi, Y.; Lin, X.; Chen, G. Blue Luminescent Graphene Quantum Dots and Graphene Oxide Prepared by Tuning the Carbonization Degree of Citric Acid. *Carbon N. Y.* **2012**, *50* (12), 4738–4743.

(79) Huang, J. J.; Rong, M. Z.; Zhang, M. Q. Preparation of Graphene Oxide and Polymer-like Quantum Dots and Their One- and Two-Photon Induced Fluorescence Properties. *Phys. Chem. Chem. Phys.* **2016**, *18* (6), 4800–4806.

(80) Zhang, D.; Zhang, C.; Liu, J.; Chen, Q.; Zhu, X.; Liang, C. Carbon-Encapsulated Metal/Metal Carbide/Metal Oxide Core–Shell Nanostructures Generated by Laser Ablation of Metals in Organic Solvents. *ACS Appl. Nano Mater.* **2019**, *2* (1), 28–39.

(81) Creighton, M. A.; Yuen, M. C.; Morris, N. J.; Tabor, C. E. Graphene-Based Encapsulation of Liquid Metal Particles. *Nanoscale* **2020**.

(82) Samanta, A.; Liu, Z.; Nalluri, S. K. M.; Zhang, Y.; Schatz, G. C.; Stoddart, J. F. Supramolecular Double-Helix Formation by Diastereoisomeric Conformations of Configurationally Enantiomeric Macrocycles. *J. Am. Chem. Soc.* **2016**, *138* (43), 14469–14480.

(83) Zeng, H.; Miller, R. S.; Flowers, R. A.; Gong, B. A Highly Stable, Six-Hydrogen-Bonded Molecular Duplex. *J. Am. Chem. Soc.* **2000**, *122* (11), 2635–2644.

(84) Di Blasio, B.; Benedetti, E.; Pavone, V.; Pedone, C.; Gerber, C.; Lorenzi, G. P. Regularly Alternating L,D-Peptides. II. The Double-Stranded Right-Handed Antiparallel β-Helix in the Structure of t-Boc-(L-Phe-D-Phe)4-OMe. *Biopolymers* **1989**, *28* (1), 203–214.

(85) Engelkamp, H.; Middelbeek, S.; R., J. M.; Nolte. Self-Assembly of Disk-Shaped Molecules to Coiled-Coil Aggregates with Tunable Helicity. *Science (80).* **1999**, *284* (5415), 785–788.

(86) Berl, V.; Huc, I.; Khoury, R. G.; Krische, M. J.; Lehn, J.-M. Interconversion of Single and Double Helices Formed from Synthetic Molecular Strands. *Nature* **2000**, *407* (6805), 720–723.

(87) Xiao, L.; Lv, Y.; Dong, W.; Zhang, N.; Liu, X. Dual-Functional $WO_3$ Nanocolumns with Broadband Antireflective and High-Performance Flexible Electrochromic Properties. *ACS Appl. Mater. Interfaces* **2016**, *8* (40), 27107–27114.

(88) Na, Z.; Wang, X.; Yin, D.; Wang, L. Graphite Felts Modified by Vertical Two-

Dimensional $WO_3$ Nanowall Arrays: High-Performance Electrode Materials for Cerium-Based Redox Flow Batteries. *Nanoscale* **2018**, *10* (22), 10705–10712.

(89) Wang, F.; Zhan, X.; Cheng, Z.; Wang, Z.; Wang, Q.; Xu, K.; Safdar, M.; He, J. Tungsten Oxide@Polypyrrole Core–Shell Nanowire Arrays as Novel Negative Electrodes for Asymmetric Supercapacitors. *Small* **2015**, *11* (6), 749–755.

(90) Gao, L.; Wang, X.; Xie, Z.; Song, W.; Wang, L.; Wu, X.; Qu, F.; Chen, D.; Shen, G. High-Performance Energy-Storage Devices Based on $WO_3$ Nanowire Arrays/Carbon Cloth Integrated Electrodes. *J. Mater. Chem. A* **2013**, *1* (24), 7167–7173.

(91) Tian, Y.; Cong, S.; Su, W.; Chen, H.; Li, Q.; Geng, F.; Zhao, Z. Synergy of $W_{18}O_{49}$ and Polyaniline for Smart Supercapacitor Electrode Integrated with Energy Level Indicating Functionality. *Nano Lett.* **2014**, *14* (4), 2150–2156.

(92) Nayak, A. K.; Das, A. K.; Pradhan, D. High Performance Solid-State Asymmetric Supercapacitor Using Green Synthesized Graphene–$WO_3$ Nanowires Nanocomposite. *ACS Sustain. Chem. Eng.* **2017**, *5* (11), 10128–10138.

(93) Huang, X.; Liu, H.; Zhang, X.; Jiang, H. High Performance All-Solid-State Flexible Micro-Pseudocapacitor Based on Hierarchically Nanostructured Tungsten Trioxide Composite. *ACS Appl. Mater. Interfaces* **2015**, *7* (50), 27845–27852.

(94) Gupta, S. P.; More, M. A.; Late, D. J.; Walke, P. S. High-Rate Quasi-Solid-State Hybrid Supercapacitor of Hierarchical Flowers of Hydrated Tungsten Oxide Nanosheets. *Electrochim. Acta* **2021**, *366*.

(95) Peng, H.; Ma, G.; Sun, K.; Mu, J.; Luo, M.; Lei, Z. High-Performance Aqueous Asymmetric Supercapacitor Based on Carbon Nanofibers Network and Tungsten Trioxide Nanorod Bundles Electrodes. *Electrochim. Acta* **2014**, *147*, 54–61.

(96) Sun, K.; Hua, F.; Cui, S.; Zhu, Y.; Peng, H.; Ma, G. An Asymmetric Supercapacitor Based on Controllable $WO_3$ Nanorod Bundle and Alfalfa-Derived Porous Carbon. *RSC Adv.* **2021**, *11* (59), 37631–37642.

(97) Zheng, F.; Xi, C.; Xu, J.; Yu, Y.; Yang, W.; Hu, P.; Li, Y.; Zhen, Q.; Bashir, S.; Liu, J. L. Facile Preparation of $WO_3$ Nano-Fibers with Super Large Aspect Ratio for High Performance Supercapacitor. *J. Alloys Compd.* **2019**, *772*, 933–942.

(98) Kim, K.-W.; Yun, T. Y.; You, S.-H.; Tang, X.; Lee, J.; Seo, Y.; Kim, Y.-T.; Kim, S. H.; Moon, H. C.; Kim, J. K. Extremely Fast Electrochromic Supercapacitors Based on

Mesoporous $WO_3$ Prepared by an Evaporation-Induced Self-Assembly. *NPG Asia Mater.* **2020**, *12* (1), 84.

(99) Rani, A.; Reddy, R.; Sharma, U.; Mukherjee, P.; Mishra, P.; Kuila, A.; Sim, L. C.; Saravanan, P. A Review on the Progress of Nanostructure Materials for Energy Harnessing and Environmental Remediation. *J. Nanostructure Chem.* **2018**, *8* (3), 255–291.

# CHAPTER IV:

# $MoO_{3-x}$ MICROSTRUCTURES AS CHARGE STORAGE ELECTRODE MATERIALS

\

## 4.1 PROLOGUE

Designing nanostructured transition metal oxides by tuning their dimensionality from 0D to 3D nanostructures has demonstrated exceptional material performance in a vast range of energy and environmental applications.[1–4] The remarkable performance and vast utility of graphene sheets in varied applications such as electronics, photovoltaics, and energy storage systems paved the way for a pursuit in the exploration of new two-dimensional (2D) materials.[5–7] The exceptional mechanical and electronic properties associated with the 2D materials make them significant contributors to technological innovation and development.[8,9] The unique properties of 2D nano/micro-materials often arise from the charge carrier's quantum confinement along a single plane.[10] Characteristic material properties such as their surface heterostructure, surface-to-volume ratio, density, stacking efficiency, and defect structure of 2D architectures govern their energy application utilization.[11,12] A control, if established over these properties of 2D nano/micromaterials, enable them as suitable candidates for next-generation electronic devices, especially supercapacitors. Although there are several reports on the design and synthesis of 2D materials, tailoring their properties via facile and cost-effective synthesis routes remains a challenge to be addressed to achieve sustainable development.[13,14]

Among 2D microstructured transition metal oxides, the non-stoichiometric molybdenum oxides ($MoO_{3-x}$) have gained immense popularity due to their ability to maintain multiple oxidation states, which in turn impart it with exceptional electrochemical performance.[15,16] $\alpha$-$MoO_3$ possesses a layered crystal structure that consists of $MoO_6$ octahedra with well-defined planes which are held together by weak van der Waals (vdW) forces.[17–19] Thus, the existence of weak vdW interlayer interactions along with strong intralayer chemical bonds (Mo-O) enables $MoO_3$ to be exfoliated much like graphene and deposited in the form of 2D films consisting of a large surface-to-volume ratios.[16] If appropriately tuned, the suitable aspect ratio of $MoO_3$ can lead to a higher number of catalytically active edge sites. As a result of a greater number of exposed surface facets associated with 2D architecture, these materials inherently exhibit enhancement in surface defect structure such as anion vacancies, dislocation defects such as edges, kinks, terraces, etc. which enhances the surface-active centers and endow greater charge storage properties.[20] Due to these distinguishing characteristics and ecofriendly nature, 2D $MoO_{3-x}$ has found a place in various applications especially in charge-storage devices.

Therefore, in the present work, we emphasize the combined role of protonated urea and the pH-dependent chemistry of polymolybdate ions, as a simple tool to achieve tunable 2D $MoO_{3-x}$ architectures. The tunable synthesis has been achieved by establishing control over the hydrolysis and polycondensation processes by optimizing protonated urea concentration and solution pH to produce 2D $MoO_{3-x}$ truncated microplates and microdisks. The present approach enables a tailored synthesis for the generation of 2D $MoO_{3-x}$ microstructures, which showcases excellent supercapacitor performance in a three-electrode and a two-electrode asymmetric device configuration. These results have been discussed in more detail in the subsequent sections. Thus in the present chapter, various microstructures of $MoO_{3-x}$ have been presented that are synthesized using modified sol-gel methods. The synthesis were performed using various structure directing agents such as urea, carbohydrazide, semicarbazide, N-methylurea, tetramethylurea and citric acid. The details of chemicals used and synthesis procedures are presented in sections 2.1 and 2.2, respectively. The effect of various synthesis parameters such as solution pH, calcination temperature, reaction time, metal to SDA ratio on the morphology of $MoO_{3-x}$ was investigated in detail. The synthesized $MoO_{3-x}$ were characterized using the different characterization techniques as listed in section 2.3. All the synthesized $MoO_{3-x}$ microstructures were used to fabricate electrodes which were evaluated for their charge-storage performance. The novel findings of this investigation have been presented in detail in the results and discussion section 4.2, along with the conclusions of this study in section 4.9.

## 4.2 RESULTS AND DISCUSSIONS

### 4.2.1 Morphological studies

Figure 4.1 presents the microstructural characterization (SEM, TEM, and SAED) for the different $MoO_{3-x}$ morphologies obtained under different pH conditions. It was observed that different $MoO_{3-x}$ morphologies could be obtained by tuning the synthesis pH. The pH 3, 5, and 8 produced $MoO_{3-x}$ microplates, $MoO_{3-x}$ microdisks, and an unstructured agglomerated morphology, (henceforth denoted as MP, MD, and MA) respectively. More detailed information about the microstructure was deduced from the results of HRTEM and SAED analysis. The HRTEM analysis of MP and MD revealed the lattice fringes with d-spacing values of ≈ 0.346 nm and 0.326 nm corresponding to the (040) and (021) planes of orthorhombic $MoO_{3-x}$, respectively.[21,22] The dominance of (040) planes also suggests the unidirectional growth of $MoO_{3-x}$ microplates. Mixed fringes corresponding to both the (040) and (021) planes were observed in the case of MA, which resulted from unstructured, heavily agglomerated morphology. The SAED patterns (Figure 4.1 C, F, and I) revealed the monocrystalline nature in MP, MD, and MA, respectively but the brightness and intensity of the spots decreased in the order MP > MD > MA, indicating that the $MoO_{3-x}$ microplates were relatively more crystalline among the three materials.

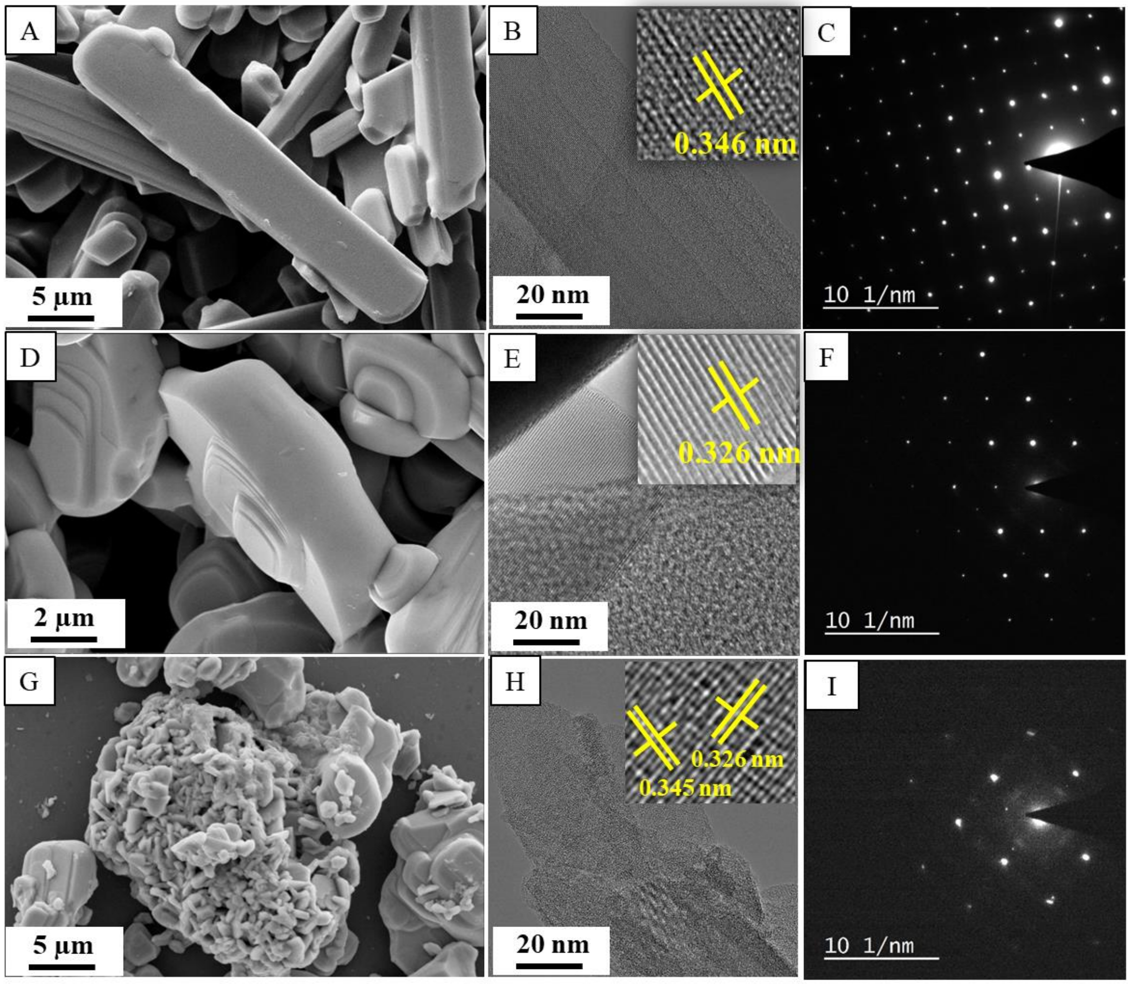

**Figure 4.1:** SEM micrographs (A, D & G); HRTEM micrographs (B, E & H); and SAED (D, F & I) analysis of pH 2.5, 5, and 8 respectively.

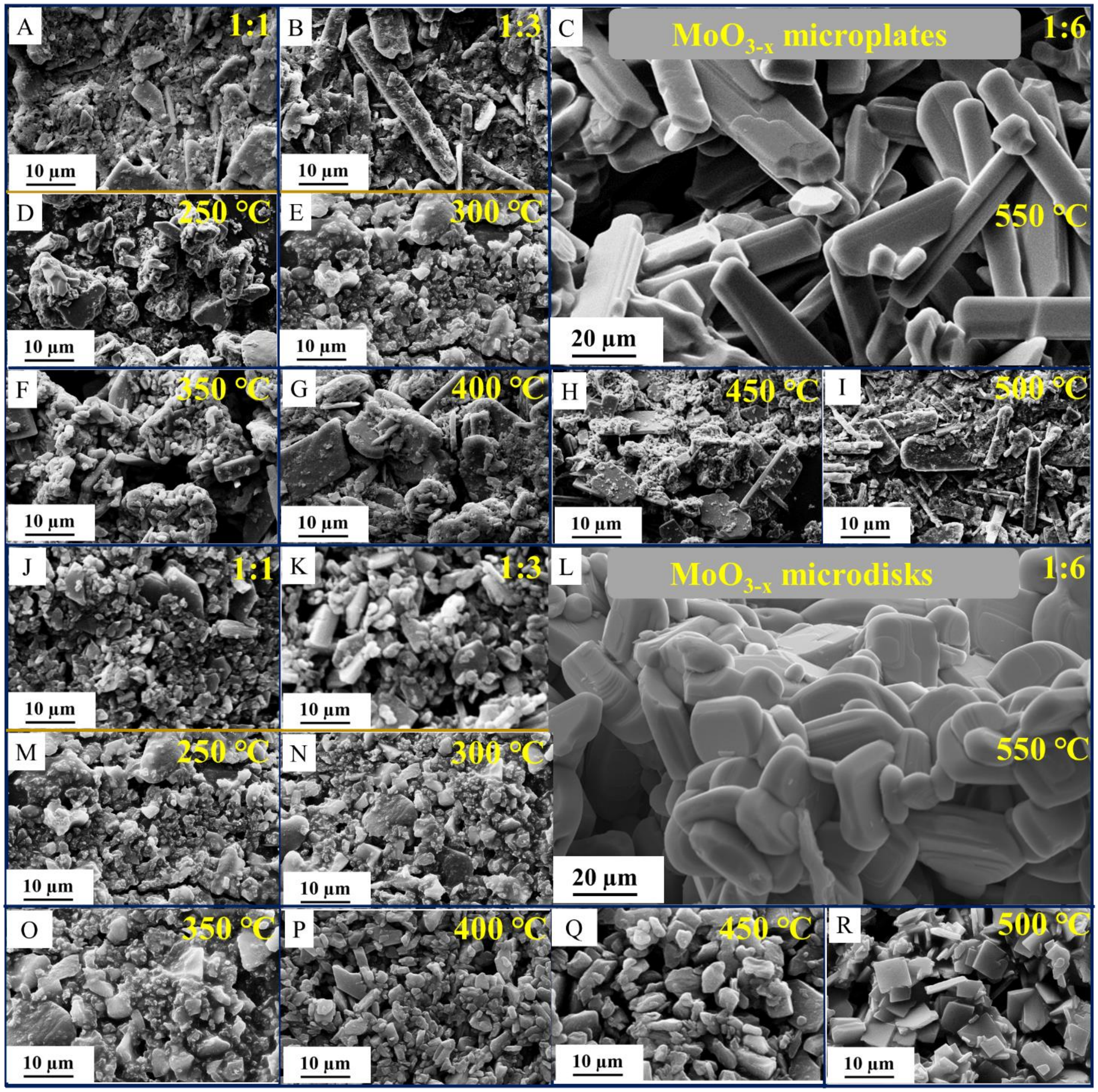

**Figure 4.2:** SEM images (A, B, and F, G) Mo: Urea ratio of 1:1 and 1:3 for MP and MD formation. (D-I and M-R) Intermediate calcination stages from 250-550 °C for MP and MD. C and L are the SEM images of MP and MD at optimized conditions.

Additional factors which influenced the MP and MD morphologies, such as Mo : Urea ratio and calcination temperature, were also investigated. Figure 4.2 (A-C) and (J-L) show the different ratios of Mo : Urea for MP and MD, respectively. It was observed that Mo : Urea ratio $\geq$ 1 : 6 was effective in producing consistent morphologies of MP and MD.

Furthermore, it was also observed that in the absence of urea, no microstructure formation took place. (refer figure SF19 in Annexure-I) The requirement of excess protons to neutralize the isopolymolybdate anions, as mentioned by Lou *et al.*[23] could be one of the reasons, along with the requirement of sufficient thermal energy produced during urea combustion to construct the 2D architecture. SEM analysis of samples obtained within the calcination range of 250 to 550 ℃ revealed the gradual formation of MP and MD.

### 4.2.2 TG-DTA studies

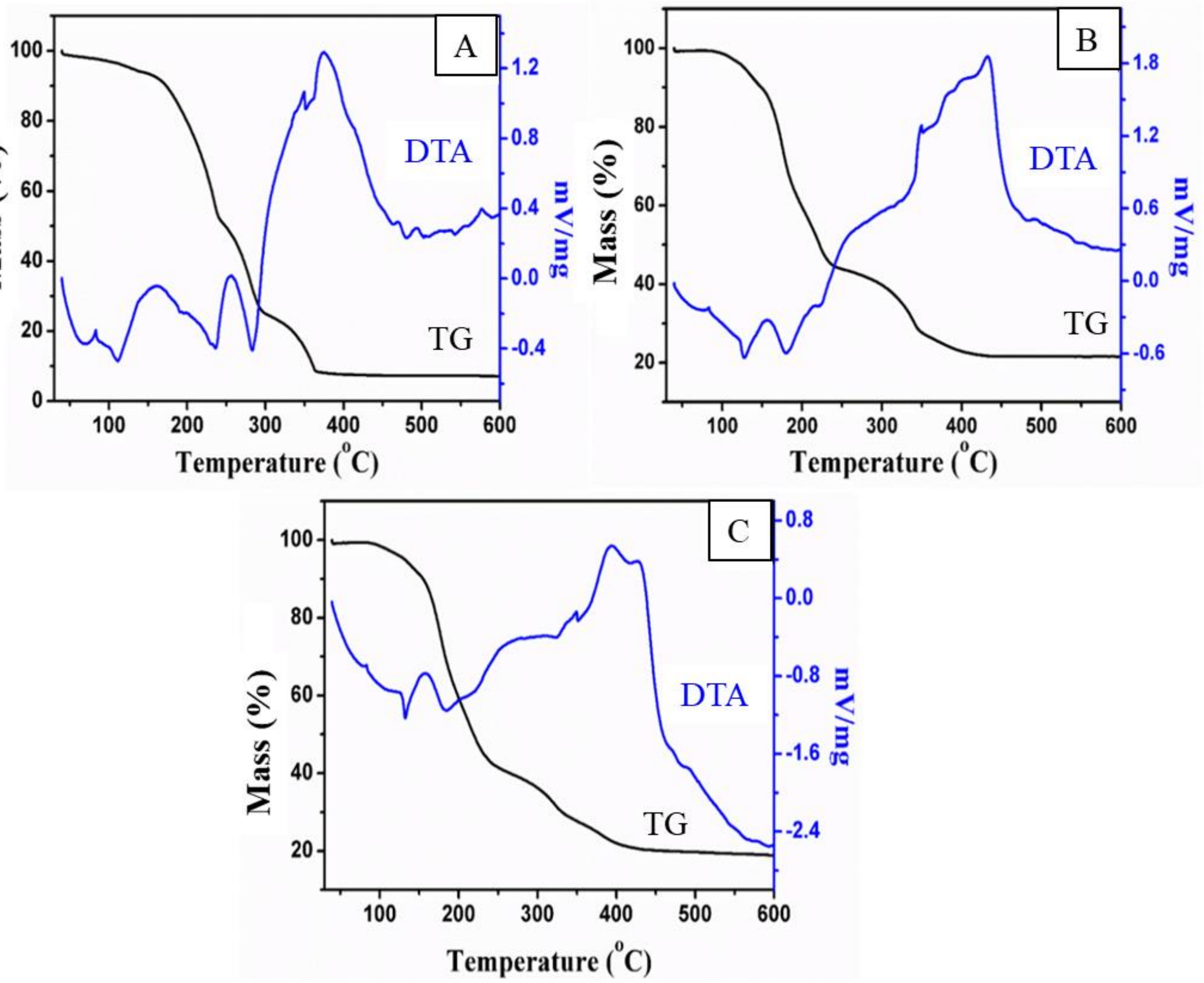

**Figure 4.3:** TG-DTA analysis of (A) MP, (B) MD, and (C) MA

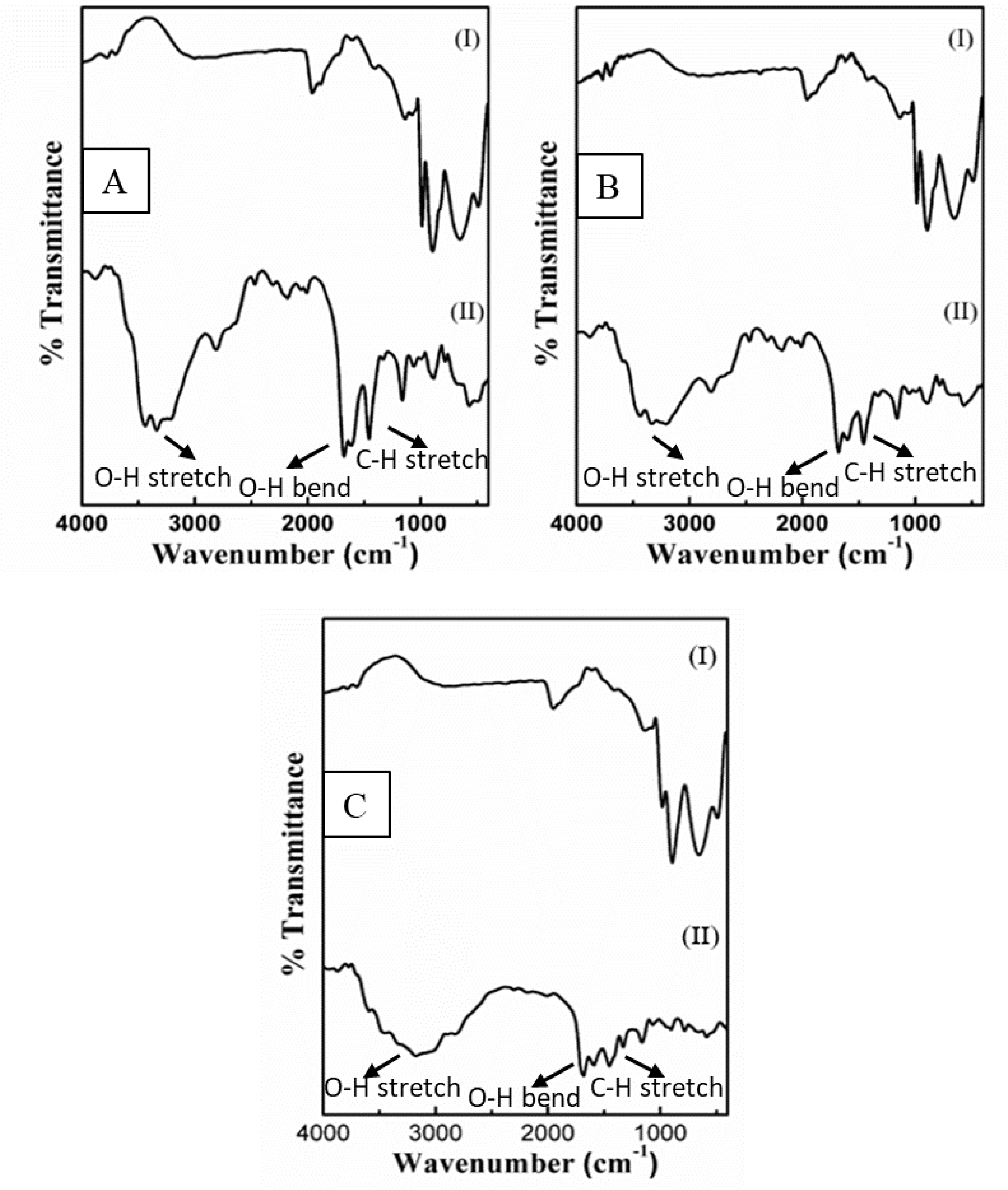

**Figure 4.4:** IR studies of (A) MP, (B) MD, and (C) MA wherein (I) represents post calcination and (II) represents pre-calcination.

The TG-DTA and IR analysis were used to qualitatively analyze the ammonium heptamolybdate (AHM) -urea mixtures and the subsequent transformation to $MoO_{3-x}$ (refer figure 4.3). Figure 4.3 shows the TG-DTA analysis of the ammonium heptamolybdate-urea mixture formed at different pH values of 2.5, 5, and 8. A multistep weight loss pattern corresponding to the hybrid precursor's decomposition was observed in all three compounds. The initial three weight losses at temperature ≤ 150 ℃, from 150 to 210 ℃ and 210 to 300 ℃, supported by endothermic peaks, are due to the loss of ammonia molecules, which may create a partial reducing environment.[24] Minor decomposition of uncoordinated urea can also be expected within this temperature regime. The significant weight loss observed above 300 ℃, which is supported by an exothermic peak in DTA, was due to the complete combustion of urea into $NO_x$, $CO_2$, and $H_2O$, leading to the formation of an oxide of molybdenum.[25,26]

### 4.2.3 IR studies

The IR studies were also used as a qualitative measurement (refer figure 4.4) wherein it was observed that the initially present band at 3455, 1676, and 1447 $cm^{-1}$ corresponding to O-H stretching, O-H bending, and C-H stretching frequencies in the AHM-Urea mixtures disappeared and only Mo-O vibrations were observed at 1000 $cm^{-1}$, post calcination, suggesting complete removal of urea and formation of oxides of molybdenum.[3,27,28]

### 4.2.4 XRD studies

Figure 4.5 shows the XRD patterns of MP, MD, and MA. The three XRD patterns were indexed to the thermodynamically most stable, i.e., orthorhombic $\alpha$-$MoO_3$ crystal structure using the JCPDS card number 05-0508, which has the lattice parameters of $a$ = 3.962 Å, $b$ = 3.858 Å, and $c$ = 3.697 Å.[21,29] No impurity peaks were observed in the XRD patterns which suggest high phase purity of the compounds. $\alpha$-$MoO_3$ can be imagined as consisting of a double layer with corner-sharing chains of $MoO_6$ octahedra arranged in a zigzag pattern. The $MoO_6$ octahedra in $\alpha$-$MoO_3$ are held together by covalent forces in the $a$ and $c$ axis, while weak van der Waals forces exist along the $b$ axis. The peaks with the most substantial intensity observed for $MoO_{3-x}$ microplates correspond to the (020), (040), and (060) planes suggesting the (0k0) plane pattern, which is typically observed for 2D materials. However, the order of (0k0) planes changes when we observe the XRD pattern of MD and MA, indicating a different growth direction of the planes associated with the change in morphology. Both (020) and (060) planes dominated in MD, while the (040) and (060) dominated in MA. It was interesting to note that there was a significant difference in the relative intensity ratios of (020), (040), and (060) planes of the three materials. The comparative ratio analysis were as follows: MP (0.22, 1, 0.25), MD (1.18, 1, 1.63), and MA (0.71, 1, 0.87). The plane's dominance observed in the XRD patterns was consistent with the d-spacing values calculated from the HRTEM analysis discussed earlier.

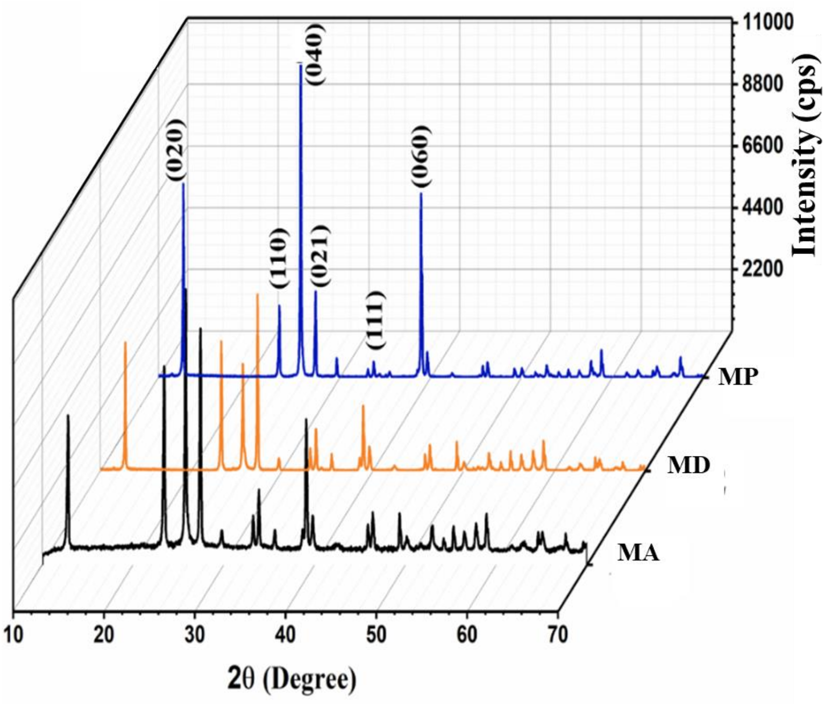

**Figure 4.5:** XRD analysis of (A) MP, (B) MD, and (C) MA.

### 4.2.5 Raman studies

Figure 4.6 shows the Raman spectra for MP, MD, and MA. The Raman spectra showed the typical signature vibrations of $MoO_{3-x}$ with strong peaks at 283, 668, 820, and 998 $cm^{-1}$ which were in agreement with the previously reported $\alpha$-$MoO_3$.[30,31] The Raman peak at 998 $cm^{-1}$ can be assigned to the asymmetric terminal oxygen's ($Mo^{+6}$=O) stretching mode and is indicative of the formation of a layered structure. The highest intensity peak observed in Raman is at 820 $cm^{-1}$, which indicates bi-coordinated oxygen ($Mo_2$-O) whereas the peak due to tri-coordinated oxygen ($Mo_3$-O) is observed at 668 $cm^{-1}$. The peak at 283 $cm^{-1}$ can be assigned to the wagging vibration (O-Mo-O). Intensity ratios of the high-intensity peak at

820 cm$^{-1}$ to the low-intensity peak at 283 cm$^{-1}$ revealed the ratios as 4.51, 3.27 and 2.63 for MP, MD and MA. The relatively higher intensity ratios of the peaks for MP indicated the layers comprising the microplates were much thinner compared to MD and MA and are also indicative of greater oxygen vacancies in MP. Additionally, the sharpness of the peaks in Raman spectra is proportional to the crystallinity and structural order, which were observed to be the highest for MP, followed by MD and MA.

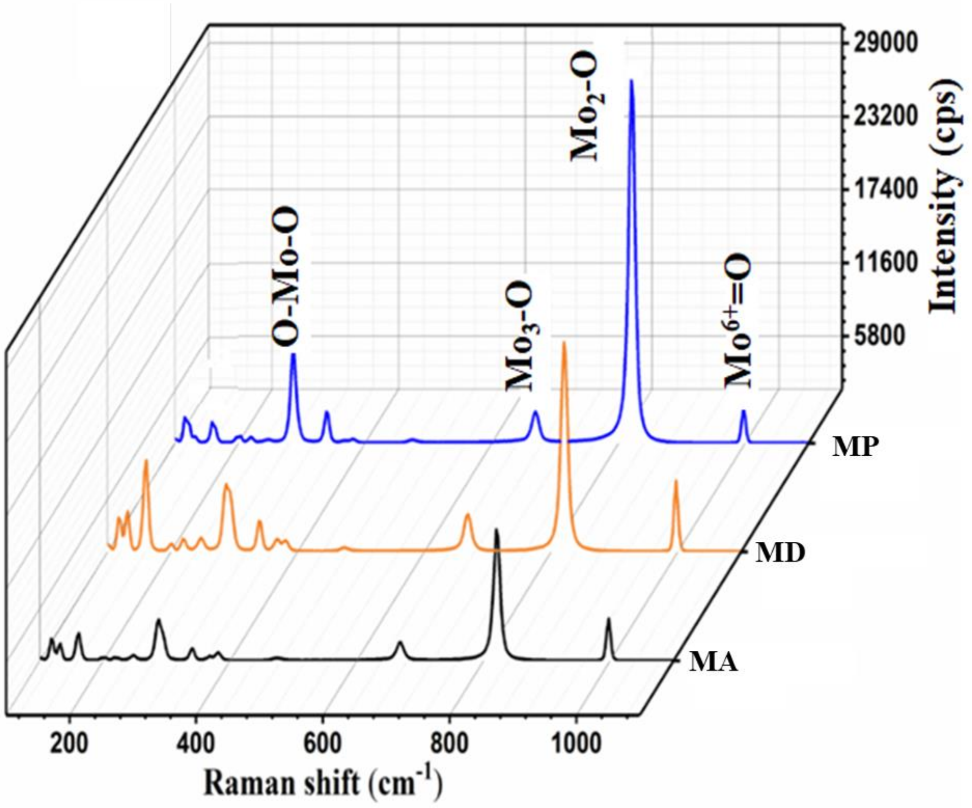

**Figure 4.6:** Raman analysis of (A) MP, (B) MD, and (C) MA.

### 4.2.6 XPS and EPR studies

In order to elucidate the electronic properties of $MoO_{3-x}$ microstructures, EPR and XPS analysis were performed. As shown in figure 4.7, the EPR spectrum of the $MoO_{3-x}$ exhibited a hyperfine structure with both perpendiculars and parallel bands corresponding to the Mo$^{+5}$ centers and located at the g values of 1.935 and 1.896 respectively.[32,33] The presence of a signal at g=2.003 corresponds to free electrons, which indicated that $MoO_{3-x}$ possessed a certain number of oxygen vacancies. The lower signal intensity of MD in comparison to MP suggested greater oxygen vacancies in the latter case. The XPS spectra of both MP and MD have been presented in figure 4.7 B-F.

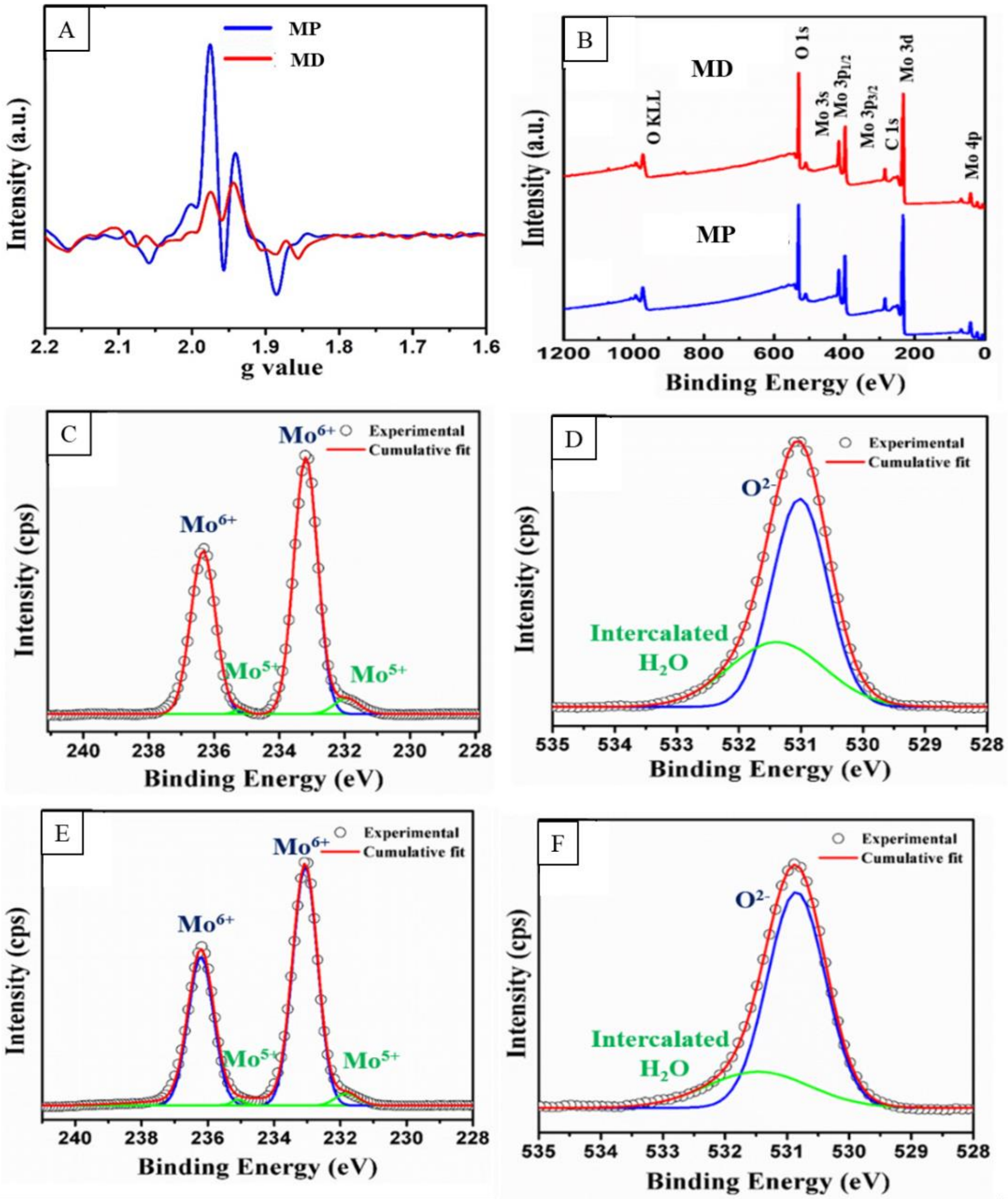

**Figure 4.7:** (A) Overlay of EPR spectra, (B) Overlay of XPS full scan spectra, (C and D) Narrow scan spectra of Mo3d and O1s of MP, (E and F) Narrow scan spectra of Mo3d and O1s of MD.

A quantitative estimate of the surface redox states and oxygen vacancies of MP and MD was estimated from the narrow scan XPS spectra of Mo3d and presented in table 4.1. The high-intensity peaks at the binding energies of 232.8 and 236.1 eV can be ascribed to $Mo^{+6}$ $3d_{5/2}$ and $Mo^{+6}$ $3d_{3/2}$ and the peaks at the binding energies of 231.5 and 234.6 eV can be denoted as the peaks for $Mo^{+5}$ $3d_{5/2}$ and $Mo^{+5}$ $3d_{3/2}$. The peak area integration of the $Mo^{+6}$ and $Mo^{+5}$ species revealed a greater percentage of $Mo^{+5}$ in MP (4.9 %) in comparison to MD (2.3 %). Figure 4.7 D and F presents the narrow scan XPS spectra of O1s species of MP and MD, respectively. The peak in the O1s spectra observed at the binding energy of 530.8 eV can be assigned to lattice oxygen ($O^{2-}$), whereas the peak observed at the binding energy of 531.9 eV is due to intercalated $H_2O$ and is also another indicator for the presence of oxygen vacancies in the material which are observed to be higher for the MP.[34–36]

| **Material** | **Narrow scan** | **Species** | **XPS area integration (%)** | **Area ratio $Mo^{5+}$ / $Mo^{6+}$** |
|---|---|---|---|---|
| MP | Mo 3d | $Mo^{6+}$ | 95.04 | 0.05 |
| | | $Mo^{5+}$ | 4.96 | |
| | O 1s | $O^{2-}$ | 65.5 | |
| | | Intercalated $H_2O$ | 34.5 | |
| MD | Mo 3d | $Mo^{6+}$ | 97.71 | 0.02 |
| | | $Mo^{5+}$ | 2.29 | |
| | O 1s | $O^{2-}$ | 76.31 | |
| | | Intercalated $H_2O$ | 23.69 | |

**Table 4.1:** The percentage of species obtained from the XPS peak area integration of narrow scan spectra.

### 4.2.7 Plausible growth mechanism for 2D $MoO_{3-x}$ microplates and microdisks

The plausible growth mechanism for forming of MP and MD is schematically illustrated in figure 4.8. Ammonium heptamolybdate is known to produce layered $MoO_3$ upon decomposition in a reaction, which is similar to a combustion process. The $MoO_3$ thus produced comprises of long chains of $MoO_6$ octahedra, which exhibit morphologically incomplete and uncontrolled growth. In order to gain control over the growth process of

$MoO_{3-x}$, control over the nucleation and growth steps during synthesis must be established. This has been achieved in the present work by making use of protonated urea both as an additive and a fuel. Despite being a simple molecule, urea has versatile characteristics. The acid-base properties related to its amine and carbonyl groups and the potential for hydrogen bonding make urea a crucial biological molecule. Moreover, urea is known to protonate in aqueous acids, and the degree of its protonation can be tuned based on the solution pH. The process is hypothesized to be initiated during the hydrolysis of ammonium heptamolybdate molecule in water, leading to $NH_4^+$ and $OH^-$ ions .

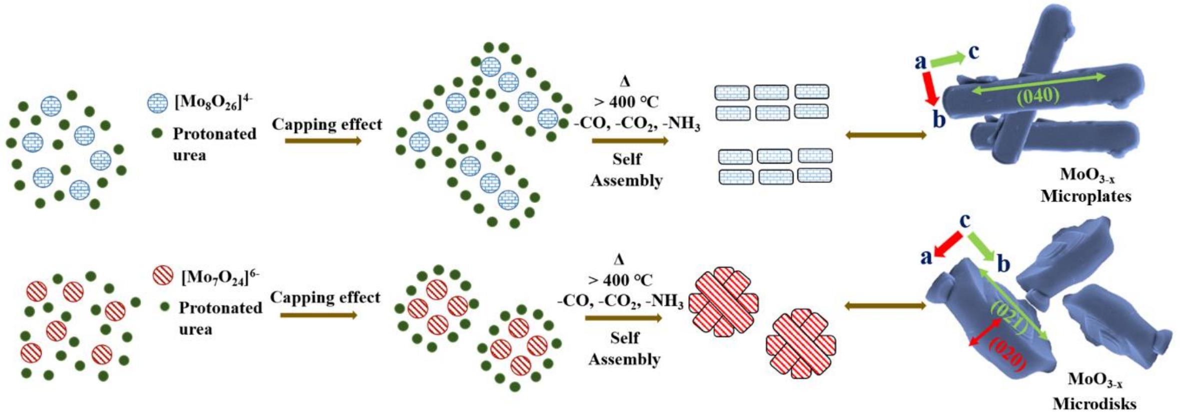

**Figure 4.8:** Schematic illustration for the plausible growth mechanism of MP and MD.

The type of molybdenum species in the solution is tuned at this stage by controlling the pH. At pH values > 6.5, the predominant species is the tetrahedral $[MoO_4]^{2-}$ ions. Lowering the solution pH leads to polymerization condensation resulting in the formation of heptamolybdate ion $[Mo_7O_{24}]^{6-}$ within the pH range of 5 to 6 and octamolybdate ions $[Mo_8O_{26}]^{4-}$ at an even lower pH.[37–39] Both these ions are built up from linked $MoO_6$ octahedra. The polymolybdate ions are known to be strongly influenced by protons. Hence the addition of protonated urea at this stage is able to interact with the $Mo^{6+}$ atoms strongly. Thus, the strength of the interaction depends on the protonation degree of urea, which is a function of pH and acts as a capping agent to direct the orientational growth of $MoO_{3-x}$ particles and its subsequent transformation to 2D morphologies during the combustion stage. Thus we observe that at a pH of 3 or lower, the interaction of octamolybdate ions with the protonated urea leads to the formation of MP post-combustion with a large 2D aspect ratio with excess oxygen vacancies while as the pH gradient is shifted in favor of heptamolybdate ions $[Mo_7O_{24}]^{6-}$, the MD formation dominates.

The temperature-dependent transformation observed in MP indicates that the $MoO_{3-x}$ nanoparticles fuse under the effect of high combustion temperature to initially produce tiny plate-like structures. These plates subsequently attach laterally to the adjacent plates along the *c* direction and grow into microplates having a truncated 2D morphology, preferentially growing along the (040) plane. Whereas the formation of the $MoO_{3-x}$ microdisks can be viewed as vertical stacking of initially formed more or less hexagonal structures along the *a* direction. The unstructured agglomerated particle morphology observed in MA with no definite directional growth observed at pH > 6.5 can be attributed to the lack of protonation in urea hence its lack of ability to direct structural growth in basic medium. Furthermore, the effect of these structural and chemical differences on the synthesized material's charge storage performance was evaluated using electrochemical measurements and have been presented in the subsequent section 4.3.

## 4.3 EVALUATING THE CHARGE STORAGE PROPERTIES OF MICROSTRUCTURED 2D $MoO_{3-x}$ SYNTHESIZED USING UREA

### 4.3.1 Three electrode charge storage studies

The synthesized $MoO_{3-x}$ microstructures were subjected to electrochemical testing to evaluate their supercapacitor performance. The supercapacitor performance was studied using cyclic voltammetry (CV), galvanostatic charge-discharge (GCD), and electrochemical impedance spectroscopic (EIS) measurements. 1 M $H_2SO_4$ was employed as an electrolyte for all the electrochemical studies. Figure 4.9 shows the result of the measurements in a three-electrode setup. The overlays of CV curves for MP, MD, and MA have been shown in figure 4.9 A at a fixed scan rate of 10 mV $s^{-1}$. Interestingly, the material’s exhibited multiple pairs of redox peaks typical of $MoO_{3-x}$ since they can sustain multiple oxidation states ($Mo^{6+}$, $Mo^{5+}$, and $Mo^{4+}$) owing to their pseudo-capacitive behavior.[40–43] The redox peaks can be attributed to the insertion and extraction of $H^+$ ions as described by the below reaction 1.[44] The multiple oxidation states of $MoO_{3-x}$ are known to have a significant contribution to the overall capacitance of the materials.[45]

$$\mathrm{MoO_{3-x}} + n\mathrm{H^+} + ne^- \leftrightarrow \mathrm{H_nMoO_{3-x}} \qquad (4.1)$$

The largest area under the CV was observed for MP, which can be attributed to its large surface-to-volume ratio and higher crystallinity, which was confirmed through Raman, XRD, and SAED analysis.

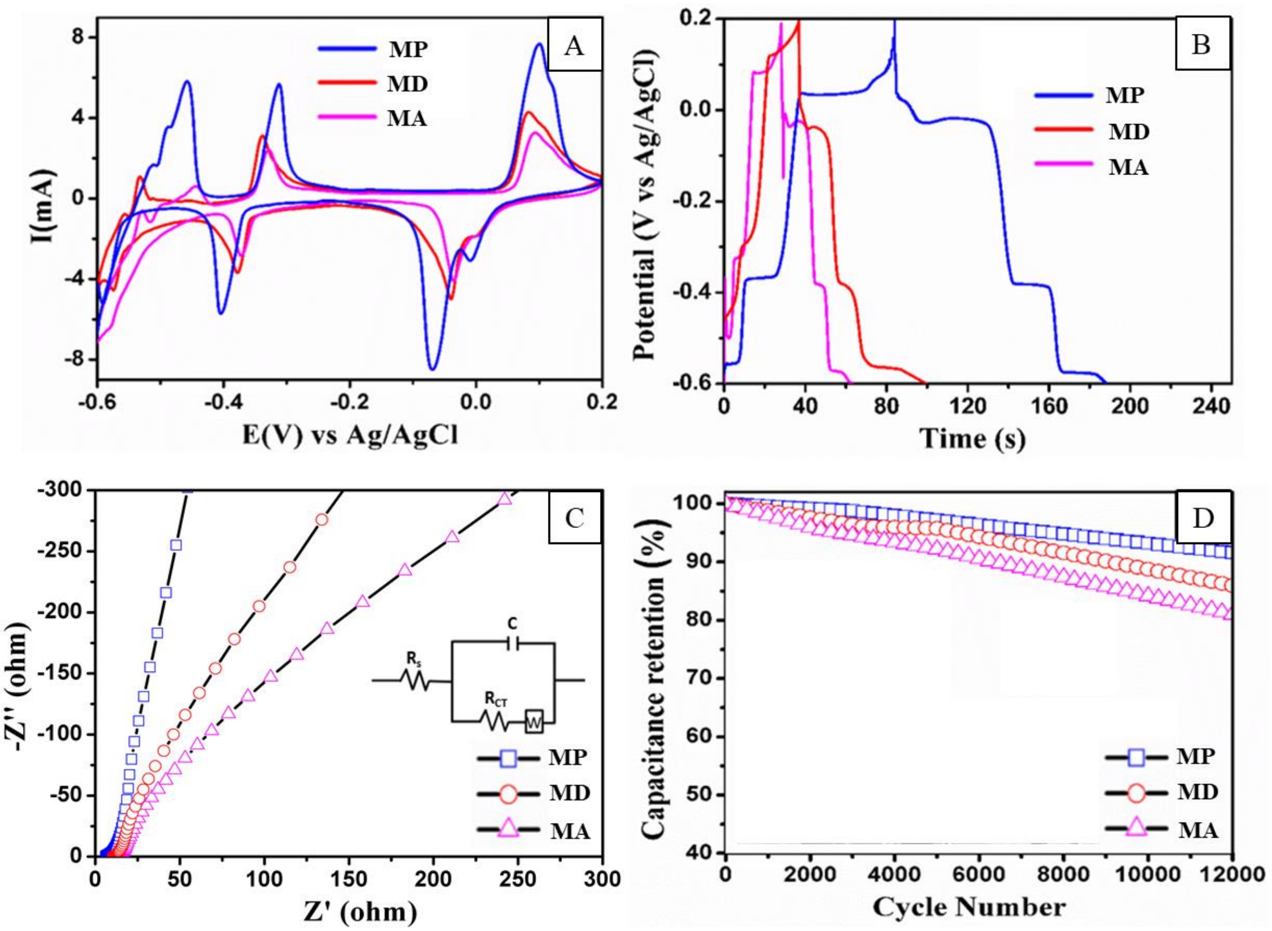

**Figure 4.9:** Supercapacitor performance investigated via (A) CV analysis at a scan rate of 10 mV $s^{-1}$; (B) GCD analysis at the current density of 20 A $g^{-1}$; (C) Nyquist plots in the frequency range of 1 mHz to 1 MHz; and (D) cycling stability performance evaluated at a constant current density of 40 A $g^{-1}$.

Scan rate-dependent CV analysis were also performed for different scan rates from 10 to 200 mV $s^{-1}$ and have been presented in figure SF20 in Annexure-I. It was observed that at faster scan rates, the redox peaks could still be identified, reflecting faster $H^+$ intercalation/deintercalation ability of the materials.[46] It was also noted that with an increase in scan rates, the reduction and oxidation peaks moved to lower and higher potential values, respectively, indicating the lag in proton and electron pathways caused due to rapid cycling. From the scan rate-dependent CV measurements, the values of anodic peak current ($I_p$) were obtained. Using the slope of the square root of scan rate ($v^{1/2}$) versus the anodic peak current graph, the diffusion coefficient of $H^+$ ions was calculated using the Randles-Sevcik equation as described in 2.4.4.[25,47]

| **Material code** | **Electroactive surface area ($cm^2$)** | **BET surface area ($m^2\ g^{-1}$)** |
|---|---|---|
| MP | 0.92 | 12.9 |
| MD | 0.85 | 9.5 |
| MA | 0.65 | 7.7 |

**Table 4.2:** Summary of the electroactive and BET surface area for $MoO_{3-x}$ microstructures.

The $D_0$ values of $1.41 \times 10^{-4}$, $1.05 \times 10^{-4}$, and $0.38 \times 10^{-4}$ $cm^2\ s^{-1}$ were obtained for MP, MD, and MA, respectively. The highest $D_0$ value observed for MP could be a result of thinner microlayers of MP facilitating the diffusion of $H^+$ ions through the $MoO_{3-x}$ matrix compared to MD and MA. To further investigate the role of surface morphology on improved electrochemical activity of $MoO_{3-x}$ microstructures, chronoamperometric measurements were performed to estimate the electroactive surface area using the method described in section 2.4.3. The obtained areas are summarized in Table 4.3 along with an comparison to their BET surface area results. The results revealed electroactive areas of 0.92, 0.85, and 0.65 $cm^{2,}$ and BET surface area analysis revealed the surface area values of 12.9, 9.5, and 7.7 $m^2\ g^{-1}$ for MP, MD, and MA respectively (See figure SF21 in Annexure-I). The higher electroactive and surface area of MP in comparison to MD and MA could be another reason for its improved diffusion coefficient.

Figure 4.9 B shows the overlay of GCD curves at the current density of 20 A $g^{-1.}$ Corresponding to the four pairs of redox peaks observed in the CV analysis, four GCD plateaus were observed. The greatest discharge time was observed for MP, indicating its superior charge storage capability. The specific capacitance was calculated from the CV and GCD curves (using equations described in section 2.4.1). The highest capacitance of 625.2, 528.8, and 480.8 F g$^{-1}$ at a scan rate of 5 mV s$^{-1}$ and 410.6, 226.4, and 140.2 F g$^{-1}$ at a current density of 20 A g$^{-1}$ were obtained from CV and GCD analysis for MP, MD, and MA respectively (refer Tables 4.2 and 4.3).

| Scan rate (mV s$^{-1}$) | Specific capacitance (F g$^{-1}$) (Error bar ± 2%) | | | | | |
|---|---|---|---|---|---|---|
| | MP | | MD | | MA | |
| | 3 Elec. | 2 Elec. | 3 Elec. | 2 Elec. | 3 Elec. | 2 Elec. |
| 5 | 625.2 | 220.4 | 528.8 | 167.5 | 480.8 | 114.6 |
| 10 | 576.9 | 117.1 | 432.6 | 95.8 | 408.7 | 60.5 |
| 20 | 480.8 | 66.9 | 360.5 | 46.5 | 324.5 | 26.1 |
| 50 | 384.6 | 40.4 | 288.5 | 32.9 | 240.4 | 20.3 |
| 100 | 336.5 | 32.4 | 216.3 | 25.3 | 192.3 | 15.9 |

**Table 4.3:** Summary of specific capacitance values calculated from CV curves obtained for the different $MoO_{3-x}$ microstructures.

To better understand the observed order of specific capacitance, electrochemical impedance measurements at open circuit potential values within the frequency region of 1 mHz to 1 MHz were recorded and are presented in figure 4.9 C. The Nyquist plots comprised of two regions wherein a linear dependence was observed in the low-frequency region, which can be attributed to the solution resistance (Rs), whereas a semicircle was observed in the high-frequency region which can be ascribed to charge transfer resistance.[48] A representative circuit diagram which best describes the system is presented as an inset in figure 4.9 C. The circuit diagram comprises of a charge transfer resistor ($R_{CT}$) that is connected with a capacitor and a Warburg resistor (W) in parallel and solution resistor ($R_S$) in series. The solution resistance values of 6.1, 10.5, and 13.8 Ω were observed for MP, MA, and MA respectively. This indicated greater conductivity of $MoO_{3-x}$ microplates along with easy access to the electrolytic phase, which can be correlated to the presence of oxygen vacancies, thinner microlayers that provide accessible diffusion pathways along with suitable aspect ratio in the material.[46] The three material's cycling stability was also evaluated by performing continuous charge-discharge measurements (see figure 6D). MP demonstrated excellent stability with capacitance retention of 91.6 % (292.6 F g$^{-1}$), whereas MD demonstrated capacitance retention of 85.9% (99.3 F g$^{-1}$), and MA showed capacitance retention of 81% (77.3 F g$^{-1}$) for up to 12000 cycles, compared to their initial specific capacitance as reported in table 4.4.. The excellent stability demonstrated by 3DW and WN indicate their potential for device scale applications and have been evaluated for the same in the next section 3.3.2.

| Current density (A g$^{-1}$) (3 Elec./2 Elec.) | Specific capacitance (F g$^{-1}$) (Error bar ± 2%) | | | | | |
|---|---|---|---|---|---|---|
| | MP | | MD | | WA | |
| | 3 Elec. | 2 Elec. | 3 Elec. | 2 Elec. | 3 Elec. | 2 Elec. |
| 20/2 | 410.6 | 141.2 | 226.4 | 112.2 | 140.2 | 59.3 |
| 30/4 | 342.3 | 130.3 | 156.3 | 101.1 | 107.8 | 48.2 |
| 40/6 | 319.5 | 102.6 | 115.7 | 85.2 | 95.5 | 42.5 |
| 50/8 | 281.1 | 88.3 | 103.3 | 74.3 | 74.6 | 38.3 |
| 60/10 | 188.4 | 75.5 | 94.8 | 62.7 | 56.1 | 32.6 |

**Table 4.4:** Summary of specific capacitance values calculated from GCD curves obtained for the different $MoO_{3-x}$ microstructures.

### 4.3.2 Electrochemical performance of the $MoO_{3-x}$//AC asymmetric supercapacitor device

To evaluate the practical applicability of the synthesized $MoO_{3-x}$ microstructures, an asymmetric supercapacitor device was assembled using $MoO_{3-x}$ microstructures fabricated onto carbon paper as the cathode and activated carbon (AC) fabricated onto another carbon paper as an anode using the methodology described in section 2.3.2.1. Figure 4.10 A shows the CV curves of MP and AC electrodes at a fixed scan rate of 10 mV s$^{-1}$, from which it was observed that the faradaic pseudocapacitance of MP was almost four times greater than the double-layer capacitance of the AC fabricated electrode. The material loading onto the electrodes was modified accordingly.

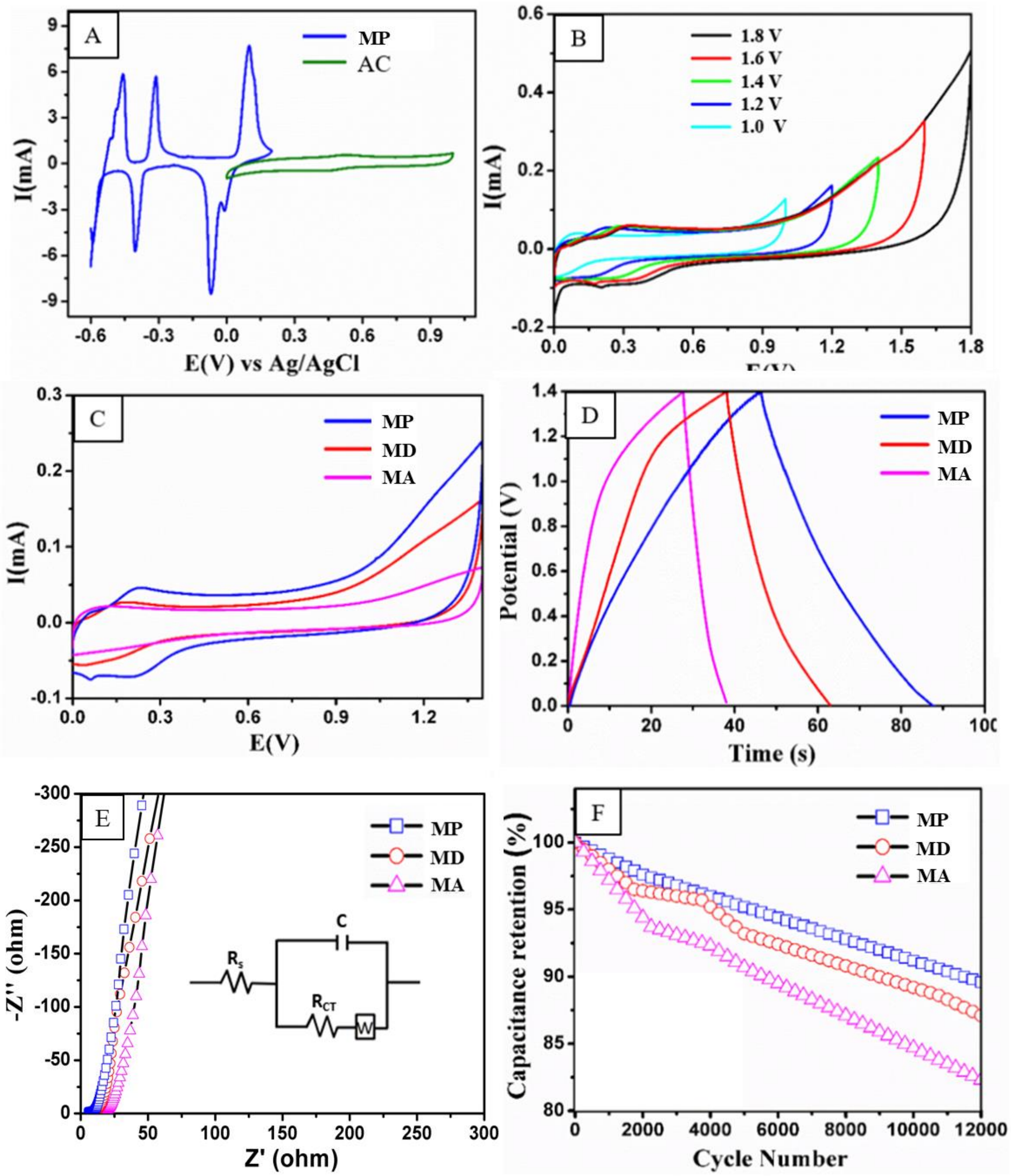

**Figure 4.10:** (A) CV curves of MP and AC recorded at a scan rate of 10 mV $s^{-1}$; (B) CV curves of MP//AC at variable voltage windows; (C) Overlay of CV curves recorded at a scan rate of 10 mV $s^{-1}$; (D) Overlay of GCD analysis recorded at the current density of 2 A $g^{-1}$; (E) Overlays of Nyquist plots in the frequency range of 1 mHz to 1 MHz; and (F) Overlays of cycling stability performance measured in a two-electrode asymmetric setup evaluated at 6 A $g^{-1}$.

The voltage window of the asymmetric supercapacitor device was also extended effectively while avoiding excess polarization as shown in figure 4.10 B, and was evaluated from 1 V to 1.8 V. The testing of the asymmetric supercapacitor device was performed at the optimum voltage window of 1.4 V. An overlay of the cyclic voltammograms at a fixed scan rate of 10 mV $s^{-1}$ and galvanostatic charge-discharge studies at a constant current density of 2 A $g^{-1}$ has been shown in figure 4.10 C and D respectively, which indicates both greater voltammogram area and longer discharge time for MP electrodes in comparison to MD and MA.

Scan rate dependent CV and current density-dependent GCD studies were also performed (refer figure SF 23 and SF 24 in Annexure-I), and the specific capacitance thus observed has been tabulated in table 4.3 and 4.4 (Equations 2.4 and 2.5). The highest specific capacitance of 220.4 F $g^{-1}$ at a scan rate of 5 mV $s^{-1}$ and 141.2 F $g^{-1}$ at a current density of 2 A $g^{-1}$ was demonstrated by MP. The observed results of specific capacitance measurements were in line with the results of three-electrode studies. From the EIS studies, the Rs values of 5.9, 9.4, and 16.9 Ω were shown by MP, MD, and MA, respectively. A representative circuit diagram which best describes the system is presented as an inset in figure 4.10 E. The circuit diagram comprises of a charge transfer resistor ($R_{CT}$) that is connected with a capacitor and a Warburg resistor (W) in parallel and solution resistor ($R_S$) in series.

Additionally, exceptional cycling stability was also observed for the $MoO_{3-x}$ microstructures when tested over 12000 continuous charge-discharge cycles. Capacitance retention of 89.6 (91.9 F $g^{-1}$), 87.1 (74.2 F $g^{-1}$), and 82.3 (34.9 F $g^{-1}$) % were observed for MP, MD, and MA electrodes compared to their initial specific capacitance as reported in table 4.4. Power density and energy density are the most significant parameters of any supercapacitor device. The Ragone plot displaying the performance of the assembled asymmetric supercapacitors has been presented in figure 4.11 (Equation 2.6 and 2.7). The highest power density of 1021 W $kg^{-1}$ and energy density of 41 W h $kg^{-1}$ were demonstrated by the MP, followed by the performance of MD, which displayed a power density of 1015 W $kg^{-1}$ and energy density of 30 W h $kg^{-1}$. In contrast, the MA, due to the irregular morphology demonstrated the least performance.

The results of the supercapacitor device were on par with literature reports. Wang *et al.*[44] reported the energy and power density of 25.7 W h $kg^{-1}$ and 1485.3 W $kg^{-1}$ for hydrothermally prepared $MoO_3$ nanobelts. Wu *et al.*[46] achieved the energy and power density of 111 W h kg$^{-1}$ and 803 W kg$^{-1}$ for $MoO_{3-x}$ nanobelts prepared using the hydrothermal method. Barzegar *et al*.[49] reported the energy and power density of 16.7 W h kg$^{-1}$ and 325 W kg$^{-1}$ for hydrothermally prepared $MoO_3$. The use of complex synthetic approaches involving hydrothermal/solvothermal conditions increases the overall cost of the process. Our results were also comparable with the asymmetric devices involving graphene and molybdenum, such as the supercapacitor device reported by Chang *et al.*[50] with the combination of graphene/$MnO_2$//graphene/$MoO_3$, which demonstrated energy and power density of 42.6 W h kg$^{-1}$ and 276 W kg$^{-1}$. A similar comparison is evident with the work of Liu *et al.*[51] who has reported the device combination of $NiMoO_4$-rGO//N-doped graphene with energy and power density of 30.3 W h kg$^{-1}$ and 187 W kg$^{-1}$ respectively. The exceptional capacitance performance and high electrochemical stability of the $MoO_{3-x}$ microplates was a cumulative outcome of the presence of a greater number of oxygen vacancies accompanied by surface redox states, large surface-to-volume ratio and thinner microlayers facilitating the diffusion of $H^+$ ions through the $MoO_3$ matrix.

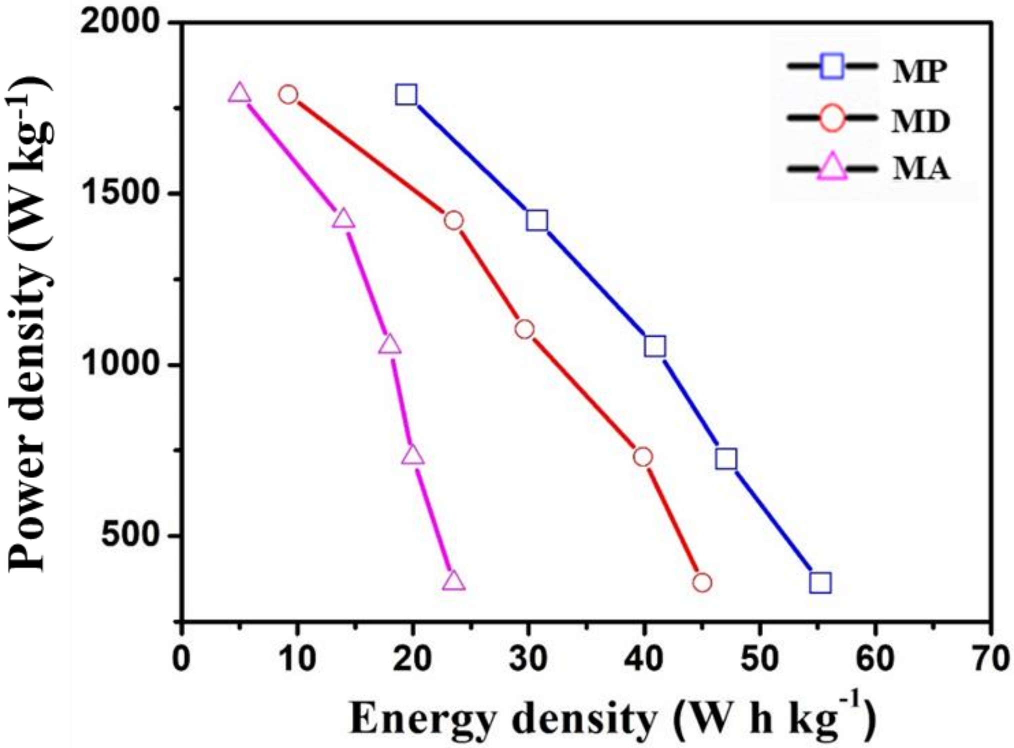

**Figure 4.11:** Ragone plot demonstrating the device performance of $MoO_{3-x}$ microstructures.

## 4.4 EFFECT SUBSTITUTED UREAS ON GROWTH CHARACTERISTICS OF $MoO_{3-x}$ MICROSTRUCTURES

In comparison to urea, substituted ureas have been far less explored for the rational design of nanomaterials, despite the fact that they can also form relatively strong hydrogen-bonded motifs. In section 3.4, we demonstrated the influence of urea substitution on the growth characteristics of $WO_{3-x}$ nanorods. It was observed that -NH substitution (such as crbohydrazide and semicarbazide) promoted the growth of $WO_{3-x}$ nanorods, while -CH substitution (such as N-methylurea and tetramethylurea) has a detrimental influence on the $WO_{3-x}$ morphologies. In view of those results, a similar study is performed on $MoO_{3-x}$ in the present section.

### 4.4.1 SEM studies

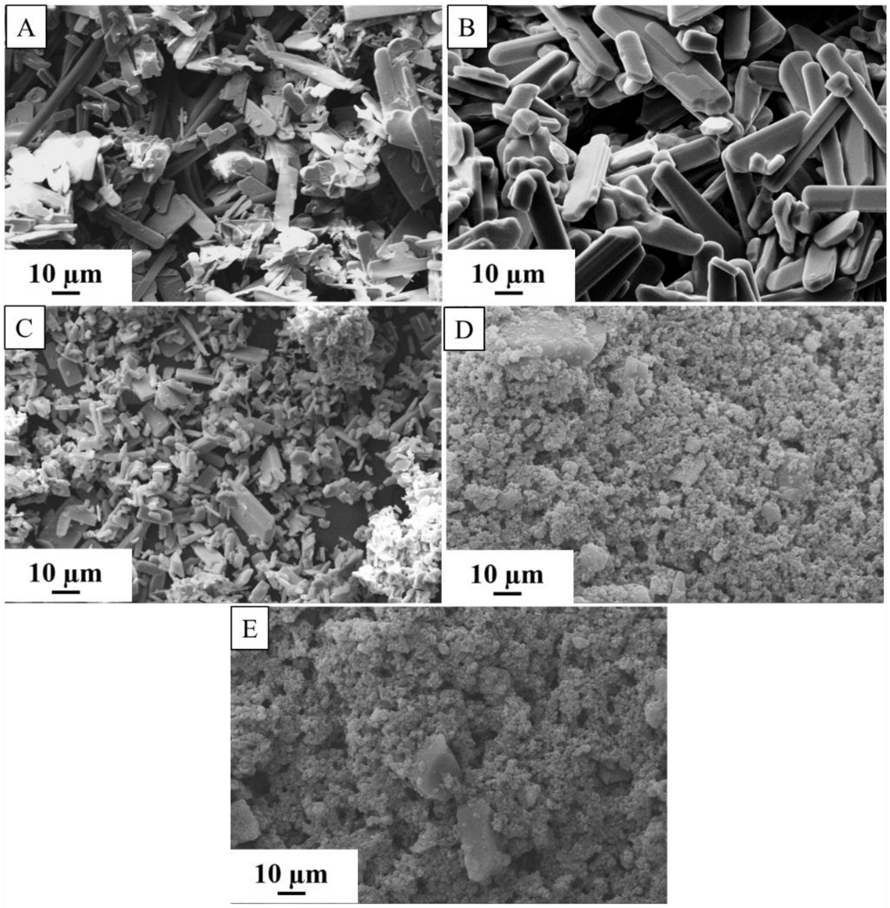

**Figure 4.12:** SEM images of $MoO_{3-x}$ synthesized by calcining ammonium molybdate with (A) carbohydrazide, (B) urea, (C) semicarbazide, (D) N-methylurea and, (E) tetramethylurea.

Figure 4.12 A-F present the SEM images of synthesized $MoO_{3-x}$ microstructures synthesized using carbohydrazide, urea, semicarbazide, N-methyl urea, and tetramethylurea, and shall be referred to as MC, MP, MSC, MM, and MT respectively and have been synthesized using the methodologies described in section 2.2.7. It is evident from the SEM results that the calcination of ammonium heptamolybdate with carbohydrazide and urea produces $MoO_{3-x}$ micoplates. Whereas moving in the direction of NH- substitution, the MSC yielded relatively poor microplate characteristics as evident from figure 4.12 C. From figure 4.12 D and E it was observed that CH- substituted ureas such as N-methylurea and teramethylurea did not produce any microstructures.

### 4.4.2 HRTEM studies

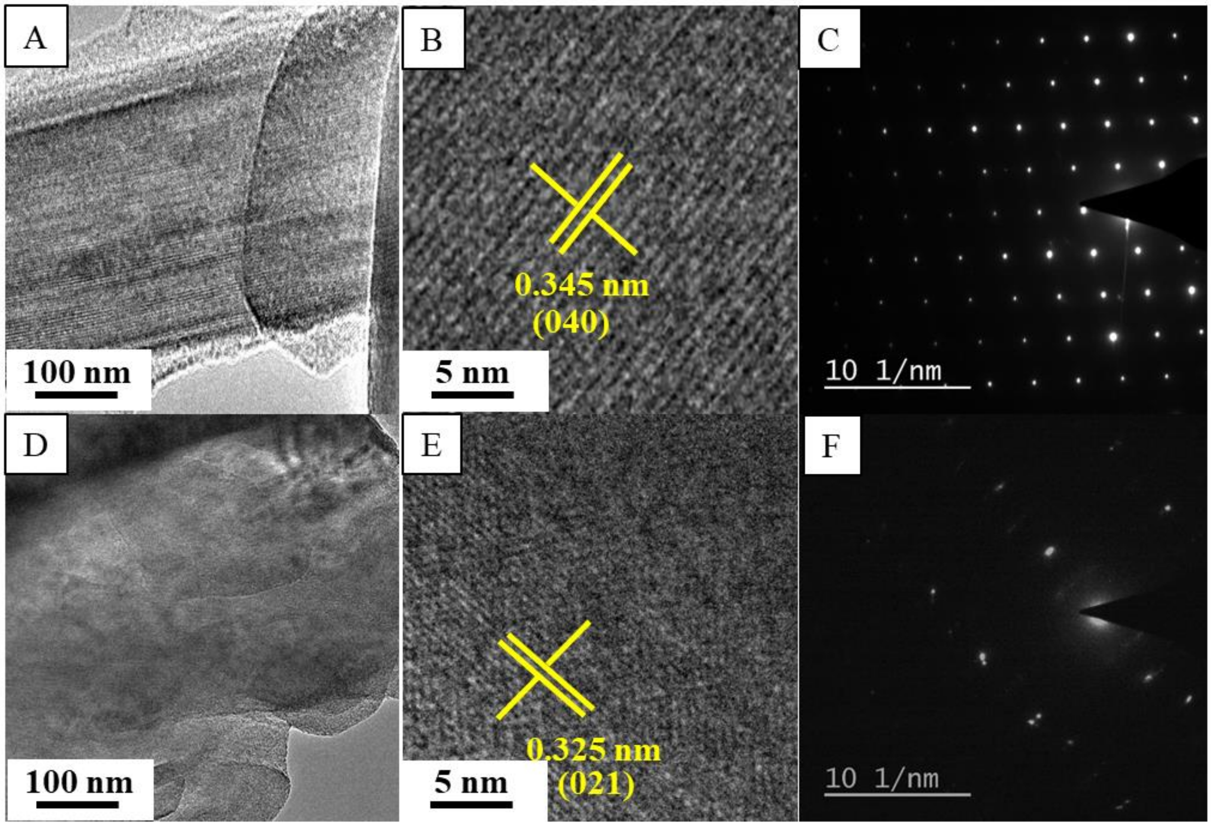

**Figure 4.13:** The TEM, HRTEM, and SAED analysis (A-C) for MC and (D-F) for MT, respectively.

To investigate the detailed morphological and structural characteristics, the synthesized $MoO_{3-x}$ microstructures were subjected to HRTEM and SAED analysis. The typical representative results, one containing microplates (MC) and the second without the microstructures (MT) are presented in figure 4.13. Figure 4.13 TEM and HRTEM images of MC shown in figure 4.13 A-B revealed the lattice fringes with a d-spacing of 0.345 nm, which matches with the (040) plane of orthorhombic $MoO_{3-x}$ in agreement with the literature reports.[52,53] The selected-area electron diffraction (SAED) pattern (Figure 4.13 C) also reveals the (002) plane, which could be indexed to a orthorhombic phase of $MoO_3$ (JCPDS No. 05-0508) for MC. However, MT which did not have any microstructural characteristics and had fringes with a d-spacing of 0.325 nm, which matched with the (021) plane of orthorhombic $MoO_{3-x}$.[52,53] The regular intensities of bright spots in the SAED pattern and the monocrystalline surface character were both more profound in the case of MC compared to MT.

### 4.4.3 XRD studies

Further analysis of the surface crystal structure and growth patterns of different planes in the synthesized $MoO_{3-x}$ morphologies were performed using an X-ray powder diffractometer. Figure 4.14 A-D represents the XRD pattern of all the synthesized $MoO_{3-x}$ using substituted ureas. All the $MoO_{3-x}$ samples indicated the formation of a stable orthorhombic phase (JCPDS card number 05-0508), with peaks appearing at 2θ values of 12.5, 23.1, 25.8, 27.2, 33.9, and 39.3 having miller indices (002), (110), (040), (021), (111), and (060) respectively, and were as reported in the literature.[52,53] Since the observed peaks were intense, sharp, and of narrow width with no peaks of secondary phases present, it could be concluded that the synthesized $MoO_{3-x}$ were of high phase purity and crystallinity. It was interesting to note that the obtained $MoO_{3-x}$ morphologies had significant differences in the intensities of their strongest peaks. The peaks with the most substantial intensity observed corresponded to the (020), (040), and (060) planes suggesting the (0k0) plane pattern, which indicates that the material has a direction parallel to the plane of the surface. However, the order of (0k0) planes changed when we observed the XRD patterns wherein MC had a similar trend to MP (refer figure 4.5) of MD with a ratio of (0.23, 1, 0.26). The ratio for MSC was (0.26, 1, 0.27) while MM and MT had significantly different ratios of (0.34, 1, 0.41) and (0.35, 1, 0.42), respectively. The (040) plane was dominant in both MC and MSC, while its intensity decreased in MM and MT suggesting a deviation from the microplate-like morphology. The plane's dominance observed in the XRD patterns were consistent with the d-spacing values calculated from the HRTEM analysis discussed earlier.

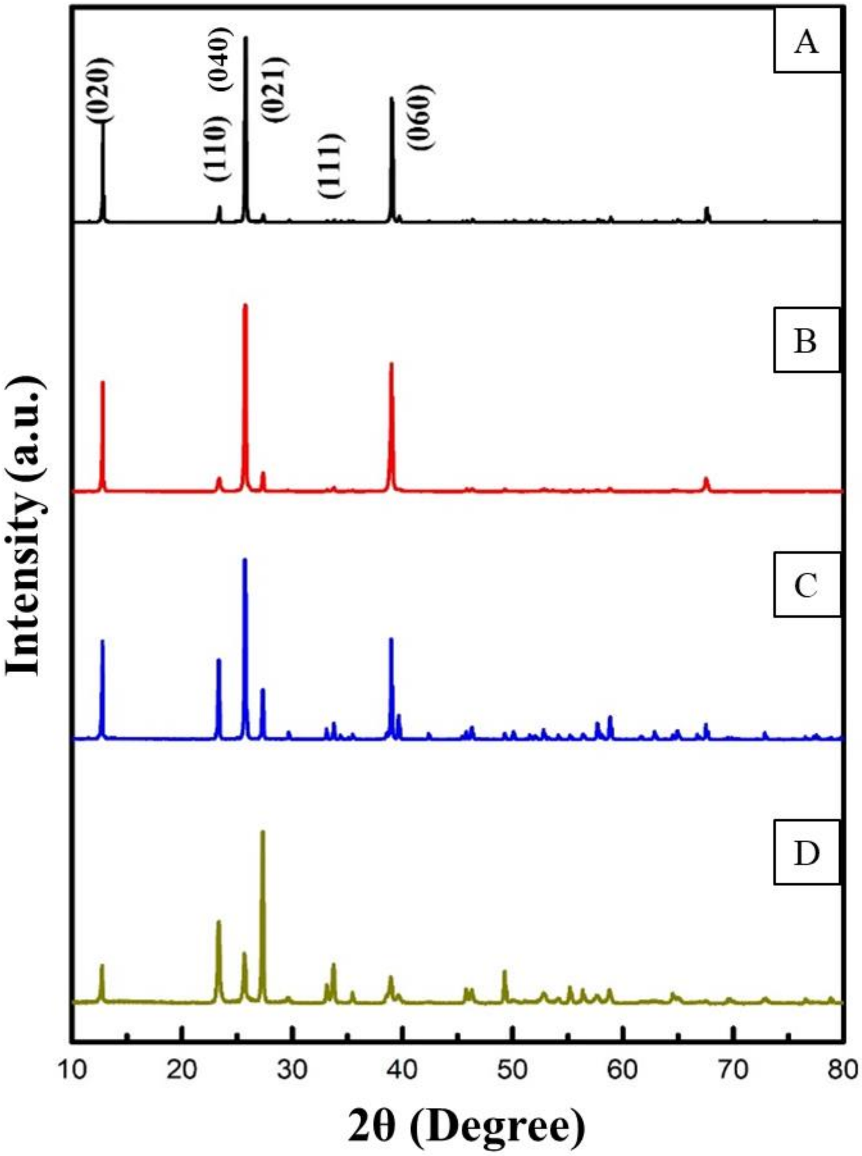

**Figure 4.14:** XRD patterns of (A) MC, (B) MSC, (C) MM, and (D) MT.

### 4.4.4 XPS studies

In order to elucidate the electronic properties of $MoO_{3-x}$ microstructures, XPS analysis was performed. XPS was employed to analyze representative samples of microstructures (MC) and particle agglomerates (MT). The XPS spectra of both MC and MT have been presented in figure 4.14 A-F.

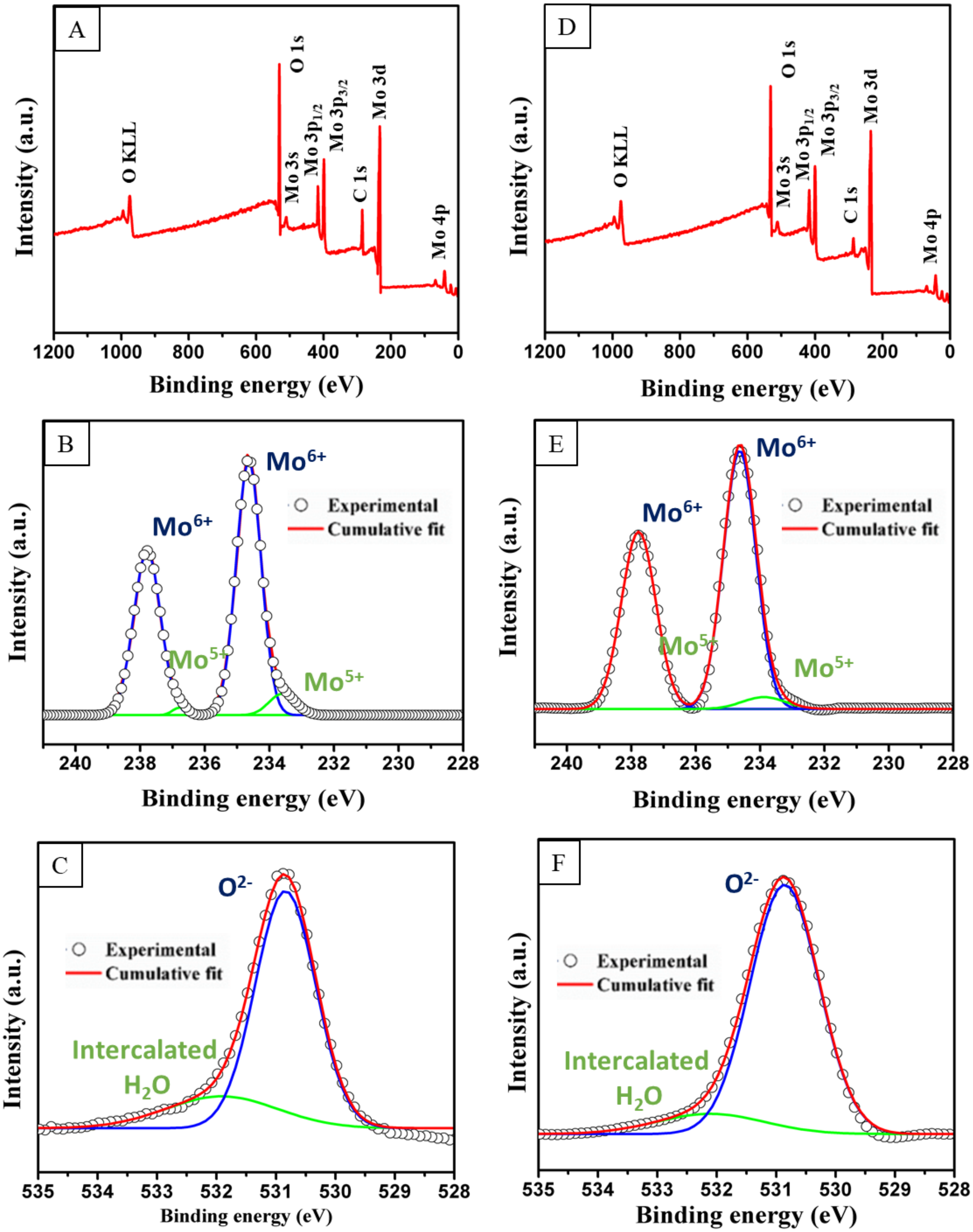

**Figure 4.15:** XPS spectra of (A-C) MC and (D-F) MT.

A quantitative estimate of the surface redox states and oxygen vacancies of MC and MT was estimated from the narrow scan XPS spectra of Mo3d and presented in table 4.1. The high-intensity peaks at the binding energies of 232.8 and 236.1 eV can be ascribed to $Mo^{+6}$ $3d_{5/2}$ and $Mo^{+6}$ $3d_{3/2}$ and the peaks at the binding energies of 231.5 and 234.6 eV can be denoted as the peaks for $Mo^{+5}$ $3d_{5/2}$ and $Mo^{+5}$ $3d_{3/2}$. The peak area integration of the $Mo^{+6}$ and $Mo^{+5}$ species revealed a greater percentage of $Mo^{+5}$ in MC (5.1 %) which was close to MP as well (4.9 %) in comparison to MT (1.2 %). Figure 4.15 C and F presents the narrow scan XPS spectra of O1s species of MC and MT, respectively.

| **Material** | **Narrow scan** | **Tungsten species** | **XPS area integration (%)** | **Area ratio $W^{5+}$ / $W^{6+}$** |
|---|---|---|---|---|
| MC | Mo 3d | $Mo^{6+}$ | 94.9 | 0.05 |
| | | $Mo^{5+}$ | 5.1 | |
| | O 1s | $O^{2-}$ | 65.2 | |
| | | Intercalated $H_2O$ | 34.8 | |
| MT | Mo 3d | $Mo^{6+}$ | 98.8 | 0.01 |
| | | $Mo^{5+}$ | 1.2 | |
| | O 1s | $O^{2-}$ | 87.7 | |
| | | Intercalated $H_2O$ | 12.3 | |

**Table 4.5:** The percentage of species obtained from the XPS peak area integration of narrow scan spectra of MC and MT.

The peak in the O1s spectra observed at the binding energy of 530.8 eV can be assigned to lattice oxygen ($O^{2-}$), whereas the peak observed at the binding energy of 531.9 eV were due to intercalated $H_2O$ and is also another indicator for the presence of oxygen vacancies in the material which are observed to be higher for the MC. Therefore, the above findings clearly suggested that the NH- substitution in urea enhanced the presence of surface oxygen defects on the surface of microplates, which could serve as active centre that promotes the electrochemical charge-storage processes. On the contrary, the inefficiency of CH-substituted ureas in forming microstructures thus resulted in the retention of the agglomerated particle morphologies with relatively lesser oxygen defects, an observation similar to the one observed for $WO_{3-x}$.

### 4.4.5 TG-DTA and IR studies

All the above findings and trends of SEM, HRTEM, XRD, and XPS studies confirm that the type of NH- and CH- substitution in urea significantly alters the growth characteristics of $MO_{3-x}$ microstructures. This alteration in the growth characteristics could arise from the differences in the thermal decomposition processes of CH- and NH- substituted ureas. Therefore, thermogravimetric analysis were performed on the as-synthesized metal precursor -CH/-NH substituted urea mixtures to obtain greater insight into the oxidation process.

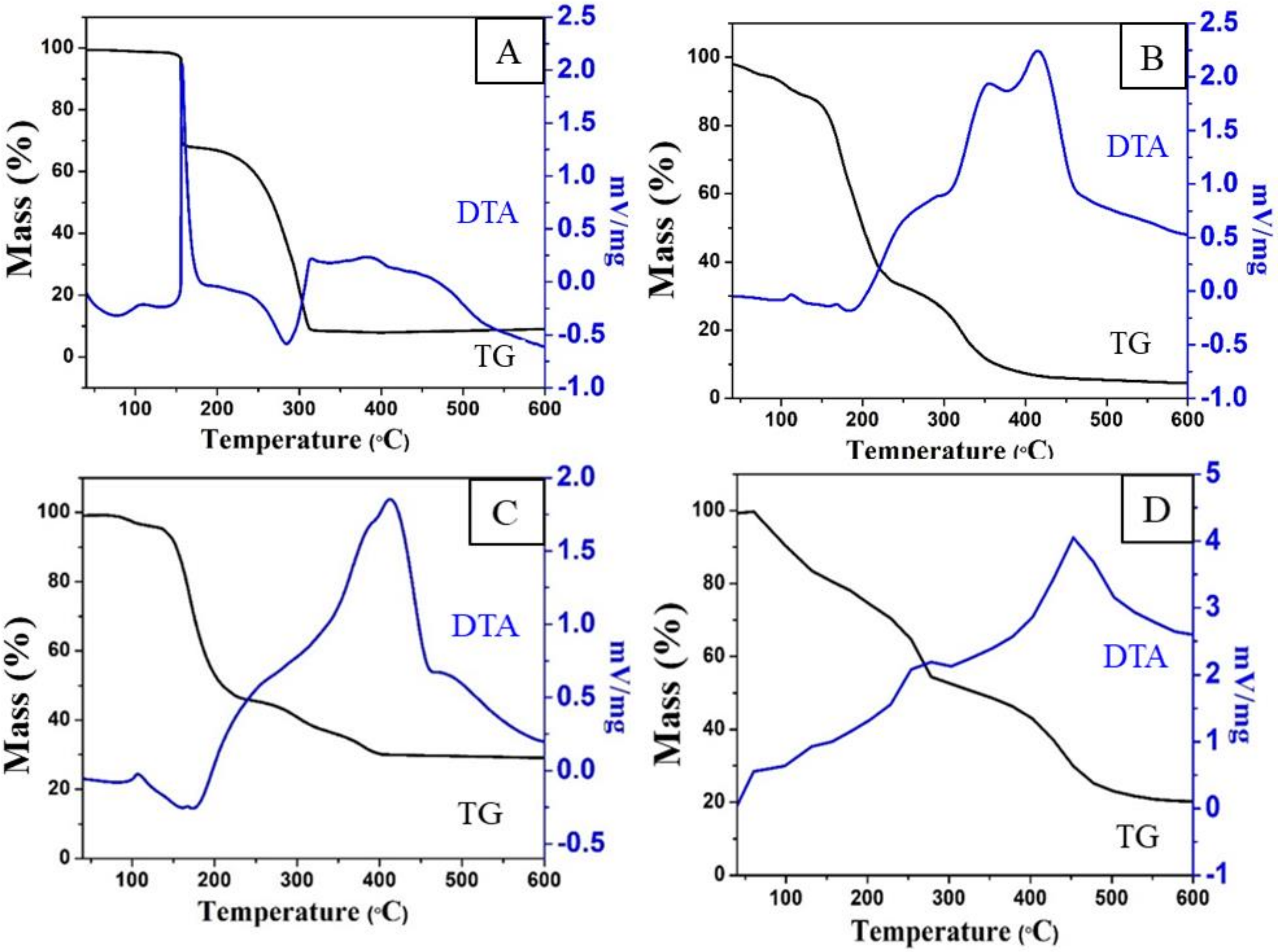

**Figure 4.16:** TG-DTA curve of the as-synthesized mixture of (A) ammonium heptamolybdate–carbohydrazide, (B) ammonium heptamolybdate-semicarbazide (C) ammonium heptamolybdate–N-methylurea and (D) ammonium heptamolybdate–tetramethylurea mixtures.

Figure 4.16 A-D represents the TG-DTA curve of the as-synthesized ammonium heptamolybdate-substituted urea mixtures. The initial weight loss observed below 150 °C, corresponding to an endothermic peak around 100-110 °C in DTA, is attributed to the loss of physically adsorbed water and is common in most of the samples. However, striking differences were observed in the subsequent decomposition rate of hybrid gels based on the type of substitution in the urea. For instance, in the case of NH- substituted carbohydrazide and semicarbazide modified precursor gels, decomposition started during its melting process i.e.,~ 155 °C for carbohydrazide and ~ 175 °C for semicarbazide. Upon further heating, a major weight loss was observed, which could be attributed to the combustion of, at first, the excess uncoordinated carbohydrazide/semicarbazide, followed by the combustion of those molecules coordinated with ammonium heptamolybdate, which required relatively higher temperatures for complete removal. In both the cases of MC and MSC, distinct two-step weight loss patterns were observed, unlike MM and MT.

Additionally, the in situ reducing atmosphere created in the case of -NH substituted ureas also could result in the formation of $MoO_{3-x}$ surface oxide, as confirmed by XPS studies. A similar effect can be observed in urea-modified precursor gels, with urea decomposition producing $NH_3$ and CO. The FTIR analysis were also performed wherein characteristic peaks due to C-H, C-N, N-H, N-N, C=O, and O-H, stretching frequencies of the corresponding substituted ureas modified mixtures were observed (refer figure SF25 in Annexure-I). These peaks get eliminated upon calcination at 500 °C in air, giving rise to O-Mo-O and Mo=O vibrations at 672 $cm^{-1}$ and 837 $cm^{-1}$ leading to the formation of $MoO_{3-x}$ in agreement with XRD and XPS studies.

## 4.5 EVALUATION OF THE CHARGE STORAGE PROPERTIES OF MICROSTRUCTURED 2D $MoO_{3-x}$ SYNTHESIZED USING SUBSTITUTED UREAS

### 4.5.1 Three electrode charge storage studies

The investigation of charge storage properties in order to investigate the effect of NH- and CH- substitution in urea to generate $MoO_{3-x}$, was carried out using cyclic voltammetry (CV), galvanostatic charge-discharge (GCD), and electrochemical impedance spectroscopy (EIS) tests. Figure 4.17 A shows an overlay cyclic voltammograms of MoO$_{3-x}$ synthesized using the different substituted ureas at a scan rate of 10 mV s$^{-1}$ in a potential window between -0.2 to 1.0 V (vs. Ag/AgCl) at 28°C ± 1°C. It is observed, that the high area under the voltammograms is shown by the MoO$_{3-x}$ microplates (MC) indicative of their large charge storage characteristics. As observed from our XRD analysis (Figure 4.14 A), MC and MP microplates have the dominance of (040) plane. The (040) plane of MoO$_{3-x}$ have been reported several times as being the reason for improved electro-catalytic activity.[54] To understand the improved kinetics associated with (040) surface dominant MoO$_{3-x}$, the diffusion coefficient (D$_0$) for H$^+$ ions was estimated by performing a scan rate-dependent study of the different MoO$_{3-x}$ modified electrodes. (refer figure SF26 in Annexure-I)

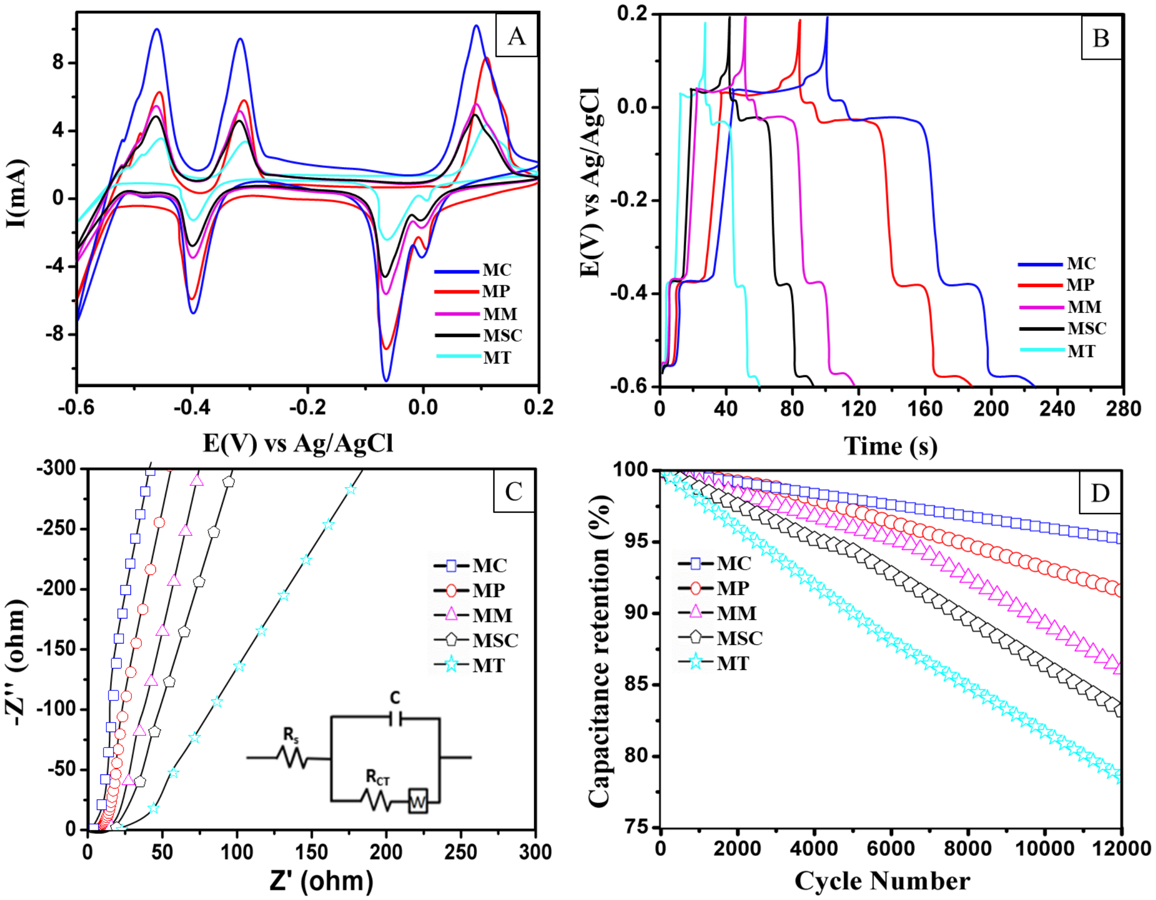

**Figure 4.17:** Supercapacitor performance investigated via (A) CV analysis at a scan rate of 10 mV s$^{-1}$; (B) GCD analysis at the current density of 20 A g$^{-1}$ ; (C) Nyquist plots in the frequency range of 1 mHz to 1 MHz; and (D) cycling stability performance evaluated at a constant current density of 40 A g$^{-1}$.

Figure SF-22 shows the CVs of the synthesized $MoO_{3-x}$ microstructures at scan rates from 25 to 250 mV $s^{-1}$. The oxidation current increases with increasing scan rate. Inset shows the graph of oxidation peak current vs square root of scan rate, which exhibits a linear regression with $R^2$ value of 0.99, which is an indication that there is no surface poisoning of the electrode surface. Furthermore, the diffusion coefficient ($D_0$) for $H^+$ ions were estimated using the Randles-Sevciks method described in section 2.4.4 The calculated $D_0$ value obtained for MC was $1.8 \times 10^{-4}$ $cm^2$ $s^{-1}$ which was close to MP with a value of $1.4 \times 10^{-4}$ $cm^2$ $s^{-1}$, while that of MM was $1.1 \times 10^{-4}$ $cm^2$ $s^{-1}$. MSC and MT demonstrated the lowest values of $0.7 \times 10^{-4}$ $cm^2$ $s^{-1}$ and $0.5 \times 10^{-4}$ $cm^2$ $s^{-1,}$ respectively, which could be ascribed to their particle-like morphologies. The greater $D_0$ values for MC and MP indicate the ease with which the $H^+$ ions can diffuse in as well as out of the $MoO_{3-x}$ matrix. To understand the reason behind the difference in $D_0$ values between the morphologies, the electroactive areas of the materials were estimated using the method described in section 2.4.3.

| **Material code** | **Electroactive surface area ($cm^2$)** | **BET surface area ($m^2$ $g^{-1}$)** |
|---|---|---|
| MC | 0.98 | 14.2 |
| MP | 0.92 | 12.9 |
| MM | 0.71 | 10.4 |
| MSC | 0.65 | 9.1 |
| MT | 0.41 | 7.0 |

**Table 4.6:** Summary of the electroactive and BET surface area for the different $MoO_{3-x}$ synthesized using substituted ureas.

MC resulted in the highest electroactive area of 0.98 $cm^2$ followed by MP (0.92 $cm^2$), while MM, MSC had relatively lower electroactive areas of 0.71 $cm^2$, 0.65 $cm^2$ respectively with WT (0.41 $cm^2$) being the lowest electroactive surface. The BET surface area analysis results were in trend with the electroactive area results and were observed to be 14.2, 12.9, 10.4, 9.1, and 7.0 $m^2$ $g^{-1}$ for MC, MP, MM, WSC, and MT, respectively. (refer figure SF27 in Annexure-I) The decrease in the electroactive areas from the microplates to particle agglomerates (refer table 4.6) can be understood as a consequence of the reduction in surface oxygen defects and decreased presence of intercalated $H_2O$ as observed from the XPS analysis (refer table 4.5).

The values of specific capacitance for synthesized microstructures were calculated from cyclic voltammograms as well as galvanostatic charge-discharge analysis using the formulas described in section 2.4.1. A typical overlay of the cyclic voltammograms recorded at a scan rate of 10 mV $s^{-1}$ is shown in figure 4.18 A. The values of specific capacitance at various scanning rates have been tabulated in table 4.7. The highest specific capacitance of 641.3 F $g^{-1}$ was observed for MC, followed by MP (625.2 F $g^{-1}$), while MM, MSC, and MT produced relatively lower values of 593.3, 573.6, and 520.1 F $g^{-1}$.

| Scan rate (mV $s^{-1}$) | Specific capacitance (F $g^{-1}$) (Error bar ± 2%) | | | | | | | |
|---|---|---|---|---|---|---|---|---|
| | MC | | MM | | MSC | | MT | |
| | 3 Elec. | 2 Elec. | 3 Elec. | 2 Elec. | 3 Elec. | 2 Elec. | 3 Elec. | 2 Elec. |
| 5 | 641.3 | 238.1 | 593.2 | 201.3 | 573.6 | 191.2 | 520.1 | 175.3 |
| 10 | 586.4 | 129.3 | 562.3 | 114.2 | 541.2 | 106.5 | 501.3 | 92.7 |
| 20 | 493.5 | 75.3 | 478.1 | 62.3 | 463.9 | 53.6 | 415.2 | 42.6 |
| 50 | 397.3 | 52.8 | 362.2 | 43.2 | 341.1 | 39.2 | 301.9 | 35.2 |
| 100 | 341.3 | 46.9 | 326.9 | 39.1 | 302.5 | 31.4 | 275.6 | 25.6 |

**Table 4.7:** Summary of specific capacitance values calculated from CV curves obtained for $MoO_{3-x}$ synthesized using substituted ureas.

Furthermore, these observations were confirmed by performing galvanostatic charge-discharge analysis at various current densities from 20 to 60 A $g^{-1}$ (refer figure SF28 in Annexure I). A typical overlay of the charge-discharge curve recorded at a current density of

20 A $g^{-1}$ is shown in figure 4.18 C. Specific capacitance calculated from charge-discharge curve at various current densities, and their values are tabulated in table 4.8. The values for specific capacitance at the current density of 20 A $g^{-1}$ are observed to be 435.2 F $g^{-1}$, 410.6 F $g^{-1}$, 419.9 F $g^{-1}$, 402.6 F $g^{-1}$, and 382.3 F $g^{-1}$ for MC, MP, MM, MSC, and MT respectively.

| Current density (A $g^{-1}$) (Three/Two) | Specific capacitance (F $g^{-1}$) (Error bar ± 2%) | | | | | | | |
| --- | --- | --- | --- | --- | --- | --- | --- | --- |
| | MC | | MM | | MSC | | MT | |
| | 3 Elec. | 2 Elec. | 3 Elec. | 2 Elec. | 3 Elec. | 2 Elec. | 3 Elec. | 2 Elec. |
| 20/2 | 435.2 | 153.6 | 419.9 | 141.3 | 402.6 | 131.4 | 382.3 | 118.6 |
| 30/4 | 356.1 | 142.2 | 348.3 | 129.6 | 339.2 | 118.5 | 321.5 | 101.2 |
| 40/6 | 325.9 | 113.3 | 302.2 | 101.7 | 285.4 | 92.3 | 263.6 | 80.3 |
| 50/8 | 291.6 | 97.1 | 275.3 | 82.6 | 261.5 | 75.6 | 248.2 | 61.2 |
| 60/10 | 194.7 | 86.4 | 179.4 | 71.5 | 160.3 | 62.3 | 147.7 | 40.6 |

**Table 4.8:** Summary of specific capacitance values calculated from GCD analysis obtained for $MoO_{3-x}$ synthesized using substituted ureas.

In order to better understand the observed order of specific capacitance, electrochemical impedance measurements at open circuit potential values within the frequency region of 1mHz to 1MHz were recorded and are presented in figure 4.18 D. The Nyquist plots comprised of two regions wherein a linear dependence was observed in the low-frequency region, which can be attributed to the solution resistance (Rs), whereas a semicircle was observed in the high-frequency region, which could be ascribed to the charge transfer resistance.[48] A representative circuit diagram which best describes the system is presented as an inset in figure 4.17 C. The circuit diagram comprises of a charge transfer resistor ($R_{CT}$) that is connected with a capacitor and a Warburg resistor (W) in parallel and solution resistor ($R_S$) in series. The solution resistance values of 6.1, 8.4, 15.3, 20.8, and 38.7 Ω were observed for MC, MP, MM, MSC, and MT, respectively, indicating greater conductivity of

$MoO_{3-x}$ microplates along with easy access to the electrolytic phase which can be correlated to the presence of oxygen vacancies in the materials.[46]

Electrode stability is also an important parameter for evaluating the performance of capacitor electrode materials.[55] It was observed that the morphology of the electrode material had an impact on its stability. The stability of the modified electrodes was studied by performing continuous galvanostatic charge-discharge measurements and has been presented in Figure 4.17 D. It was observed that the electrode films prepared from $MoO_{3-x}$ microplates were significantly more stable than those prepared with nanoparticles with the order of capacitance retention being MC (95.1 %) (309.9 F $g^{-1}$) > MP (91.7 %) (292.6 F $g^{-1}$) > MM (86.3 %) (260.7 F $g^{-1}$) > MSC (83.5 %) (238.3 F $g^{-1}$) > MT (78.6 %) (207.1 F $g^{-1}$) compared to their initial specific capacitance as reported in table 4.8.. The excellent stability demonstrated by MC and MP indicated their potential for device scale applications and have been evaluated for the same in the next section 4.5.2.

### 4.5.2 Electrochemical performance of the $MoO_{3-x}$//AC asymmetric supercapacitor device

To evaluate the influence of substituted urea towards the charge storage characteristics of $MoO_{3-x}$ microstructures and to evaluate their practical applicability, asymmetric supercapacitor devices were assembled using $MoO_{3-x}$ microstructures fabricated onto carbon paper as the anode and activated carbon (AC) fabricated onto another carbon paper as an cathode using the methodology described in section 2.3.2.1. Figure 4.19 A displays an overlay of the cyclic voltammograms at a fixed scan rate of 5 mV $s^{-1}$ and galvanostatic charge-discharge studies at a constant current density of 2 A $g^{-1}$ has been presented as figure 4.19 B. The two figures indicate both greater voltammogram area and longer discharge time for MC and MP electrodes in comparison to MM, MSC and MT.

Scan rate dependent CV and current density-dependent GCD studies were also performed (refer figures SF29 and SF 30 in Annexure-I), and the specific capacitance thus obtained has been tabulated in tables 4.7 and 4.8 (Equations 2.4 and 2.5). The highest specific capacitance of 238.1 F $g^{-1}$ at a scan rate of 5 mV $s^{-1}$ and 153.6 F $g^{-1}$ at a current density of 2 A $g^{-1}$ was demonstrated by MC. The observed results of specific capacitance measurements were in line with the results of three-electrode studies. The EIS studies showed the Rs values of 5.1, 5.9, 8.6, 10.2, and 14.6 Ω by MC, MP, MM, MSC, and MT, respectively. A representative circuit diagram which best describes the system is presented as an inset in figure 4.18 C. The circuit diagram comprises of a charge transfer resistor ($R_{CT}$) that is connected with a capacitor and a Warburg resistor (W) in parallel and solution resistor ($R_S$) in series. Additionally, exceptional cycling stability was also demonstrated by MC and MP when testing over 12000 continuous charge-discharge cycles as demonstrated in figure 4.18 D. Capacitance retention of 90.5 (102.5 F $g^{-1}$), 89.7 (74.2 F $g^{-1}$), 80.9 (82.2 F $g^{-1}$), 79.7 (73.5 F $g^{-1}$), and 73.5 % (59.1 F $g^{-1}$) were observed for MC, MP, MM, MSC, and MT electrodes compared to their initial specific capacitance as reported in table 4.8.

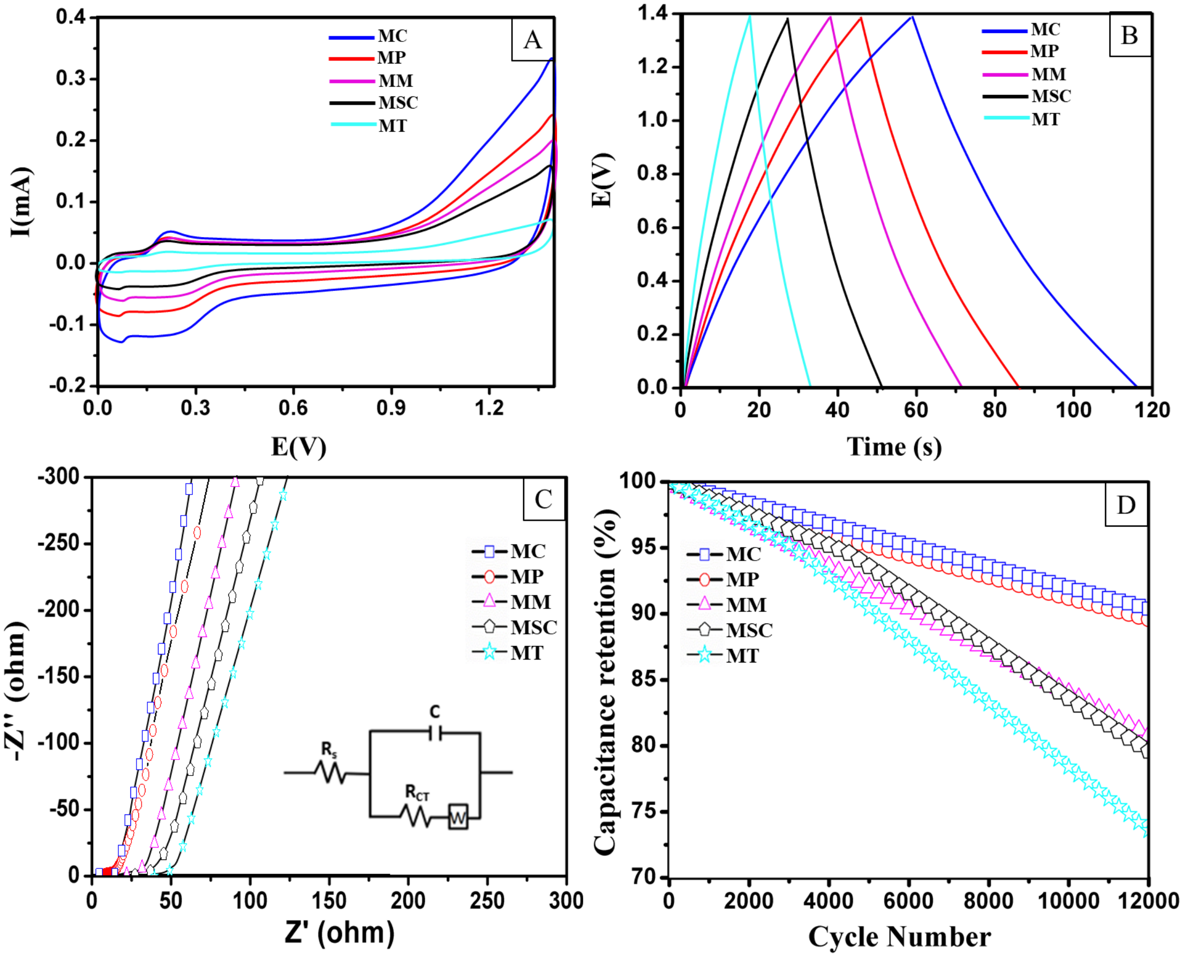

**Figure 4.18:** (A) Overlay of CV curves recorded at a scan rate of 5 mV $s^{-1}$ (B) Overlay of GCD analysis recorded at the current density of 2 A $g^{-1}$ (C) Overlays of Nyquist plots in the frequency range of 1 mHz to 1 MHz and (D) Overlays of cycling stability performance measured in a two-electrode asymmetric setup evaluated at 6 A $g^{-1}$.

Power density and energy density are the most significant parameters of any supercapacitor device. The Ragone plot displaying the performance of the assembled asymmetric supercapacitors have been presented as figure 4.19 (Equations 2.6 and 2.7). The highest power density of 1030 W $kg^{-1}$ and energy density of 44 W h $kg^{-1}$ were demonstrated by the MC, followed by the performance of MP, which displayed a power density of 1021 W $kg^{-1}$ and energy density of 41 W h $kg^{-1}$. In contrast, the MM, MSC and MT due to poor morphological features, demonstrated the least performance. The exceptional capacitance performance and high electrochemical stability of the $MoO_{3-x}$ microstructures can be considered as a cumulative outcome of the presence of a greater number of oxygen vacancies accompanied by surface redox states and microstructured features which facilitate the diffusion of $H^+$ ions through the $MoO_{3-x}$ matrix. The $MoO_{3-x}$ microstructures synthesized so far are capable of acting as excellent charge storage materials at high current densities while maintaining excellent electrochemical stability. However, they can still be improved further if assembled into even higher dimensional microstructures. This has been the motivation that has led to the synthesis of $MoO_{3-x}$ microflowers which have been presented in the next section 4.6.

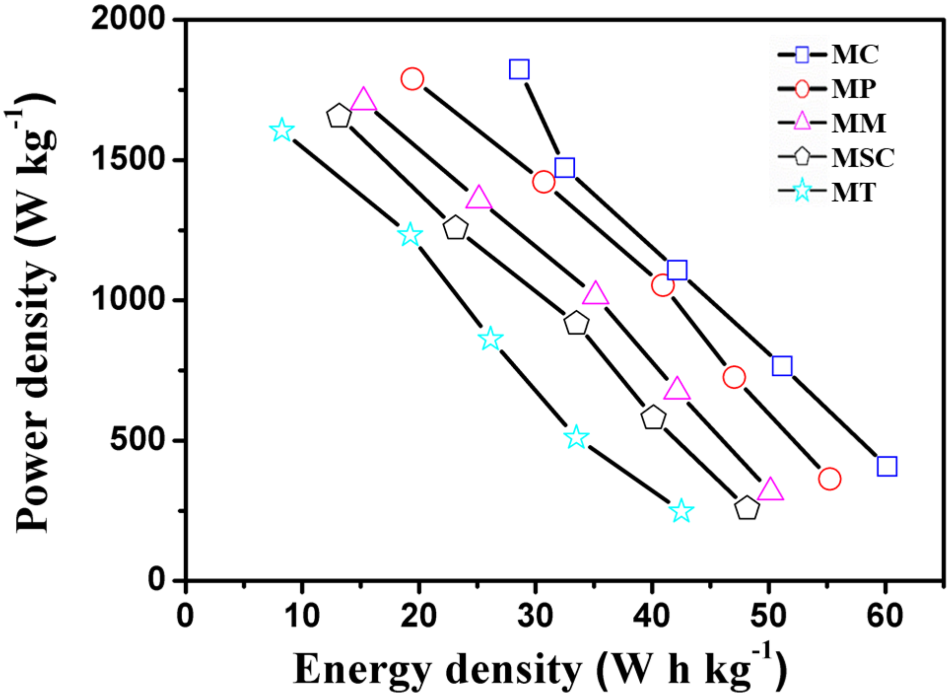

**Figure 4.19:** Ragone plot demonstrating the device performance of $MoO_{3-x}$ microstructures.

## 4.6 DESIGNING 3D $MoO_{3-x}$ MICROFLOWERS WITH EXCEPTIONAL CHARGE STORAGE PERFORMANCE

3D microstructures have immense potential applications in the field of energy harvesting, bioengineering, optical diagnostics, drug delivery etc.[56–58] The curiosity and fascination towards self-assembled microstructures has lead material chemists around the world to synthesize structures using organic and inorganic molecules, and gain insight into self-assembly mechanisms, study material properties and its utilization in potential applications. Tuning the nanomaterial design into higher dimensional structures is extremely challenging due to the complexity of self-assembling mechanisms. Recently, Nag and co-workers synthesized bimetallic Au-Cu alloy microflowers as surface-enhanced Raman spectroscopy substrates using thermolysis of metal-alkyl ammonium halide precursors.[59] Wang and co-workers synthesized ZnO nanorod-based microflowers decorated with $Fe_3O_4$ using a hydrothermal system followed by annealing technique and demonstrated their application for electromagnetic wave absorption.[60] Yu and co-workers synthesized $MoS_2$ microflowers decorated on $VS_2$ microflakes using a chemical vapor deposition technique and demonstrated them for electrolytic hydrogene evolution reaction.[61] Ding and co-workers designed a microflower comprised of Cu/$Cu_xO$/Nitrogenated carbon by pyrolysis of a Cu metal-organic framework. They demonstrated the material as both a electrocatalysts as well as a horseradish peroxidase mimic.[62] Hatamie and co-workers designed Yttrium hexacyanoferrate microflowers on freestanding graphene substrate using a template-assisted chemical vapor deposition technique and demonstrated them as ascorbic acid detectors.[63]

Although these methods produce microflower-like structures, use of expensive templates and post-separation complexities limit their large-scale production. Therefore, a great deal of further research is required to develop simple and scalable methods for preparing microflowers of semiconductor oxides, especially with reference to their utilization in energy and environmental applications. Therefore, this section presents a facile citric acid-assisted synthetic route for producing $MoO_{3-x}$ microflowers. The design strategy utilizes a citric acid-ammonium heptamolybdate hybrid mixture, controlled pH, and calcination treatment in order to generate $MoO_{3-x}$ microflowers. Furthermore, these $MoO_{3-x}$ microflowers are demonstarted for their charge-storage performance.

### 4.6.1 SEM studies

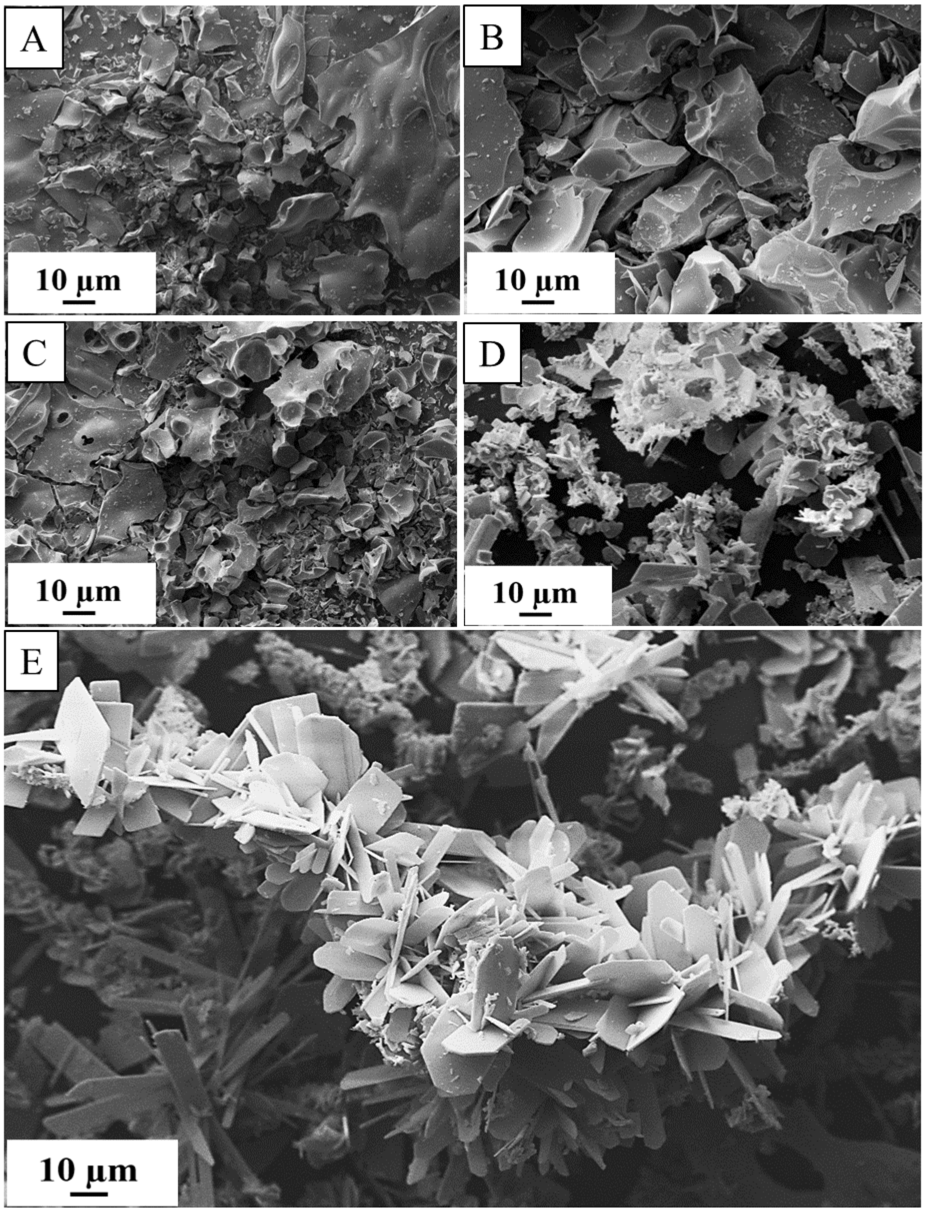

**Figure 4.20:** (A-E) SEM micrograph of temperature-dependent morphological transformation of ammonoium heptamolybdate-citric acid hybrid mixture (A) 150 °C, (B) 250 °C , (C) 350 °C, (D) 450 °C, and (E) 550 °C.

Calcination of ammonium heptamolybdate-citric acid hybrid mixture resulted in the formation of MMF. Figure 4.20 (A-E) presents the temperature-dependent morphological transformation and growth of $MoO_{3-x}$ microflowers (hereafter referred to as MMF). Initially, at temperature below 350 °C, no microstructures were observed due to the presence of excess citric acid in the mixture. At temperatures above 350 °C, a microplate-like transient structures appeared, which arrange into $MoO_{3-x}$ microflowers at a temperature of 550 °C. Other parameters such as Mo to citric acid ratio and solution pH, which could also play a key role towards the synthesis of MMF were investigated, and the SEM results have been presented in figure 4.20.

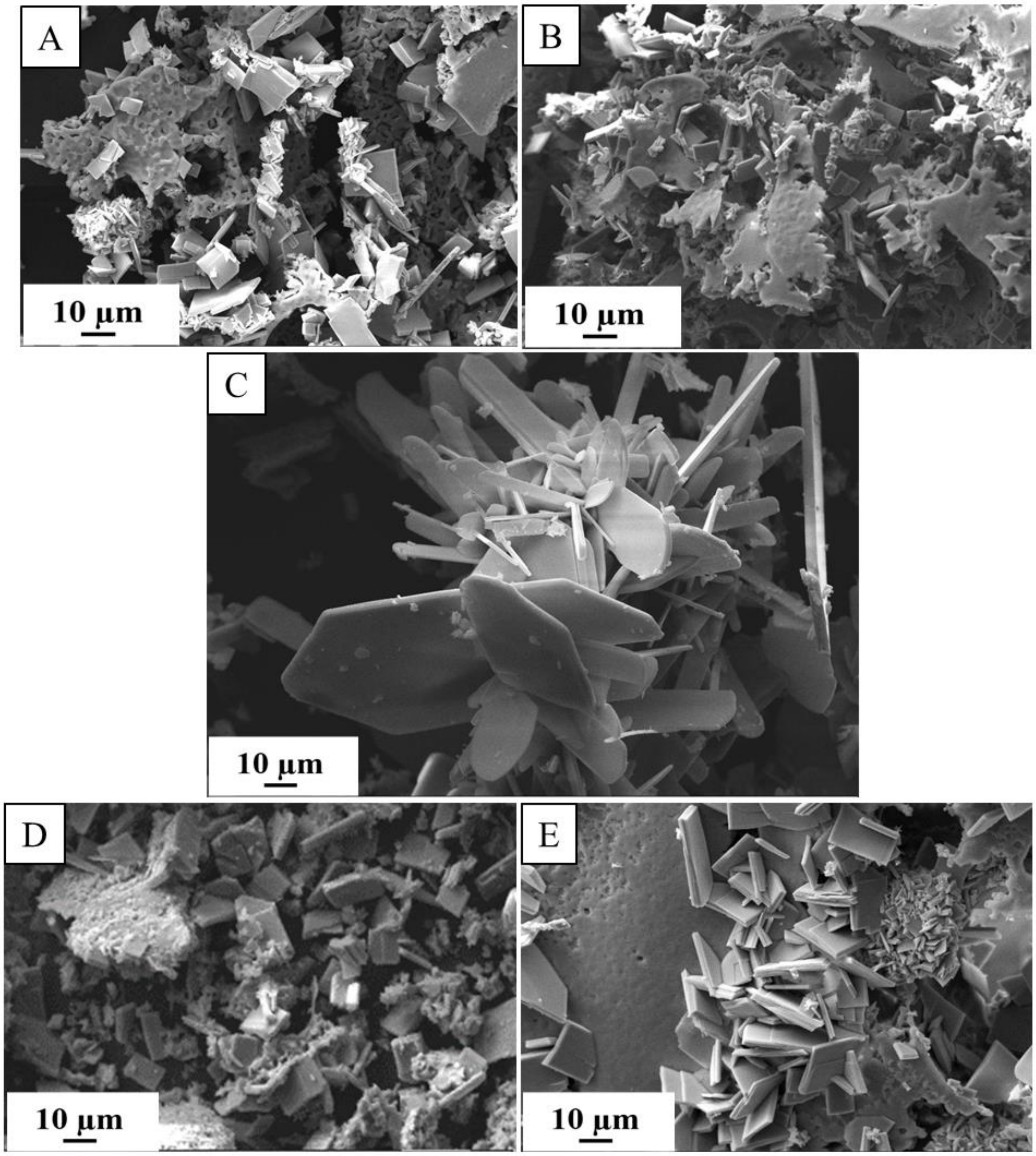

**Figure 4.21: (A-C)** SEM micrograph of $MoO_{3-x}$ microflowers at different Mo: Citric acid ratio (A) 1:1, (B) 1:3, and (C) 1:6. and (C-E) SEM micrograph of $MoO_{3-x}$ microflowers at at different pH values of (C) 2.5, (D) 5 and (E) 8.

As observed from figure 4.20 (A-C), it was confirmed that Mo : citric acid ratio ≥ 1 : 6 was effective in producing consistent morphologies of MMF. The requirement of excess protons to neutralize the isopolymolybdate anions, as mentioned by Lou *et al.*[23] could be one of the reasons, along with the requirement of sufficient thermal energy produced during the combustion process to construct the microflowers. Additionally, low pH conditions of < 2.5 was another requirement for the synthesis of microflowers. This observation was in line with the growth mechanism presented at 2.2.8 as the octamolybdate ions $[Mo_8O_{26}]^{4-}$ responsible for the formation of microplates exist at this pH value, which are the constituents of microflowers.[37–39]

### 4.6.2 HRTEM studies

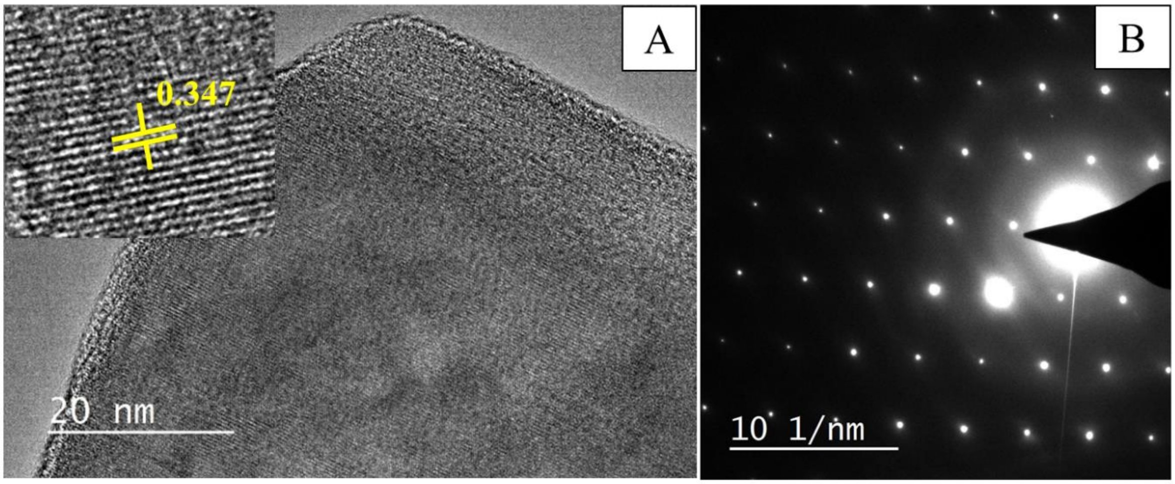

**Figure 4.22:** (A) HRTEM and (B) SAED analysis of MFF respectively.

The HRTEM and SAED analysis (refer figure 4.22) MFF revealed the lattice fringe with d-spacing of ~ 0.347 nm corresponding to the (040) plane of $MoO_{3-x}$ which is consistent with the XRD results presented in the section 4.6.4. The SAED pattern (refer figure 4.22 B), displayed bright spots due to the monocrystalline surface character of MFF.

### 4.6.3 TG-DTA studies

In the TG analysis of the ammonium heptamolybdate-citric acid mixture (refer figure 4.23), a multistep weight loss pattern corresponding to the thermal decomposition was observed. The initial weight loss at temperature ≤ 150 to 210 ℃ supported by endothermic peaks in DTA, is due to loss of ammonia molecules, which also create a partial reducing environment.[24] The minor decomposition of citric acid can also be expected within this temperature regime. The significant weight loss observed above 300 ℃, which is supported by an exothermic peak in DTA, was due to the complete combustion of citric acid into $NO_x$, $CO_2$, and $H_2O$, leading to the formation of an oxide of molybdenum.[25,26]

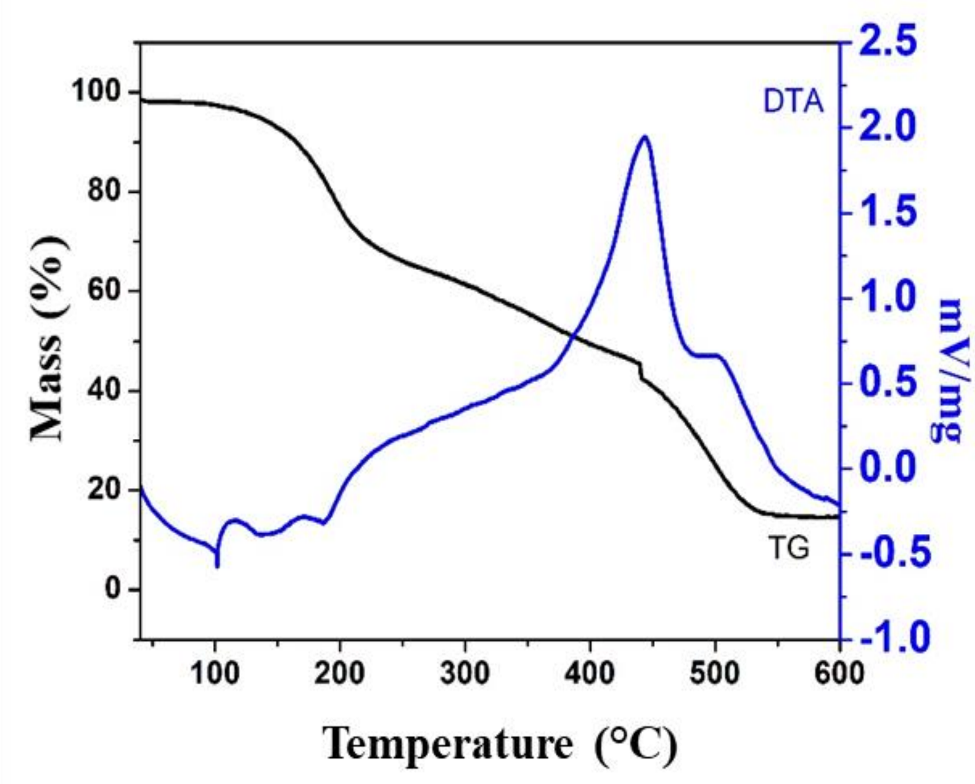

**Figure 4.23:** (A) TG-DTA of the ammonium heptamolybdate-citric acid mixture.

### 4.6.4 IR and XRD studies

IR analysis (refer figure 4.24 A) revealed the presence of a broad peak within 3600 to 2300 $cm^{-1}$ which could be a combination of O-H and C-H stretching vibrations. The O-H bending vibration was observed at 1660 $cm^{-1}$. The C=O and C-O stretching frequencies of citric acid present in the mixture were observed at the characteristic wavenumbers of 1722 and 1207 $cm^{-1}$ at 250 °C, respectively. These signals were eliminated at higher temperatures > 450 °C confirming the decomposition of citric acid. A broad peak corresponding to the presence of O-Mo-O and Mo=O vibration within 1020 to 535 $cm^{-1}$ was indicative of the oxide formation at the temperature of 550 °C.[64]

Figure 4.24 B presents the XRD patterns depicting a gradual transformation of ammonium-heptamolybdate mixture into the orthorhombic phase (JCPDS card number 05-0508), of $MoO_{3-x}$. It was observed that no indexable peaks could be obtained at temperatures > 350 °C due to the presence of excess carbon in the sample. However, the XRD peaks appeared at temperatures < 450 °C. In the MMF obtained at 550 °C, the material showed peaks at $2\theta$ values of 12.5, 23.1, 25.8, 27.2, 33.9, and 39.3, having miller indices (002), (110), (040), (021), (111), and (060), respectively and were as reported in literature corresponding to the orthorhombic phase of $MoO_{3-x}$.[52,53] Since the observed peaks were intense, sharp, and of narrow width with no peaks of secondary phases present, it could be concluded that the synthesized MMF was of high phase purity and crystallinity.

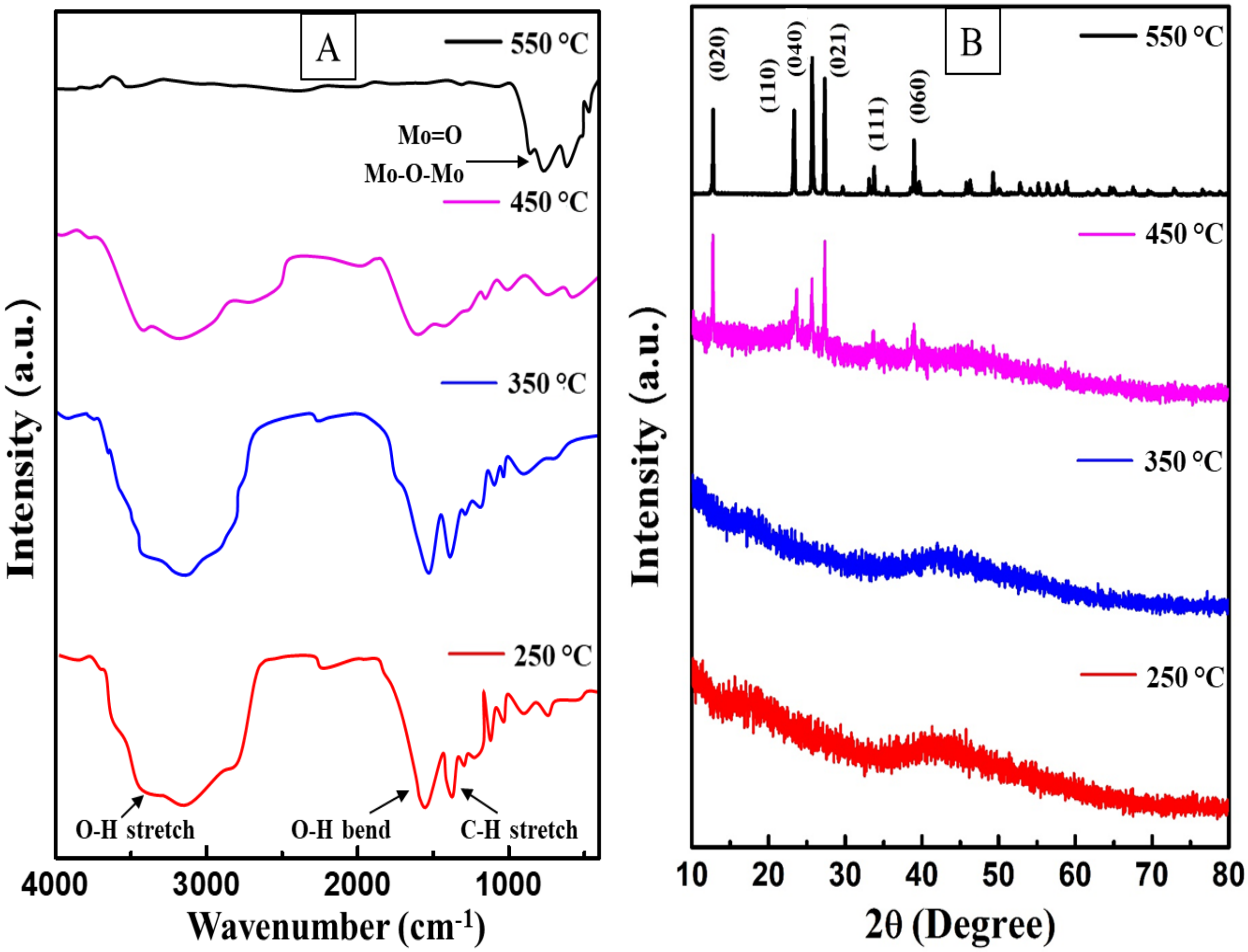

**Figure 4.24:** (A) IR spectra and (B) XRD patterns depicting transformation of ammonium heptamolybdate-citric acid mixture at various temperatures from 250 to 550 °C.

### 4.6.5 Raman and XPS studies

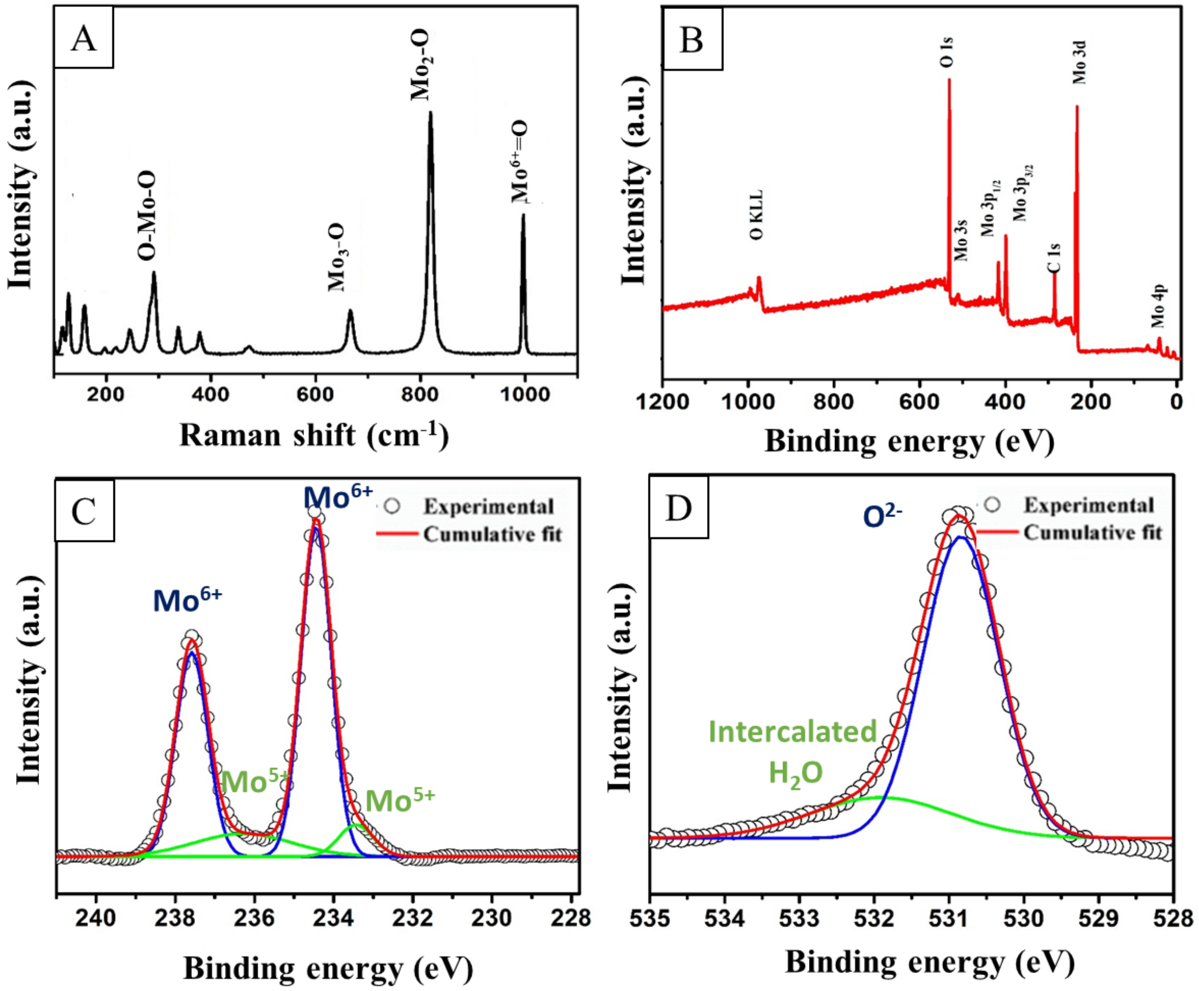

**Figure 4.25:** (A) Raman spectrum and (B-D) XPS spectra of MMF.

Figure 4.25 A shows the Raman spectrum for MMF. The Raman spectrum showed the typical signature vibrations of $MoO_{3-x}$ with strong peaks at 283, 668, 820, and 998 cm$^{-1}$ which were in agreement with the previously reported $\alpha$-$MoO_3$.[30,31] The Raman peak at 998 cm$^{-1}$ can be assigned to the asymmetric terminal oxygen's (Mo$^{+6}$=O) stretching mode and is indicative of the formation of a layered structure. The highest intensity peak observed in Raman is at 820 cm$^{-1}$, which indicates bi-coordinated oxygen ($Mo_2$-O) whereas the peak due to tri-coordinated oxygen ($Mo_3$-O) is observed at 668 cm$^{-1}$. The peak at 283 cm$^{-1}$ can be assigned to the wagging vibration (O-Mo-O). Additionally, since the sharpness of the peaks in Raman spectra is proportional to the crystallinity and structural order, it could be concluded that the synthesized $MoO_{3-x}$ were crystalline in nature, as also confirmed through the XRD analysis.

In order to elucidate the electronic properties of $MoO_{3-x}$ microflowers XPS analysis were performed. A quantitative estimate of the surface redox states and oxygen vacancies of MMF was estimated from the narrow scan XPS spectra of Mo3d and is presented in table 4.9. The high-intensity peaks at the binding energies of 232.8 and 236.1 eV can be ascribed to $Mo^{+6}$ $3d_{5/2}$ and $Mo^{+6}$ $3d_{3/2}$ and the peaks at the binding energies of 231.5 and 234.6 eV can be denoted as the peaks for $Mo^{+5}$ $3d_{5/2}$ and $Mo^{+5}$ $3d_{3/2}$. The peak area integration of the $Mo^{+6}$ and $Mo^{+5}$ species revealed a $Mo^{+5}$ percentage of 17.4 % which is highest among all the previously synthesized $MoO_{3-x}$ microstructures. The peak in the O1s spectra observed at the binding energy of 530.8 eV can be assigned to lattice oxygen ($O^{2-}$), whereas the peak observed at the binding energy of 531.9 eV is due to intercalated $H_2O$ and is also another indicator for presence of oxygen vacancies in the material [34–36]

| Material | Narrow scan | Tungsten species | XPS area integration (%) | Area ratio $W^{5+}$ / $W^{6+}$ |
|---|---|---|---|---|
| MMF | Mo 3d | $Mo^{6+}$ | 82.6 | 0.21 |
| | | $Mo^{5+}$ | 17.4 | |
| | O 1s | $O^{2-}$ | 53.3 | |
| | | Intercalated $H_2O$ | 46.7 | |

**Table 4.9:** The percentage of species obtained from the XPS peak area integration of narrow scan spectra of MMF.

### 4.6.7 Growth mechanism of 3D $MoO_{3-x}$ microflowers

A schematic representation of the plausible growth mechanism of MMF is illustrated in figure 4.26. Ammonium heptamolybdate is known to produce layered $MoO_3$ upon decomposition in a reaction, which is similar to a combustion process. The $MoO_3$ thus produced comprises of long chains of $MoO_6$ octahedra, which exhibit morphologically incomplete and uncontrolled growth. In order to gain control over the growth process of

$MoO_{3-x}$, control over the nucleation and growth steps during synthesis must be established. This has been achieved in the present work by making use of citric acid, both as an additive and a fuel. Citric acid is a well-known naturally available organic surface modifier, used in nanomaterial synthesis. Being a weak triprotic acid with three carboxylic groups that are able to cap metal ions under controlled pH conditions, allows synthetic tunability for designing microstructures.

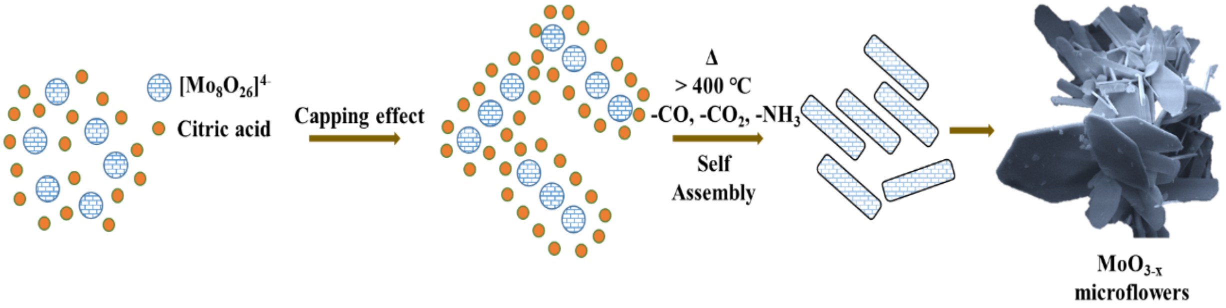

**Figure 4.26:** Schematic illustration for the plausible growth mechanism of MMF.

The process is hypothesized to be initiated during the hydrolysis of ammonium heptamolybdate molecule in water, leading to $NH_4^+$ ions and $OH^-$ group release. The type of molybdenum species in the solution is tuned at this stage by controlling the pH. At pH values of 2.5, ammonium octamolybdate ions $[Mo_8O_{26}]^{4-}$ are known to exist in the solution. Our previous studies have proven that the octamolybdate species are useful for synthesizing $MoO_{3-x}$ microplates. Thus, considering the fact that the microflowers are an assembly of similar microplates rearranged in a hierarchical manner, it is desirable to maintain the $[Mo_8O_{26}]^{4-}$ species in solution. Citric acid when added under these conditions is able to interact with the $Mo^{+6}$ atoms strongly. The strength of interaction is a function of pH and helps citric acid to act as a capping agent to direct the orientational growth of $MoO_{3-x}$ particles and their subsequent transformation to microflowers during the combustion stage. Thus, we observe that at a low pH of 2.5, the interaction of octamolybdate ions with the citric acid leads to the formation of MMF post-combustion with a large 2D aspect ratio while as the pH gradient is shifted in favor of heptamolybdate ions $[Mo_7O_{24}]^{6-}$ at higher pH values, no microstructures were obtained. The temperature-dependent transformation observed in MMF indicates that the $MoO_{3-x}$ nanoparticles fuse under the effect of high combustion temperature to initially produce microplates. These microplates subsequently join together in an hierarchical manner forming $MoO_{3-x}$ microflowers. Furthermore, the microflowers were investigated for their charge storage performance using electrochemical measurements and have been presented in the subsequent section 4.7.

## 4.7 Evaluation of the charge storage properties of 3D $MoO_{3-x}$ microflowers

### 4.7.1 Three electrode charge storage studies

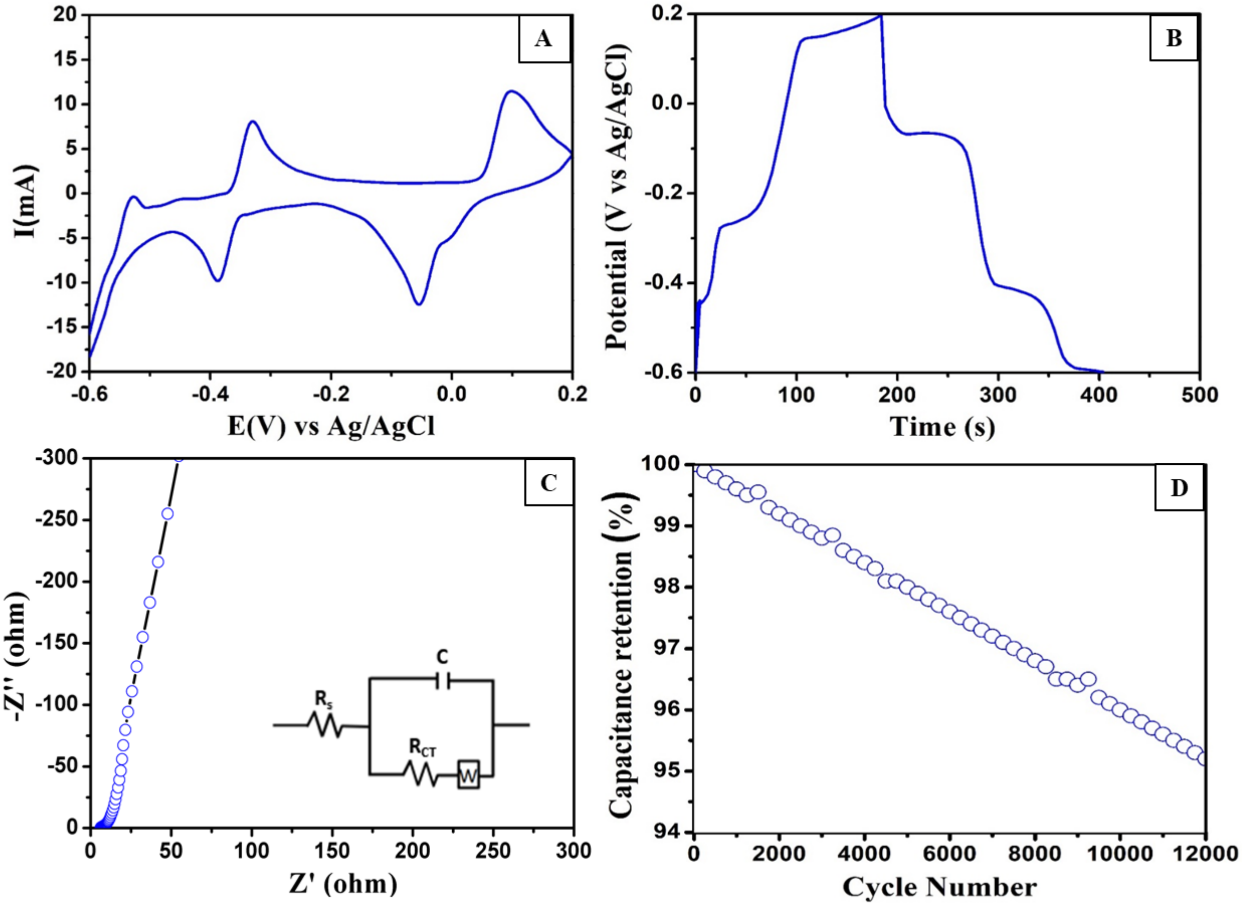

**Figure 4.27:** Supercapacitor performance investigated via (A) CV analysis at a scan rate of 10 mV $s^{-1}$; (B) GCD analysis at the current density of 2 A $g^{-1}$ ; (C) Nyquist plots in the frequency range of 1 mHz to 1 MHz; and (D) cycling stability performance evaluated at a constant current density of 40 A $g^{-1}$.

The synthesized $MoO_{3-x}$ microflowers were subjected to electrochemical testing to evaluate their supercapacitor performance. The supercapacitor performance was studied using cyclic voltammetry (CV), galvanostatic charge-discharge (GCD), and electrochemical impedance spectroscopic (EIS) measurements. 1 M $H_2SO_4$ was employed as an electrolyte for all the electrochemical studies. Figure 4.27 shows the result of measurements in a three-electrode setup. MMF exhibited multiple pairs of redox peaks typical of $MoO_{3-x}$ since they can sustain multiple oxidation states ($Mo^{6+}$, $Mo^{5+}$, and $Mo^{4+}$) owing to their pseudo-capacitive behavior.[40–43] The redox peaks can be attributed to the insertion and extraction of $H^+$ ions as described by the reaction 4.1 mentioned in section 4.3.[44] The multiple oxidation states of $MoO_{3-x}$ are known to have a significant contribution to the overall capacitance of the materials.[45]

| Material code | MMF | | | | |
|---|---|---|---|---|---|
| Scan rate (mV $s^{-1}$) | 5 | 10 | 20 | 50 | 100 |
| Specific capacitamce (F $g^{-1}$) (3 Elec.) (Error bar ± 2%) | 663.7 | 591.6 | 526.7 | 470.2 | 412.5 |
| Specific capacitamce (F $g^{-1}$) (2 Elec.) (Error bar ± 2%) | 246.2 | 156.9 | 91.6 | 75.8 | 60.5 |

**Table 4.10:** Summary of specific capacitance values calculated from CV curves obtained for MMF.

Scan rate-dependent CV analysis were also performed for different scan rates from 10 to 200 mV $s^{-1}$ and have been presented in figure SF33 in Annexure I. It was observed that at faster scan rates, the redox peaks could still be identified, reflecting the faster $H^+$ intercalation/deintercalation ability of the materials.[46] It was also noted that with an increase in scan rates, the reduction and oxidation peaks moved to lower and higher potential values, respectively, indicating the lag in proton and electron pathways caused due to rapid cycling. From the scan rate-dependent CV measurements, the values of anodic peak current ($I_p$) were obtained. Using the slope of the square root of scan rate ($v^{1/2}$) versus the anodic peak current graph, the diffusion coefficient of $H^+$ ions was calculated using the Randles-Sevcik equation as described in 2.4.4.[25,47] The $D_0$ values of $2.32 \times 10^{-4}$ $cm^2$ $s^{-1}$ was obtained which is the highest compared to any of our previously synthesized $MoO_{3-x}$ microstructures. The highest $D_0$ value observed for MP could be a result of microflower-like morphology of MMF that facilitates the diffusion of $H^+$ ions through the $MoO_{3-x}$ matrix. To investigate further, the role of surface morphology on improved electrochemical activity of $MoO_{3-x}$ microstructures, chronoamperometric measurements were performed in order to estimate the electroactive surface area using the method described in section 2.4.3. The results revealed electroactive areas of 0.99 $cm^{2,}$ and BET surface area analysis revealed the surface area values of 15.6 $m^2$ $g^{-1}$ (refer figure SF32 in Annexure-I).

| Material code | MMF | | | | |
|---|---|---|---|---|---|
| Current density (A $g^{-1}$) (3 Elec./2 Elec.) | 20/2 | 30/4 | 40/6 | 50/8 | 60/10 |
| Specific capacitance (F $g^{-1}$) (3 Elec.) (Error bar ± 2%) | 491.2 | 402.8 | 345.5 | 276.8 | 201.3 |
| Specific capacitance (F $g^{-1}$) (2 Elec.) (Error bar ± 2%) | 197.3 | 175.2 | 156.7 | 112.5 | 86.8 |

**Table 4.11:** Summary of specific capacitance values calculated from GCD analysis of MMF.

The values of specific capacitance for synthesized microstructures were calculated from cyclic voltammograms as well as galvanostatic charge-discharge analysis using the formulas described in section 2.4.1. A typical overlay of the cyclic voltammograms recorded at a scan rate of 10 mV $s^{-1}$ is shown in figure 4.27 A. The values of specific capacitance at various scanning rates have been tabulated in table 4.7. The highest specific capacitance of 663.7 F $g^{-1}$ at a scan rate of 5 mV $s^{-1}$ and 452.3 at a current density of 20 A $g^{-1}$ were obtained from CV and GCD analysis, respectively. (refer figure SF31 in Annexure-I).

To better understand the observed order of specific capacitance, electrochemical impedance measurements at open circuit potential values within the frequency region of 1 mHz to 1 MHz were recorded and are presented in figure 4.27 C. The Nyquist plots comprised of two regions wherein a linear dependence was observed in the low-frequency region, which can be attributed to the solution resistance (Rs), whereas a semicircle was observed in the high-frequency region which can be ascribed to charge transfer resistance.[48] A representative circuit diagram which best describes the system is presented as an inset in figure 4.27 C. The circuit diagram comprises of a charge transfer resistor ($R_{CT}$) that is connected with a capacitor and a Warburg resistor (W) in parallel and solution resistor ($R_S$) in series. The solution resistance values of 5.2 Ω was observed for MMF indicating great conductivity of

$MoO_{3-x}$ microflowers along with easy access to the electrolytic phase, which can be correlated to the presence of oxygen vacancies, thinner microlayers that provide accessible diffusion pathways along with suitable aspect ratio in the material.[46] The material's cycling stability was also evaluated by performing continuous charge-discharge measurements (refer figure 4.27 D). MMF demonstrated excellent stability with capacitance retention of 95.4 % (329.6 F $g^{-1}$), compared to its initial specific capacitance of 345.5 F $g^{-1}$. The excellent stability demonstrated by MMF indicate their potential for device scale applications and have been evaluated for the same in the next section 4.7.2.

### 4.7.2 Electrochemical performance of the MMF//AC asymmetric supercapacitor device

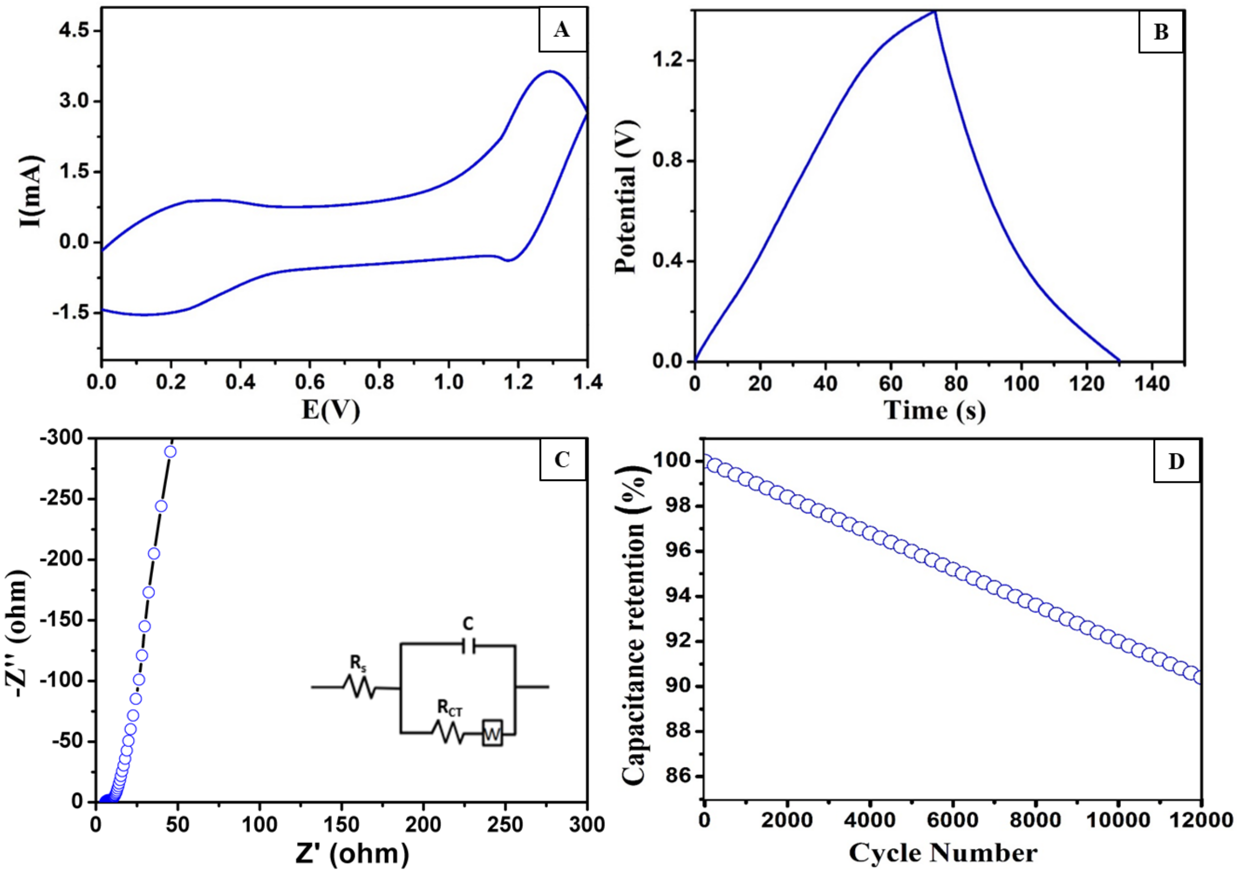

**Figure 4.28:** (A) Overlay of CV curves recorded at a scan rate of 5 mV $s^{-1}$ (B) Overlay of GCD analysis recorded at the current density of 2 A $g^{-1}$ (C) Overlays of Nyquist plots in the frequency range of 1 mHz to 1 MHz and (D) Overlays of cycling stability performance measured in a two-electrode asymmetric setup evaluated at 6 A $g^{-1}$.

To evaluate the practical applicability of the synthesized $MoO_{3-x}$ microflowers, an asymmetric supercapacitor device was assembled using microflowers fabricated onto carbon paper as the anode and activated carbon (AC) fabricated onto another carbon paper as a cathode using the methodology described in section 2.3.2.1. Figure 4.28 A displays an overlay of the cyclic voltammograms at a fixed scan rate of 5 mV $s^{-1}$ and galvanostatic charge-discharge studies at a constant current density of 2 A $g^{-1}$ has been presented as figure 4.28 B. Scan rate dependent CV and current density-dependent GCD studies were also performed (see figures SF33 Annexure-I), and the specific capacitance thus obtained has been tabulated in tables 4.10 and 4.11 respectively (Equations 2.4 and 2.5).

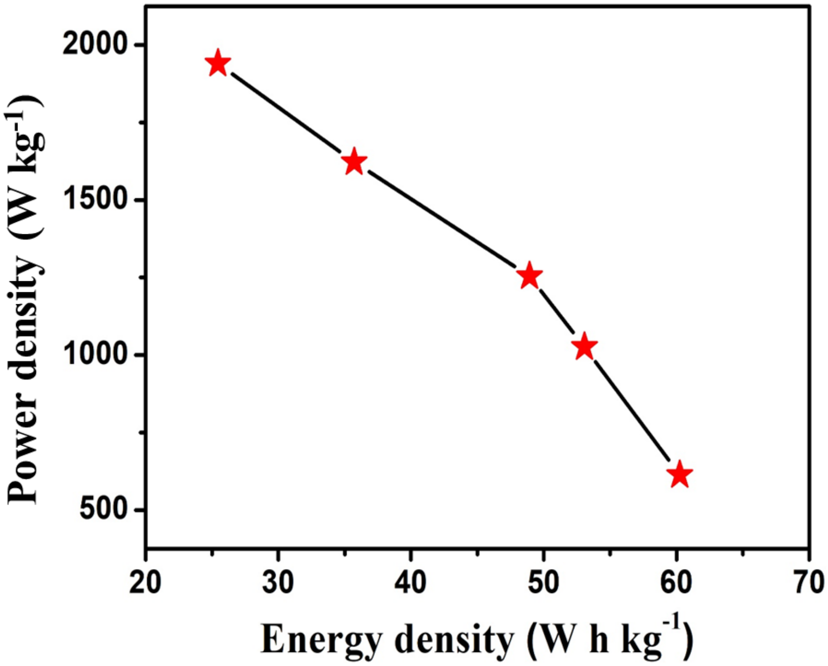

**Figure 4.29:** Ragone plot demonstrating the device performance of MMF.

The highest specific capacitance of 246.2 F $g^{-1}$ at a scan rate of 5 mV $s^{-1}$ and 197.3 F $g^{-1}$ at a current density of 2 A $g^{-1}$ was demonstrated by MMF. The observed results of specific capacitance measurements were in line with the results of three-electrode studies. The EIS studies showed the Rs values of 5.1 Ω, indicating excellent charge-storage characteristics. A representative circuit diagram which best describes the system is presented as an inset in figure 4.28 C. The circuit diagram comprises of a charge transfer resistor ($R_{CT}$) that is connected with a capacitor and a Warburg resistor (W) in parallel and solution resistor ($R_S$) in series.Additionally, exceptional cycling stability was also demonstrated by MMF when tested over 12000 continuous charge-discharge cycles. The material demonstrated excellent capacitance retention of 91.3 % (121.7 F $g^{-1}$), as presented in figure 4.28 D, compared to its initial specific capacitance of 156.7 F $g^{-1}$.

Power density and energy density are the most significant parameters of any supercapacitor device. The Ragone plot displaying the performance of the assembled asymmetric supercapacitors has been presented as figure 4.29 (Equation 2.6 and 2.7). Highest power density of 1498 W $kg^{-1}$ and energy density of 45 W h $kg^{-1}$ were demonstrated by the MMF. The exceptional capacitance performance and high electrochemical stability of MMF can be considered as a cumulative outcome of the presence of a greater number of oxygen vacancies accompanied by surface redox states and microflower-like structure which facilitate the enhanced charge storage performance of the material.

## 4.8 The impact of microstructuring in $MoO_{3-x}$ on the charge storage performance

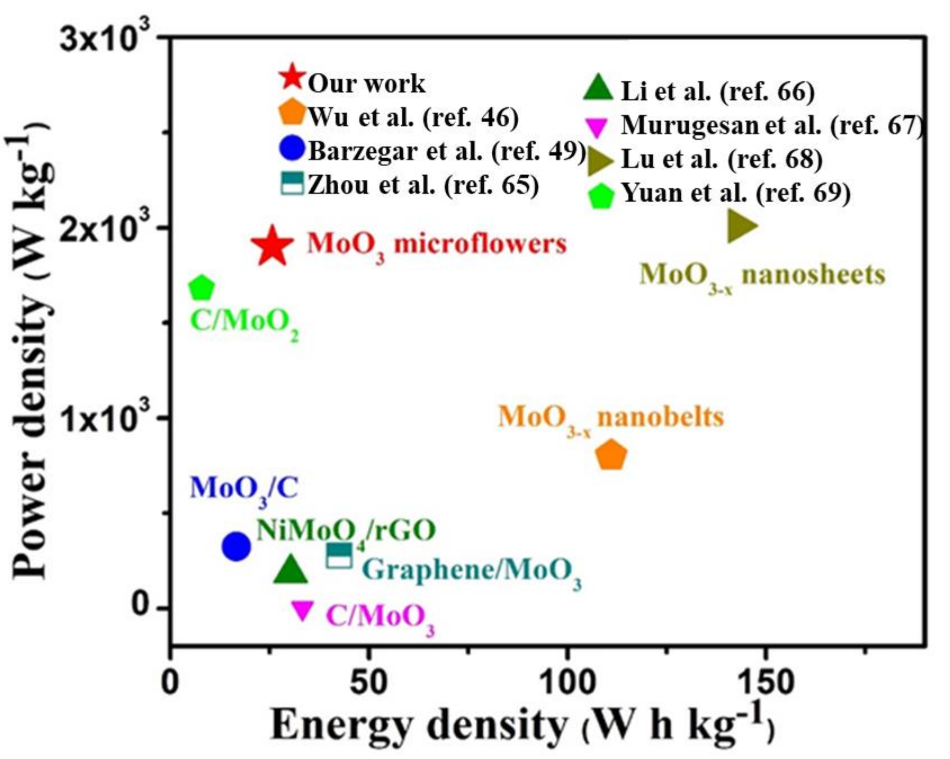

**Figure 4.30:** Comparative analysis of our synthesized $MoO_{3-x}$ with some literature reports.[46,49,65–69]

It is known through literature that nano/microstructuring provides several catalytic advantages to materials, such as generation of kink sites, exposure of catalytically active facets, enhanced material stability, larger surface area, improvements in the long-range anisotropy, etc.[70] Introspecting the charge storage performance of all the synthesized $MoO_{3-x}$, it appears that MA being the simplest microstructure, displayed the least charge storage performance with specific capacitance of 59.2 F $g^{-1}$ along with energy and power density values of 18.9 W h $kg^{-1}$ and 1008.3 W $kg^{-1}$ as shown in Figure 4.30. When dimensionality was increased from the agglomerated nanoparticles to microplates and microdisks of $MoO_{3-x}$, improvement in the charge storage performance was observed, with specific capacitance being doubled to 141.2 F $g^{-1}$ with the energy and power density values of 41.2 W h $kg^{-1}$ and 1021.3 W $kg^{-1}$ for MP, while MD demonstrated specific capacitance of 112.2 F $g^{-1}$ with the energy and power density values of 30.3 W h $kg^{-1}$ and 1015.8 W $kg^{-1}$. The microflowers of $MoO_{3-x}$ demonstrated even better results both in terms of specific capacitance and power performance. These results were at par or in some cases even better than the complex microstructures of $MoO_{3-x}$ reported in literature as presented in figure 4.31. The MMF demonstrated remarkable specific capacitance of 151.6 F $g^{-1}$ with the energy and power density values of 45.7 W h $kg^{-1}$ and 1497.3 W $kg^{-1}$. The observed trend thus present a definite trend in terms of material dimensionality and their charge storage performances.

## 4.9 CONCLUSIONS

This study demonstrates the synthesis of $MoO_{3-x}$ microstructures such as microplates, microdisks, microflowers etc. Fuels such as urea, N-methylurea, tetramethylurea, carbohydrazide, semicarbazide, and citric acid were utilized in a dual role of a structure-directing agent and also as fuel to synthesize complex microstructures of $MoO_{3-x}$. We studied the urea chemistry with heptamolybdate $[Mo_7O_{24}]^{6-}$ and octamolybdate $[Mo_8O_{26}]^{4-}$ ions and used them to synthesize 2D microplates and microdisks of $MoO_{3-x}$. It was observed that the heptamolybdate species played a key role in the formation of microdisks while the octamolybdate species promoted the growth of $MoO_{3-x}$ microplates. It was also confirmed that urea, when utilized under protonated conditions and in a molybdenum to urea ratio of 1:6 or above, could produce $MoO_{3-x}$ microstructures very effectively. Detailed investigation into the growth mechanism by perturbing different synthesis conditions of pH, temperature, time, and ratio were carried out. Furthermore, the microstructure promoting effect of urea, –NH substituted ureas (such as Carbohydrazide and Semicarbazide) and –CH substituted ureas (N-methylurea and tetramethylurea) were also investigated. Similar to $WO_{3-x}$ nanostructures, it was observed that the –NH substitution promoted the growth of the $MoO_{3-x}$ microstructures, while –CH substitution had a detrimental influence on the morphology. Meanwhile, using a citric acid-assisted reflux method was utilized to synthesize $MoO_{3-x}$ microflowers. The synthesized microstructures were characterized using IR, XRD, TG-DTA, SEM, HRTEM, SAED, Raman, EPR, XPS, etc. Detailed spectroscopic analysis revealed that microstructuring enabled effective induction and distribution of oxygen vacancies along with $Mo^{5+}/Mo^{6+}$ and also led to the preferential orientation of the active surface planes such as (040), which were beneficial for the charge storage performance of microstructured $MoO_{3-x}$. Furthermore, all the microstructured $MoO_{3-x}$ were evaluated for their charge-storage performance. $MoO_{3-x}$ microflowers demonstrated the highest performance of all microstructured molybdenum electrodes with an energy density of 45.7 W h $kg^{-1}$ at a power density of 1498.3 W $kg^{-1}$. It is concluded that microstructuring enabled faster electrode-electrolyte interfacial kinetics, improving the material's electrical conductivity and electrochemical cycling stability. These microstructured $MoO_{3-x}$ electrodes with improved charge storage performance have significant potential for commercial device-scale applications.

## 4.10 REFERENCES

(1) Fernández-García, M.; Martínez-Arias, A.; Hanson, J. C.; Rodriguez, J. A. Nanostructured Oxides in Chemistry: Characterization and Properties. *Chem. Rev.* **2004**, *104* (9), 4063–4104.

(2) Naik, A. P.; Mittal, H.; Wadi, V. S.; Sane, L.; Raj, A.; Alhassan, S. M.; Al Alili, A.; Bhosale, S. V; Morajkar, P. P.; Alili], A. [Al; Bhosale, S. V; Morajkar, P. P. Super Porous $TiO_2$ Photocatalyst: Tailoring the Agglomerate Porosity into Robust Structural Mesoporosity with Enhanced Surface Area for Efficient Remediation of Azo Dye Polluted Waste Water. *J. Environ. Manage.* **2020**, *258*, 110029.

(3) Salkar, A. V.; Naik, A. P.; Joshi, V. S.; Haram, S. K.; Morajkar, P. P. Designing a 3D Nanoporous Network: Via Self-Assembly of $WO_3$ Nanorods for Improved Electrocapacitive Performance. *CrystEngComm* **2018**, *20* (42), 6683–6694.

(4) Sun, H.; Pan, J.; Yan, X.; Shen, W.; Zhong, W.; Cheng, X. $MnO_2$ Nanoneedles Loaded on Silicon Oxycarbide-Derived Hierarchically Porous Carbon for Supercapacitor Electrodes with Enhanced Electrochemical Performance. *Ceram. Int.* **2019**, *45* (18, Part A), 24802–24810.

(5) Mas-Ballesté, R.; Gómez-Navarro, C.; Gómez-Herrero, J.; Zamora, F. 2D Materials: To Graphene and Beyond. *Nanoscale* **2011**, *3* (1), 20–30.

(6) Butler, S. Z.; Hollen, S. M.; Cao, L.; Cui, Y.; Gupta, J. A.; Gutiérrez, H. R.; Heinz, T. F.; Hong, S. S.; Huang, J.; Ismach, A. F.; Johnston-Halperin, E.; Kuno, M.; Plashnitsa, V. V.; Robinson, R. D.; Ruoff, R. S.; Salahuddin, S.; Shan, J.; Shi, L.; Spencer, M. G.; Terrones, M.; Windl, W.; Goldberger, J. E. Progress, Challenges, and Opportunities in Two-Dimensional Materials beyond Graphene. *ACS Nano* **2013**, *7* (4), 2898–2926.

(7) Choudhuri, I.; Bhauriyal, P.; Pathak, B. Recent Advances in Graphene-like 2D Materials for Spintronics Applications. *Chem. Mater.* **2019**, *31* (20), 8260–8285.

(8) Tu, Q.; Spanopoulos, I.; Vasileiadou, E. S.; Li, X.; Kanatzidis, M. G.; Shekhawat, G. S.; Dravid, V. P. Exploring the Factors Affecting the Mechanical Properties of 2D Hybrid Organic-Inorganic Perovskites. *ACS Appl. Mater. Interfaces* **2020**, *12* (18), 20440–20447.

(9) Zhang, H. Introduction: 2D Materials Chemistry. *Chem. Rev.* **2018**, *118* (13), 6089–6090.

(10) Cipriano, L. A.; Di Liberto, G.; Tosoni, S.; Pacchioni, G. Quantum Confinement in Group III–V Semiconductor 2D Nanostructures. *Nanoscale* **2020**, *12* (33), 17494–17501.

(11) Khan, K.; Tareen, A. K.; Aslam, M.; Wang, R.; Zhang, Y.; Mahmood, A.; Ouyang, Z.; Zhang, H.; Guo, Z. Recent Developments in Emerging Two-Dimensional Materials

and Their Applications. *J. Mater. Chem. C* **2020**, *8* (2), 387–440.

(12) Wang, X.; Xia, F. Stacked 2D Materials Shed Light. *Nat. Mater.* **2015**, *14* (3), 264–265.

(13) Liu, Z.; Lau, S. P.; Yan, F. Functionalized Graphene and Other Two-Dimensional Materials for Photovoltaic Devices: Device Design and Processing. *Chem. Soc. Rev.* **2015**, *44* (15), 5638–5679.

(14) Zeng, M.; Xiao, Y.; Liu, J.; Yang, K.; Fu, L. Exploring Two-Dimensional Materials toward the Next-Generation Circuits: From Monomer Design to Assembly Control. *Chem. Rev.* **2018**, *118* (13), 6236–6296.

(15) Crowley, K.; Ye, G.; He, R.; Abbasi, K.; Gao, X. P. A. α-MoO3 as a Conductive 2D Oxide: Tunable n-Type Electrical Transport via Oxygen Vacancy and Fluorine Doping. *ACS Appl. Nano Mater.* **2018**, *1* (11), 6407–6413.

(16) Novak, T. G.; Kim, J. J.; Tiwari, A. P.; Kim, J. J.; Lee, S.; Lee, J.; Jeon, S. 2D $MoO_3$ Nanosheets Synthesized by Exfoliation and Oxidation of $MoS_2$ for High Contrast and Fast Response Time Electrochromic Devices. *ACS Sustain. Chem. Eng.* **2020**, *8* (30), 11276–11282.

(17) Inzani, K.; Grande, T.; Vullum-Bruer, F.; Selbach, S. M. A van Der Waals Density Functional Study of $MoO_3$ and Its Oxygen Vacancies. *J. Phys. Chem. C* **2016**, *120* (16), 8959–8968.

(18) Sun, Y.; Wang, J.; Zhao, B.; Cai, R.; Ran, R.; Shao, Z. Binder-Free α-$MoO_3$ Nanobelt Electrode for Lithium-Ion Batteries Utilizing van Der Waals Forces for Film Formation and Connection with Current Collector. *J. Mater. Chem. A* **2013**, *1* (15), 4736–4746.

(19) Parviz, D.; Kazemeini, M.; Rashidi, A. M.; Jafari Jozani, K. Synthesis and Characterization of $MoO_3$ Nanostructures by Solution Combustion Method Employing Morphology and Size Control. *J. Nanoparticle Res.* **2010**, *12* (4), 1509–1521.

(20) Liu, H.; Lee, C. J. J.; Guo, S.; Chi, D. New Insights into Planar Defects in Layered α-$MoO_3$ Crystals. *Langmuir* **2018**, *34* (46), 14003–14011.

(21) Chen, D.; Liu, M.; Yin, L.; Li, T.; Yang, Z.; Li, X.; Fan, B.; Wang, H.; Zhang, R.; Li, Z.; Xu, H.; Lu, H.; Yang, D.; Sun, J.; Gao, L. Single-Crystalline $MoO_3$ Nanoplates: Topochemical Synthesis and Enhanced Ethanol-Sensing Performance. *J. Mater. Chem.* **2011**, *21* (25), 9332–9342.

(22) Jiang, J.; Liu, J.; Peng, S.; Qian, D.; Luo, D.; Wang, Q.; Tian, Z.; Liu, Y. Facile Synthesis of α-$MoO_3$ Nanobelts and Their Pseudocapacitive Behavior in an Aqueous Li2SO4 Solution. *J. Mater. Chem. A* **2013**, *1* (7), 2588–2594.

(23) Lou, X. W.; Zeng, H. C. Hydrothermal Synthesis of α-$MoO_3$ Nanorods via Acidification of Ammonium Heptamolybdate Tetrahydrate. *Chem. Mater.* **2002**, *14* (11), 4781–4789.

(24) Wang, L.; Zhang, G. H.; Chou, K. C. Study on Reduction Reaction of $MoO_2$ Powder with NH3. *J. Am. Ceram. Soc.* **2017**, *100* (4), 1368–1376.

(25) Salkar, A. V; Fernandes, R. X.; Bhosale, S. V; Morajkar, P. P. NH- and CH-Substituted Ureas as Self-Assembly Directing Motifs for Facile Synthesis and Electrocapacitive Applications of Advanced $WO_{3-x}$ One-Dimensional Nanorods. *ACS Appl. Energy Mater.* **2019**, *2* (12), 8724–8736.

(26) Tischer, S.; Börnhorst, M.; Amsler, J.; Schoch, G.; Deutschmann, O. Thermodynamics and Reaction Mechanism of Urea Decomposition. *Phys. Chem. Chem. Phys.* **2019**, *21* (30), 16785–16797.

(27) Yan, J.; Li, L.; Ji, Y.; Li, P.; Kong, L.; Cai, X.; Li, Y.; Ma, T.; Liu, S. (Frank). Nitrogen-Promoted Molybdenum Dioxide Nanosheets for Electrochemical Hydrogen Generation. *J. Mater. Chem. A* **2018**, *6* (26), 12532–12540.

(28) Cannon, C. G. Infrared Frequencies of Amide, Urea, and Urethane Groups. *J. Phys. Chem.* **1976**, *80* (11), 1247–1248.

(29) Kimura, T.; Yao, H. Magnetic Circular Dichroism of Substoichiometric Molybdenum Oxide ($MoO_{3-x}$) Nanoarchitectures with Polaronic Defects. *J. Phys. Chem. C* **2019**, *123* (30), 18620–18628.

(30) Prabhu B, R.; Bramhaiah, K.; Singh, K. K.; John, N. S. Single Sea Urchin–$MoO_3$ Nanostructure for Surface Enhanced Raman Spectroscopy of Dyes. *Nanoscale Adv.* **2019**, *1* (6), 2426–2434.

(31) Dieterle, M.; Weinberg, G.; Mestl, G. Raman Spectroscopy of Molybdenum Oxides Part I. Structural Characterization of Oxygen Defects in $MoO_{3-x}$ by DR UV/VIS Raman Spectroscopy and X-Ray Diffraction. *Phys. Chem. Chem. Phys.* **2002**, *4* (5), 812–821.

(32) Guo, C.; Yan, P.; Zhu, C.; Wei, C.; Liu, W.; Wu, W.; Wang, X.; Zheng, L.; Wang, J.; Du, Y.; Chen, J.; Xu, Q. Amorphous MoO3−x Nanosheets Prepared by the Reduction of Crystalline $MoO_3$ by Mo Metal for LSPR and Photothermal Conversion. *Chem. Commun.* **2019**, *55* (83), 12527–12530.

(33) Sobańska, K.; Krasowska, A.; Mazur, T.; Podolska-Serafin, K.; Pietrzyk, P.; Sojka, Z. Diagnostic Features of EPR Spectra of Superoxide Intermediates on Catalytic Surfaces and Molecular Interpretation of Their G and A Tensors. *Top. Catal.* **2015**, *58* (12–13), 796–810.

(34) Dong, W. J.; Ham, J.; Jung, G. H.; Son, J. H.; Lee, J.-L. Ultrafast Laser-Assisted Synthesis of Hydrogenated Molybdenum Oxides for Flexible Organic Solar Cells. *J. Mater. Chem. A* **2016**, *4* (13), 4755–4762.

(35) Vasilopoulou, M.; Douvas, A. M.; Georgiadou, D. G.; Palilis, L. C.; Kennou, S.; Sygellou, L.; Soultati, A.; Kostis, I.; Papadimitropoulos, G.; Davazoglou, D.; Argitis, P. The Influence of Hydrogenation and Oxygen Vacancies on Molybdenum Oxides Work Function and Gap States for Application in Organic Optoelectronics. *J. Am. Chem. Soc.* **2012**, *134* (39), 16178–16187.

(36) Naik, A. P.; Salkar, A. V.; Peña, G. D. J. G. J. G.; Sawant, J. V.; Bharath, G.; Banat,

F.; Bhosale, S. V.; Morajkar, P. P. Facile Synthesis of Fibrous, Mesoporous $Ni_{1-x}O$ Nanosponge Supported on Ni Foam for Enhanced Pseudocapacitor Applications. *J. Mater. Sci.* **2020**, *55* (26), 12232–12248.

(37) Krishnan, C. V.; Garnett, M.; Hsiao, B.; Chu, B. Electrochemical Measurements of Isopolyoxomolybdates: 1. pH Dependent Behavior of Sodium Molybdate. *Int. J. Electrochem. Sci.* **2007**, *2* (1), 29–51.

(38) Busey, R. H.; Keller, O. L. Structure of the Aqueous Pertechnetate Ion by Raman and Infrared Spectroscopy. Raman and Infrared Spectra of Crystalline $KTcO_4$, $KReO_4$, $Na_2MoO_4$, $Na_2WO_4$, $Na_2MoO_4 \cdot 2H_2O$, and $Na_2WO_4 \cdot 2H_2O$. *J. Chem. Phys.* **1964**, *41* (1), 215–225.

(39) Aveston, J.; Anacker, E. W.; Johnson, J. S. Hydrolysis of Molybdenum(VI). Ultracentrifugation, Acidity Measurements, and Raman Spectra of Polymolybdates. *Inorg. Chem.* **1964**, *3* (5), 735–746.

(40) Ma, L.; Fan, H.; Fu, K.; Zhao, Y. Metal-Organic Framework/Layered Carbon Nitride Nano–Sandwiches for Superior Asymmetric Supercapacitor. *ChemistrySelect* **2016**, *1* (13), 3730–3738.

(41) Ma, L.; Fan, H.; Wei, X.; Chen, S.; Hu, Q.; Liu, Y.; Zhi, C.; Lu, W.; Zapien, J. A.; Huang, H. Towards High Areal Capacitance{,} Rate Capability and Tailorable Supercapacitors: $Co_3O_4$@polypyrrole Core–Shell Nanorod Bundle Array Electrodes. *J. Mater. Chem. A* **2018**, *6* (39), 19058–19065.

(42) Zhao, N.; Fan, H.; Zhang, M.; Ren, X.; Wang, C.; Peng, H.; Li, H.; Jiang, X.; Cao, X. Facile Preparation of Ni-Doped $MnCO_3$ Materials with Controlled Morphology for High-Performance Supercapacitor Electrodes. *Ceram. Int.* **2019**, *45* (5), 5266–5275.

(43) Xiong, T.; Su, H.; Yang, F.; Tan, Q.; Appadurai, P. B. S.; Afuwape, A. A.; Guo, K.; Huang, Y.; Wang, Z.; Balogun, M.-S. (Jie T. Harmonizing Self-Supportive VN/$MoS_2$ Pseudocapacitance Core-Shell Electrodes for Boosting the Areal Capacity of Lithium Storage. *Mater. Today Energy* **2020**, *17*, 100461.

(44) Wang, L.; Gao, L.; Wang, J.; Shen, Y. $MoO_3$ Nanobelts for High-Performance Asymmetric Supercapacitor. *J. Mater. Sci.* **2019**, *54* (21), 13685–13693.

(45) Thangasamy, P.; Ilayaraja, N.; Jeyakumar, D.; Sathish, M. Electrochemical Cycling and beyond: Unrevealed Activation of $MoO_3$ for Electrochemical Hydrogen Evolution Reactions. *Chem. Commun.* **2017**, *53* (14), 2245–2248.

(46) Wu, Q.-L.; Zhao, S.-X.; Yu, L.; Zheng, X.-X.; Wang, Y.-F.; Yu, L.-Q.; Nan, C.-W.; Cao, G. Oxygen Vacancy-Enriched $MoO_{3-x}$ Nanobelts for Asymmetric Supercapacitors with Excellent Room/Low Temperature Performance. *J. Mater. Chem. A* **2019**, *7* (21), 13205–13214.

(47) Salkar, A. V.; Naik, A. P.; Bhosale, S. V.; Morajkar, P. P. Designing a Rare DNA-Like Double Helical Microfiber Superstructure via Self-Assembly of In Situ Carbon Fiber-Encapsulated $WO_{3-x}$ Nanorods as an Advanced Supercapacitor Material. *ACS Appl. Mater. Interfaces* **2021**, *13* (1), 1288–1300.

(48) Nagaraju, P.; Arivanandhan, M.; Alsalme, A.; Alghamdi, A.; Jayavel, R. Enhanced Electrochemical Performance of α-$MoO_3$/Graphene Nanocomposites Prepared by an in Situ Microwave Irradiation Technique for Energy Storage Applications. *RSC Adv.* **2020**, *10* (38), 22836–22847.

(49) Barzegar, F.; Bello, A.; Momodu, D. Y.; Dangbegnon, J. K.; Taghizadeh, F.; Madito, M. J.; Masikhwa, T. M.; Manyala, N. Asymmetric Supercapacitor Based on an α-$MoO_3$ Cathode and Porous Activated Carbon Anode Materials. *RSC Adv.* **2015**, *5* (47), 37462–37468.

(50) Chang, J.; Jin, M.; Yao, F.; Kim, T. H.; Le, V. T.; Yue, H.; Gunes, F.; Li, B.; Ghosh, A.; Xie, S.; Lee, Y. H. Asymmetric Supercapacitors Based on Graphene/$MnO_2$ Nanospheres and Graphene/$MoO_3$ Nanosheets with High Energy Density. *Adv. Funct. Mater.* **2013**, *23* (40), 5074–5083.

(51) Liu, T.; Chai, H.; Jia, D.; Su, Y.; Wang, T.; Zhou, W. Rapid Microwave-Assisted Synthesis of Mesoporous $NiMoO_4$ Nanorod/Reduced Graphene Oxide Composites for

High-Performance Supercapacitors. *Electrochim. Acta* **2015**, *180*, 998–1006.

(52) Chithambararaj, A.; Rajeswari Yogamalar, N.; Bose, A. C. Hydrothermally Synthesized H-$MoO_3$ and α-$MoO_3$ Nanocrystals: New Findings on Crystal-Structure-Dependent Charge Transport. *Cryst. Growth Des.* **2016**, *16* (4), 1984–1995.

(53) Chen, Y.; Lu, C.; Xu, L.; Ma, Y.; Hou, W.; Zhu, J.-J. Single-Crystalline Orthorhombic Molybdenum Oxide Nanobelts: Synthesis and Photocatalytic Properties. *CrystEngComm* **2010**, *12* (11), 3740–3747.

(54) Kwong, W. L.; Koshy, P.; Hart, J. N.; Xu, W.; Sorrell, C. C. Critical Role of {002} Preferred Orientation on Electronic Band Structure of Electrodeposited Monoclinic $WO_3$ Thin Films. *Sustain. Energy Fuels* **2018**, *2* (10), 2224–2236.

(55) Lokhande, V.; Lokhande, A.; Namkoong, G.; Kim, J. H.; Ji, T. Charge Storage in WO $_3$ Polymorphs and Their Application as Supercapacitor Electrode Material. *Results Phys.* **2019**, *12* (February 2019), 2012–2020.

(56) Malyshev, D. A.; Dhami, K.; Lavergne, T.; Chen, T.; Dai, N.; Foster, J. M.; Corrêa, I. R.; Romesberg, F. E. A Semi-Synthetic Organism with an Expanded Genetic Alphabet. *Nature* **2014**, *509* (7500), 385–388.

(57) Nielsen, P. E. Peptide Nucleic Acid: A Versatile Tool in Genetic Diagnostics and Molecular Biology. *Curr. Opin. Biotechnol.* **2001**, *12* (1), 16–20.

(58) Zhao, M.-Q.; Zhang, Q.; Tian, G.-L.; Wei, F. Emerging Double Helical Nanostructures. *Nanoscale* **2014**, *6* (16), 9339–9354.

(59) Kaja, S.; Nag, A. Bimetallic Ag–Cu Alloy Microflowers as SERS Substrates with Single-Molecule Detection Limit. *Langmuir* **2021**, *37* (44), 13027–13037.

(60) Ma, W.; Yang, R.; Wang, T. ZnO Nanorod-Based Microflowers Decorated with $Fe_3O_4$ Nanoparticles for Electromagnetic Wave Absorption. *ACS Appl. Nano Mater.* **2020**, *3* (8), 8319–8327.

(61) Yu, S. H.; Tang, Z.; Shao, Y.; Dai, H.; Wang, H. Y.; Yan, J.; Pan, H.; Chua, D. H. C. In Situ Hybridizing $MoS_2$ Microflowers on $VS_2$ Microflakes in a One-Pot CVD Process for Electrolytic Hydrogen Evolution Reaction. *ACS Appl. Energy Mater.* **2019**, *2* (8), 5799–5808.

(62) Ding, L.; Yan, F.; Zhang, Y.; Liu, L.; Yu, X.; Liu, H. Microflowers Comprised of Cu/CuxO/NC Nanosheets as Electrocatalysts and Horseradish Peroxidase Mimics. *ACS Appl. Nano Mater.* **2020**, *3* (1), 617–623.

(63) Hatamie, A.; Rahmati, R.; Rezvani, E.; Angizi, S.; Simchi, A. Yttrium Hexacyanoferrate Microflowers on Freestanding Three-Dimensional Graphene Substrates for Ascorbic Acid Detection. *ACS Appl. Nano Mater.* **2019**, *2* (4), 2212–2221.

(64) Yin, J.; Cao, H.; Zhang, J.; Qu, M.; Zhou, Z. Synthesis and Applications of γ-Tungsten Oxide Hierarchical Nanostructures. *Cryst. Growth Des.* **2013**, *13* (2), 759–769.

(65) Zhou, J.; Song, J.; Li, H.; Feng, X.; Huang, Z.; Chen, S.; Ma, Y.; Wang, L.; Yan, X. The Synthesis of Shape-Controlled α-$MoO_3$/Graphene Nanocomposites for High Performance Supercapacitors. *New J. Chem.* **2015**, *39* (11), 8780–8786.

(66) Li, Y.; Jian, J.; Fan, Y.; Wang, H.; Yu, L.; Cheng, G.; Zhou, J.; Sun, M. Facile One-Pot Synthesis of a $NiMoO_4$/Reduced Graphene Oxide Composite as a Pseudocapacitor with Superior Performance. *RSC Adv.* **2016**, *6* (73), 69627–69633.

(67) Murugesan, D.; Prakash, S.; Ponpandian, N.; Manisankar, P.; Viswanathan, C. Two Dimensional α-$MoO_3$ Nanosheets Decorated Carbon Cloth Electrodes for High-Performance Supercapacitors. *Colloids Surfaces A Physicochem. Eng. Asp.* **2019**, *569* (February), 137–144.

(68) Lu, Q.-L.; Zhao, S.-X.; Chen, C.-K.; Wang, X.; Deng, Y.-F.; Nan, C.-W. A Novel Pseudocapacitance Mechanism of Elm Seed-like Mesoporous $MoO_{3-x}$ Nanosheets as Electrodes for Supercapacitors. *J. Mater. Chem. A* **2016**, *4* (38), 14560–14566.

(69) Yuan, X.; Yan, X.; Zhou, C.; Wang, D.; Zhu, Y.; Wang, J.; Tao, X.; Cheng, X.

Promising Carbon Nanosheets Decorated by Self-Assembled $MoO_2$ Nanoparticles: Controllable Synthesis, Boosting Performance and Application in Symmetric Coin Cell Supercapacitors. *Ceram. Int.* **2020**, *46* (12), 19981–19989.

(70) Rani, A.; Reddy, R.; Sharma, U.; Mukherjee, P.; Mishra, P.; Kuila, A.; Sim, L. C.; Saravanan, P. A Review on the Progress of Nanostructure Materials for Energy Harnessing and Environmental Remediation. *J. Nanostructure Chem.* **2018**, *8* (3), 255–291.

# CHAPTER V:

# CONCLUSIONS OF THE THESIS

## 5.1 CONCLUSIONS

The world energy scenario is rapidly shifting from fossil fuels to cleaner, greener, and sustainable carbon-free energy technologies such as supercapacitors which rely on the fundamental properties of the electrode materials used to fabricate these energy devices. Tungsten and Molybdenum oxides have emerged as prominent metal oxides for supercapacitor applications due to i) tunable non-stoichiometry, surface-redox states and their ability to intercalate with ease small cations such as $H^+$ into their lattice. Although, both these metal oxides have promising activity for energy storage applications, their low conductivity and poor electrochemical stability pose a limitation for device scale application. Therefore, this thesis attempted to address these issues via innovative syntheses strategies to design a plethora of nano and microstructured $WO_{3-x}$ and $MoO_{3-x}$ with improved charge storage characteristics.

Although, $WO_{3-x}$ and $MoO_{3-x}$ are believed to be analogs to each other in several aspects, it has been demonstrated in the present thesis that the type of nano and microstructures that they can produce differ significantly in terms of both morphologies as well as their physico-chemical properties. By effectively utilizing the rich poly-tungstate and molybdate chemistry in combination with fuels that could also serve as SDA's (such as Urea, Carbohydrazide, Semicarbazide, N-methylurea, Tetramethylurea, and Citric acid) numerous nano and microstructures of the two oxides have been synthesized. These nanostructures include; $WO_{3-x}$ nanoparticles, nanorods, 2D sheets, 3D hierarchical structures, $WO_{3-x}$/C microfibers, while the $MoO_{3-x}$ microstructures include nanoparticles, 2D microplates, 2D microdisks, and 3D microflowers. The charge storage performances of these morphologies have been depicted schematically in figure 5.1.

Nanorods of $WO_3$ were synthesized by utilizing protonated ureas i.e., 1) urea when mono-protonated at the carbonyl oxygen can results in the formation of an iminium cation ($-C=NH_2^+$) which helps it to act as a SDA and facilitates the kinetics of nanostructural growth, and 2) the exothermic decomposition of urea can satisfy the thermodynamic requirements for transforming particles of $WO_3$ into stable $WO_{3-x}$ nanorods. Our first hypothesis of urea protonation was proved by the fact that, nanorods of $WO_{3-x}$ were produced only when the pH of the tungstic acid-urea hybrid gel was acidic (pH 2.5). Furthermore, the significance of protonation at the C=O group was confirmed by replacing urea with thiourea, wherein the lack of protonation center hinders the growth of nanostructures. The second hypothesis which considered the exothermic decomposition of urea and its ability to "stitch" nanoparticles of $WO_3$ into $WO_{3-x}$ nanorods was evaluated by carefully analyzing its decomposition pattern along with morphological transformation at each stage of calcination. Furthermore, by varying the metal : urea ratios, solution pH, calcination temperature and time, the mechanism of growth of various nanostructures of $WO_3$ was demonstrated. Furthermore, $WO_{3-x}$ nanorods were transformed into 2D $WO_{3-x}$ microsheets when subjected to calcination temperatures above 600 °C as a result of sintering of $WO_{3-x}$ nanorods. Furthermore, the $WO_{3-x}$ nanorods when calined at lower calcination temperature of 450 °C and at longer times of > 4 h could transform into 3D $WO_{3-x}$ hierarchical structures.

Meanwhile, under similar conditions of urea protonation, two different morphologies of $MoO_{3-x}$ could be synthesized, namely the $MoO_{3-x}$ microplates and microdisks. The difference in the two structures of $MoO_{3-x}$ was identified as an influence of the type of polymolybdate species being present in the solution. The heptamolybdate $[Mo_7O_{24}]^{6-}$ species promoted the growth of $MoO_{3-x}$ microdisks, while the octamolybdate $[Mo_8O_{26}]^{4-}$ species supported the growth of $MoO_{3-x}$ microplates.

Additionally, a further assessment of the nano and microstructure promoting effect of urea, was confirmed by utilizing –NH substituted (Carbohydrazide and Semicarbazide) and –CH substituted (N-methylurea and tetramethylurea) ureas. It was confirmed that the –NH substitution promoted the growth of the nano and microstructures, while –CH substitution had a detrimental influence on the morphology in both $WO_{3-x}$ and $MoO_{3-x}$.The improved results obtained for -NH substituted ureas was a result of their higher exothermicity which was caused due to in-situ production of hydrazine during combustion. This also helped to create a reducing atmosphere that endowed the material with greater oxygen vacancies.

Further, 3D microstructures of $WO_{3-x}$ and $MoO_{3-x}$ were achieved by utilizing a citric acid-assisted synthesis route. It was demonstrated that citric acid, being a weak triprotic acid with three carboxylic groups could be used to cap metal ions under controlled pH conditions, which allowed synthetic tunability for designing 3D nano and microstructures. $WO_{3-x}/C$ microfibers could be synthesized using this route to produce highly disordered and reactive carbon-fiber encapsulated $WO_{3-x}$ heterostructure. These carbon fibers could be removed easily at higher calcination temperature to produce hierarchical assembly of 1D $WO_{3-x}$ nanorods. Meanwhile, $MoO_{3-x}$ could be transformed into 3D microflower-like structures with high oxygen vacancies and increased non-stoichiometry using a similar citric acid assisted route.

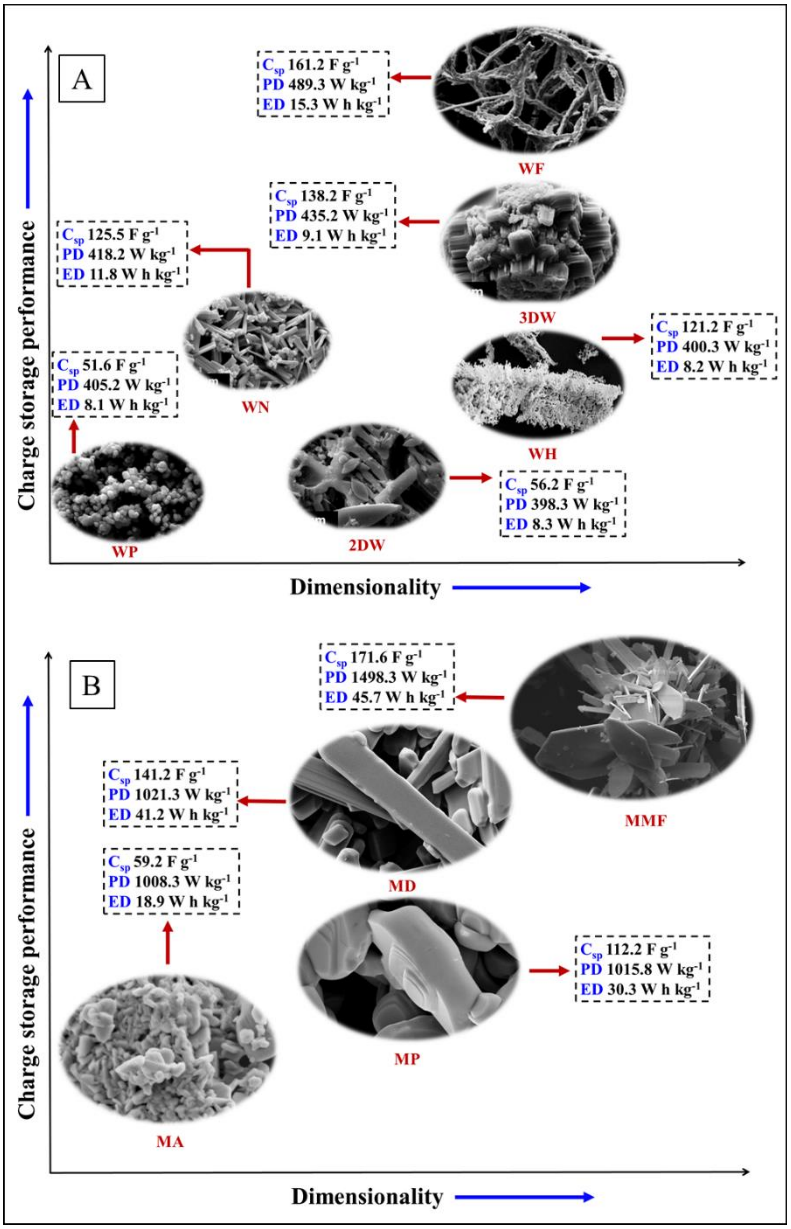

**Figure 5.1:** Schematic illustration depicting the dimensionality-based charge storage performance of the various nano and microstructures of (A) $WO_{3-x}$ and (B) $MoO_{3-x}$.

All these unique morphologies of $WO_{3-x}$ and $MoO_{3-x}$ were evaluated for their electrochemical charge storage performance. Characteristic trends relating to the charge storage performance to the material dimensionality were observed and have been presented as the schematic 5.1. The $WO_{3-x}$ nanorods demonstrated a device-scale specific capacitance of 125.5 F $g^{-1}$ at a current density of 2 A $g^{-1}$ with power and energy densities of 418.2 W $kg^{-1}$ and 11.8 W h $kg^{-1}$, respectively. $WO_{3-x}$ nanorods also demonstrated capacitance retention of 88% when evaluated over 12,000 continuous GCD cycles. Through XRD characterization, it was revealed that the $WO_{3-x}$ nanorods had a monoclinic phase, with (002) being its highest intensity plane. If the nanorods were transformed into the 2D microsheets the value of specific capacitance, decreased to 56.2 F $g^{-1}$ while the energy and power densities values dropped to 398.3 W $kg^{-1}$ and 8.3 W h $kg^{-1}$, respectively. The capacitance retention also dropped to 58 % over 12,000 continuous GCD cycles. The decrease was due to the loss of non-stoichiometry and oxygen vacancies in the sintered 2D $WO_{3,}$ which was confirmed through the XPS analysis.

Meanwhile, when the $WO_{3-x}$ nanorods were transformed into the 3D hierarchical structures, the specific capacitance increased to 138.2 F $g^{-1,}$ and power and energy densities increased to 435.2 W $kg^{-1}$ and 9.1 W h $kg^{-1}$ respectively. The capacitance retention also increased to 90 % when evaluated over 12,000 continuous GCD cycles. By calculating the diffusion coefficient, it was noted that the 3D $WO_{3-x}$ hierarchical structures possessed the highest $D_0$ value of $5.9 \times 10^{-9}$ $cm^2$ $s^{-1}$ along with a higher electroactive area of 0.87 $cm^2$ which confirmed that the 3D morphology enabled faster diffusion of $H^+$ ions through the $WO_{3-x}$ matrix.

On the other hand, 2D $MoO_{3-x}$ microplates and microdisks possessed inherently higher charge-storage characteristics due to their large surface-to-volume aspect ratios and layered structure. The $MoO_{3-x}$ microdisks demonstrated a specific capacitance of 112.2 F $g^{-1}$ with power and energy densities of 1015.8 W $kg^{-1}$ and 30.3 W h $kg^{-1}$. In contrast, the microplates owing to their greater oxygen vacancies, non-stoichiometry, and preferentially oriented (040) plane, demonstrated a higher specific capacitance of 171.6 F $g^{-1}$ and power and energy densities of 1021.3 W $kg^{-1}$ and 41.2 W h $kg^{-1}$. Furthermore, the $MoO_{3-x}$ microplates and microdisks demonstrated 86 and 92 % capacitance retention when evaluated over 12,000 continuous GCD cycles, respectively.

Among the complex higher dimensional microstructures, the $WO_{3-x}$/C microfibers revealed a specific capacitance of 161.2 F $g^{-1}$ with power and energy densities of 489.3 W $kg^{-1}$ and 15.3 W h $kg^{-1}$, respectively. The $WO_{3-x}$/C microfibers also demonstrated a capacitance retention of 88 % when evaluated over 12,000 continuous GCD cycles. At the same time, the $MoO_{3-x}$ microflowers revealed a specific capacitance of 171.6 F $g^{-1}$ with power and energy densities of 1498.3 W $kg^{-1}$ and 45.7 W h $kg^{-1}$, respectively, along with capacitance retention of 91 %. In both the $WO_{3-x}$ and $MoO_{3-x}$ nano/microstructures, the interfacial solution resistance was reduced due to nanostructuring as conformed through EIS studies. This proved that the nano and microstructuring enabled faster electrode-electrolyte interfacial kinetics, improving the material's electrical conductivity and electrochemical cycling stability. Therefore, it can be concluded that this thesis has made an honest preliminary attempt to synthesize several nano and microstructures of $WO_{3-x}$ and $MoO_{3-x}$ that can store high electrochemical energy, with potential for developing high-performance supercapacitors.

# Appendix I

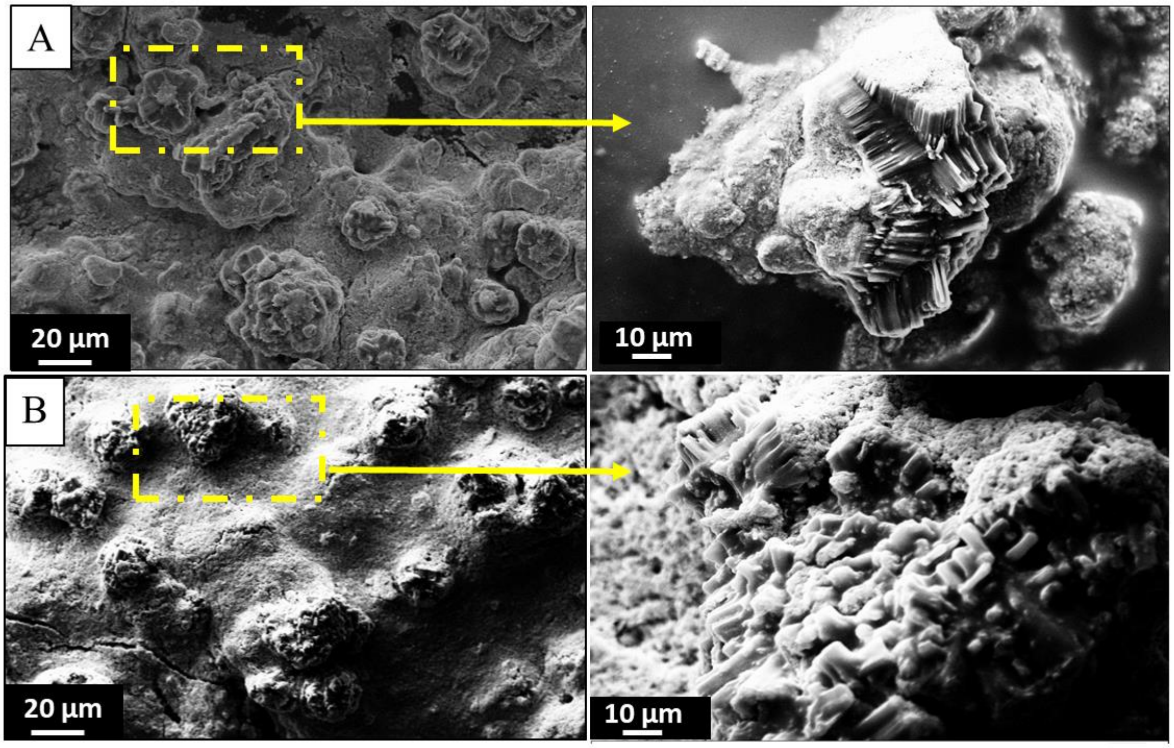

**Figure SF1:** SEM images showing sintering effect and loss of porous nanostructured morphology of 3DW at longer calcination time of A) 6h and B) 8h respectively.

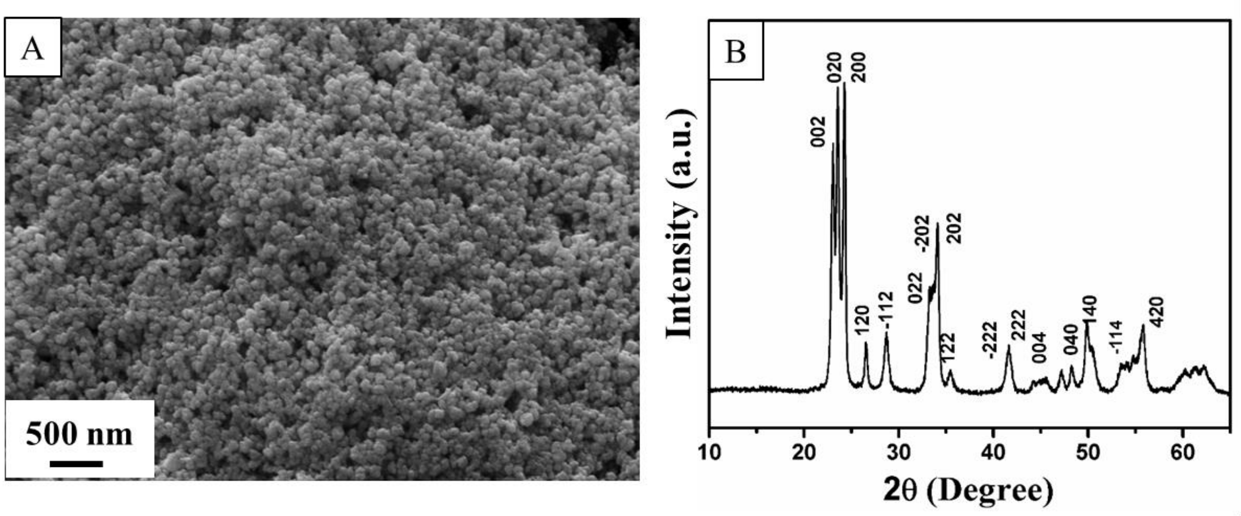

**Figure SF2:** (A) SEM images and (B) XRD pattern of $WO_3$ synthesized using thiourea.

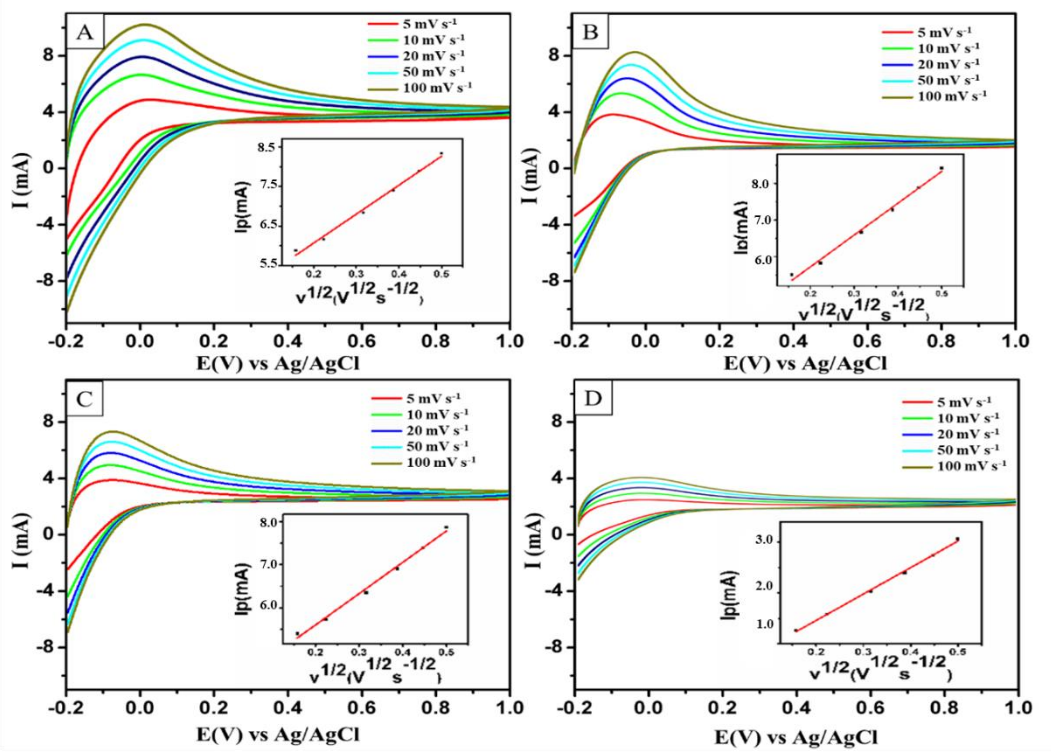

**Figure SF3:** Overlay of CVs recorded in a three-electrode system at different scan rates for (A) 3DW (B) WN (C) WP, and (D) 2DW with insets depicting the graph for current $I_p$ vs. square root of scan speed $v^{1/2}$.

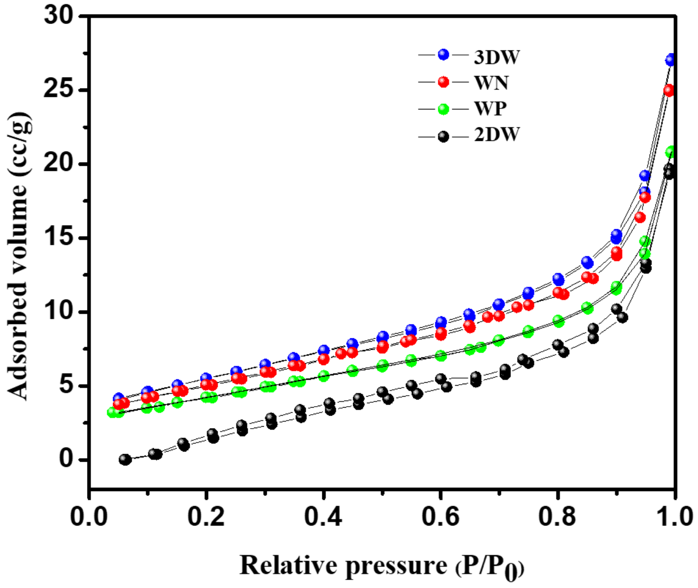

**Figure SF4:** BET surface area analysis for (A) 3DW (B) WN (C) WP, and (D) 2DW.

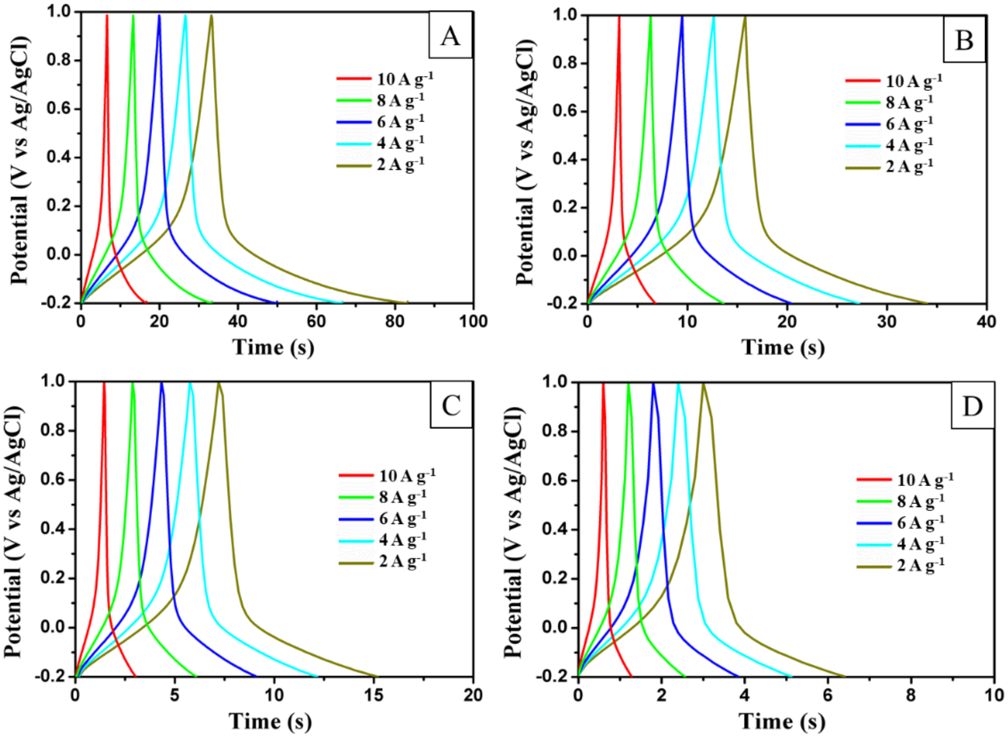

**Figure SF5:** Overlay of GCDs recorded in a three-electrode system at different current densities for (A) 3DW (B) WN (C) WP, and (D) 2DW.

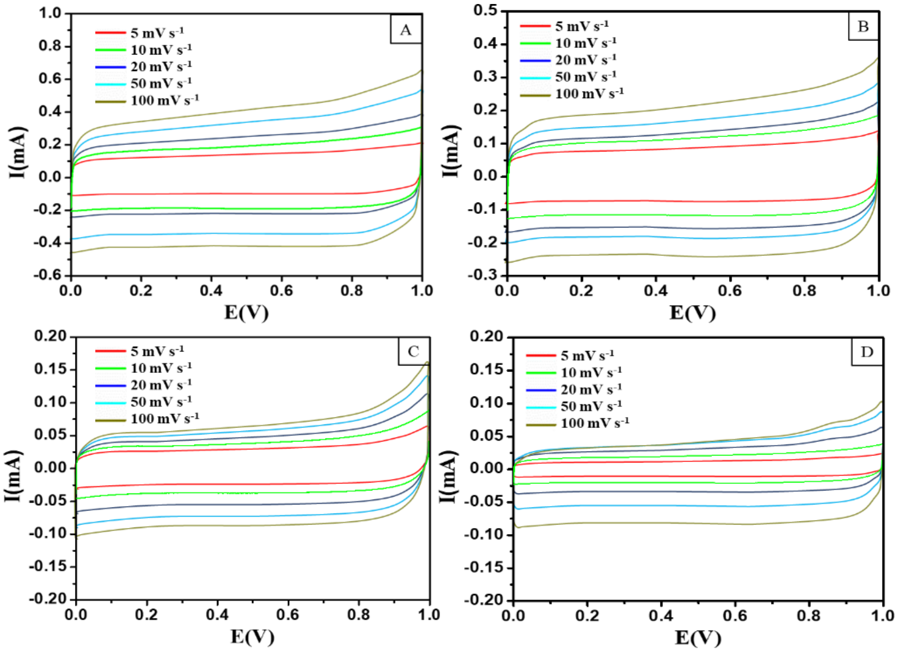

**Figure SF6:** Overlay of CVs recorded in a two-electrode system at different scan rates for (A) 3DW (B) WN (C) WP, and (D) 2DW.

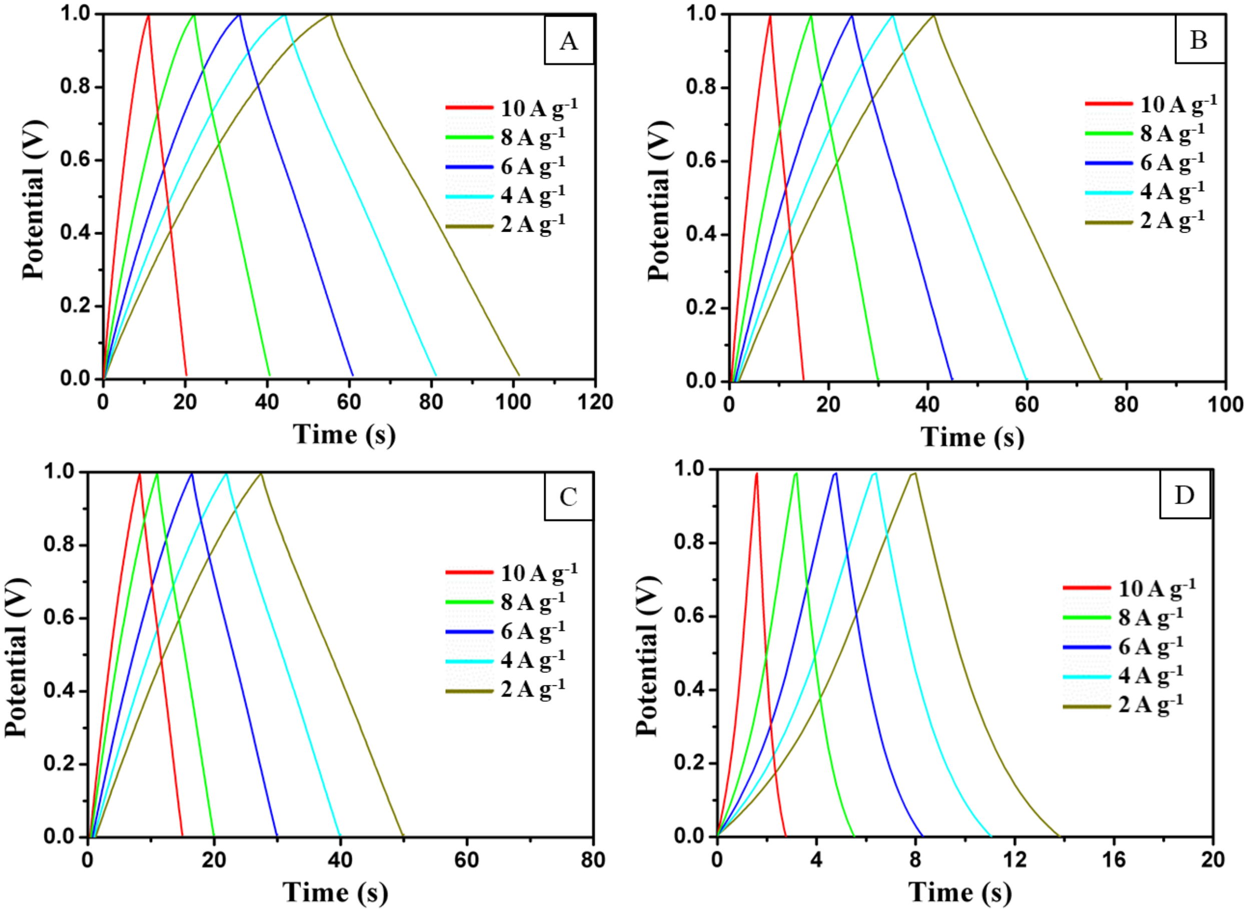

**Figure SF7:** Overlay of GCDs recorded in a two-electrode system at different current densities for (A) 3DW (B) WN (C) WP, and (D) 2DW.

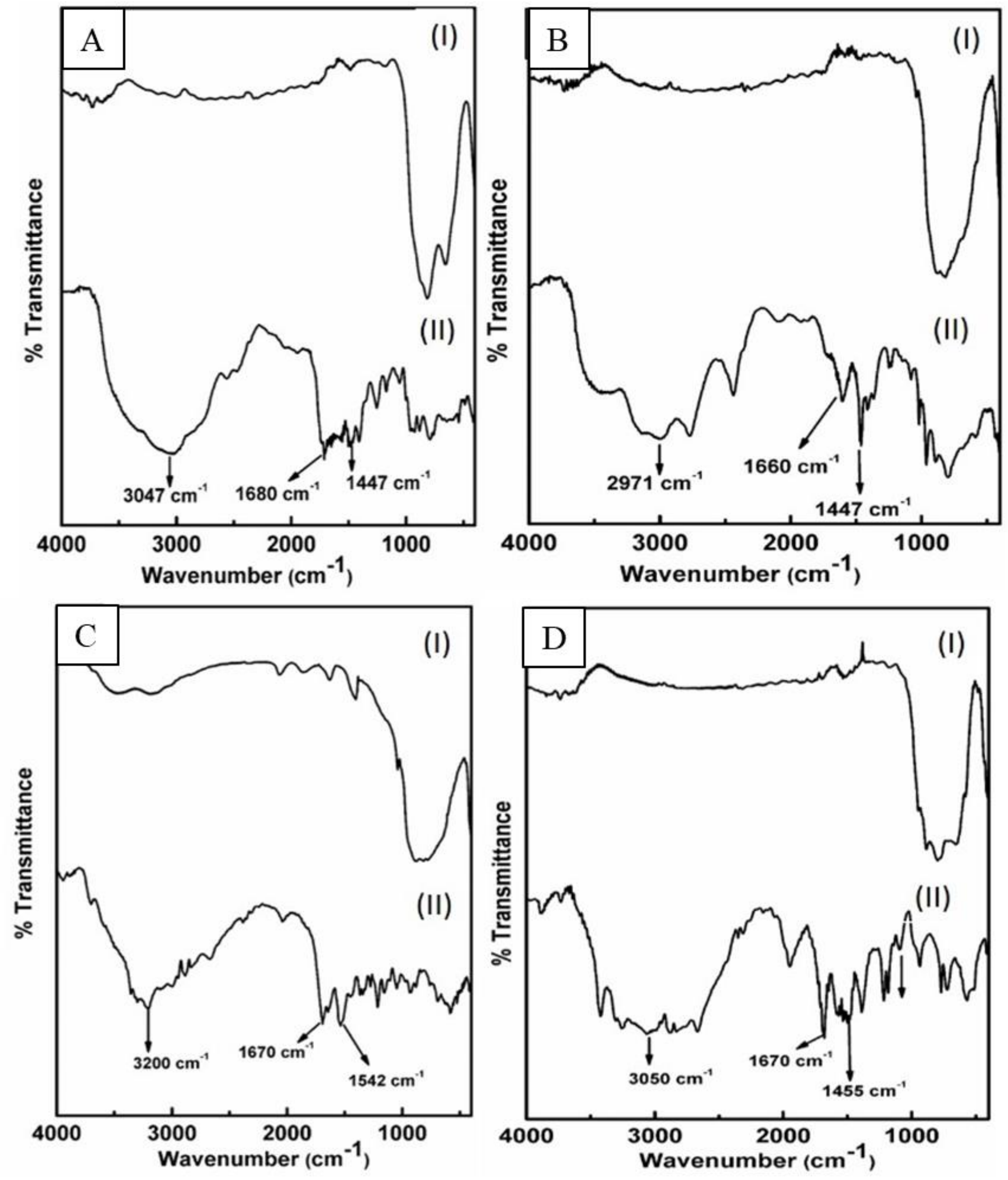

**Figure SF8:** IR studies of (A) WC (B) WM (C) WSC, and (D) WT, wherein (I) represents post calcination and (II) represents pre-calcination.

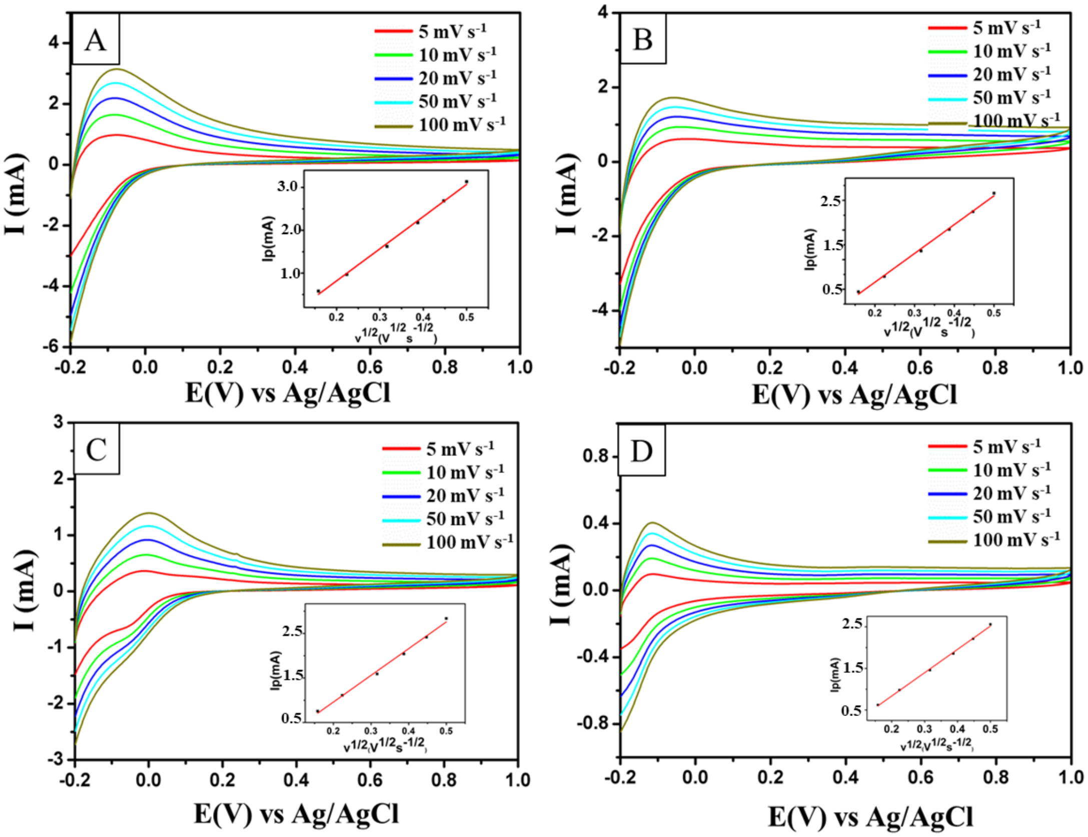

**Figure SF9:** Overlay of CVs recorded in a three-electrode system at different scan rates for (A) WC (B) WM (C) WSC, and (D) WT with insets depicting the graph for current $I_p$ vs. square root of scan speed $v^{1/2}$.

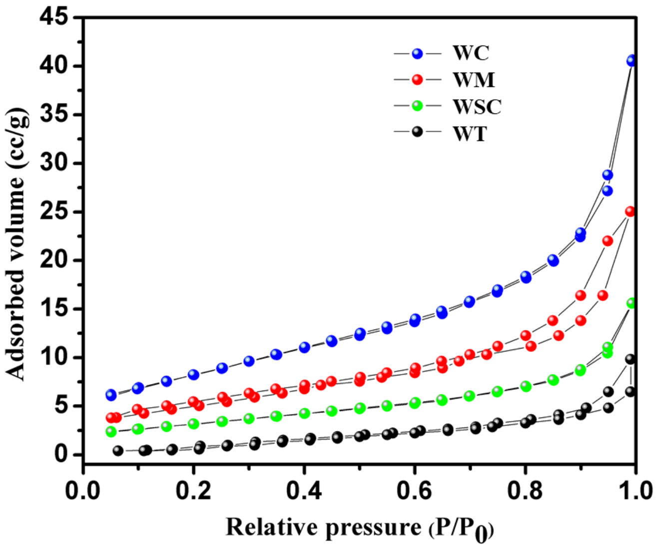

**Figure SF10:** BET surface area analysis for (A) WC (B) WM (C) WSC, and (D) WT.

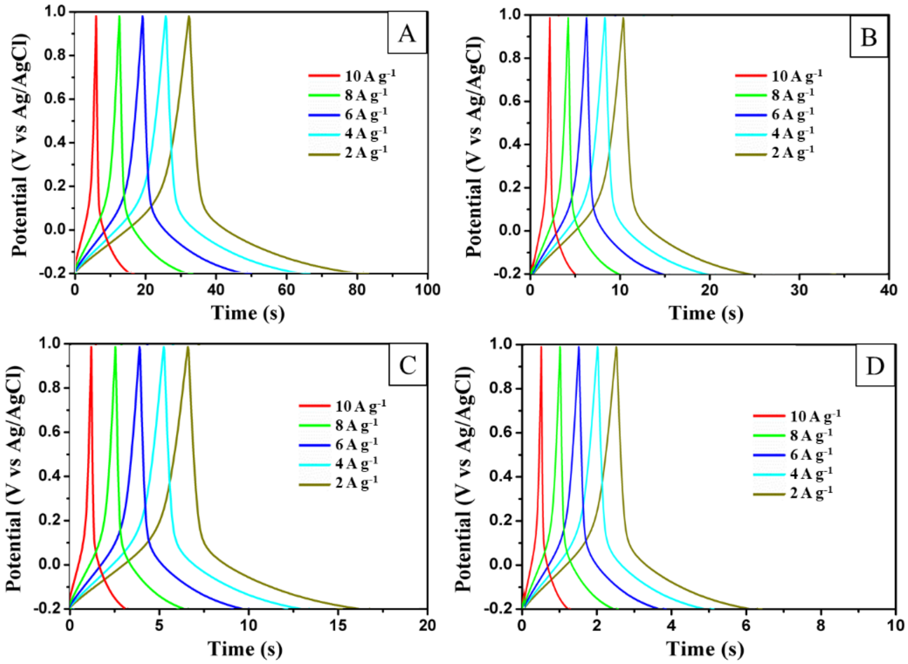

**Figure SF11:** Overlay of GCDs recorded in a three-electrode system at different current densities for (A) WC (B) WM (C) WSC, and (D) WT.

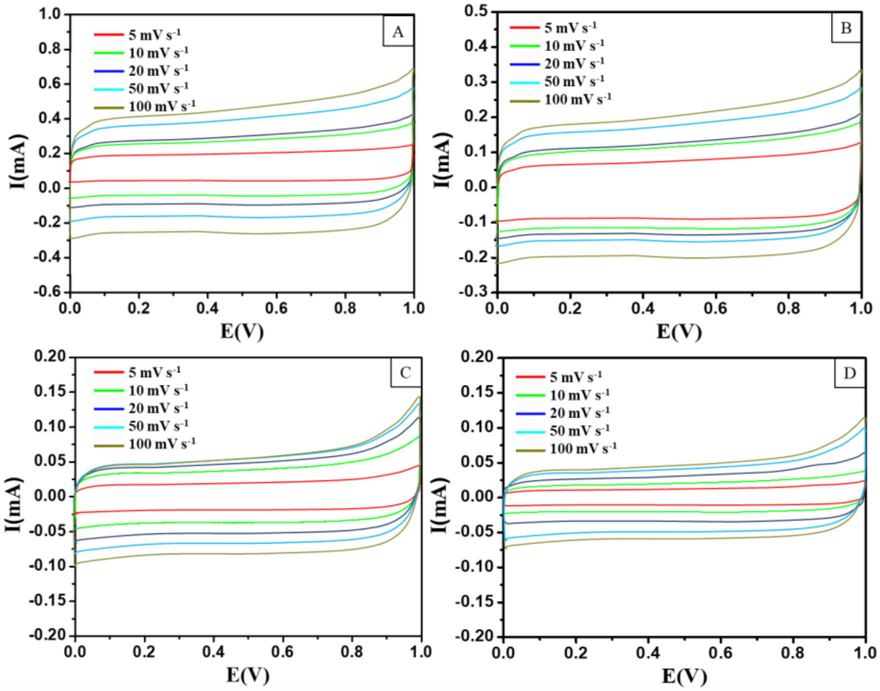

**Figure SF12:** Overlay of CVs recorded in a two-electrode system at different scan rates for (A) WC (B) WM (C) WSC, and (D) WT.

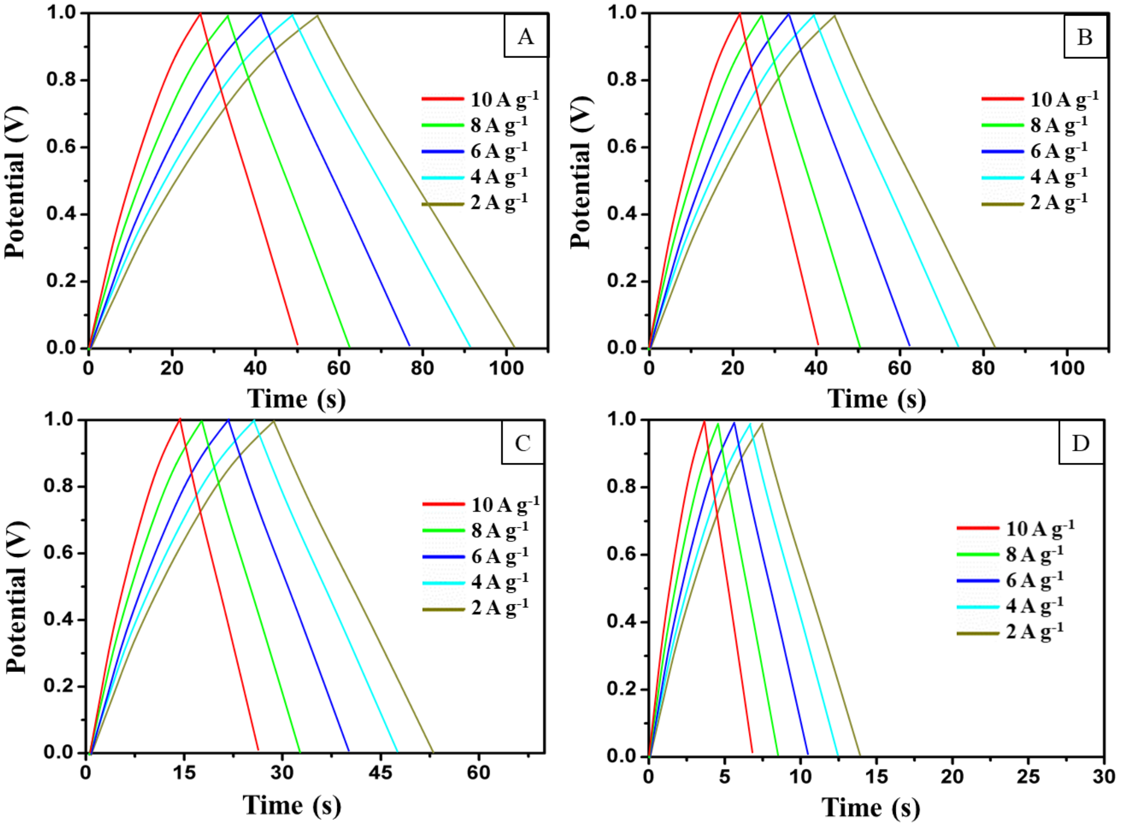

**Figure SF13:** Overlay of GCDs recorded in a two-electrode system at different current densities for (A) WC (B) WM (C) WSC, and (D) WT.

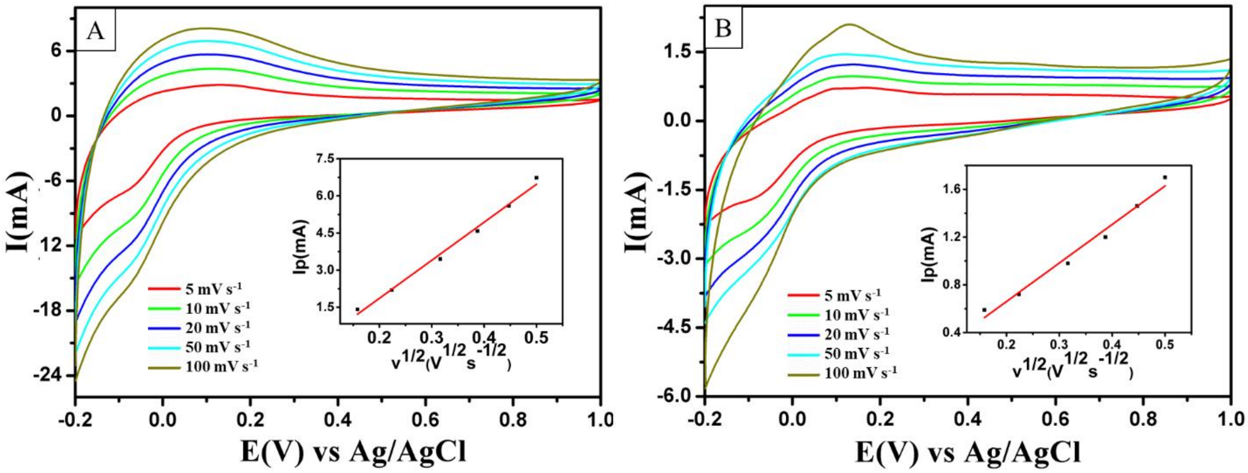

**Figure SF14:** Overlay of CVs recorded in a three-electrode system at different scan rates for (A) WF and (B) WH with insets depicting the graph for current $I_p$ vs. square root of scan speed $v^{1/2}$.

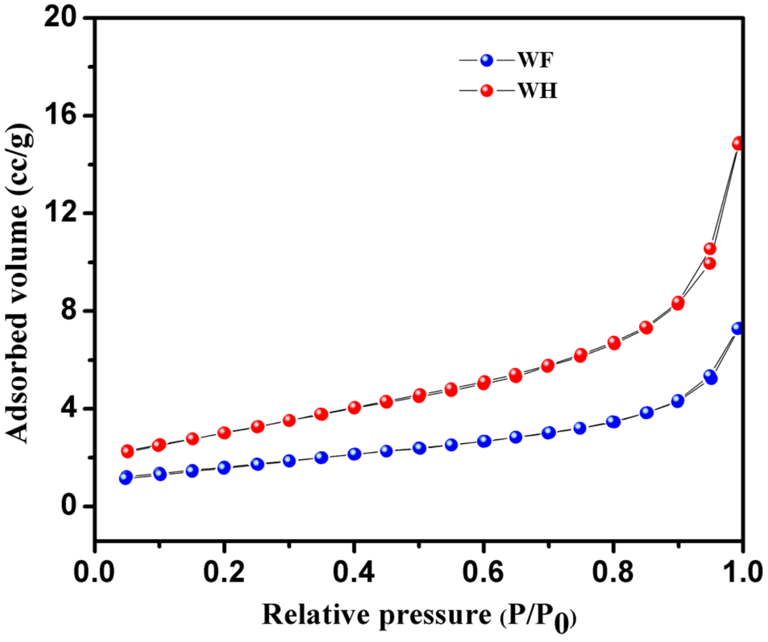

**Figure SF15:** BET surface area analysis for (A) WF and (B) WH.

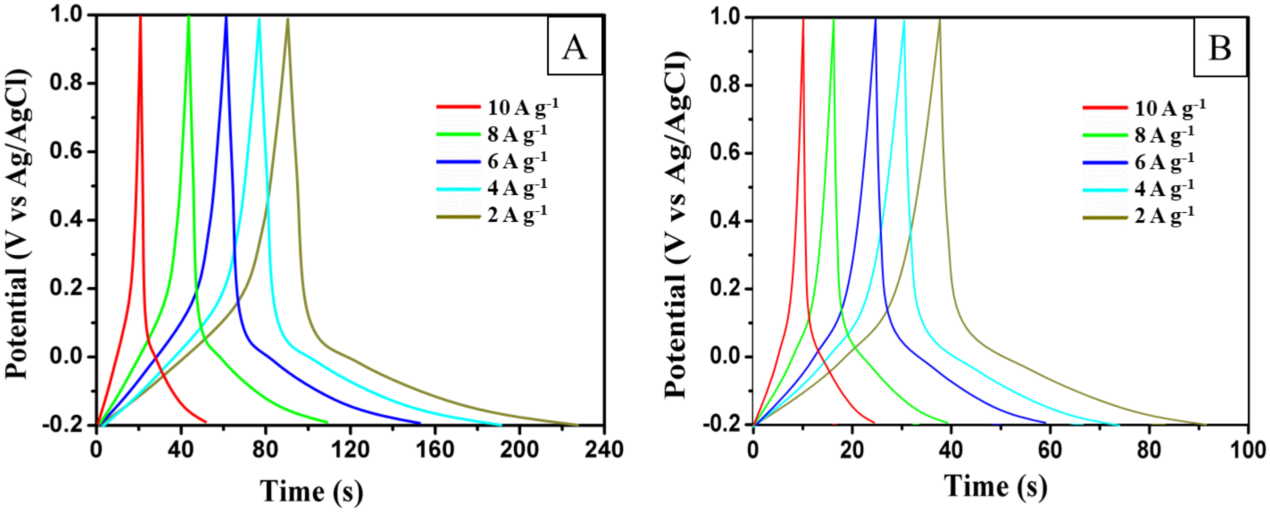

**Figure SF16:** Overlay of GCDs recorded in a three-electrode system at different current densities for (A) WF and (B) WH.

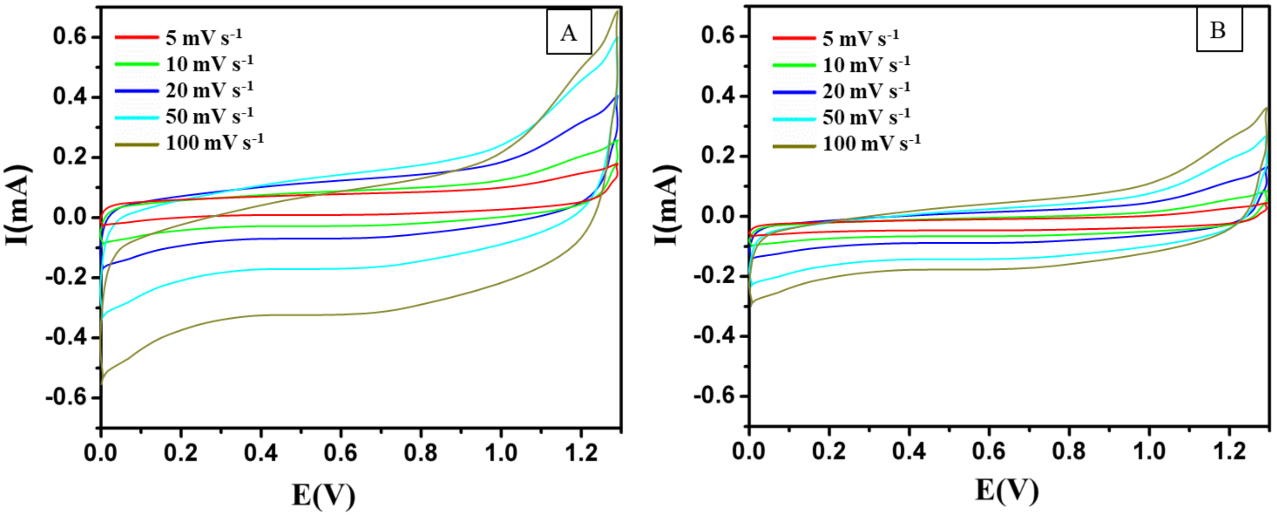

**Figure SF17:** Overlay of CVs recorded in a two-electrode system at different scan rates for (A) WF and (B) WH.

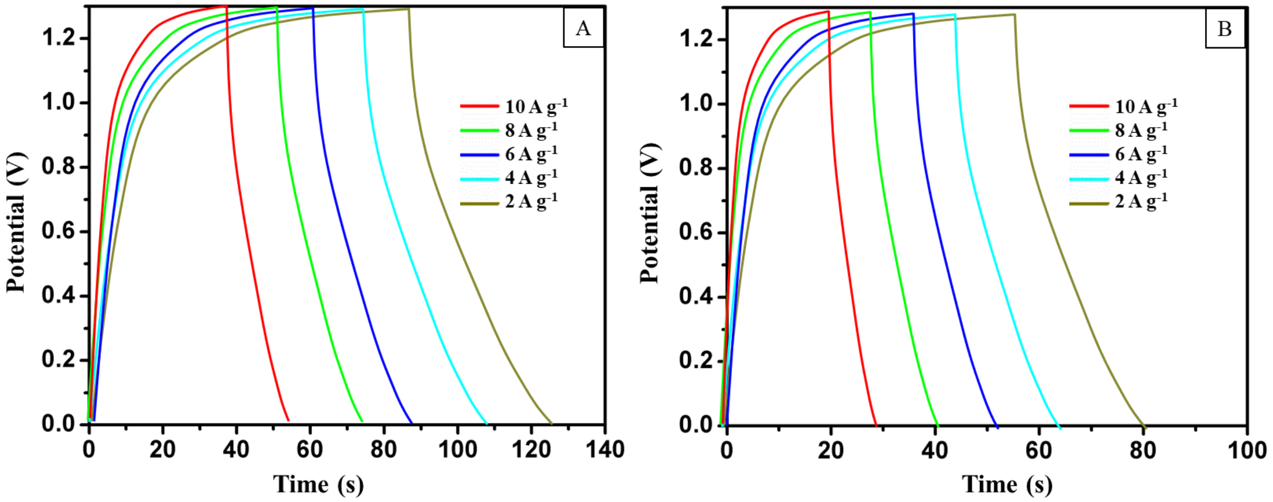

**Figure SF18:** Overlay of GCDs recorded in a two-electrode system at different current densities for (A) WF and (B) WH.

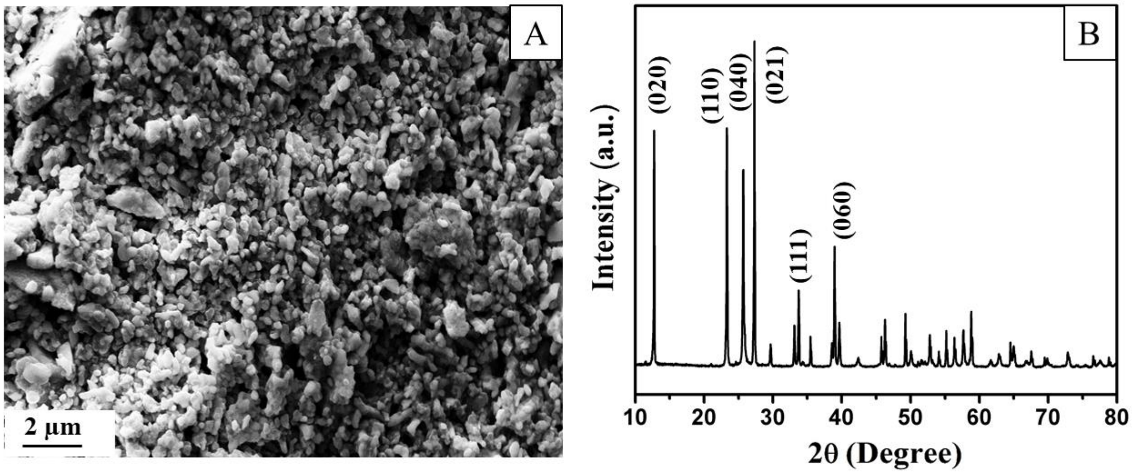

**Figure SF19:** (A) SEM images and (B) XRD pattern of $MoO_3$ synthesized without urea.

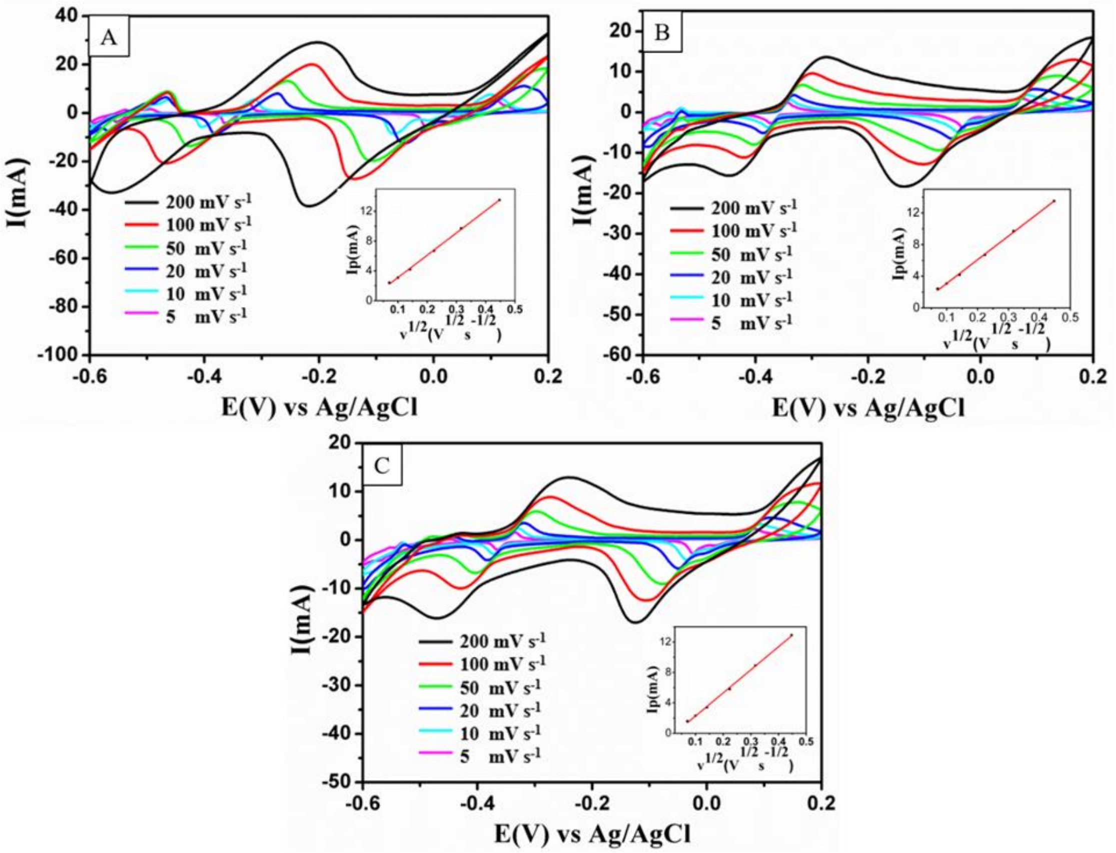

**Figure SF20:** Overlay of CVs recorded in a three-electrode system at different scan rates for (A) MP (B) MD, and (C) MA with insets depicting the graph for current $I_p$ vs. square root of scan speed $v^{1/2}$.

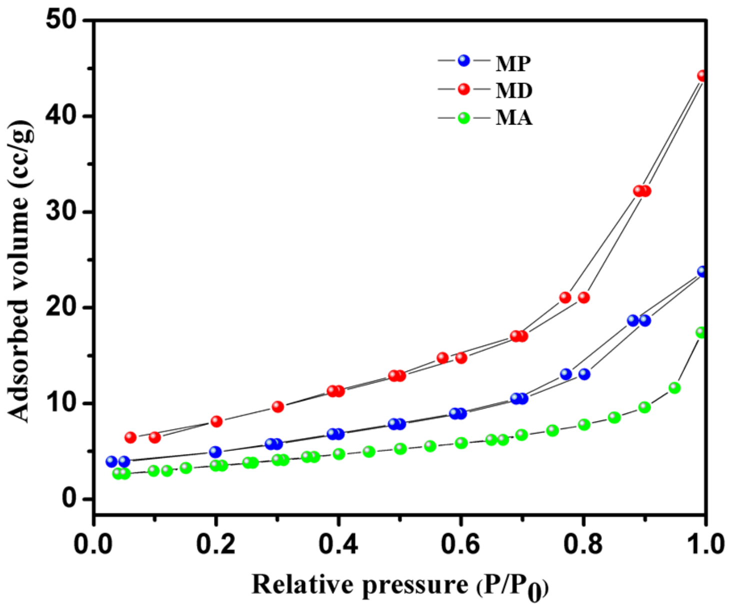

**Figure SF21:** BET surface area analysis for (A) MP (B) MD, and (C) MA.

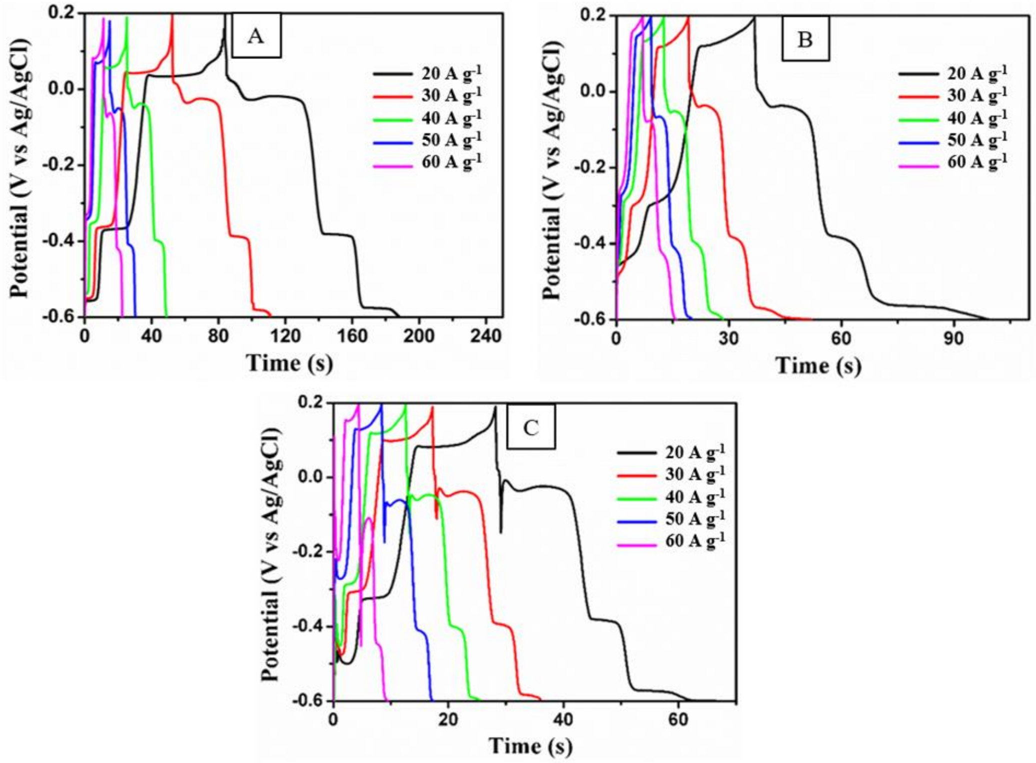

**Figure SF22:** Overlay of GCDs recorded in a three-electrode system at different current densities for (A) MP (B) MD, and (C) MA.

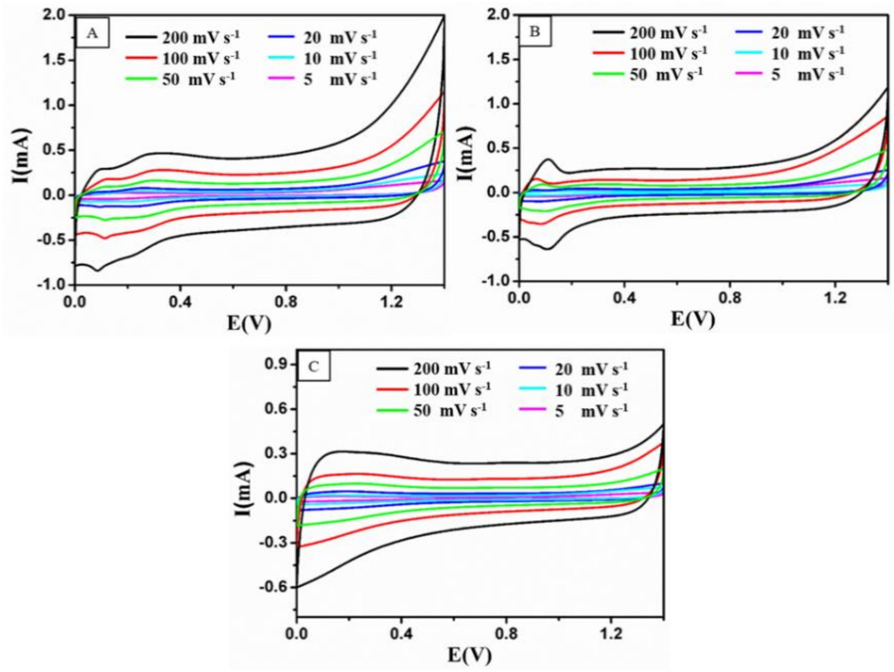

**Figure SF23:** Overlay of CVs recorded in a two-electrode system at different scan rates for (A) MP (B) MD, and (C) MA.

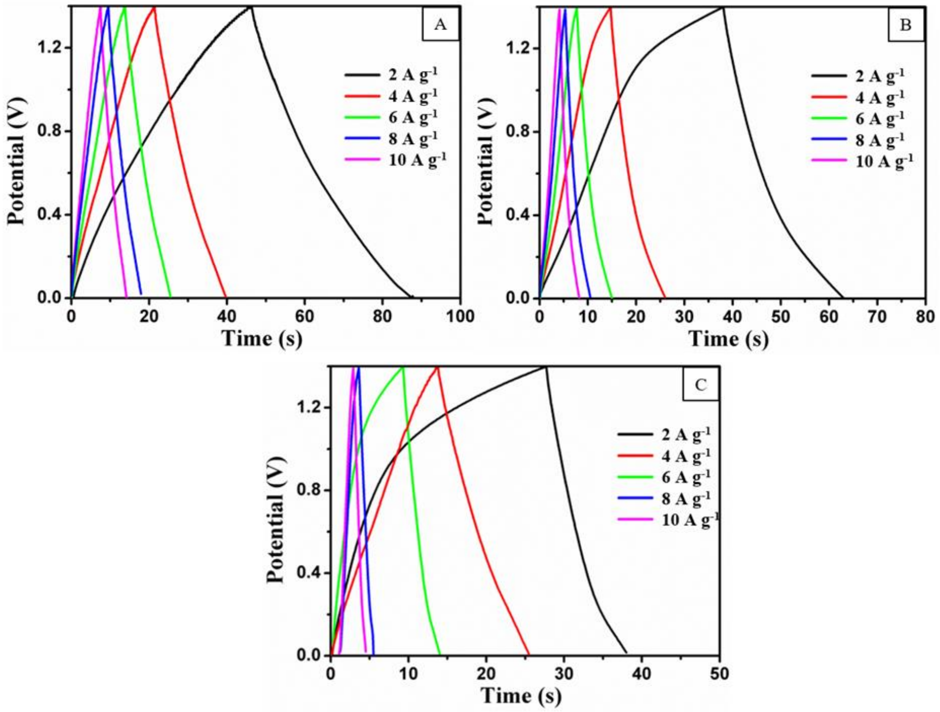

**Figure SF24:** Overlay of GCDs recorded in a two-electrode system at different current densities for (A) MP (B) MD, and (C) MA.

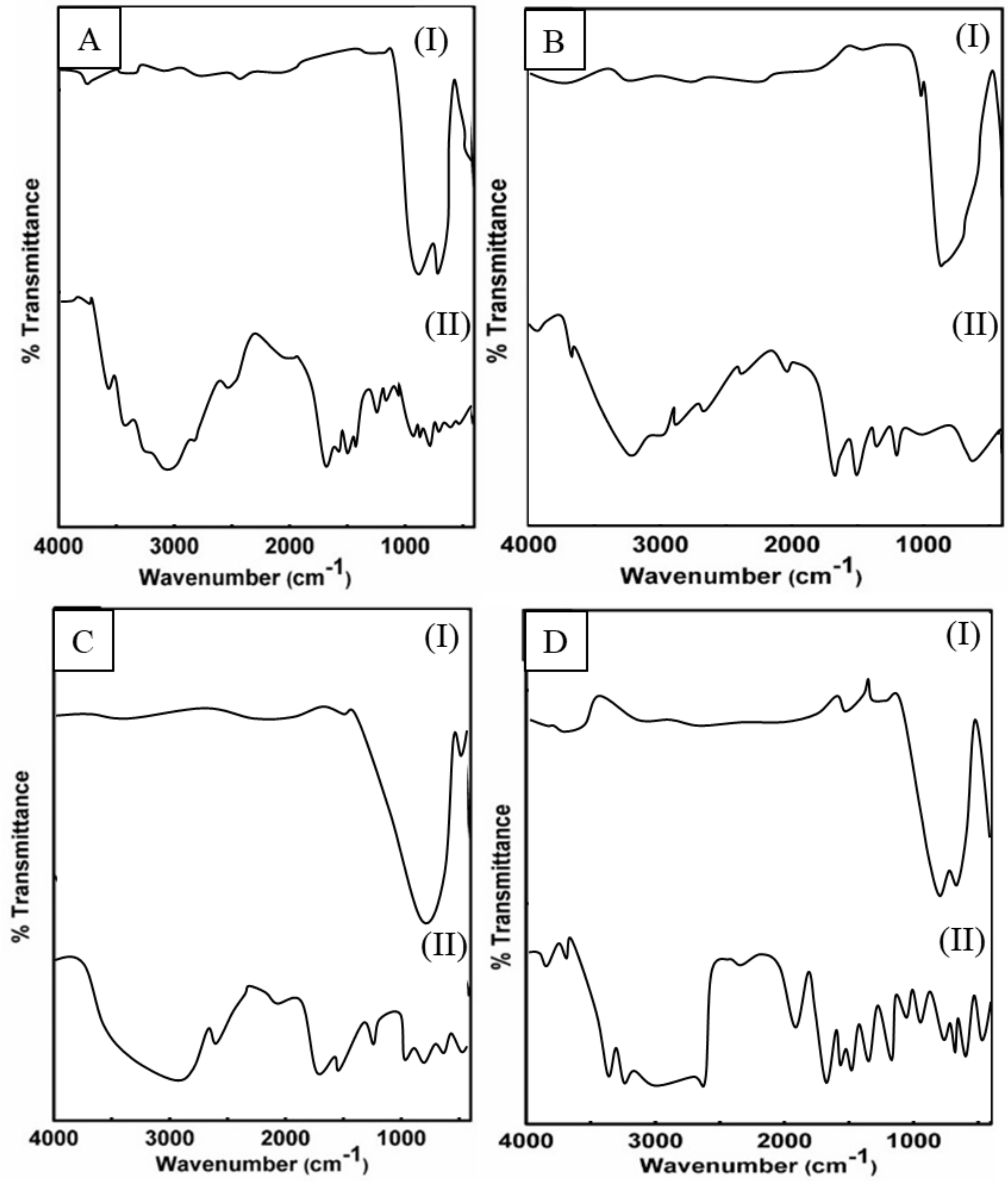

**Figure SF25:** IR studies of (A) MC (B) MM (C) MSC, and (D) MT, wherein (I) represents post calcination and (II) represents pre-calcination.

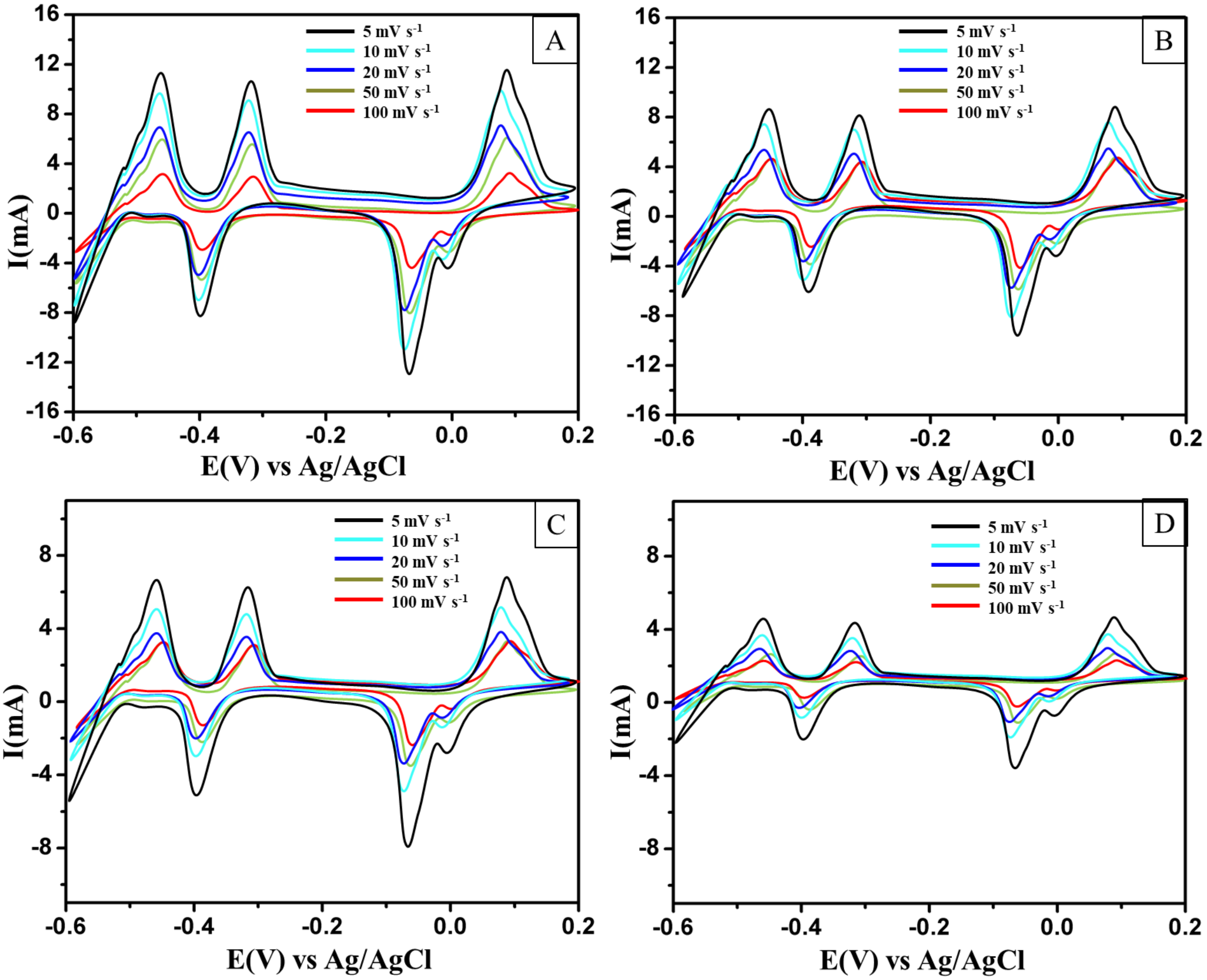

**Figure SF26:** Overlay of CVs recorded in a three-electrode system at different scan rates for (A) MC (B) MM (C) MSC, and (D) MT.

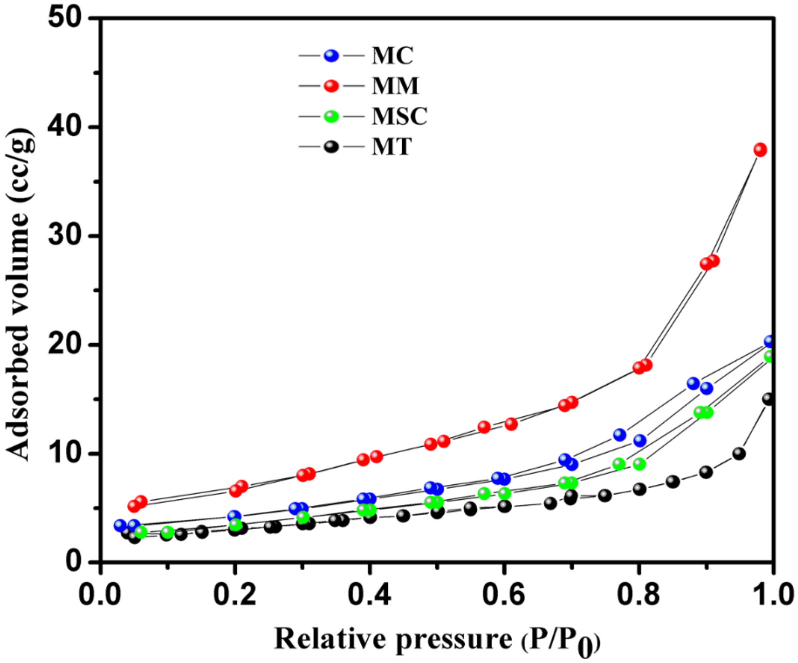

**Figure SF27:** BET surface area analysis for (A) MC (B) MM (C) MSC, and (D) MT.

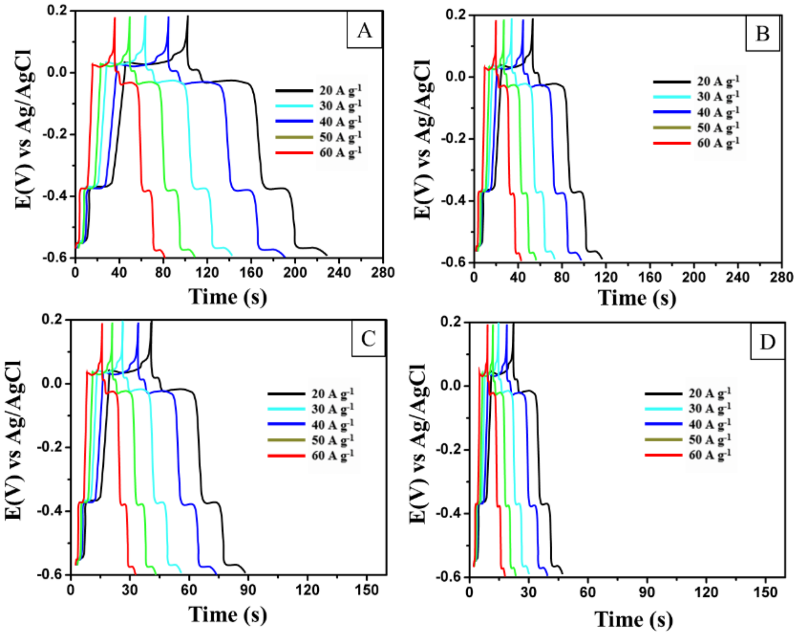

**Figure SF28:** Overlay of GCDs recorded in a three-electrode system at different current densities for (A) MC (B) MM (C) MSC, and (D) MT.

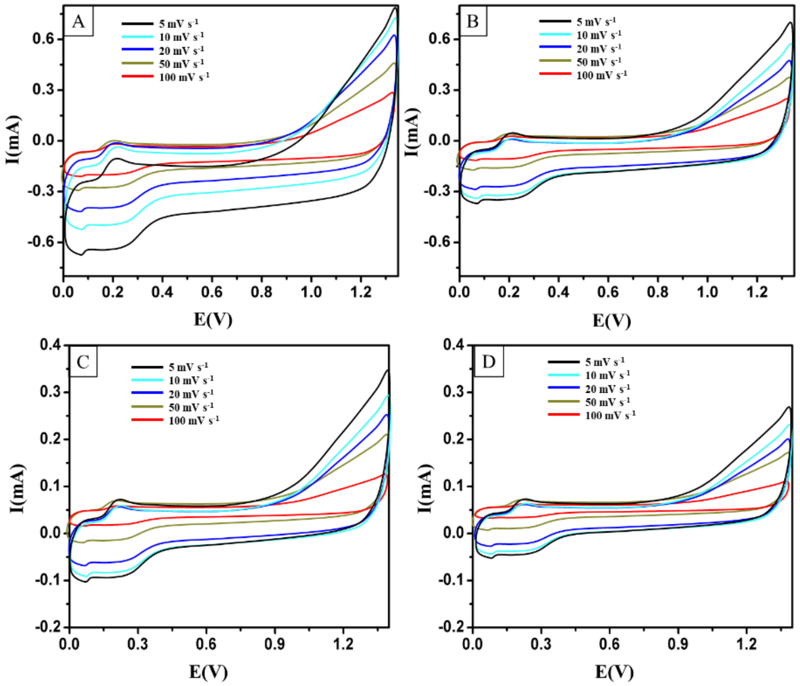

**Figure SF29:** Overlay of CVs recorded in a two-electrode system at different scan rates for (A) MC (B) MM (C) MSC, and (D) MT.

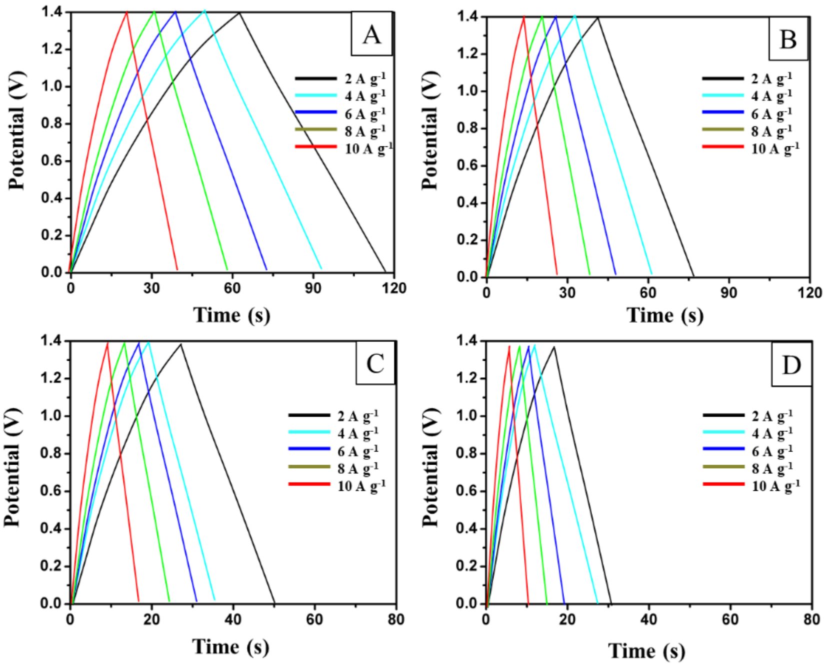

**Figure SF30:** Overlay of GCDs recorded in a two-electrode system at different current densities for (A) MC (B) MM (C) MSC, and (D) MT.

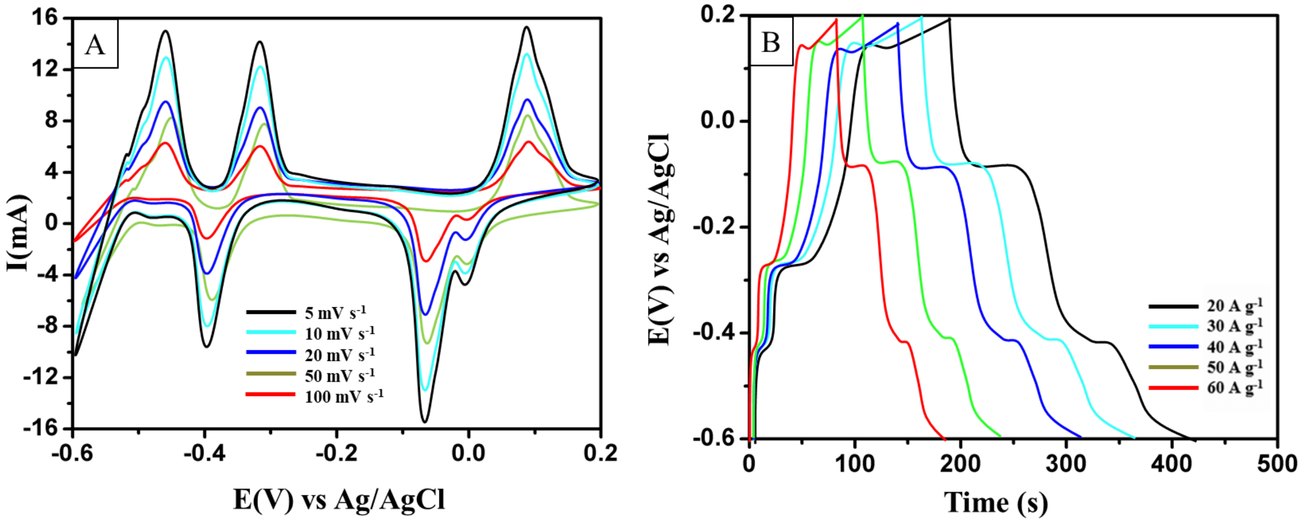

**Figure SF31:** Overlay of CVs and GCDs recorded in a three-electrode system at different scan rates and current densities for MMF.

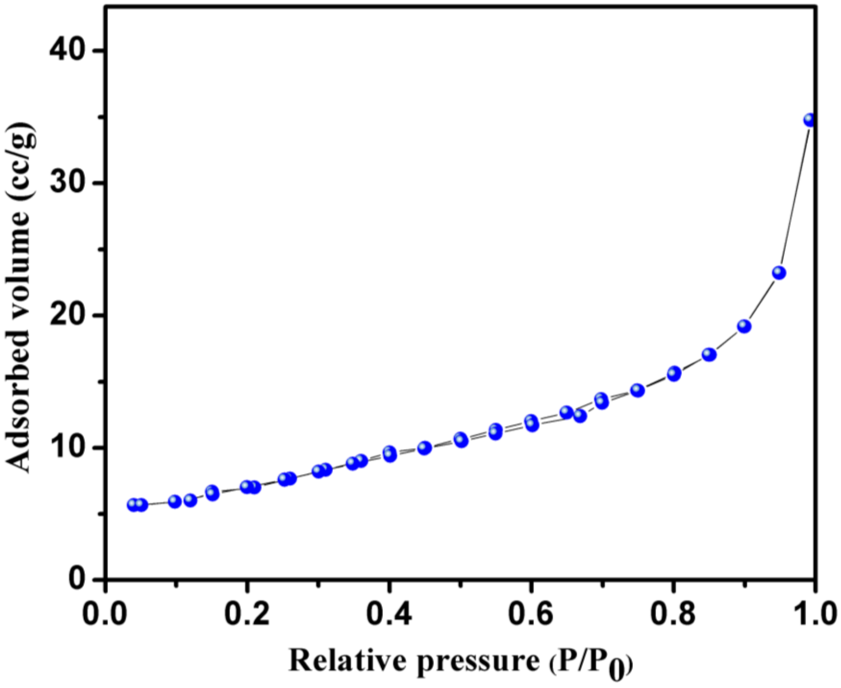

**Figure SF32:** BET surface area analysis for MMF.

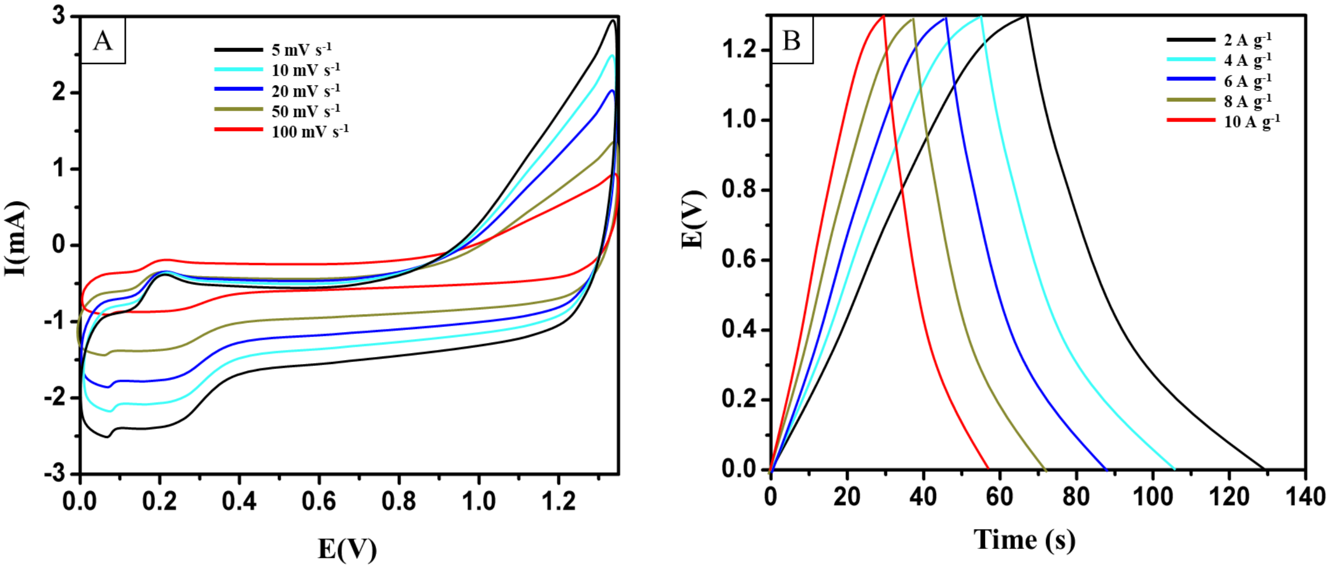

**Figure SF33:** Overlay of CVs GCDs recorded in a two-electrode system at different scan rates current densities for MMF.

# Appendix II

## Patent:

1. **Morajkar P. P.** and **Salkar A. V.**, Method for Synthesizing Tungsten Trioxide nanorods, 2018, Indian Patent No. 374807.

## Book chapter:

1. **Salkar, A. V.**; **Bhosale, S. V.**; **Morajkar, P. P.** 6 - Nanostructured $WO_{3-x}$ Based Advanced Supercapacitors for Sustainable Energy Applications. In *Advances in Metal Oxides and Their Composites for Emerging Applications*; Delekar, S. D., Ed.; Metal Oxides; Elsevier, 2022; 213–238.

## Research publications Appended to thesis:

1. **Salkar, A. V.**; Naik, A. P.; Joshi, V. S.; Haram, S. K.; **Morajkar, P. P.*** Designing a 3D Nanoporous Network: Via Self-Assembly of $WO_3$ Nanorods for Improved Electrocapacitive Performance. RSC, **CrystEngComm** 2018, *20* (42), 6683–6694. **(IF: 3.5)**
2. **Salkar, A. V.**; Fernandes, R. X.; Bhosale, S. V; **Morajkar, P. P.*** NH- and CH-Substituted Ureas as Self-Assembly Directing Motifs for Facile Synthesis and Electrocapacitive Applications of Advanced $WO_{3-x}$ One-Dimensional Nanorods. **ACS, Appl. Energy Mater.** 2019, *2* (12), 8724–8736. **(IF: 6.9)**
3. **Salkar, A. V.**; Naik, A. P.; Bhosale, S. V; **Morajkar, P. P.*** Designing a Rare DNA-Like Double Helical Micro Fiber Superstructure via Self-Assembly of In Situ Carbon Fiber-Encapsulated $WO_{3-x}$ Nanorods as an Advanced Supercapacitor Material. **ACS, Appl. Mater. Interfaces.** 2021**,** *3*, 1288-1300. **(IF: 10.3)**
4. **Salkar, A. V.**; Naik, A.P.; Guererro Pena, G.D.J.; Bharath, G.; Abu Haija, M.; Banat, F.; **Morajkar, P. P.*** 2D α-$MoO_{3-x}$ truncated microplates and microdisks as electroactive materials for highly efficient asymmetric supercapacitors. **ELSEVIER, Journal of Energy Storage.** 2022, *48,* 103958. **(IF: 8.9)**

## Other research publications through DST-INNO-INDIGO research project which provided research fellowship & financial support:

5. Biradar, M. R.; **Salkar, A. V.; Morajkar, P. P.***; Bhosale, S. V; Bhosale, S. V. High-Performance Supercapacitor Electrode Based on Naphthoquinone-Appended Dopamine Neurotransmitter as an Efficient Energy Storage Material. **RSC, *New J. Chem.*** 2021, *45* (11), 5154–5164. **(IF: 3.5)**

6. Biradar, M. R.; **Salkar, A. V.; Morajkar, P. P.***; Bhosale, S. V; Bhosale, S. V. Designing Neurotransmitter Dopamine-Functionalized Naphthalene Diimide Molecular Architectures for High-Performance Organic Supercapacitor Electrode Materials. **RSC, *New J. Chem.*** 2021, *45* (21), 9346–9357. **(IF: 3.5)**

7. Naik, A. P.; **Salkar, A. V.**; Peña, G. D. J. G. J. G.; Sawant, J. V.; Bharath, G.; Banat, F.; Bhosale, S. V.; **Morajkar, P. P.*** Facile Synthesis of Fibrous, Mesoporous $Ni_{1-x}O$ Nanosponge Supported on Ni Foam for Enhanced Pseudocapacitor Applications. **ELSEVIER, *J. Mater. Sci.*** 2020, *55* (26), 12232–12248. **(IF: 4.6)**

8. Shetgaonkar S., **Salkar A. V.** and **Morajkar P.P.*** Advances in Electrochemical and Catalytic performance of nanostructured $FeCo_2O_4$ and its composites, **Wiley, *Chemistry - An Asian Journal*,** 2021, *16*, 2871-2895. **(IF 4.8)**

9. Da Costa S., **Salkar A.V.**, Krishnasamy A., Fernandes R. X., **Morajkar P.P.***, Investigating the Oxidative Reactivity and Nanostructural Characteristics of Diffusion Flame Generated Soot Using Methyl Crotonate and Methyl Butyrate Blended Diesel Fuels. **ELSEVIER, *Fuel*** 2022, *309*, 122141. **(IF 6.6)**

10. Ali, W. A.; Bharath, G.; **Morajkar, P. P.**; **Salkar, A. V.**; Haija, M. A.; Banat, F. Morphology-Dependent Catalytic Activity of Tungsten Trioxide $WO_3$ Nanostructures for Hydrogenation of Furfural to Furfuryl Alcohol. **IOP Science, *J. Phys. D. Appl. Phys.*** 2021, *54* (30), 305502. **(IF: 3.2)**

11. **Morajkar, P. P.**; Guerrero, G. D. J.; Raj, A.; Elkadi, M.; Rahman, R. K.; **Salkar, A. V.**; Pillay, A.; Anjana, T.; Cha, M. S. Effects of Camphor Oil Addition to Diesel on the Nanostructures and Oxidative Reactivity of Combustion-Generated Soot. **ACS,**

***Energy & Fuels*** 2019, *33* (12), 12852–12864. **(IF: 3.6)**

12. Abdrabou, M. K.; **Morajkar, P. P.**; Guerrero Peña, G. D. J.; Raj, A.; Elkadi, M.; **Salkar, A. V.** Effect of 5-Membered Bicyclic Hydrocarbon Additives on Nanostructural Disorder and Oxidative Reactivity of Diffusion Flame-Generated Diesel Soot. **ELSEVIER,** ***Fuel*** 2020, *275*, 117918. **(IF: 6.6)**

13. **Morajkar, P. P.**; Abdrabou, M. K.; **Salkar, A. V.**; Raj, A.; Elkadi, M.; Anjum, D. H. Nanostructural Disorder and Reactivity Comparison of Flame Soot and Engine Soot Using Diesel and Jatropha Biodiesel/Diesel Blend as Fuels. **ACS,** ***Energy & Fuels*** 2020, *34* (10), 12960–12971. **(IF: 3.6)**

14. Biradar, M. R.; **Salkar, A. V.; Morajkar, P. P.**; Bhosale, S. V; Bhosale, S. V. Pyrazine-based organic electrode material for high-performance supercapacitor applications. **ELSEVIER,** ***Journal of Energy Storage***. 2022, *48*, 103953. **(Impact factor: 8.9)**

# Appendix III

## Participation and presentation at National & International conferences:

1. **A.V. Salkar**, R. X. Fernandes, S.V. Bhosale & P.P. Morajkar, "NH- and CH-substituted urea's as self-assembly directing motifs for facile synthesis and electrocapacitive applications of advanced $WO_{3-x}$ 1D nanorods" **(Poster)**, Advanced Materials for Renewable Energy and Sustainable Environment (AMRESE -2020), organized by Govt. College of Arts, Science & Commerce Khandola, Marcela Goa from January 31- February 1, 2020. (Poster No. P-5). **(Best Poster Prize)**
2. **A.V. Salkar**, A.P. Naik, S.V. Bhosale & P.P. Morajkar, "Designing a DNA-like double helical WO3-x/C microfiber superstructure for supercapacitor application" **(Oral)** Nanomaterials for Environmental Applications" (NFEA) **(Oral)** organized by Post-Graduate Department of Chemistry, P.E.S's R.S.N. College of Arts and Science, Farmagudi, Ponda-Goa on **)** on 28th & 29th December 2020. **(Best oral presentation prize)**
3. **A.V. Salkar**, A.P. Naik & P.P. Morajkar, "Synthesis of Nanostructured $WO_3$ nanorods for its electrochemical applications" **(Poster),** International conference on Advances in Material Science & Applied Biology (AMSAB 2019) organized by Narsee Monjee Institute of Management Studies (NMIMS), Mumbai from January 08-10, 2019. (Poster AMC 02)
4. **A.V. Salkar**, A.P. Naik & P.P. Morajkar, "Designing a 3D nanoporous network via self-assembly of $WO_3$ nanorods for improved electrocapacitive performance" **(Poster)**, National conference on Advancement in Science and technology (NCAST 2019) organized by Government College of Arts, Science & Commerce, Khandola, Goa on February 09, 2019. (Poster 09)
5. **A.V. Salkar**, A.P. Naik & P.P. Morajkar, "3D Nanostructured $WO_3$ with improved electrocapacitance" **(Poster)** Two- day workshop on Material Science between university of Porto, University of Coimbra and Goa university at the School of Chemical Sciences, Goa university on November 18-19, 2019. (Poster 04)

6. **A.V. Salkar**, A.P. Naik, S.V. Bhosale & P.P. Morajkar, "Designing a 3D nanoporous network via self-assembly of $WO_3$ nanorods for improved electrocapacitive performance" **(Poster)** National conference on Advancement in Science and technology (NCAST 2019) organized by Government College of Arts, Science & Commerce, Khandola, Goa on February 09, 2019. (Poster 09)
7. **A.V. Salkar** & P.P. Morajkar, "Nanostructured materials for advance catalysis" **(Oral)** INNO INDIGO S&T BiofCFD project workshop organized by the Department of Chemistry, University of Helsinki, Finland during July 21-24, 2019.
8. **A.V. Salkar**, A.P. Naik & P.P. Morajkar, "Designing nanostructured tungsten trioxide for improved electrocapacitive performance" **(Poster)** National conference on New Frontiers In Chemistry-From Fundamentals to Applications (NFCFA 2019) organized by BITS Pilani Goa from December 20-22, 2019. (Poster No.38)
9. Workshop on "Scientific writing" from May 07-10, 2019 organized by Department of Electronics in association with Electronics Alumni Association and IQAC, Goa University.
10. INNO INDIGO S&T BiofCFD project workshop organized by the Department of Chemistry, University of Helsinki, Finland during July 21-24, 2019.
11. International virtual conference on Advances in Molecular Material research (AMMR 2021) organized by Visva-Bharati, India, Osaka University, Japan and Jadavpur University, India on 3-5 February 2021.
12. Symposium on the theme "Frontiers in Organic Synthesis" organized by the School of Chemical Sciences, Goa University on 27th March 2021.
13. Symposium on "Recent Trends in Inorganic Chemistry" organized by the School of Chemical Sciences, Goa University on 24th April 2021.
14. International virtual symposium on "Fuels for Environmental Sustainability" organized by the Government College of Arts, Science and Commerce, Khandola, Goa on 8-9th October 2021.